Multiscale Modelling of Neurosteroid-mediated Seizure Trajectories in Childhood Absence Epilepsy

by

Maliha Ahmed

A thesis
presented to the University of Waterloo
in fulfillment of the
thesis requirement for the degree of
Doctor of Philosophy
in
Applied Mathematics

Waterloo, Ontario, Canada, 2025

© Maliha Ahmed 2025

Examining Committee Membership

The following served on the Examining Committee for this thesis. The decision of the Examining Committee is by majority vote.

External Examiner:	William Lytton Distinguished Professor, Dept. of Neurology, Downstate Health Sciences University
Supervisor(s):	Sue Ann Campbell Professor, Dept. of Applied Mathematics, University of Waterloo
Internal Member:	Brian Ingalls Professor, Dept. of Applied Mathematics, University of Waterloo Marek Stastna Professor, Dept. of Applied Mathematics, University of Waterloo
Internal-External Member:	Jeff Orchard Associate Professor, David R. Cheriton School of Computer Science, University of Waterloo

Author's Declaration

I hereby declare that I am the sole author of this thesis. This is a true copy of the thesis, including any required final revisions, as accepted by my examiners.

I understand that my thesis may be made electronically available to the public.

Abstract

Childhood absence epilepsy (CAE) is a pediatric generalized epilepsy disorder characterized by brief episodes of impaired consciousness and distinctive 2.5–5 Hz spike-wave discharges (SWDs) on electroencephalography. With a well-established genetic aetiology, this condition tends to resolve spontaneously during adolescence in most cases. While several mechanisms have been proposed for remission, understanding remains insufficient to guide early intervention practices.

In this thesis, we first utilize a conductance-based thalamocortical network model that exhibits characteristic SWDs, to demonstrate that allopregnanolone—a progesterone metabolite known to enhance GABAa receptor-mediated inhibition—has an ameliorating effect on SWDs. To investigate the divergence between this finding and clinical observations, we developed an enhanced thalamocortical model that incorporates a layered cortical structure to explore regional cortical heterogeneity and frontocortical connectivity as potential resistance factors to ALLO-mediated recovery. Our results suggest that non-resolving CAE may be due not only to increased frontocortical connectivity but also to the composition of cell types within the network. Specifically, a higher proportion of bursting-type cells may prevent the therapeutic effects of allopregnanolone. We extended our investigation to examine whether these findings apply to CAE caused by different genetic mechanisms, particularly mutations in sodium channel genes by modelling their effects at the individual neuron level. Furthermore, we examined the degree to which these alterations lead to network-level pathological activity, as well as the influence of ALLO on these genetically distinct networks. Our results demonstrate that ALLO facilitates recovery from SWDs regardless of the underlying mutation type. However, enhanced frontocortical connectivity prevents recovery in some mutation types, particularly when mutation effects are severe.

Altogether, the multi-scale computational framework developed in this thesis demonstrates that CAE remission is determined by complex interactions between hormonal influences, genetic factors, and network connectivity patterns. The results suggest that certain genetic mutations may predispose individuals toward either remission or non-remission, which can be further modulated by connectivity profiles. In particular, enhanced frontocortical connectivity appears to be a significant factor in resistance to hormone-mediated remission. Additionally, this thesis develops techniques for analyzing transitions between distinct dynamical states in neural systems, incorporates genetic and hormonal factors into conductance-based models, and provides a computational framework to identify key parameters governing epileptic activity. These approaches not only advance our understanding of CAE specifically, but offer generalizable insights into the mathematical modelling of neurological conditions characterized by spontaneous shifts in brain dynamics.

Acknowledgements

Alhamdulillah. All praise is due to Allah Almighty for His countless blessings. By His grace, I have been blessed with the opportunity to acquire knowledge and complete this work, so it may benefit others.

First and foremost, I would like to thank my supervisor, Dr. Sue Ann Campbell, for her guidance and unwavering support throughout this journey. I am deeply grateful for your incredible patience during the breakthroughs and the breakdowns. Whenever needed, you provided me with assurance and optimism, and for that, I will always be grateful.

I would also like to thank Dr. Brian Ingalls, Dr. Marek Stastna, Dr. Jeff Orchard, and Dr. William Lytton for being a part of my PhD advisory and examination committee, and for dedicating your time to read this thesis. I am especially grateful to Dr. Ingalls for his support and availability in answering my questions, and to Dr. Stastna for inspiring me to present my results in new ways and encouraging me to aim high.

I am deeply grateful to the following individuals for their unique and invaluable contributions throughout my academic journey: Dr. Ghazal Geshnizjani, Dr. Parker Glynn-Adey, Dr. Yu-Ru Liu, and Dr. Zohreh Shahbazi.

I am incredibly blessed to have my family—without whom this journey would not have been possible. To my parents, Yaseen Sultana and Zaki Ahmed, thank you for your guidance, your sacrifices, and for being my pillars of strength throughout my life. To my brothers, Uqba and Shahbaz, thank you for always being my source of guidance and comfort. To my sisters, Tayyaba and Madeeha, thank you for being my cheerleaders and for your unwavering belief in me. To Safa and Hana, thank you for brightening our lives and being a beautiful distraction from work.

Thank you to my dearest colleagues and friends—Ala' Alalabi, Amrita Punnavajhala, Megha Manoj, Sefah Frimpong, and Stéphanie Abo—for your selflessness, our countless discussions about research and life, for standing by me through challenges, and for celebrating my achievements. To my forever hero, Shah Rukh Khan, thank you for being my most unconventional source of wisdom in life. A special thank you to Apinaiya, Arooj, and Seun for your constant support through it all.

Finally, to all my family members and friends who have given their support, encouragement, and blessings, I am deeply grateful.

Dedication

This thesis is dedicated to my parents, Zaki Ahmed and Yaseen Sultana. *JazakAllah Khair* for **everything**.

Table of Contents

Examining Committee ii

Author's Declaration iii

Abstract iv

Acknowledgements v

Dedication vi

List of Figures xi

List of Tables xxiv

1 Introduction 1

2 Background 8

2.1 Neuroanatomy 8

2.2 Neuron electrophysiology 13

2.3 Modelling neurons 15

2.3.1 Experimental characterization of ionic currents 19

2.3.2 Hodgkin-Huxley model 19

2.3.3 Compartmental modelling of neurons 22

2.4 Modelling synapses . . . 23
2.5 Simulating using NEURON and NetPyNE . . . 25
2.6 Thalamocortical circuitry and generation of spindles and spike-wave discharges 27
2.7 Neurotransmitters, hormones and absence epilepsy . . . 29
2.7.1 Neurotransmitter function and absence epilepsy . . . 29
2.7.2 Hormones and absence epilepsy . . . 30
2.7.3 Hormones and their mechanisms of action . . . 31

3 Modelling the effect of allopregnanolone on the resolution of spike-wave discharges 33

3.1 Introduction . . . 34
3.2 Materials and methods . . . 36
3.2.1 Modelling the effect of genetic mutations on GABAa and T-type Ca^{2+} currents . . . 39
3.2.2 Modelling the effect of allopregnanolone . . . 40
3.3 Results . . . 41
3.3.1 Baseline healthy and diseased states using control synapses . . . 41
3.3.2 Allopregnanolone has an ameliorating effect on SWDs . . . 42
3.3.3 Exploring the selective action of allopregnanolone . . . 45
3.4 Discussion . . . 46
3.5 Conclusion . . . 50

4 A minimal thalamocortical model for investigating regional cortical heterogeneity and frontocortical connectivity in childhood absence epilepsy network dynamics 51

4.1 Introduction . . . 52
4.2 Materials and methods . . . 53
4.2.1 Model description . . . 53
4.2.2 Model fitting procedure . . . 59

4.2.3 Tools for analysis . . . 66
4.2.4 Modelling the effect of genetic mutations on GABAa current . . . 68
4.2.5 Modelling the effect of allopregnanolone . . . 68
4.2.6 Modelling regional neuronal heterogeneity and enhanced frontocortical connectivity . . . 69
4.3 Results . . . 71
4.3.1 Baseline state characterization and allopregnanolone effects on the fitted model . . . 71
4.3.2 Regional neuronal heterogeneity in the cortex does not alter ALLO-mediated network dynamics . . . 73
4.3.3 Enhanced frontocortical connectivity alters SWD resolution based on network architecture . . . 75
4.4 Discussion . . . 76
4.5 Conclusion . . . 78

5 Modelling the impact of sodium channel mutations on remission and non-remission in childhood absence epilepsy 89

5.1 Introduction . . . 90
5.2 Materials and methods . . . 91
5.2.1 Modelling voltage-gated sodium channel mutations . . . 92
5.2.2 Modelling and evaluating the effect of mutations on network activity 95
5.3 Results . . . 97
5.3.1 Effects of *SCN2A* and *SCN8A* mutations on single neuron activity in the cortex and thalamus . . . 97
5.3.2 *SCN2A* and *SCN8A* mutations associated with remission are modulated by frontocortical connectivity and variant-specific factors . . . 103
5.4 Discussion . . . 108
5.5 Conclusion . . . 111

6 Conclusions 116

References **119**

APPENDICES **139**

A Appendix for Chapter 3 **140**

A.1 Model components . . . 140

A.1.1 Summary of currents . . . 141

A.1.2 Calcium dynamics . . . 145

A.1.3 Synaptic dynamics . . . 146

A.2 Model parameters . . . 147

B Appendix for Chapter 4 **149**

B.1 Model components . . . 149

B.1.1 Summary of currents . . . 151

B.1.2 Calcium dynamics . . . 160

B.1.3 Synaptic dynamics . . . 161

B.2 Model parameters . . . 163

B.3 Model fitting: choice of fitting parameters . . . 163

B.4 Model fitting: staged parameter fitting process . . . 167

B.5 Synchrony measure . . . 171

B.6 Allopregnanolone application experiment curve fitting . . . 175

C Appendix for Chapter 5 **177**

C.1 Redefining steady-state activation/inactivation of I_{Naf} in TC and RE cells 177

C.2 Effect of modifying the maximal I_{K2} conductance in modelling the $SCN2A$ mutation . . . 179

List of Figures

1.1 Electroencephalographic (EEG) recordings in human patients displaying spindle oscillations (A) and an approximately 3 Hz spike-wave pattern (B). Adapted from a public domain image and [24], respectively; both via Wikimedia Commons. 2

1.2 Spectrum of mathematical models used in computational neuroscience, organized along two primary axes: biological realism and scale. Exemplar models are positioned according to their typical level of abstraction and spatial scale [85, 124, 192, 106, 49, 20, 159, 93, 147, 205, 65, 150, 72, 91, 33]. 5

2.1 An illustration of a typical pyramidal neuron. Created with BioRender.com. 9

2.2 An example of an action potential. 9

2.3 The four major lobes of the cerebral cortex–frontal, parietal, temporal, and occipital–along with the thalamus. Created with BioRender.com. 10

2.4 Schematic illustrating projections from and within the layered structure of the cortex (pink), including inputs from the thalamus (blue). Arrows indicate the direction of projection. Created with BioRender.com. 12

2.5 Examples of neuronal firing patterns include tonic or regular spiking (left), bursting (middle), and spike-frequency adaptation (right). 13

2.6 Schematic of a chemical synapse illustrating neurotransmitter release from the presynaptic axon terminal upon excitation (green signal), followed by receptor binding on the postsynaptic membrane. The resulting postsynaptic response may be excitatory (blue) or inhibitory (red), depending on the type of neurotransmitter involved. Created with BioRender.com. 14

2.7 An equivalent electrical circuit representation of a neuronal membrane with multiple ion channels. Created with BioRender.com. 16

2.8 Demonstration of the effects of varying $V_{1/2}$ (A) and k (B) on the steady-state activation curve described by Equation (2.12) (and similarly for Equation (2.13)). Shifting $V_{1/2}$ in the depolarizing or hyperpolarizing direction alters the voltage at which the ion channel transitions between states, while modifying k changes the steepness of this transition. 20

2.9 Steady-state functions (A) and voltage-dependent time constants (B) for the gating variables m, h, and n in the Hodgkin-Huxley model given by Equations (2.14)–(2.18). The resting potential is at $V = 0$ mV and marked by a closed circle on each curve. 21

2.10 (A): Responses of the Hodgkin-Huxley model to varying I_{app} (in $\mu A/cm^2$) given as a pulse input for a duration of 10ms or 80ms (for the longer train of action potentials). (B): A simulated single action potential together with the time course of each gating variable, for $I_{app} = 2.3\mu A/cm^2$. 22

2.11 Comparison of single-compartment and multi-compartment neuron models. (Left): A single-compartment model represents the neuron as a single cylindrical segment with a single equivalent electrical circuit. (Right): A multi-compartment model divides the neuron into multiple connected segments, each modelled with its own circuit components. Created with BioRender.com. 23

2.12 The schematic diagram of the thalamocortical circuit shows the connections between cortical pyramidal neurons (PY), cortical interneurons (IN), thalamic relay neurons (TC) and thalamic reticular neurons (RE). Blue arrows indicate excitatory connections, while red arrows represent inhibitory connections. 28

3.1 Schematic representation of the thalamocortical network. Each neuron is represented by a dot, and each layer consists of 100 cells with synaptic connectivity within and between layers as shown. Within the cortex and thalamus, each neuron connects to 11 postsynaptic neurons while between the cortex and thalamus, each neuron connects to 21 postsynaptic neurons as shown. Adapted from Destexhe et al. [49]. 39

3.2 A comparison of simulated GABA current for a single spike using parameters corresponding to Control and post-ALLO synapses given by Equations (3.10)–(3.11) and Table 3.1. 41

3.3 A raster plot of the full network exhibiting spindle oscillations (A) and SWD (B) behaviour. The network in (B) was simulated using the cortical disinhibition mechanism only. (C): Network behaviour corresponding to spindle oscillations exhibits maximal power at a frequency of 8.5 Hz. (D): SWD behaviour using the cortical disinhibition mechanism results in maximal power at 4.5 Hz. (E): The network displays SWD behaviour using the altered-Ca^{2+} conductance mechanism with maximal power at approximately 3.5 Hz. All of the simulations were performed using Control GABAa-receptor mediated synapses. 43

3.4 Heatmap showing relative power in the frequency range corresponding to SWDs for combinations of cortical GABAa conductance (given as % baseline value) and a vertical shift in the inactivation time of the T-type Ca^{2+} current in RE neurons. Label C corresponds to network behaviour as simulated in Figure 3.3C exhibiting spindle oscillations, Label D corresponds to simulation in Figure 3.3D exhibiting SWDs, and Label E corresponds to simulation in Figure 3.3E exhibiting SWDs using a mixed-mechanism approach as described in Section 3.3.1. Note: there is a change in scale along the horizontal axis at a value of 15% baseline maximal GABAa conductance. 44

3.5 Power spectral density for network behaviour simulated using Control synapses (A and C) and post-ALLO synapses (B and D). (A,B): The network was initialized using the cortical disinhibition mechanism only (8% baseline cortical GABAa conductance). (C,D): The network was initialized using the altered Ca^{2+} conductance and GABAa conductance mechanism (τ_0 = 60 ms and cortical GABAa at 25% of baseline). The shaded regions represent relative power in either the SWD (2.5–5 Hz; red) or Spindles (7–10 Hz; green) frequency range. Note that the y-axes differ between panels to reflect differences in maximal power, which result from distinct disease mechanisms. 45

3.6 Relative power in frequency range corresponding to spindle oscillations and spike-wave discharges (A) and the peak frequency (B) for network simulations with post-ALLO synapses between specific neuron types in the cortex and thalamus. For all the simulations, the diseased state was produced using the cortical disinhibition mechanism only. (C): Power spectral density for network behaviour after implementing the effect of ALLO only on IN-PY and RE-TC synapses together. 47

4.1 Schematic representation of the thalamocortical network. Each neuron is represented by a dot with synaptic connectivity within and between layers as shown. The number of postsynaptic neurons each neuron connects to varies by layer and is represented by the highlighted groups as shown. . . . 56

4.2 Characterizing spindle oscillations in the cortex. (Left): Raster plot of cortical pyramidal (PY) population illustrating across-population synchrony. (Right): Close-up of individual traces of the first 30 PY cells illustrating single spikes with a few doublets. These simulations were obtained using our previous model [3]. 60

4.3 Characterizing spindle oscillations in the thalamus. (Left): Raster plot of TC population illustrating alternating bursts of synchrony across population. (Right): Close-up of individual traces of the first 30 TC cells illustrating doublet spiking with some single spikes. These simulations were obtained using our previous model [3]. 61

4.4 For each synapse type, select values of $\bar{g}_{syn}$, α and β used to perform a grid search. 63

4.5 (A): For each synapse type, multiple parameter triplets ($\bar{g}_{syn}$, α, β) yielded good fits (solid blue points). Points with gray outlines represent the sampled parameter space, with solid red points indicating our selected parameter triplets. (B): Testing model sensitivity to deviations from the nominal values (solid red points) by up to 75% (RSRS and RSIB), 90% (RSNRS), and 65% (RSLTS) in each parameter dimension. Transparent points with blue outlines represent good fits as in panel A, and in black outlines, the parameter cloud tested for sensitivity. Solid green points indicate parameter sets that maintained good network performance despite these deviations. 65

4.6 A comparison of the relative changes in $\bar{g}_{max}$, α, β and T_{dur} between control GABAa receptor activity and activity post-application of ALLO based on fitting the solution of equation (4.19)–(4.21) to data from different studies. Note that the multiple bars for (Sullivan and Moenter, 2003) represent different amounts of ALLO application used in the same study, in order of increasing concentration. The experimental parameters we used to model the effect of ALLO is highlighted in dark red. 70

4.7 A comparison of GABA concentrations versus allopregnanolone concentrations used across different studies, illustrating their physiological relevance. Points in the upper-left corner represent more physiologically relevant conditions (higher GABA, lower allopregnanolone concentrations). The experimental parameters from the study highlighted in red were used as the basis for modelling the effect of ALLO. 71

4.8 A schematic diagram of the thalamocortical circuit shows connections between cortical neurons of the RS, IB, NRS, and LTS type, and thalamic neurons (TC and RE). Blue arrows indicate excitatory synaptic connections, while red arrows represent inhibitory ones. Enhanced frontocortical connectivity is illustrated with thicker green arrows, which also represent excitatory synapses. 72

4.9 Raster plot of the 72-25 (nIB:nRS) fitted model demonstrates spindle oscillations (A), transitioning to spike-wave discharges (D) through cortical disinhibition, modelled as a reduction in baseline GABAa conductance from 100% to 10%. (B) and (E): Sample voltage traces from cell index 0 in each population, with LFP traces (in blue) computed using the method outlined in Section 4.2.3. The network activity during spindle oscillations exhibits a peak power at 7 Hz (C), whereas the SWD state shows peak power at 5 Hz (F). All simulations were conducted using Control GABAa-receptor mediated synapses. 80

4.10 Network frequency response to varying levels of cortical GABAa-receptor mediated inhibition. The colour of each bar represents the relative power within the frequency range associated with SWDs. 81

4.11 Power spectral density of the 75-25 (nIB:nRS) fitted model using Control synapses (A) and post-ALLO synapses (B), calculated from filtered LFP traces (in orange), as described in Section 4.2.3. The network was initialized with cortical disinhibition (10% baseline cortical GABAa conductance). Shaded regions indicate relative power within the frequency ranges associated with SWDs (2.5–5 Hz; red) or Spindle oscillations (7–10 Hz; green). . 81

4.12 Network frequency response to varying levels of cortical GABAa-receptor mediated inhibition, using the 5-95 (left) and 95-5 (right) (nIB:nRS) model configurations. The colour of each bar represents the relative power within the frequency range associated with SWDs. 82

4.13 Spectral power analysis showing time-frequency representations of network activity for the 5-95 and 95-5 (nIB:nRS) model configurations, using 100% (A, C) and 10% (B, D) baseline cortical GABAa conductance. For both models, fully inhibited networks exhibit maximal power at 7.5 Hz, while partially disinhibited networks show maximal power at 5 Hz. LFP traces (in blue) were calculated using the population-based method described in Section 4.2.3. 83

4.14 Power spectral density of the 5-95 (A1–A3) and 95-5 (C1–C3) (nIB:nRS) model configurations, calculated from filtered LFP traces (in orange). Shaded regions indicate relative power within the frequency ranges associated with SWDs (2.5–5 Hz; red) or Spindle oscillations (7–10 Hz; green). (A1, C1): Networks with Control synapses and full cortical inhibition, exhibiting spindle oscillations at 7.5 Hz. (A2, C2): Networks with Control synapses and reduced cortical GABAa conductance (10% baseline), exhibiting SWDs at 5 Hz. (A3, C3): Networks initialized with cortical disinhibition as in (A2, C2) but using post-ALLO synapses, showing transition to a physiological state under the effect of allopregnanolone. (B1): Relationship between relative power in spindles range and peak network frequency for fully inhibited networks. (B2): Relationship between relative power in SWDs range and peak network frequency for partially disinhibited networks. (B3): Relationship between relative power in spindles range and peak network frequency for networks under the effect of ALLO. 84

4.15 Spectral power analysis showing time-frequency representations of network activity for the 50-50 (nIB:nRS) model configuration with enhanced frontal cortical connectivity, using $(F_{IBIB}, F_{IBNRS}, F_{NRSIB}) = (7, 5, 3)$. (A): Network behaviour using Control synapses and full cortical inhibition exhibits maximal power at 5.5 Hz. (B): Network behaviour using Control synapses under partial disinhibition (10% baseline cortical GABAa conductance) shows maximal power at 4 Hz. (C) Network initialized with cortical disinhibition as in (B) but using post-ALLO synapses shows a lack of restorative effect from ALLO, with a maximal frequency of 2.5 Hz. LFP traces (in blue) were calculated using the method described in Section 4.2.3. 85

4.16 3D visualization of the grid search results across $8^3 = 512$ parameter combinations within the $(F_{IBIB}, F_{IBNRS}, F_{NRSIB})$ parameter space using the 50-50 (nIB:nRS) model configuration. (A–C): Initial search using Control synapses with cortical GABAa conductance at 10% baseline, were filtered by examining the magnitude of: (A): relative power within spindles range, (B) relative power within SWDs range, and (C): peak frequency from power spectral density analysis. (D): Filtered parameter combinations from the initial search. (E): Parameter combinations that produce spindle-like oscillations when simulated with cortical GABAa conductance restored to normal (100% baseline) levels. (F): Parameter combinations that produce continued SWDs (in red) when the network is simulated using 10% baseline cortical GABAa conductance and post-ALLO synapses. (G): Final parameter set of $(F_{IBIB}, F_{IBNRS}, F_{NRSIB})$ for which the 50-50 (nIB:nRS) model exhibits continued SWDs post application of ALLO. 86

4.17 Power spectral density of the 5-95 (A1–A3) and 95-5 (C1–C3) (nIB:nRS) model configurations with enhanced frontal cortical connectivity, calculated from filtered LFP traces (in orange). Shaded regions represent relative power within frequency ranges associated with SWDs (2.5–5 Hz; red) or Spindle oscillations (7–10 Hz; green). (A1, C1): Networks with Control synapses and full cortical inhibition, exhibiting spindle oscillations at 6.5 Hz and 7 Hz for the 5-95 and 95-5 models, respectively. (A2, C2): Networks with Control synapses and reduced cortical GABAa conductance (10% baseline), exhibiting SWDs at 4 Hz and 3 Hz for the 5-95 and 95-5 model, respectively. (A3, C3): Networks initialized with cortical disinhibition as in (A2, C2) but using post-ALLO synapses. The transition to a physiological state under the effect of allopregnanolone occurs for the 5-95 model configuration, but not the 95-5 model. (B1): Relationship between relative power in spindles range and peak network frequency for fully inhibited networks (B1) and networks under the effect of ALLO (B3). (B2): Relationship between relative power in SWDs range and peak network frequency for partially disinhibited networks. 87

4.18 Comparison of network responses between the 5-95 and 95-5 (nIB:nRS) model configurations under two cortical GABAa conductance conditions (100% and 10% baseline). (A, C): Relative power in the spindle/SWDs frequency range. (B, D): Corresponding peak frequencies of network activity. Each condition is shown under baseline (orange) and increased frontocortical connectivity (purple). 88

5.1 (A) and (B): Voltage traces of Layer 5 Regular Spiking (RS) cortical neuron for varying input currents and mutation strengths (with input current held at 1.7 nA for 500 ms) for each $SCN2A$ and $SCN8A$ mutation type. (C): Spike-count response curve with each $SCN2A$ and $SCN8A$ mutation strength fixed at 75% and 20% respectively. 99

5.2 (A) and (B): Voltage traces of Layer 5 Intrinsically Bursting (IB) cortical neuron for varying input currents and mutation strengths (with input current held at 1.2 nA for 500 ms) for each $SCN2A$ and $SCN8A$ mutation type. (C): Spike-count response curve with each $SCN2A$ and $SCN8A$ mutation strength fixed at 75% and 20% respectively. 100

5.3 (A) and (B): Voltage traces of Layer 6 Non-tufted Regular Spiking (NRS) cortical neuron for varying input currents and mutation strengths (with input current held at 1.4 nA for 500 ms) for each $SCN2A$ and $SCN8A$ mutation type. (C): Spike-count response curve with each $SCN2A$ and $SCN8A$ mutation strength fixed at 75% and 15% respectively. 101

5.4 (A) and (B): Voltage traces of Low-threshold Spiking (LTS) Interneuron in the cortex for varying input currents and mutation strengths (with input current held at 0.6 nA for 500 ms) for each $SCN2A$ and $SCN8A$ mutation type. (C): Spike-count response curve with each $SCN2A$ and $SCN8A$ mutation strength fixed at 75% and 15% respectively. 102

5.5 Exploring the effect of the strength of $SCN2A$ mutation on the mean amplitude of action potentials and spike count in Layer 5 RS (A), Layer 5 IB (B), Layer 6 NRS (C), and Deep LTS (D) cortical cells. The applied input current was held at 1.7, 1.2, 1.4, and 0.6 nA respectively. 103

5.6 Exploring the effect of the strength of each $SCN8A$ mutation type on the mean amplitude of action potentials and spike count in Layer 5 RS (A), Layer 5 IB (B), Layer 6 NRS (C), and Deep LTS (D) cortical cells. The applied input current was held at 1.7, 1.2, 1.4, and 0.6 nA respectively. . . 104

5.7 (A): Voltage traces of thalamacortical (TC) neuron for varying input currents and mutation strengths (with input current held at 0.7 nA for 500 ms) for each $SCN8A$ mutation type. (B): Spike-count response curve with each mutation strength fixed at 60%. 105

5.8 Exploring the effect of the strength of each $SCN8A$ mutation type on the mean amplitude of action potentials (A) and spike count (B) in the TC cell. The applied input current was held at 0.7 nA. The inset in the left panel is a close-up of the curves corresponding to $Scn8a^{med-jo}$ and $Scn8a^{V929F}$. . . 106

5.9 (A): Voltage traces of thalamic reticular (RE) neuron for varying input currents and mutation strengths (with input current held at 0.5 nA for 500 ms) for each $SCN8A$ mutation type. (B): Spike-count response curve with each mutation strength fixed at 60%. 107

5.10 Exploring the effect of the strength of each $SCN8A$ mutation type on the spike count (A), mean spike amplitude of the initial burst (B) and the time to last spike (C) in the RE cell. The applied input current was held at 0.5 nA. 107

5.11 Effects of the $Scn2a^{+/-}$ mutation on network behaviour and response to allopregnanolone. (A): Mutation scores across different target cell types and mutation strengths up to 150%. Lower scores (red) indicate pathological activity, while higher scores (blue) indicate deviations away from this pattern. (B): Occurrence of spike-wave discharge (SWD) states, defined as network frequency between 2.5–5 Hz and maximal power within the SWD-associated frequency range. (C1–C2): Comparison of mutation scores (C1) and peak network frequency (C2) between Control (blue) and post-ALLO (orange) conditions at varying mutation strengths during which the network exhibited a SWD state. (C3–C4): Comparison of mutation scores (C3) and peak network frequency (C4) between networks with frontocortical connectivity at baseline levels (orange) and increased levels (purple). The orange bars are identical to those shown in (C1–C2) for comparison. 112

5.12 Effects of the $Scn8a^{V929F}$ mutation on network behaviour and response to allopregnanolone. (A): Mutation scores across different target cell types and mutation strengths up to 100%. Lower scores (red) indicate pathological activity, while higher scores (blue) indicate deviations away from this pattern. (B): Occurrence of spike-wave discharge (SWD) states, defined as network frequency between 2.5–5 Hz and maximal power within the SWD-associated frequency range. SWD states were observed when the target population included only LTS cells or both LTS and RE cells, at specific mutation strengths. (C1–C2, D1–D2): Comparison of mutation scores (C1, D1) and peak network frequency (C2, D2) between Control (blue) and post-ALLO (orange) conditions at varying mutation strengths during which the network exhibited an SWD state—when the target population consisted only of LTS cells (C1–C2) or both LTS and RE cells (D1–D2). (C3–C4, D3–D4): Comparison of mutation scores (C3, D3) and peak network frequency (C4, D4) between networks with frontocortical connectivity at baseline levels (orange) and increased levels (purple) for each corresponding target population group. The orange bars are identical to those shown in (C1–C2, D1–D2) for comparison. 113

5.13 Effects of the $Scn8a^{med-jo}$ mutation on network behaviour and response to allopregnanolone. (A): Mutation scores across different target cell types and mutation strengths up to 100%. Lower scores (red) indicate pathological activity, while higher scores (blue) indicate deviations away from this pattern. (B): Occurrence of spike-wave discharge (SWD) states, defined as network frequency between 2.5–5 Hz and maximal power within the SWD-associated frequency range. (C1–C2): Comparison of mutation scores (C1) and peak network frequency (C2) between Control (blue) and post-ALLO (orange) conditions at varying mutation strengths during which the network exhibited a SWD state. (C3–C4): Comparison of mutation scores (C3) and peak network frequency (C4) between networks with frontocortical connectivity at baseline levels (orange) and increased levels (purple). The orange bars are identical to those shown in (C1–C2) for comparison. 114

5.14 Effects of the $Scn8a^{med}$ mutation on network behaviour and response to allopregnanolone. (A): Mutation scores across different target cell types and mutation strengths up to 100%. Lower scores (red) indicate pathological activity, while higher scores (blue) indicate deviations away from this pattern. (B): Occurrence of spike-wave discharge (SWD) states, defined as network frequency between 2.5–5 Hz and maximal power within the SWD-associated frequency range. (C1–C2): Comparison of mutation scores (C1) and peak network frequency (C2) between Control (blue) and post-ALLO (orange) conditions at varying mutation strengths during which the network exhibited a SWD state. (C3–C4): Comparison of mutation scores (C3) and peak network frequency (C4) between networks with frontocortical connectivity at baseline levels (orange) and increased levels (purple). The orange bars are identical to those shown in (C1–C2) for comparison. 115

B.1 Exploring how variations in synaptic parameters affect postsynaptic firing in a 2-cell network of layer 6 non-tufted regular spiking (NRS) neurons. Using default parameters ($g_{max} = 1\mu$S, $\alpha = 0.94(\text{ms} \cdot \text{mM})^{-1}$, $\beta = 0.18\text{ms}^{-1}$, $C_{max} = 0.5$ and $C_{dur} = 0.3$), distorted firing is observed in *Cell 1* (A), which is similar in effect to a strong applied current in *Cell 0* (B). (C): Firing behaviour of *Cell 1* under one-at-a-time variation of each synaptic parameter. The units of applied current are in nA. 165

B.2 Poor model fitting results for (A) spindle oscillations and (B) spike-wave discharges using only maximal synaptic conductances as fitting parameters. Population-level activity matches target metrics while individual neuron voltage traces show distorted action potentials. 166

B.3 (A): For each synapse type, multiple parameter triplets ($\bar{g}_{syn}$, α, β) yielded good fits (solid blue points). Points with gray outlines represent the sampled parameter space, with solid red points indicating our selected parameter triplets. (B): Testing model sensitivity to deviations from the nominal values (solid red points) by up to 90% (IBRS and IBLTS), 70% (IBIB), and 75% (IBNRS) in each parameter dimension. Transparent points with blue outlines represent good fits as in panel A, and in black outlines, the parameter cloud tested for sensitivity. Solid green points indicate parameter sets that maintained good network performance despite these deviations. 167

B.4 (A): For each synapse type, multiple parameter triplets ($\bar{g}_{syn}$, α, β) yielded good fits (solid blue points). Points with gray outlines represent the sampled parameter space, with solid red points indicating our selected parameter triplets. (B): Testing model sensitivity to deviations from the nominal values (solid red points) by up to 100% (NRSRS and NRSIB), 30% (NRSLTS), and 50% (NRSNRS, NRSTC and NRSRE) in each parameter dimension. Transparent points with blue outlines represent good fits as in panel A, and in black outlines, the parameter cloud tested for sensitivity. Solid green points indicate parameter sets that maintained good network performance despite these deviations. 168

B.5 (A): For each synapse type, multiple parameter triplets ($\bar{g}_{syn}$, α, β) yielded good fits (solid blue points). Points with gray outlines represent the sampled parameter space, with solid red points indicating our selected parameter triplets. (B): Testing model sensitivity to deviations from the nominal values (solid red points) by up to 50% (LTSRSa), 200% (LTSIBa), and 75% (LTSNRSa) in each parameter dimension. Transparent points with blue outlines represent good fits as in panel A, and in black outlines, the parameter cloud tested for sensitivity. Solid green points indicate parameter sets that maintained good network performance despite these deviations. 169

B.6 (A): For each synapse type, multiple parameter triplets ($\bar{g}_{syn}$, α, β) yielded good fits (solid blue points). Points with gray outlines represent the sampled parameter space, with solid red points indicating our selected parameter triplets. (B): Testing model sensitivity to deviations from the nominal values (solid red points) by up to 35% (TCRS), and 30% (TCIB, TCNRS and TCLTS) in each parameter dimension. Transparent points with blue outlines represent good fits as in panel A, and in black outlines, the parameter cloud tested for sensitivity. Solid green points indicate parameter sets that maintained good network performance despite these deviations. 170

B.7 An illustration of undesirable averaging effects of using a population average $V(t)$ to calculate synchrony measure for a small subset of the PY population (cell indices 0 to 4). Voltage traces of pairs of cells from the subset are given in (A)-(J) while voltage traces of the full subset are given in (K). In each case, the average voltage is plotted in red, and the synchrony measure is given in the heading. (L): A comparison of the synchrony measure between individual pairs ($S_{i,j}$) and a measure using the full subset (S_{pop}). The synchrony measure using the full subset is significantly lower than the measure between any pairs of cells in the subset. 172

B.8 (A): Synchrony matrix with a measure $S_{i,j}$ for every pair of cells in the PY population from 11 to 11.5s for the simulated experiment using GABAa conductance at 100% baseline value. S_{pop} (pairwise average) equal to 0.6959 refers to our modified population synchrony, whereas S_{pop} (population average) equal to 0.3913 refers to a population synchrony using a population-averaged voltage as described in [76, 77, 78]. (B): Voltage traces of the PY population with the population average voltage given in red. (C) Average pairwise synchrony measure $\overline{S}_i$ for PY cells. 173

B.9 Distribution of synchrony measure $S_{20,j}$ (between neuron of index 20 and all other neurons in the TC population) over two different time intervals. . . . 174

B.10 Sample curve fits of inhibitory postsynaptic currents post application of allopregnanolone, without (A) and with (B) pre-scaling data by factoring out the voltage dependent term. 176

C.1 Comparison of the original and redefined steady-state activation and inactivation functions for the fast sodium channel in TC and RE cells. 178

C.2 Spike-count responses of excitatory cortical cells under the $Scn2a^{+/-}$ mutation. (Top row): Responses with a fixed 33% reduction in I_{K2} conductance, across varying mutation strengths. (Bottom row): Responses at 100% mutation strength, with varying levels of I_{K2} conductance reduction (33-100%). Based on this analysis, we set the I_{K2} conductance reduction to 75% (adjusted from 33% reported in [212]) to qualitatively match experimentally observed neuronal firing patterns. 179

List of Tables

3.1 Rise and decay time constants, and neurotransmitter duration for Control and post-ALLO synapses given by Equations (3.10)–(3.11). 41

4.1 The number of presynaptic neurons that each postsynaptic neuron connects to ($nPrePost$) in a network with the following architecture: 25 layer 5 RS cells, 75 layer 5 IB cells, 75 layer 6 NRS cells, 100 deep layer LTS cells, 100 TC cells, and 100 RE cells. For example, nRSIB = 4 means that each IB cell receives input from 4 RS cells. 57

4.2 Maximal synaptic conductance, $\bar{g}_{syn}$ parameters (in μS) for each synapse type, chosen to produce a default network state exhibiting spindle oscillations. 58

4.3 Forward (binding) rate, α parameters (in (ms·mM)$^{-1}$) for each synapse type, chosen to produce a default network state exhibiting spindle oscillations. Note that α values for inhibitory synapses presented here correspond only to GABAa synapses. 58

4.4 Backward (unbinding) rate, β parameters (in ms^{-1}) for each synapse type, chosen to produce a default network state exhibiting spindle oscillations. Note that β values for inhibitory synapses presented here correspond only to GABAa synapses. 59

5.1 Comparison of parameters of the steady-state activation and inactivation properties of wild-type and $SCN8A$ variants as reported by Kohrman et al. [108] ($Scn8a^{med-jo}$) and Oliva et al. [156] ($Scn8a^{V929F}$). 93

5.2 Modifications to the fast sodium current (I_{Naf}) parameters as a result of mutations of $SCN2A$ or $SCN8A$. Note that alterations to the activation and inactivation curve parameters were implemented as a relative change (given in %) between the wild-type and mutant channel activity. 95

5.3 Modification to the slowly activating and inactivating potassium current (I_{K2}) maximal conductance as a result of $SCN2A$ mutation. 95

5.4 Average action potential amplitude and half-width as a result of $Scn2a^{+/-}$ with varying mutation strengths (given as percentages) on different cortical cells. Both spike features were measured using the *eFEL* Python package's *AP_amplitude_from_voltagebase* and *spike_half_width* functions. Both features were averaged across all spikes. 98

A.1 Description of the currents used for all neuron types. 141

A.2 Maximal conductance parameters (in mS/cm^2) for each neuron type. . . . 148

A.3 Maximal synaptic conductance parameters (in μS) for each synapse type to produce a default network state exhibiting spindle oscillations. 148

B.1 Description of the currents used for all neuron types. 150

B.2 Maximal conductance parameters (in mS/cm^2) for each neuron type. . . . 163

B.3 The number of presynaptic neurons that each postsynaptic neuron connects to ($nPrePost$) in the 5-95 (nIB:nRS) model configuration. 164

B.4 The number of presynaptic neurons that each postsynaptic neuron connects to ($nPrePost$) in the 95-5 (nIB:nRS) model configuration. 164

Chapter 1

Introduction

Initially thought to be a spiritual disease, epilepsy is one of the oldest recognized conditions dating back to 2000 BC [144]. It is one of the most common neurological diseases of the brain affecting over 65 million people worldwide of all ages, races, and social classes [10, 144]. It is characterized by recurrent unprovoked seizures, which are brief, abnormal, excessive discharges of neuronal activity in the brain. During a seizure, abnormal neuronal activity can cause recruitment of neighbouring neurons in the network resulting in a pattern of hypersynchrony due to an imbalance of excitation-inhibition within the neuronal network by means of increased excitation, reduced inhibition or both [144]. In general, epileptic seizures are well-controlled with appropriate diagnosis-dependent treatment in the large majority of cases with the rate of patients entering prolonged periods of remission or terminal remission varying with factors such as epilepsy type and age of onset [10]. There are many different types of epileptic seizures, and broadly speaking, they fall into three major groups: focal, generalized, and unknown onset seizures. While focal onset seizures originate in a localized area of the brain and sometimes have the ability to spread to both sides of the brain (bilateral), generalized onset seizures affect both sides of the brain at once. Unknown onset seizures are typically used to describe seizures wherein the onset site is unknown [60]. Within each group, seizures can be of the convulsive or non-convulsive type. Convulsive seizures present motor symptoms such as jerking movements (clonic), rigidity of muscles (tonic), weakening of muscles (atonic), muscle twitching (myoclonus) or epileptic spasms. Non-convulsive seizures, also known as absence seizures, usually present non-motor symptoms such as lack of movement (behaviour arrest) and loss of consciousness [60].

Besides identifying observable seizure characteristics, one of the methods used to detect and classify epilepsy type is through an electroencephalogram (EEG). An EEG is

a non-invasive diagnostic tool that detects abnormal electrical brain activity using small electrodes placed on various locations on a patient's scalp. These electrodes conduct and amplify electrical discharges produced by underlying neural activity. EEG signals can be categorized into various frequency bands corresponding to different behaviour and brain states. Some brain rhythms such as sleep spindles and spike-wave discharges are also described by the shape of the waveform [112]. Sleep spindles are neural oscillations exhibited in mammals during non-REM sleep and fall in the frequency range with a lower bound at 8-9 Hz or 11 Hz and an upper bound at 16 Hz for humans, as illustrated in Figure 1.1A [90]. A spike is characterized by a sharp outline and a duration of 20 to 70 milliseconds (ms) whereas a slow wave lasts more than 200 ms [5, 126]. The spike-wave discharge pattern describes brief spikes followed by a slow wave, as illustrated in Figure 1.1B.

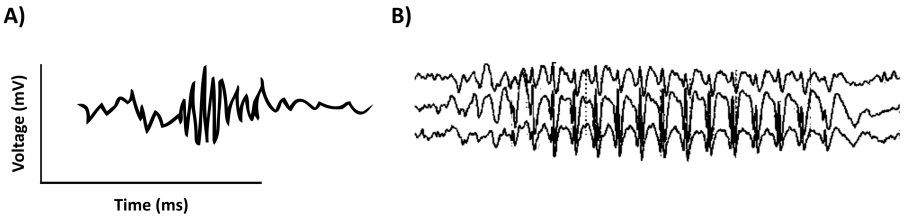

Figure 1.1: Electroencephalographic (EEG) recordings in human patients displaying spindle oscillations (A) and an approximately 3 Hz spike-wave pattern (B). Adapted from a public domain image and [24], respectively; both via Wikimedia Commons.

One of the hallmark EEG patterns observed in childhood absence epilepsy (CAE) is the presence of rhythmic 2.5–5 Hz spike-wave discharges [75, 67]. Childhood absence epilepsy is an idiopathic generalized epilepsy syndrome, accounting for approximately 18% of epilepsy in school-aged children, with a typical age of onset between 4 and 12 years. With an incidence rate of approximately 6.3–8.0 children per 100000 per year [84], it is interestingly more prevalent among girls, comprising 60–70% of CAE cases [206]. Absence seizures in CAE are characterized by brief periods of severe loss of consciousness occurring multiple times a day, with episodes lasting 3 to 20 seconds. Children may stare blankly into space, accompanied by an upward roll of their eyeballs, and oftentimes seizures may go unnoticed or be mistaken for daydreaming or inattention [84].

Based on many years of mounting experimental data, the thalamocortical circuit consisting of pyramidal neurons and interneurons in the cortex, thalamic relay neurons and reticular thalamic neurons in the thalamus is considered to play a central role in the pathophysiology of absence seizures [53]. Some electrophysiological studies also suggest that this

circuit has the ability to transform physiological sleep spindles into spike-wave discharges [75, 110].

In addition to these electrophysiological findings, the genetic landscape of CAE is complex, with various causes and molecular pathways involved. Specifically, genetic aetiology in CAE patients has been linked to mutations in genes that encode ion channels and neurotransmitter receptors [38, 172, 136]. These mutations involve sodium channel genes such as $SCN2A$ and $SCN8A$, calcium channel genes such as $CACNA1H$, $CACNA1G$, as well as genes encoding subunits of the γ-aminobutyric acid (GABA) receptor, including $GABRG2$ [35, 208, 156, 209, 109].

One of the most confounding features of CAE is its ability to resolve in adolescence, with reported remission rates ranging from 56 to 84% of cases. In some instances, however, CAE may evolve into other generalized epilepsy syndromes [84, 136]. There are many factors hypothesized to be mechanisms behind remission, including antiepileptic drugs, genetic predisposition, and pre-treatment intrinsic connectivity differences between patients who ultimately experience remission and those who do not [13, 116, 39, 29, 104, 190]. However, there remains an inadequate understanding of these factors due to their significant variability. Interestingly, circumstantial accounts of the prognosis of *untreated* epilepsy, mostly limited to resource-poor countries, show rates of spontaneous remission ranging from 31–42%, although these studies are not exclusive to childhood-onset epilepsy syndromes [113, 11]. Accurately determining the true rate of spontaneous remission in CAE would realistically require assigning newly diagnosed patients to either a treatment or no-treatment protocol, a proposition that would not be ethically sound.

Given that remission often occurs at adolescence (a time of onset of puberty), the role of sex hormones in CAE is also suspected [197]. This association is further supported by the phenomenon of catamenial exacerbation of epileptic seizures. Catamenial epilepsy refers to seizure exacerbation that coincides with cyclical changes in circulating levels of ovarian steroid hormones during the menstrual cycle [66]. The cyclical variation of steroid serum levels and its positive correlation with seizure frequency implies a neuroactive role of sex steroid hormones. There is substantial evidence from both clinical studies as well as animal experiments on the effect of progesterone (and its metabolite allopregnanolone) on human and animal EEG [204]. In particular, administration of progesterone has been shown to exacerbate absence seizures [26, 197] while allopregnanolone has the ability to enhance and prolong neurotransmitter receptor function, resulting in enhanced inhibition [24, 127].

Researching childhood absence epilepsy in clinical settings is uncommon for several reasons. Among these are the young age of patients and the potentially invasive nature

of the study. Hence, the use of animal models, especially genetic models in rats and mice, is quite common [45]. Genetic models involve animals with specific genetic defects that contribute to displaying symptoms similar to those seen in human epilepsy. They are particularly useful for studying the pathophysiology of absence seizures, as they closely resemble the spontaneous occurrence of this condition in humans [36]. Two of the most well-described models are the Wistar Albino Glaxo/Rijswijk (WAG/Rij) rats and the Genetic Absence Epilepsy in Rats from Strasbourg (GAERS) rats [95]. Similar to other genetic models of CAE, these two models exhibit bilateral and synchronized SWDs with similar waveforms on the EEG. However, there are some key differences between genetic rodent models and human patients, namely that the frequency of SWDs is higher (between 5-11 Hz), the age of SWD initiation is different, and disease remission with age is not observed [198, 95].

Another powerful method to understand the underlying brain dynamics is the use of mathematical and computational modelling tools. All mathematical models are abstractions of the system being studied, with the ultimate goal of sufficiently reducing system complexity while still preserving its key features. The choice of the model largely hinges on the question being addressed, balancing scale against complexity while concurrently utilizing existing knowledge about the system of interest. Broadly speaking, models in neuroscience can be categorized as being biophysical or phenomenological in nature, each its own level of abstraction. These categories encompass a spectrum ranging from the microscopic scale, focusing on a subcellular to cellular level, to the macroscopic scale, encompassing descriptions of specific circuits, brain regions, or the entire brain/organism level, as illustrated in Figure 1.2.

Phenomenological models describe an empirical relationship and capture patterns of relevant activity. The model-defining equations are motivated by the observed phenomena that emerge from more complex processes, making them computationally efficient. Some well-known examples include the Integrate-and-Fire models, Izhikevich model, FitzHugh-Nagumo model, among others [92]. Each of these models is capable of producing action potential-like patterns without explicitly modelling the dynamics of intrinsic ionic currents or ion channels. In addition to capturing the observed phenomena, biophysical models describe the underlying biophysical mechanisms driving it. These models can vary in complexity and computational demand, depending on the level of biological realism required. More generally, they fall under the class of *conductance-based models*. Some well-known examples include the Hodgkin-Huxley model and the Morris-Lecar model [176, 147].

Despite extensive research into childhood absence epilepsy, there remains a significant gap in our understanding of mechanisms underlying remission. Current research predominantly focuses on broad prognostic indicators, with remission typically considered only as

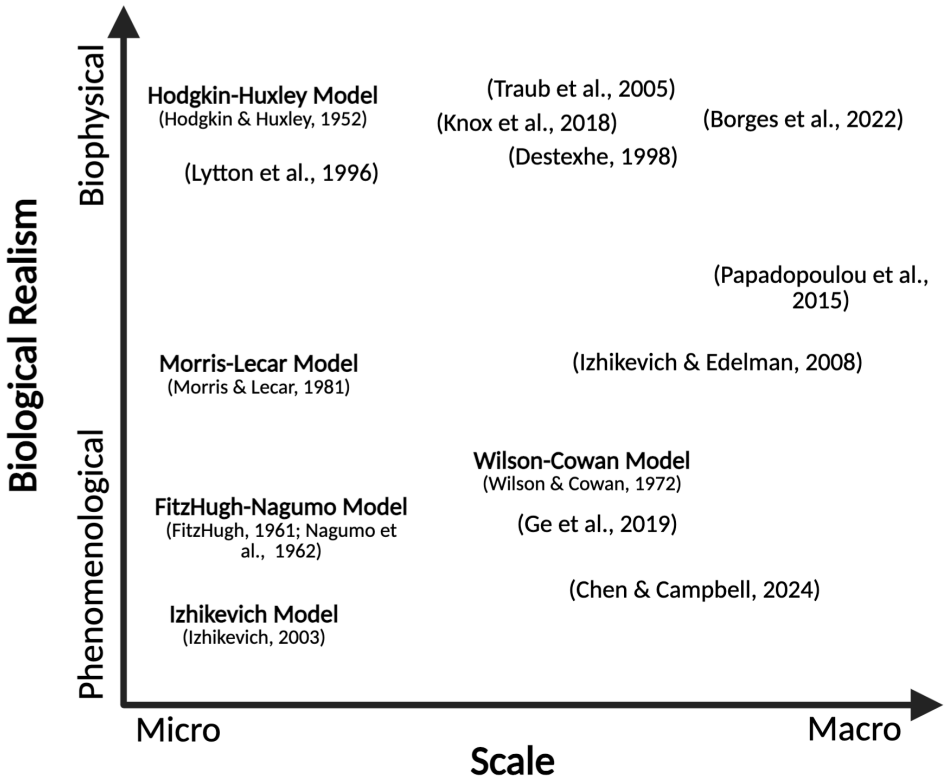

Figure 1.2: Spectrum of mathematical models used in computational neuroscience, organized along two primary axes: biological realism and scale. Exemplar models are positioned according to their typical level of abstraction and spatial scale [85, 124, 192, 106, 49, 20, 159, 93, 147, 205, 65, 150, 72, 91, 33].

a secondary outcome rather than a primary objective. While genetic analyses identifying predisposing variants, early treatment studies, and evaluations of diagnostic markers aim to predict disease trajectory, the specific biological and network-level pathways leading to remission remain underexplored. Animal models, particularly genetic models, have proven valuable for assessing the effects of antiepileptic drugs, characterizing seizure dynamics, and studying the genetic basis of the disease. Meanwhile, computational approaches have contributed significantly to our understanding of the thalamocortical dynamics that generate absence seizures. However, these approaches have not been systematically combined

to specifically model remission. This limitation is compounded by several challenges such as inconsistent definitions of remission in the literature, the practical difficulties in conducting resource-intensive longitudinal studies, and the inherent clinical heterogeneity of CAE. Beyond its biological significance, modelling CAE remission presents substantial mathematical and computational challenges. The multi-scale nature of the thalamocortical network demands the integration of processes occurring at different spatial levels, from molecular interactions at ion channels and synapses, to activity at the level of individual neurons, and the resulting network behaviour. As a result, we lack a modelling approach that comprehensively captures how various individual factors—such as hormonal influences, genetic predisposition, and alterations in network connectivity—interact across these multiple scales to facilitate disease remission.

To address this knowledge gap, this thesis develops a multi-scale, conductance-based model of the thalamocortical network that integrates hormonal modulation, genetic mutations, and cellular- and network-level factors. Across a series of investigations, the model is extended and refined to explore distinct but interrelated mechanisms underlying CAE: the effect of neurosteroids, such as allopregnanolone, on inhibitory transmission mediated by GABA receptors; the influence of neuronal heterogeneity and regional cortical connectivity; and the differential effects of disease-causing mutations in genes, including the $GABRG2$, $SCN2A$, and $SCN8A$. Through this integrated approach, the model aims to uncover mechanistic pathways that contribute to both remission and non-remission in CAE. Additionally, this thesis contributes to applied mathematics by developing techniques for analyzing transitions between distinct dynamical states in neural systems, establishing methods to incorporate genetic and hormonal factors into conductance-based models, and providing a computational framework that can help identify critical parameters governing epileptic activity. These approaches not only advance our understanding of CAE specifically, but offer generalizable insights into the mathematical modelling of neurological conditions characterized by spontaneous shifts in brain dynamics.

The remainder of this thesis is organized as follows:

In Chapter 2, we provide an overview of the neuroanatomy and electrophysiology of neurons, with a focus on the conductance-based modelling framework. This includes a detailed discussion of synaptic models and the thalamocortical circuitry relevant to absence epilepsy. We also review the role of neurotransmitters in absence epilepsy and discuss how hormonal influences—particularly the progesterone metabolite allopregnanolone—modulate inhibitory neurotransmitter systems, particularly GABAergic signalling.

In Chapter 3, we utilize a well-established conductance-based model of the thalamocortical circuit to investigate how mutations in the genes encoding ion channels (i.e., low-

threshold calcium channel) and neurotransmitter receptors (i.e., GABAa receptors) alter network behaviour. The model successfully reproduces the transition from healthy spindle oscillations to pathological spike-wave discharges through either cortical disinhibition or modifications in calcium conductance. We then model the effect of allopregnanolone by calibrating synaptic parameters to fit experimental data and explore how ALLO-mediated changes in inhibition influence spike-wave discharges. Additionally, through a systematic examination of region-specific differences in ALLO synthesis, we analyze its influence on individual components of the thalamocortical circuit. This chapter has been published in the Journal of Computational Neuroscience [3].

Chapter 4 builds on our work in Chapter 3 by developing an enhanced thalamocortical network that improves the previous representation of the cortical circuitry. Specifically, we introduce a layered cortical structure incorporating specialized neurons from cortical layers 5 and 6. This revised model balances physiological realism with computational efficiency. Using this framework, we investigate how variations in neuronal composition—including different ratios of intrinsically bursting and regular spiking neurons—affect the generation and propagation of spike-wave discharges. We also examine the impact of enhanced frontocortical connectivity on pathological network dynamics, aiming to identify network features that may distinguish resolving from non-resolving CAE networks.

In Chapter 5, we explore how sodium channel mutations implicated in CAE affect neuronal excitability and, in turn, influence network-level activity—particularly the emergence of spike-wave discharges. Building on the modelling framework from Chapter 4, we investigate whether specific sodium channel variants predispose networks to resist ALLO-mediated resolution of spike-wave discharges. This analysis provides insight into whether certain mutations may underlie a predisposition to non-remission. Additionally, we examine how these mutations interact with frontocortical connectivity to assess their potential combined contribution to persistent pathological network states, even in cases involving mutations found to be associated with remission.

Finally, in Chapter 6, we summarize the key findings of this thesis, highlight the implications of our work, and discuss its relevance to understanding the underlying mechanisms of remission in childhood absence epilepsy. We also propose potential avenues for future research, considering both experimental and computational approaches.

Chapter 2

Background

2.1 Neuroanatomy

Despite the vast diversity found in vertebrate nervous systems, they all share a basic structure: a central nervous system (CNS), which consists of the brain and spinal cord [56]. Neurons, numbering in the hundreds of billions, are the individual signalling elements that work together to keep the nervous system functioning [97]. They exhibit vast morphological and functional diversity and typically have four morphologically defined regions, each with a distinct function: the cell body (soma), dendrites, axon, and axon terminals, as illustrated in Figure 2.1. The most common structure of a neuron in vertebrates consists of a soma, a single branching axon and many dendritic branches [98]. The soma, which contains the nucleus, is fundamental to a neuron's survival. The dendrites branch out from the soma and receive incoming signals from other neurons. Most neurons have a single axon that extends from the soma and can vary in length from a millimeter to over a meter [97]. The axon's primary function is to conduct electrical impulses called *action potentials* (also referred to as a *spike*), illustrated in Figure 2.2.

As the name suggests, the CNS functions as the central control system, managing and coordinating sensory input, motor output, and higher cognitive functions. The brain is commonly divided into three broad regions: the *hindbrain*, *midbrain*, and *forebrain*. The hindbrain is responsible for several vital autonomic functions, including breathing, heart rate regulation, and the modulation of movement and motor skill learning. The midbrain governs sensory and motor functions, such as visual and auditory reflexes. The forebrain, responsible for more complex sensory processing, sensorimotor integration, and motor initiation, is composed of two major regions: one that includes the *thalamus*, and

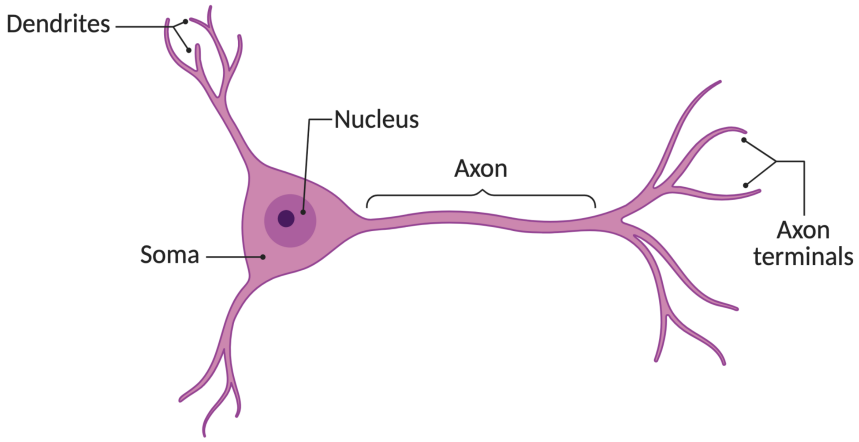

Figure 2.1: An illustration of a typical pyramidal neuron. Created with BioRender.com.

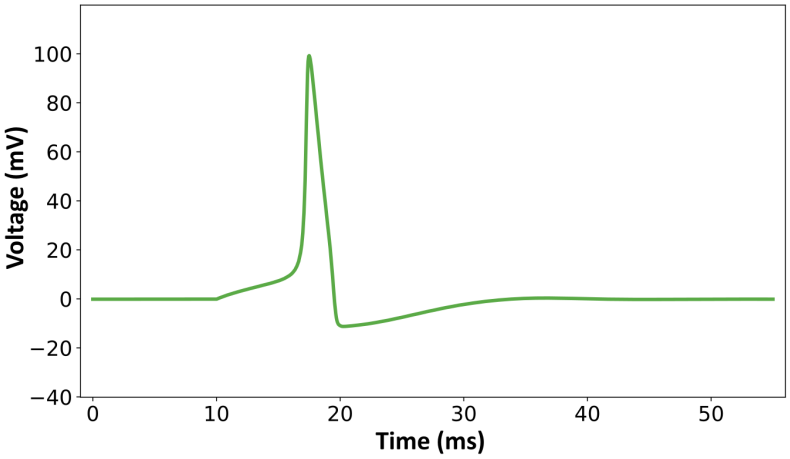

Figure 2.2: An example of an action potential.

another consisting of the cerebrum, which encompasses the visible *cerebral cortex* as well as various subcortical structures. [98].

The cerebral cortex is divided into four major lobes as illustrated in Figure 2.3: *frontal*, *parietal*, *occipital*, and *temporal*. Each lobe carries out specialized neural functions. The frontal lobe, the largest of the four, is involved in motor control and is responsible for higher executive functions essential for human behaviour, such as planning, decision-making, and

emotional regulation. The parietal lobe is responsible for perceiving and processing sensory input. The occipital lobe governs visual processing and interpretation, while the temporal lobe processes auditory information and plays a key role in language comprehension, memory, and emotional responses [98, 96].

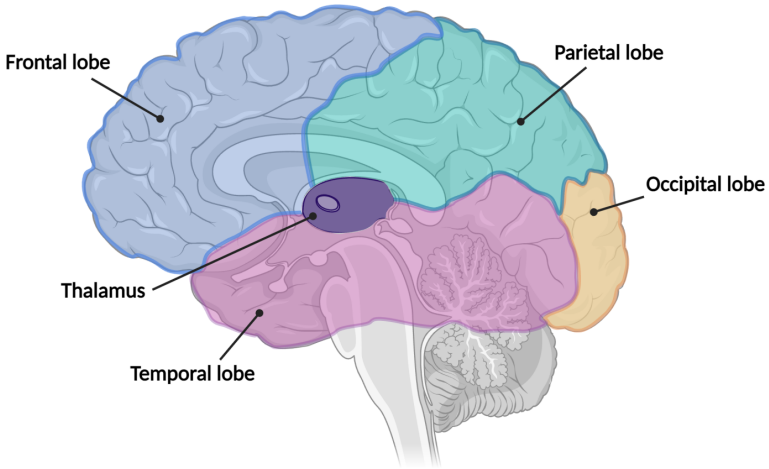

Figure 2.3: The four major lobes of the cerebral cortex–frontal, parietal, temporal, and occipital–along with the thalamus. Created with BioRender.com.

The human cerebral cortex varies in thickness from 1–4.5 mm [64] and can be divided into six distinct horizontal layers. It is predominantly composed of two types of neurons: pyramidal and non-pyramidal. Pyramidal neurons, the main source of output from the cortex, are excitatory projection neurons that can exhibit various firing behaviours, including regular spiking and bursting [7]. These neurons have pyramid-shaped cell bodies, with dendrites that may project either apically (toward the cortical surface) or basally (parallel to the surface). A single axon extends from the soma, projecting to other cortical layers or subcortical regions, including areas like the thalamus. Non-pyramidal neurons can be further classified into numerous types based on their morphology, with some being excitatory, though most are inhibitory interneurons that project locally [177, 131, 7]. The cortical layers are organized as follows: the first layer consists mostly of dendrites and axons from numerous neurons, forming several synaptic connections within this layer. Layer 2/3, known as the external pyramidal layer, contain mostly pyramidal neurons along with some non-pyramidal neurons that establish both intra-cortical and inter-cortical connections. The axons of most non-pyramidal neurons reside in layer 4. A high density of pyramidal neurons comprise layer 5, the internal pyramidal layer, and it is the main output

station of the cortex. Layer 6 contains many pyramidal cells in its upper region, while its deeper part consists of various types of excitatory non-pyramidal neurons and inhibitory interneurons [7, 161, 68].

The thalamus is a major sensory and motor relay station for the cortex, modulating the passage of specific information depending on the behavioural state [98]. It is composed of several specialized structures, known as nuclei, each receiving specific sensory input and projecting to particular cortical areas. The outer layer of the thalamus is formed by the *reticular nucleus*, which, although it does not project directly to the cortex, plays a crucial role in regulating thalamocortical communication [98]. While neurons within the reticular nucleus are inhibitory, most neurons in the other thalamic nuclei are excitatory.

As the conventional model of cortical processing suggests and illustrated in Figure 2.4, thalamic input primarily targets cortical layer 4, although some thalamic neurons also project to layers 5 and 6, and to a lesser extent, other layers. Projections from layer 4 are mainly directed to layer 1, layer 2/3, and layer 5. Layer 2/3 neurons predominantly target layer 5, with additional projections to other layers. Within layer 5, some neurons project to layer 6 and to either layer 1 or layer 2/3 [81]. Layer 6 neurons primarily project to deep layers and exclusively to the thalamus [179].

Action potentials are the main mode of communication between neurons, and they can vary in both shape and size. Different neurons exhibit distinct patterns of action potential firing, as illustrated in Figure 2.5 [117]. The axon terminals, responsible for transmitting information away from the cell body, branch out near the end of the axon. They are the main points of contact with other neurons, and their zone of communication is known as a *synapse*, illustrated in Figure 2.6. The majority of synapses in the nervous system, and those relevant to this work, are chemical synapses. The axon terminal contains vesicles filled with neurotransmitter molecules, which are chemicals involved in neurotransmission. The primary neurotransmitters are glutamate and GABA [61]. A presynaptic neuron is the one in which a signal is initiated, while a postsynaptic neuron is the one receiving the signal. The narrow space between a presynaptic and postsynaptic neuron is known as the *synaptic cleft*. Upon excitation of a presynaptic neuron and once an action potential reaches the end of the presynaptic terminal, several processes occur that result in the release of neurotransmitter molecules into the synaptic cleft. These molecules diffuse across to bind to specific receptors on the dendrites of the postsynaptic neuron, which then activate or inactivate certain ion channels, depending on the type of neurotransmitter [61]. The neurotransmitter glutamate stimulates two types of receptors: AMPA/kainate, and NMDA, both of which cause excitation of the postsynaptic membrane. On the contrary, GABA is the main inhibitory neurotransmitter. There are two main receptors for GABA: GABAa and GABAb. While GABAa receptors generally mediate fast inhibition, with

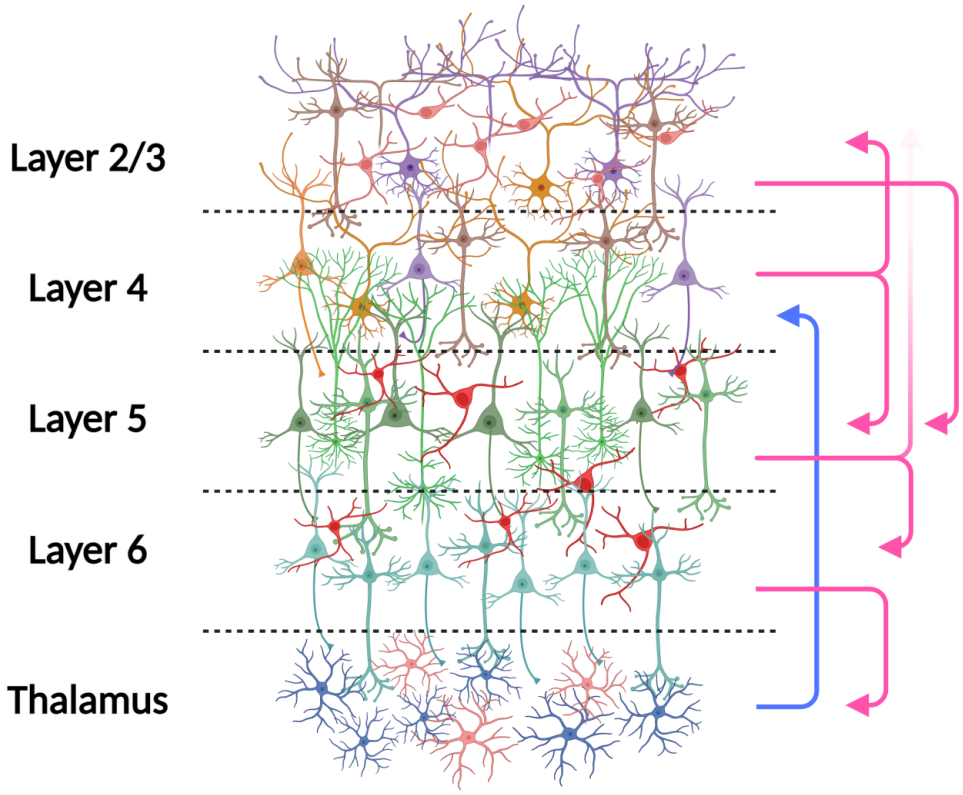

Figure 2.4: Schematic illustrating projections from and within the layered structure of the cortex (pink), including inputs from the thalamus (blue). Arrows indicate the direction of projection. Created with BioRender.com.

multiple subtypes contributing to diverse time courses, GABAb receptor activation follows a series of intracellular events, resulting in slower inhibition [61]. Additionally, GABAa-mediated inhibition can vary significantly between childhood and adulthood. Thus, the type of neurotransmitter and receptors involved determines whether the postsynaptic neuron's likelihood of initiating an action potential is increased or decreased [25].

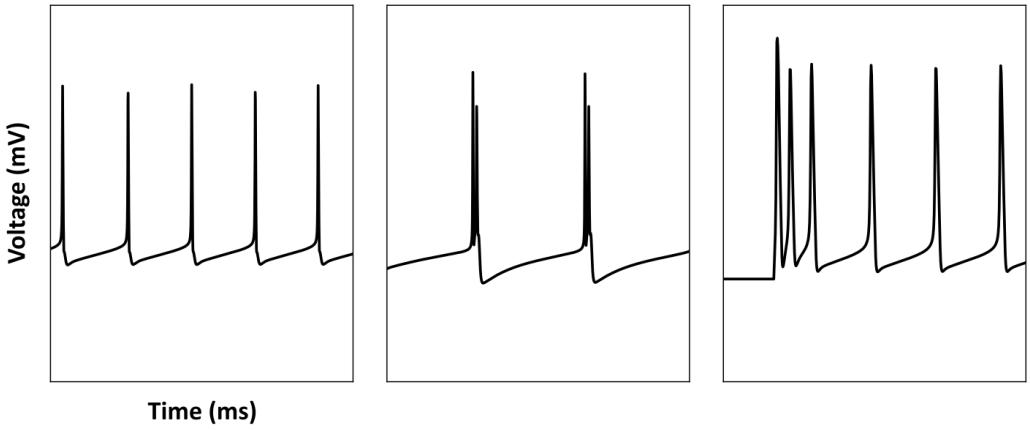

Figure 2.5: Examples of neuronal firing patterns include tonic or regular spiking (left), bursting (middle), and spike-frequency adaptation (right).

2.2 Neuron electrophysiology

The transmission of a neuronal signal within a neuron relies primarily on the movement of ions across the cell membrane, while communication between neurons typically involves chemical signalling. All living cells maintain differences in ion concentrations across their membranes, creating a potential difference known as the *membrane potential*, V_M. Mathematically, it can be defined as

$$V_M = V_{in} - V_{out}$$

where V_{in} is the potential inside the cell, and V_{out} is the potential outside the cell. The resting membrane potential is defined as the membrane potential when the cell is at rest (i.e. in a non-excited state). A typical neuron has a resting membrane potential value of approximately -70 mV [61].

The cell membrane is composed of two layers of phospholipids, known as a lipid bilayer, approximately 3 to 4 nm thick, as illustrated in Figure 2.7 [1]. Hydrophilic (polar) heads face the inside and outside of the cell, while hydrophobic (non-polar) tails face towards each other. Several ions are present on both sides of the cell membrane, including Na^+, K^+, Cl^- (chloride), Ca^{2+} (calcium), and Mg^{2+}(magnesium). In a typical neuron, they are unequally distributed such that the concentration of Na^+ and Cl^- ions is much higher outside the cell, while the relative concentration of K^+ is higher intracellularly, creating a chemical gradient across the membrane. The membrane is a poor conductor of ionic

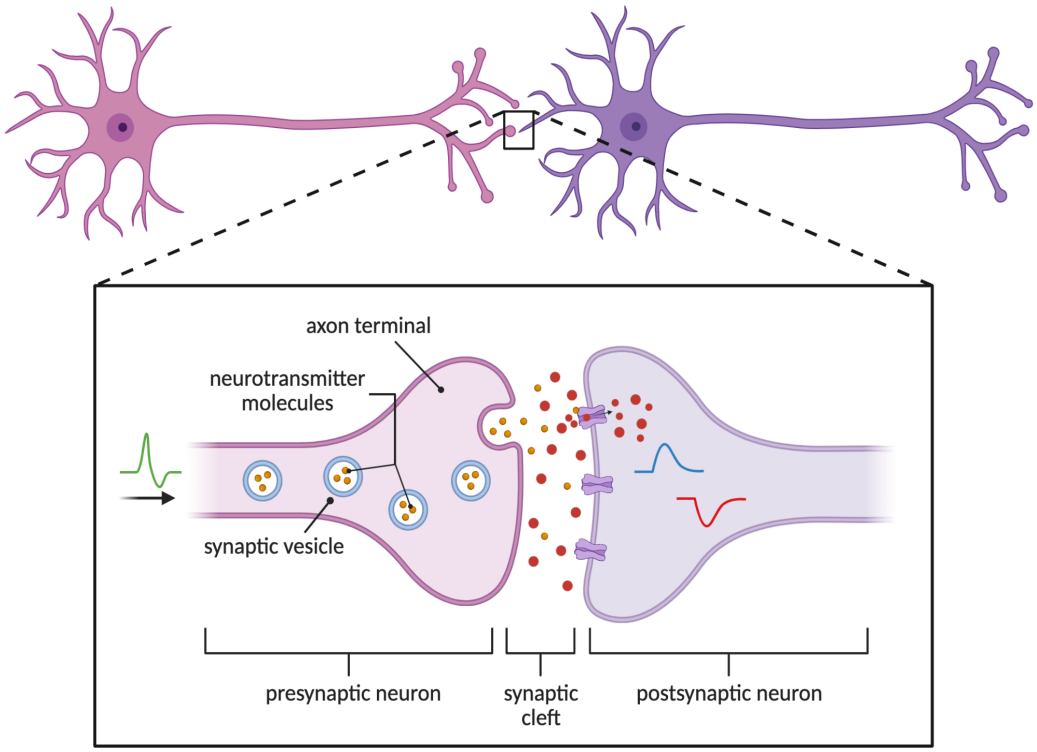

Figure 2.6: Schematic of a chemical synapse illustrating neurotransmitter release from the presynaptic axon terminal upon excitation (green signal), followed by receptor binding on the postsynaptic membrane. The resulting postsynaptic response may be excitatory (blue) or inhibitory (red), depending on the type of neurotransmitter involved. Created with BioRender.com.

currents and impermeable to most charged molecules. As a result, ions require channel proteins, namely *ion channels* and *ion pumps*, embedded in the membrane to facilitate their movement. Some ion channels are non-gated which means they are always open (i.e. *leak channels*), while others are gated with the probability of opening and closing dependent on the membrane potential, referred to as *voltage-gated channels*, or by the binding of specific molecules, referred to as *ligand-gated channels*. Ion channels are usually selective for a particular ion and transport it along its concentration gradient. This movement of ions is referred to as *passive transport*. The maintenance of concentration gradients for sodium and potassium are a product of an *active transport* mechanism, namely the Na^+/K^+ pump

which uses the energy of ATP hydrolosis to move three Na^+ ions out of the cell and two K^+ ions into the cell. The resting membrane potential is a result of both the existence of a maintained chemical gradient of mainly Na^+, K^+, and Ca^{2+} ions, and a relative permeability of the membrane to those ions [61].

Ion movement across the membrane is governed by two forces: the chemical gradient, which drives ions from areas of high to low concentration, and the electrical potential across the membrane, which attracts or repels charged particles. For a given ion, equilibrium is reached when these two forces are exactly balanced—that is, when the outward movement due to the concentration gradient is matched by the inward pull of the electrical gradient, resulting in no net flux. The membrane potential at which an electro-chemical balance of forces occurs is called the *equilibrium, reversal* or *Nernst potential* [61]. The equilibrium potential is different for different ions and can be calculated using the equation formulated by the German physical chemist, Walther Nernst in 1889, known as the Nernst equation [178]:

$$E_{ion} = -\frac{RT}{zF} \ln \frac{[X]_{in}}{[X]_{out}} \tag{2.1}$$

where R is the gas constant, T is the absolute temperature in kelvin, z is the valence of the ion, F is Faraday's constant, and $[X]_{in}$ and $[X]_{out}$ are the respective intracellular and extracellular concentration of the ion X [61].

2.3 Modelling neurons

Mathematical models in neuroscience can be classified into biophysical or phenomenological categories, varying in their complexity and level of detail, as discussed in Section 1. Phenomenological models simply describe empirical relationships and convey observed phenomena, whereas biophysical models go further by incorporating the underlying biophysical mechanisms driving these phenomena. In the context of neuron modelling, whether at the level of single neurons or entire networks, the predominant biophysical model is the conductance-based or Hodgkin-Huxley (HH) type model. This model takes into account diverse properties of ion and synaptic channels where action potentials are generated explicitly from the model dynamics.

The Nobel Prize-winning work by Alan Hodgkin and Andrew Huxley from 1938 to 1952 was one of the most significant conceptual breakthroughs in neuroscience, and transformed our understanding of neuronal function. Experimenting on a squid giant axon, they obtained the first intracellular recording of an action potential [176]. Furthermore,

using the voltage-clamp technique, they were able to determine the contribution of sodium (Na^+) and potassium (K^+) ions to the action potential. In particular, a fast inward current caused by an influx of Na^+ ions and a more slow outward current carried by K^+ ions. Their voltage-clamp protocol allowed them to conclude that both Na^+ and K^+ currents were a result of independent gating mechanisms that changed as a function of membrane potential and time [82]. Subsequently, they integrated their experimental data into a quantitative model, thereby developing the first mathematical description of neuronal excitability. This provided a framework for what are known as conductance-based models or models of the Hodgkin-Huxley formalism.

Conductance-based models are based on an equivalent circuit representation of a cell membrane, as formalized by Hodgkin and Huxley. The cell membrane is modelled as a capacitor due to its structure as a thin, insulating layer that prevents the free flow of ions, allowing opposite charges to accumulate on either side. Ion channels are modelled as resistors, and a battery represents the driving force which is a result of the ionic concentration gradient. An illustration of this representation is provided in Figure 2.7.

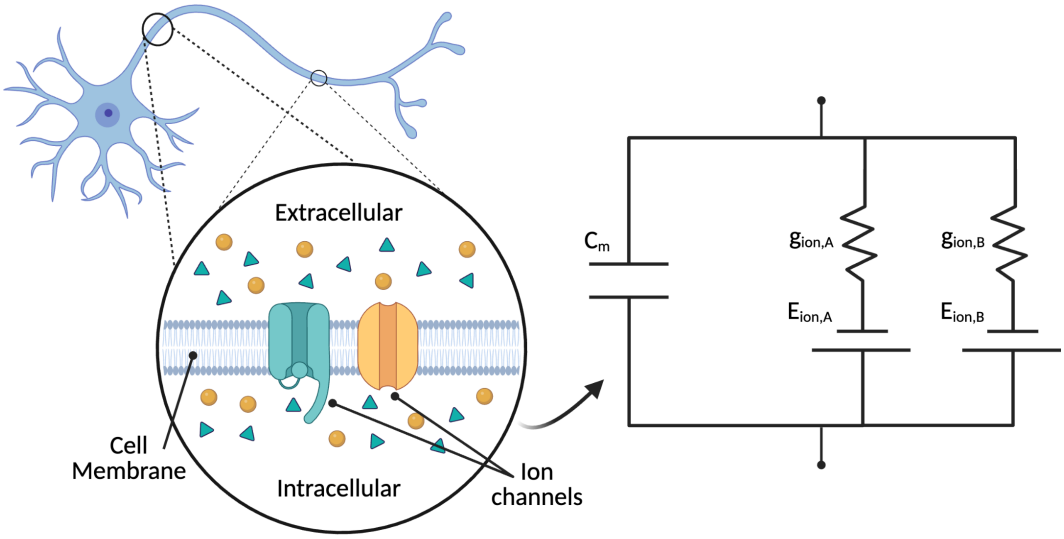

Figure 2.7: An equivalent electrical circuit representation of a neuronal membrane with multiple ion channels. Created with BioRender.com.

The membrane capacitance C_m, the voltage across the membrane V, and the distribu-

tion of excess charge Q are related by the following equation:

$$Q = C_m V \tag{2.2}$$

To determine the amount of current required to change the membrane potential at a given rate, Equation (2.2) can be differentiated with respect to time to obtain the capacitance current given by:

$$I_C = C_m \frac{dV}{dt} \tag{2.3}$$

where $I_C = \frac{dQ}{dt}$.

The total current across the membrane I_m has two components: one associated with the membrane capacitance, I_C, and another associated with the flow of ions through ion channels, I_{ion}. Each ion channel is modelled as a resistor in series with a battery, where the resistor represents ion channel permeability, R_{ion}, and the battery represents the ion's equilibrium potential, E_{ion}. The voltage difference across the cell membrane is the sum of the voltage drops across these two components, given by the following equation:

$$V = R_{ion} I_{ion} + E_{ion} \tag{2.4}$$

Rearranging,

$$V - E_{ion} = R_{ion} I_{ion} \tag{2.5}$$

where $V - E_{ion}$ is the driving force due to the ion concentration gradient across the membrane. Thus, the ionic current can be expressed as

$$I_{ion} = g_{ion} \cdot (V - E_{ion}) \tag{2.6}$$

where $g_{ion} = \frac{1}{R_{ion}}$ is the conductance of the ion channel for the particular ion. The conductance may depend on membrane voltage, as will be discussed below.

According to Kirchhoff's current law, the total current into the cell must sum to zero. This means that

$$I_C + I_{ion} = 0 \tag{2.7}$$

$$C_m \frac{dV}{dt} = -g_{ion}(V - E_{ion}) \tag{2.8}$$

In the presence of multiple ion channels, as is usually the case, the total ionic current is the sum over the different channel types. For k types of ion channels:

$$C_m \frac{dV}{dt} = -\sum_{i=1}^{k} g_i (V - E_i), \quad i = 1 \text{ to } k$$

Conductance is a result of the opening of several microscopic channels in the membrane. Ion channels may have gates of different types, namely activation and inactivation, where these gating mechanisms involve complex conformational structure changes [1]. In the case of voltage-gated channels, the probability of opening or closing of a gate depends on the membrane potential. Such gate models can be described using the following kinetic scheme:

$$C \underset{\beta(V)}{\overset{\alpha(V)}{\rightleftharpoons}} O$$

where C and O correspond to the closed and open states, respectively, and $\alpha(V)$ and $\beta(V)$ are voltage-dependent rate constants denoting the rate at which a gate transitions from the closed to open and from open to the closed state, respectively.

Let x represent the fraction of open gates, and $(1-x)$ the fraction of gates in the closed state. Then, using the law of mass action we get that:

$$\frac{dx}{dt} = \alpha(V)(1-x) - \beta(V)x = \frac{x_\infty(V) - x}{\tau_x(V)} \tag{2.9}$$

$$x_\infty(V) = \frac{\alpha(V)}{\alpha(V)+\beta(V)} \quad \text{and} \quad \tau_x(V) = \frac{1}{\alpha(V)+\beta(V)} \tag{2.10}$$

where $x_\infty(V)$ is the steady-state gating variable function and $\tau_x(V)$ represents the time course for approaching the steady-state. In other words, for a fixed voltage value V, the variable x approaches the value $x_\infty(V)$ with a time constant $\tau_x(V)$. In experimental practice, the steady-state gating function, $x_\infty(V)$, is often determined by fitting data from voltage-clamp experiments using a Boltzmann function, as will be discussed in Section 2.3.1.

More generally, the standard equation describing a single cell with a membrane containing k types of ion channels can be given by the following equation:

$$C_m \frac{dV}{dt} = -\sum_{i=1}^{k} \bar{g}_i \cdot m_i^N \cdot h_i^M \cdot (V - E_i), \quad i = 1 \text{ to } k \tag{2.11}$$

where $\bar{g}_i$ represents the maximal conductance for a particular ion channel, m and h are activation and inactivation gating variables, respectively, and N and M are integer powers which in practice are fit to data. However in some cases, these integer powers can be interpreted as a functional definition of the number of independent gating events that need to occur for the opening of a gate or the number of independent gating components in a single channel [1, 61]. In fact, the right side of Equation (2.11) may contain other current sources such as an external applied current or synaptic currents due to connectivity with other neurons, as will be discussed in Section 2.4.

2.3.1 Experimental characterization of ionic currents

To bridge the gap between ion channel models and experimental data, voltage-clamp experiments are commonly used to measure ionic currents across the membrane at controlled voltages. In these experiments, the membrane potential is continuously compared to a set command value. If a difference is detected, a current is injected to maintain the desired voltage. This injected current is equal and opposite to the membrane current, allowing the precise measurement of the ionic currents active at any given moment [4]. A key experimental outcome is the steady-state activation or inactivation curve, which describes the relationship between the steady-state value of a gating variable and the membrane potential. To obtain this curve, the ionic current (or conductance) is normalized and plotted against the membrane potential [188]. This normalized data is then typically fitted to a Boltzmann function of the following form:

$$x_\infty = \frac{1}{1 + e^{\frac{-V+V_{1/2}}{k}}} \tag{2.12}$$

$$r_\infty = \frac{1}{1 + e^{\frac{V-V_{1/2}}{k}}} \tag{2.13}$$

where x and r represent activation and inactivation gating variables, respectively, V is the membrane potential, $V_{1/2}$ is the voltage at half-activation, and k is the slope factor representing the steepness of the voltage-dependent transition between closed and open states of the channel. These curves can be shifted by altering the voltage at which the channel transitions between states. Modifying $V_{1/2}$ adjusts the voltage at which half of the channels are activated or inactivated, while changes in k affect the steepness of the transition, as illustrated in Figure 2.8. This shift provides valuable information about the channel's sensitivity to changes in membrane potential and its behaviour under different conditions, such as the application of a drug or channel mutation.

2.3.2 Hodgkin-Huxley model

The Hodgkin-Huxley model is a system of four differential equations that take the form of Equations (2.11)–(2.10) to compute the membrane potential, and characterize key properties of the ionic conductances underlying action potentials. The model includes a term representing externally applied current, I_{app}. The term representing ionic currents in Equation (2.11) is subdivided into three components of ionic currents as measured by Hodgkin and Huxley. These are Na^+, K^+ and a *Leak* current which consists mainly of chloride

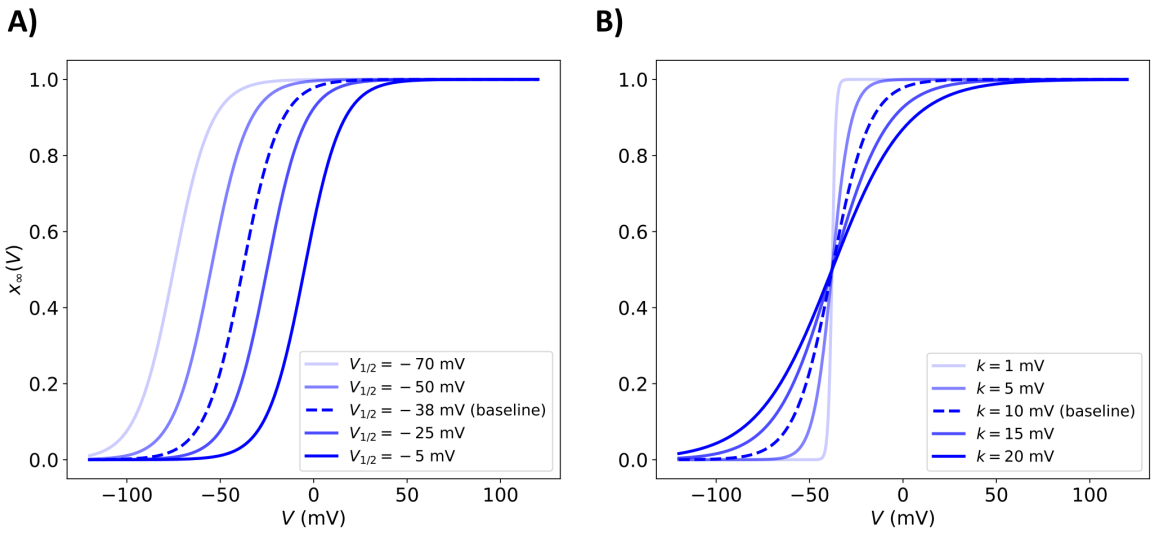

Figure 2.8: Demonstration of the effects of varying $V_{1/2}$ (A) and k (B) on the steady-state activation curve described by Equation (2.12) (and similarly for Equation (2.13)). Shifting $V_{1/2}$ in the depolarizing or hyperpolarizing direction alters the voltage at which the ion channel transitions between states, while modifying k changes the steepness of this transition.

ions but may also have other ions in small amounts. The model equations are as follows:

$$C_m \frac{dV}{dt} = I_{app} - \bar{g}_{Na} m^3 h (V - E_{Na}) - \bar{g}_K n^4 (V - E_K) - \bar{g}_{Leak} (V - E_{Leak}) \tag{2.14}$$

$$\frac{dx}{dt} = \alpha_x(V)(1 - x) - \beta_x(V) x \qquad \text{for } x = m, h, n \tag{2.15}$$

where

$$\alpha_m(V) = \frac{2.5 - 0.1(V - V_{rest})}{\exp\left(2.5 - 0.1(V - V_{rest})\right) - 1} \quad \text{and} \quad \beta_m(V) = 4 \exp\left(\frac{V_{rest} - V}{18}\right) \tag{2.16}$$

$$\alpha_h(V) = 0.07 \exp\left(\frac{V_{rest} - V}{20}\right) \quad \text{and} \quad \beta_h(V) = \frac{1}{1 + \exp\left(3 - 0.1(V - V_{rest})\right)} \tag{2.17}$$

$$\alpha_n(V) = \frac{0.1 - 0.01(V - V_{rest})}{\exp\left(1 - 0.1(V - V_{rest})\right) - 1} \quad \text{and} \quad \beta_n(V) = 0.125 \exp\left(\frac{V_{rest} - V}{80}\right) \tag{2.18}$$

where m and h are the sodium activation and inactivation variables, respectively, and n is the potassium activation variable. This means that Na^+ channels both activate and

inactivate, while the K^+ channel only activates. These equations above were derived by Hodgkin and Huxley to fit their observations of the different currents. For illustration purposes, the steady-state variable functions and time constants are given in Figure 2.9. The measured resting potential V_{rest} was originally set to 0 mV. The reversal potentials were measured to be $E_{Na} = 115 + V_{rest}$ mV, $E_K = -12 + V_{rest}$ mV, and $E_{Leak} = 10.6 + V_{rest}$ mV. The maximal conductances were measured to be $\bar{g}_{Na} = 120$ mS/cm^2, $\bar{g}_K = 36$ mS/cm^2, and $\bar{g}_{Leak} = 0.3$ mS/cm^2. The behaviour of solutions to these equations depends on the value of

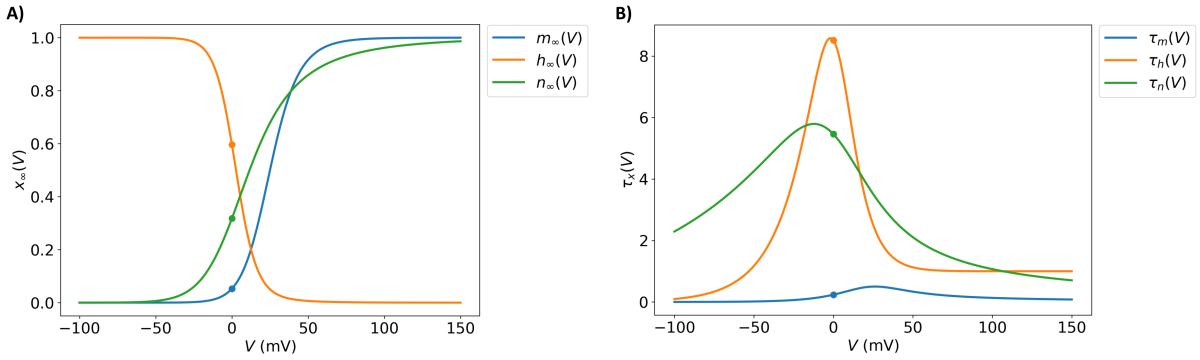

Figure 2.9: Steady-state functions (A) and voltage-dependent time constants (B) for the gating variables m, h, and n in the Hodgkin-Huxley model given by Equations (2.14)–(2.18). The resting potential is at $V = 0$ mV and marked by a closed circle on each curve.

I_{app}, with an "all-or-none" sort of a response. The applied current must be above a certain threshold in order for action potential generation. When I_{app} is below some threshold, the membrane potential returns quickly to the resting potential. However, above some threshold, an action potential is generated. For sufficiently large and sufficiently long period of applied current, the model generates a period response, as illustrated in Figure 2.10A.

A mathematical explanation of the events underlying an action potential (refer to Figure 2.10B), namely the flow of Na^+ and K^+ ions, deserves to be noted as follows: When the applied current is large enough, it causes a large change in the membrane potential which results in a change in m, h, and n (all nonzero). In particular, $m_\infty(V)$ and $n_\infty(V)$ increase while $h_\infty(V)$ decreases. This trend is initially followed by m, h, and n as well as they tend towards their steady-state activation curves. Since $\tau_m(V) << \tau_h(V), \tau_n(V)$ (see Figure 2.9B), m changes more rapidly as compared with the other gating variables (see Figure 2.10B). While $V < E_{Na}$, the Na^+ current is negative (indicating an inward flow) and since it dominates the dynamics, $\frac{dV}{dt}$ is positive. This results in a positive feedback such that

increases in V increase I_{Na} leading to a further increase in V. This corresponds to the upstroke of the action potential, also known as *depolarization*. Such a response continues until V increases towards E_{Na} and Na^+ channel inactivates with a decrease in h towards zero. As the driving force $(V - E_{Na})$ also decreases, the Na^+ current turns off. Meanwhile, the K^+ channel activates with an increase in n. Since the K^+ current dominates, $\frac{dV}{dt}$ is negative. This results in a return of V to zero, and corresponds to the downstroke of the action potential, also known as *repolarization*. Given that n and h relax back to their resting values more slowly, this causes the membrane potential to decrease beyond its resting voltage, in a phase known as *hyperpolarization*. Once the potassium channels are closed, the cell returns to its resting membrane potential.

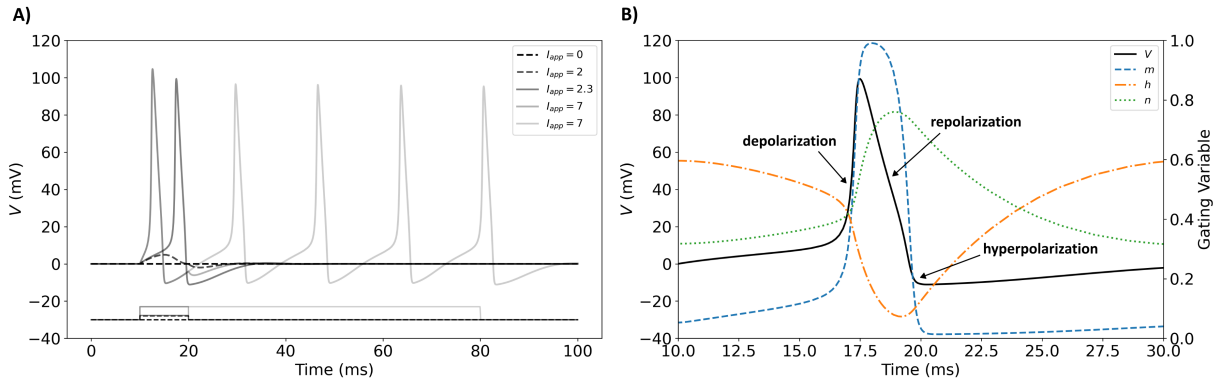

Figure 2.10: (A): Responses of the Hodgkin-Huxley model to varying I_{app} (in $\mu A/cm^2$) given as a pulse input for a duration of 10ms or 80ms (for the longer train of action potentials). (B): A simulated single action potential together with the time course of each gating variable, for $I_{app} = 2.3\mu A/cm^2$.

2.3.3 Compartmental modelling of neurons

Multi-compartment models represent the morphology of real neurons by dividing them into multiple interconnected compartments, each modelled as an electrical circuit, as illustrated in Figure 2.11 [27]. Neurons are typically depicted as a series of small cylindrical segments, with each compartment consisting of a parallel resistor and capacitor to simulate membrane properties and maintain a uniform membrane potential. These compartments are connected to one another via resistors, representing the cytoplasmic resistance between adjacent segments [97]. In this work, we exclusively use single-compartment models, in

which each neuron is represented by a single cylindrical segment, as illustrated in the left panel of Figure 2.11.

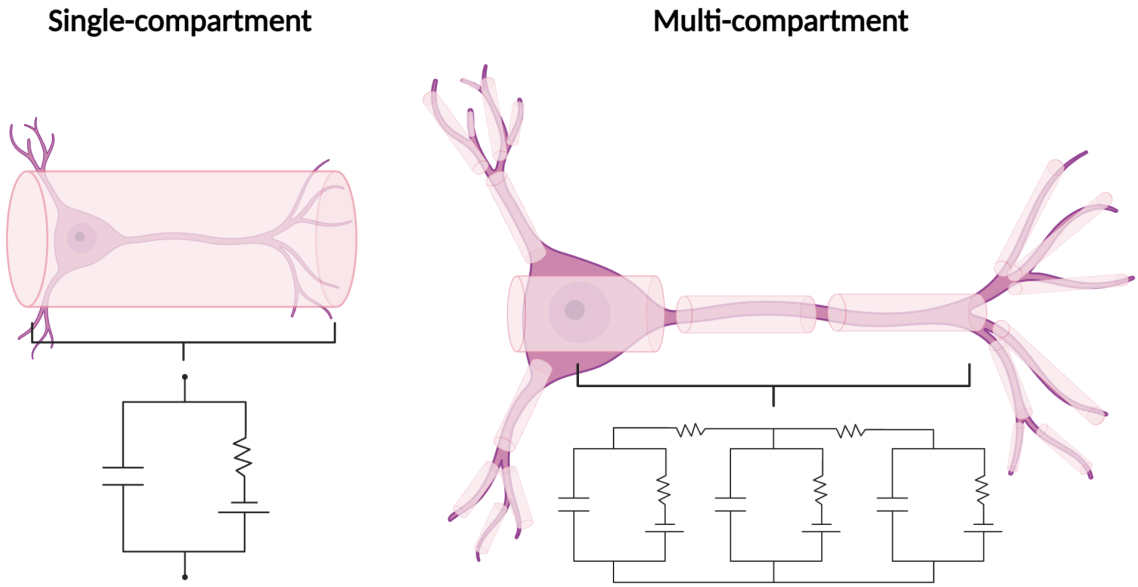

Figure 2.11: Comparison of single-compartment and multi-compartment neuron models. (Left): A single-compartment model represents the neuron as a single cylindrical segment with a single equivalent electrical circuit. (Right): A multi-compartment model divides the neuron into multiple connected segments, each modelled with its own circuit components. Created with BioRender.com.

2.4 Modelling synapses

Synapses can be modelled by focusing on the mechanism of opening of ion channels resulting in postsynaptic currents (PSCs) without the details such as diffusion of neurotransmitter molecules. Excitatory (or inhibitory) PSCs are those that increase (or decrease) the probability of a postsynaptic action potential. In addition, if the reversal potential for a PSC is greater than the action potential threshold in the postsynaptic neuron, this results in an increased probability of an action potential. Synaptic currents can be modelled in a

manner similar to ionic currents as given by the following equation:

$$I_{syn} = \bar{g}_{syn} \cdot s(t) \cdot (V_m - E_{syn}) \tag{2.19}$$

where $\bar{g}_{syn}$ is the maximal synaptic conductance, $s(t)$ is the synaptic conductance function and E_{syn} is the reversal potential of the synapse. The time-dependent conductance $s(t)$ can be modelled in several ways, with the Destexhe synapse model being one of the most widely-used models formulated by Alain Destexhe [52].

AMPA/GABAa-mediated synapse modelling

In the formalism by Destexhe, postsynaptic currents mediated by glutamate AMPA and GABAergic GABAa receptors are modelled using a gating variable $s(t)$ which denotes the fraction of open synaptic channels at time t. Open synaptic channels refer to postsynaptic receptors that neurotransmitter molecules bind to, followed by the opening of ion channels [51, 52]. In this way, the synaptic conductance function is described by:

$$\frac{ds}{dt} = \alpha[T](1 - s) - \beta s \tag{2.20}$$

where $[T]$ represents the neurotransmitter concentration released into the synaptic cleft upon the arrival of a presynaptic spike, and α and β are rate constants describing the binding of neurotransmitter. The relationship between neurotransmitter release, $[T]$, and the presynaptic voltage, V_{pre}, is assumed to take the form given by the following equation:

$$[T](V_{pre}) = \frac{C_{max}}{1 + \exp\left(\frac{-(V_{pre} - V_T)}{K_p}\right)} \tag{2.21}$$

where C_{max} is the maximal concentration of the neurotransmitter in the synaptic cleft, K_p is the steepness of voltage dependence, and V_T is the half-activation voltage. In this work, we use the values suggested by Destexhe et al.: $C_{max} = 1$ mM, $V_T = 2$ mV, and $K_p = 5$ mV [51].

Upon the arrival of a presynaptic spike at $t = t_0$, $[T]$ jumps to a maximal concentration value C_{max}, and at $t = C_{dur}$ (the duration of neurotransmitter-mediated pulse), $[T]$ falls back to 0. After the neurotransmitter-mediated pulse is gone, $s(t)$ decays exponentially. Then, solving Equation (A.37), we get:

$$s(t) = \begin{cases} s_\infty + (s(t_0) - s_\infty)e^{-\frac{t}{\tau_s}}, & t_0 \leq t < C_{dur} \\ \left[s_\infty + (s(t_0) - s_\infty)e^{-\frac{C_{dur}}{\tau_s}}\right]e^{-\beta(t - C_{dur})}, & t \geq C_{dur} \end{cases} \tag{2.22}$$

where

$$s_\infty = \frac{\alpha C_{max}}{\alpha C_{max} + \beta} \quad \text{and} \quad \tau_s = \frac{1}{\alpha C_{max} + \beta} \tag{2.23}$$

GABAb-mediated synapse modelling

GABAb-mediated synapses active *indirectly*, following a series of intracellular events [25]. In particular, the neurotransmitter binding event activates an intracellular complex called a G-protein which activates potassium channels ultimately hyperpolarizing and causing inhibition of the postsynaptic neuron [25]. In this way, the synaptic conductance function is described by:

$$g(t) = \frac{s^4}{s^4 + K_d} \tag{2.24}$$

$$\frac{dr}{dt} = K_1[T](1 - r) - K_2 r \tag{2.25}$$

$$\frac{ds}{dt} = K_3 r - K_4 s \tag{2.26}$$

where r is the fraction of GABAb receptors in the activated form, s is the normalized G-protein concentration in activated form, K_d is the dissociation constant of G-protein binding on potassium channels, and $[T]$ is defined as in Equation (2.21).

2.5 Simulating using NEURON and NetPyNE

NEURON is a simulation environment for modelling morphologically detailed individual neurons and networks of neurons [30]. While most of the programming is done using the `hoc` programming language, Python has also been adopted as an alternative interpreter more recently. NEURON offers multiple user-selected numerical integration methods with Implicit Euler being the default method of integration. In this work, we used the CVODE solver to enable variable time-step integration, providing greater accuracy and efficiency, particularly for handling stiff equations. NEURON also features a graphical user interface which includes many tools such as CellBuilder for building and simulating single- and multi-compartment cells and networks. Building cell models, either with `hoc` code or using the GUI involves first specifying the architecture and biophysical properties. Then, point processes such as a synapse or a stimulating electrode, and distributed mechanisms such as

active or passive conductances can be attached to cells with locations specified accordingly. Distributed mechanisms and point processes are user-defined and can be added with the model description language NMODL, a high-level language implemented for NEURON by Michael Hines. The process begins with the user writing a text file (a `mod` file) which describes the mechanism (e.g., a sodium current) using a set of equations such as nonlinear algebraic equations, differential equations or a kinetic reaction scheme. The NMODL translator then constructs C code which proceeds to compute the relevant data such as total current, reversal potential, and membrane potential. Each `mod` file has a particular structure to it with the *variable declaration* and *equation definition* blocks being the code's core. The variable declaration block specifies names and variables including state variables in the model. The equation definition block defines model equations (equation to calculate current, derivative equations, auxiliary functions), initial conditions, as well as specifies the method of integration. It is also the main computation block of the mechanism. Once the mechanisms are defined using `mod` files, they can be inserted into `hoc` code that describes an individual neuron model. Multiple copies of the cell can be created by creating a template of the cell (a `tem` file), and synaptic connections can be added via a Network Connection (NetCon) object with appropriate user-defined synaptic properties. In this way, networks of neurons can be simulated and analyzed according to the purpose of the study.

NetPyNE, short for **Net**works using **Py**thon and **NE**URON, is a Python package developed by Dura-Bernal et al. that allows for high-level specification of network connectivity of biological neuronal networks and simulations using the NEURON simulator [58]. One of NetPyNE's key features is its ability to perform parameter optimization and exploration that can be applied on both the single-cell level as well as on the network level. NetPyNE's standardized declarative language provides transparent and comprehensive model descriptions which are separate from the underlying technical implementation. Model specifications are translated into appropriate NEURON components via built-in algorithms. With the use of raw-code descriptions in many existing models, there is a lack of model standardization which makes understanding, reproducibility and reusability of models and the simulated results challenging. In fact, several models published in other languages including NEURON directly are being converted for use with NetPyNE to increase the model's usability. Building network models begins with defining all the required parameters such as population size, cell properties (which may use the same `mod` files as those used in NEURON, as well as existing cell models written as `tem` files), connectivity rules, simulation options including integration step size, duration, and defining variables to record for analysis. A user may define these inputs pragmatically with NetPyNE's declarative language or use the NetPyNE GUI. Then, a single function call executes NetPyNE's use of NEURON as its back-end simulator. Simulation results can also be exported for use

with other tools such as MATLAB.

2.6 Thalamocortical circuitry and generation of spindles and spike-wave discharges

The thalamocortical circuit is involved in numerous processes, including cognition, the sleep-wake cycle, and various neurological disorders [120]. This circuit is considered to play a critical role in both the generation of physiological sleep spindles as well as the pathophysiology of absence seizures. Spindles are neural oscillations exhibited in mammals during non-rapid eye movement sleep, known to vary in frequency and cortical source across different brain regions [169]. Typically, spindles are characterized by bursts of 7–10 Hz activity on an electroencephalogram (EEG) in humans, as shown in Figure 1.1A [169]. Some electrophysiological studies suggest that the thalamocortical circuit has the ability to gradually transform sleep spindles into pathological 2.5–5 Hz spike-wave discharges (SWDs), one of the hallmark features of childhood absence epilepsy (CAE) [75, 110].

As illustrated in Figure 2.12, the circuit consists of reciprocal pathways connecting the thalamus and cortex, forming a feedback loop between the two structures [49]. Both regions contain excitatory and inhibitory neurons that regulate thalamocortical communication. In this schematic, cortical pyramidal (PY) neurons are not representative of any specific cortical layer. Within the cortex, PY neurons project to other PY neurons and also make excitatory connections to the inhibitory cortical interneurons (IN), which modulate intracortical excitation. Similarly, in the thalamus, thalamocortical (TC) relay neurons excite inhibitory reticular (RE) neurons, which in turn inhibit both TC and other RE neurons. Across structures, PY neurons project to both TC and RE neurons, while TC neurons project to both PY and IN cells. For example, activation of PY neurons leads to excitation of both TC and RE cells. In turn, TC neurons excite both PY and RE cells, while RE neurons provide inhibitory feedback to TC cells, forming a negative feedback loop. The dynamics of these interactions are influenced by the strength of feedback, which ultimately contributes to the emergence of rhythmic activity [8, 19].

Some theories assume that the electrical activity associated with absence seizures originates in the thalamus and is triggered by cells in the reticular nucleus [16, 31], while others emphasize that activity originates in specific regions of the cortex. Classical studies of genetic model of absence seizures including the Wistar Albino Glaxo from Rijswijk (WAG/Rij) and the Genetic Absence Epilepsy Rats from Strasbourg (GAERS) rats characterized the key role of localized cortical regions, particularly the peri-oral region and the

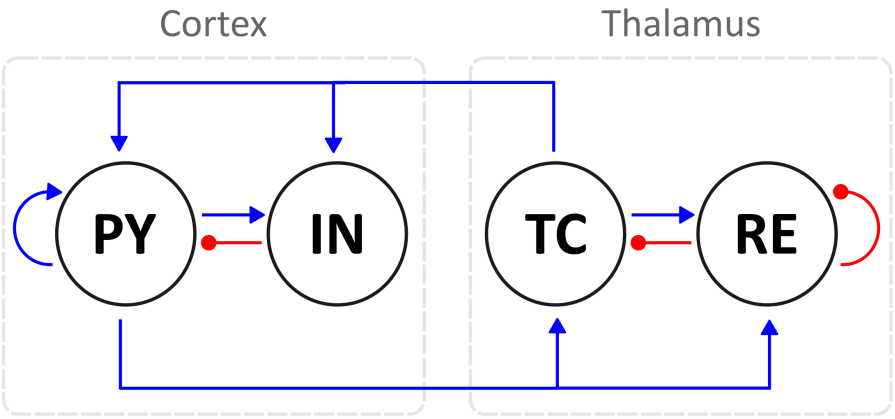

Figure 2.12: The schematic diagram of the thalamocortical circuit shows the connections between cortical pyramidal neurons (PY), cortical interneurons (IN), thalamic relay neurons (TC) and thalamic reticular neurons (RE). Blue arrows indicate excitatory connections, while red arrows represent inhibitory connections.

barrel field region of the primary somatosensory cortex respectively, as the originators of absence seizures [141, 186]. Studies have also shown distinguishable onset and propagation patterns of spontaneous SWD activity in two different absence seizure mouse models. In particular, a pharmacologically induced model (gamma-hydroxybutyric acid, GHB model) and a transgenic model (phospholipase beta4 knock-out, PLCβ4 model) showed a majority of SWDs initiated in the prefrontal cortex and the somatosensory cortex, respectively. These studies suggest that various initiation sites are observed across different mouse and rat models—both genetic and pharmacological—as well as in children with absence seizures. In this way, it is suggested that these cortical initiation regions can be referred to as the cortical initiation network (CIN). The complete manifestation of clinical symptoms in these seizures depends on the interaction between cortical and thalamic networks, both of which are crucial for the generalization of the seizure [145, 39, 19, 17]. However, in some cases, spike-wave activity can be generated independently by either the cortex or the thalamus, suggesting that there are multiple potential underlying causes of these seizures that may vary across individuals [31, 94]. In fact, the characteristic 2.5–5 Hz spike-wave discharge seen in CAE can also be highly variable even in the same individual, with variations in amplitude, duration, and frequency throughout the SWD [39].

2.7 Neurotransmitters, hormones and absence epilepsy

2.7.1 Neurotransmitter function and absence epilepsy

As discussed in Section 2.6, EEG recordings from humans and animals both indicate the essential role of the cortex, thalamic relay nucleus, and the reticular nucleus in the development of SWDs with none of them being able to sustain these pathophysiological oscillations on their own. Further pharmacological data has shown that both inhibitory and excitatory neurotransmissions are crucial in the development and control of absence seizures [37, 189, 182]. One of the most prevalent factors in the alteration of SWDs is the function of neurotransmitters, particularly GABAa. GABAa receptor-mediated inhibition consists of both a phasic and a tonic component. Phasic GABAa inhibition refers to the interaction of GABA with GABAa receptors at the synapses, while tonic inhibition refers to the binding of GABA to extrasynaptic GABAa receptors [22]. Since this research will focus on phasic GABAa inhibition, we present evidence that concerns only this component and we will henceforth refer to it simply as GABAa inhibition without the explicit mention of it as being phasic.

The long-standing view of a widespread GABA *loss-of-function* refers to spike-wave discharges being a result of reduced GABA function across the thalamocortical network, and this was often supported by experimental studies in which the entire brain circuit was influenced. However, this view is challenged by several studies suggesting otherwise [9]. In 1989, Peeters et al. investigated the influence of muscimol (a GABAa receptor agonist) and bicuculline (a GABAa receptor antagonist) on EEG activity in WAG/Rij rats [163]. Administration of muscimol resulted in a dose-dependent increase in the number of observed SWDs, while after bicuculline injection, there was a dose-dependent decrease. A similar result of dose-dependent increase in duration of SWDs has been noted in adult GAERS, another well-established genetic model of absence epilepsy, following administration of vigabatrin (antiepileptic medication that increases GABA concentrations) [41].

In fact, there is evidence of the role of GABAa in the pathophysiology of absence seizures being brain region-specific. In the cortex, a *hypofunction* of GABAergic neurons is shown to aggravate SWDs. Intracellular recordings from layer 2/3 and layer 5 cortical pyramidal neurons from cortical slices of WAG/Rij rats have revealed a decrease in cortical GABAergic inhibition [42, 123]. On the contrary, in the thalamus, a *hyperfunction* of the GABAergic system is known to contribute towards the exacerbation of SWDs [164]. In 1991, Liu et al. studied the effect of injecting vigabatrin (GVG) and muscimol in different regions of the thalamus on aggravating SWDs in adult GAERS [119]. It was found that activation of GABA transmission in the thalamic relay nuclei (TC neurons) after muscimol

and GVG injections increased SWD duration. In contrast, activation of the reticular nuclei (RE neurons) following injections of muscimol and GVG suppressed SWDs.

In order to study this in silico, Bouwman et al. used a computational model to simulate the effect of vigabatrin action by targeting specific regions of the thalamocortical network [21]. This was conducted by increasing the output of GABAergic neurons projecting to the following: both cortex and thalamus (PY, TC, and RE cells), only cortex (PY cells), only thalamus (TC and RE cells), and only thalamic relay nucleus (TC cells). Their results showed a decrease in total SWD duration following an increased GABA concentration in the full network, only thalamus, and only cortex. On the contrary, increasing GABAergic transmission in TC cells only increased the total duration of SWDs. There were no simulations performed that pertain to increased GABA in RE cells. However, the obtained results were consistent with clinical and pharmacological observations as noted earlier.

2.7.2 Hormones and absence epilepsy

Adolescence is a critical transitional period during development that features the maturation of reproductive hormones and striking changes in sex hormonal levels associated with puberty. Given that remission in most cases of CAE occurs during this time, this suggests an association of gonadal hormones with epilepsy. This association is further supported by the phenomenon of catamenial seizure exacerbation [197]. This refers to the periodicity of seizure exacerbation that aligns with the cyclical changes in circulating levels of ovarian steroid hormones (the menstrual cycle). There is substantial evidence from clinical studies as well as animal experiments on the effect of sex steroid hormones particularly progesterone on neuronal excitability, seizures, and epilepsy, including absence epilepsy.

Estrogen and progesterone are major steroid hormones that impact sexual development during puberty and are associated with reproduction. They can be synthesized locally in the central and peripheral nervous system or derived from the gonads or adrenal gland. They are both synthesized from pregnenolone which itself is derived from cholesterol [174, 69]. There are three major forms of estrogen that cause estrogenic activity: estrone, estradiol, and estriol. Their concentration levels vary as per the endocrine state of the body. Estrone is the primary form of estrogen after menopause and estriol during pregnancy, while estradiol is the most potent, prevalent and primary form during reproductive years [44]. The metabolism of progesterone involves the production of allopregnanolone (ALLO), a neuroactive steroid. Neurosteroids, like allopregnanolone may be synthesized within the nervous system or accumulate in the brain via systemic circulation after being derived by the gonads (in females) and by the adrenal glands (in both sexes) [73]. They rapidly

modulate neuronal excitability through both genomic and non-genomic mechanisms. There is substantial evidence from both clinical studies as well as animal experiments on the effect of progesterone (and allopregnanolone) on human and animal EEG [204].

Administration of progesterone in both humans and animal has been shown to result in an exacerbation of absence seizures. In human experiments, oral and intramuscular administration of progesterone resulted in a consistent and remarkable increase in frequency of absence seizures a few hours after administration. The frequency of seizures remained high for several weeks after injections [79]. In animal experiments using female WAG/Rij rats, a common model for generalized absence epilepsy, fluctuations in increased incidence of SWDs was correlated with fluctuating peak physiological concentrations of progesterone during the ovarian cycle [197]. Further data from a pharmacological experiment by Luijtelaar et al. revealed a causal relationship [197]. A dose-dependent increase in the number and total duration of SWDs was observed after injection of progesterone with similar results in male WAG/Rij rats following administration of allopregnanolone [26].

On the contrary, the effect of estrogen on SWDs has been found to be insignificant in the case of typical absence epilepsy. Administration of synthetic estrogens both intravenously and orally displayed no effect on absence frequency [79]. Similarly, in WAG/Rij female rats, the number of SWDs was not different at the time of peak physiological concentration of estradiol during the ovarian cycle, from any other time [197]. To check whether this effect could differ with higher concentrations of estradiol than that present physiologically, Luijtelaar et al. studied the effects of administration of estradiol at large doses. It was found to have no significant effect on SWDs in WAG/Rij rats [197].

2.7.3 Hormones and their mechanisms of action

Steroid hormones can have an affect on neuronal excitability through both genomic and nongenomic means. Genomic mechanisms involve steroid hormone binding and forming complexes within the cell nucleus. This is followed by the binding to a hormone response element in a target gene which then regulates the expression of that gene resulting in protein synthesis. This process is slow and generally occurs on a much longer time scale relative to nongenomic mechanisms. Nongenomic mechanisms include binding to and direct modulation of neurotransmitter-gated ion channels [207].

Allopregnanolone, a neuroactive steroid, has the ability to modulate neuronal excitability through both genomic (i.e., through regulating gene expression) and nongenomic means (i.e., modifying ion conductance, second messengers, and activating signalling pathways)

[211]. At the nongenomic level, its effect on GABAa receptors depends on its concentration. At nanomolar concentrations, ALLO is a positive allosteric modulator of the GABAa receptor [165, 168, 114]. This means that it binds to a site on the GABAa receptor that is different from the site its endogenous agonist such as GABA molecule would bind at. It then modulates the response of the receptor to a stimulus. Specifically, it increases the probability of the channel being in the open state and enhances the receptor's response to GABA by increasing its efficacy [24, 127]. At micromolar concentrations, ALLO can activate GABAa receptors independently of GABA [196, 12]. Its overall effect is to potentiate GABA action particularly by decreasing the rise time and increasing the decay time of the evoked current, an effect consistently observed across various experimental conditions [127, 162, 187, 185, 121]. Additionally, under some conditions, an increase in current amplitude is also observed [162, 187, 127].

Chapter 3

Modelling the effect of allopregnanolone on the resolution of spike-wave discharges

This chapter is based on the paper: M Ahmed and SA Campbell. Modelling the effect of allopregnanolone on the resolution of spike-wave discharges. *Journal of Computational Neuroscience*, 53:115-130 , 2024.

3.1 Introduction

Childhood absence epilepsy (CAE) is an idiopathic generalized epilepsy disorder which affects children between the ages of 4-12 years [84]. It is characterized by sudden brief periods of impaired consciousness occurring several times a day. Unlike some other epilepsy types, but similar to certain idiopathic forms, CAE is more common in girls than boys [38]. One of the most confounding features of this disease is its age-dependent expression, and the ability to spontaneously resolve in adolescence, with remission occurring in about 70% of cases, while in others it can progress into more severe types of epilepsy [38]. There are several hypothesized mechanisms involved in remission, including antiepileptic drugs, differences in circuitry arrangements and genetic predisposition or dynamic epigenetic processes. However, there remains an inadequate understanding of some of these factors that can inform early intervention practices.

Clinically, CAE is diagnosed using an electroencephalogram (EEG) where recordings exhibit bilateral synchronous 2.5–5 Hz spike-wave discharges (SWDs) [84]. The recorded EEG can thus be used as an indicator for underlying brain activity and neuronal networks that may be involved in giving rise to such oscillations. Based on many years of accumulating evidence from animal models, the thalamocortical circuit consisting of pyramidal neurons in the cortex, thalamic relay neurons and thalamic reticular neurons in the thalamus is considered to be important in the generation of normal 7–10 Hz sleep spindles, as well as in the pathophysiology of absence seizures [180]. According to the cortical focus theory, the cortex is considered as the driving source for the origin of SWDs, with a cortical focus initiating rhythmic discharges followed by propagation towards generalized activity through intracortical pathways and the thalamus, thus forming an integrated network [140].

There is a considerable amount of evidence towards a strong contribution to the development of SWDs by genes encoding receptors for the inhibitory neurotransmitter GABA, as well as ion channels including calcium channels, sodium channels, and potassium channels [156, 35, 122, 109]. Here we focus on the effect of genes encoding T-type calcium channels and GABAa receptors, which we describe in more detail below.

T-type calcium channels (most prominently Cav3.1, Cav3.2 and Cav3.3) are known to play a key role in the generation and maintenance of spike-wave discharges as they are fundamental in thalamic burst firing [34]. Cav3.2 channels encoded by the $CACNA1H$ gene are mainly expressed in thalamic reticular neurons and in some pyramidal neurons in the cortex [34]. There is a spectrum of $CACNA1H$ variants linked to CAE which results in enhanced T-type calcium current and consequently alters the firing of thalamic neurons to generate SWDs [35]. For instance, the P640L variant of Cav3.2 induces changes

in the biophysical properties of the channel including altered current (in)activation time constants, current amplitudes, as well as shifts in voltage dependence on (in)activation [74].

Pharmacological data has shown that inhibitory and excitatory neurotransmissions are crucial in the development and control of absence seizures [37, 189]. One of the most prevalent factors in the alteration of SWDs is the function of GABA. The intrinsic properties of GABAa receptors (GABAaRs) may vary depending on different subunit compositions. Receptors containing α1-3, β1-3 and γ2 subunits are more commonly localized in postsynaptic sites, and receptors predominantly composed of $\alpha 1\beta 2\gamma 2$ subunits comprise approximately 43-60% of all GABAaRs in the adult brain [201, 209]. Mutations in the $GABRG2$ gene which encodes the γ2 subunit of the GABAaR is most strongly associated with CAE, while variants of $GABRA1$, $GABRB2$ and $GABRB3$ genes are weakly implicated as reported in some studies [209, 70]. For instance, a $GABRG2$ heterozygous missense variant R82Q as well as the R43Q mutation were reported to reduce γ2 surface expression due to abnormal trafficking resulting in reduced GABAaR currents, reduced surface expression of GABAaRs in pyramidal neurons in the cortex, as well as reduction in miniature inhibitory postsynaptic currents in layer 2/3 cortical neurons [125, 40, 130]. Thus, the overall effect of GABAaR subunit gene mutations is disinhibition causing abnormality in cortical network function.

Furthermore, given that remission often occurs at adolescence (a time of onset of puberty), the association of sex hormones with CAE is also suspected [197]. Interestingly, sex hormones have also been implicated in the exacerbation of seizures, as seen in the phenomenon of catamenial epilepsy. This condition is characterized by the periodic worsening of seizures that aligns with the cyclical changes in circulating levels of ovarian steroid hormones during the menstrual cycle [66]. The cyclical variation of steroid serum levels and its positive correlation with seizure frequency suggest a neuroactive role of sex steroid hormones, with context-dependent effects that may contribute to both remission and exacerbation.

Progesterone is one of the major steroid hormones that impacts sexual development during puberty. While it is often recognized as a female hormone, its presence and significance in males are also important [73]. It can be synthesized locally in the central and peripheral nervous system or derived from the gonads or adrenal gland [174, 69]. The metabolism of progesterone involves the production of allopregnanolone (ALLO), a neuroactive steroid. Neurosteroids such as allopregnanolone, may be synthesized de novo in the nervous system or accumulate in the brain through the bloodstream after metabolism of adrenal or gonadal steroids [69]. They rapidly modulate neuronal excitability through both genomic (i.e., regulation of gene expression) and non-genomic mechanisms (i.e., mod-

ulation of neurotransmitter-gated ion channels, and activation of signalling cascades) [23]. There is substantial evidence from both clinical studies as well as animal experiments on the effect of progesterone (and allopregnanolone) on human and animal EEG [204]. Administration of progesterone has been shown to result in an exacerbation of absence seizures [197, 26]. Allopregnanolone is a positive allosteric modulator of the GABAaR. In particular, it increases the probability that an agonist will bind to the receptor as well as the receptor efficacy [24, 127]. The overall effect is to enhance and prolong the action of GABA, resulting in enhanced inhibitory connections.

It is certainly understood that childhood absence epilepsy is a multifactorial disorder which poses many challenges, but also unique opportunities for exploration, when it comes to computational modelling. The objective of this study was to use a well-established conductance-based thalamocortical model associated with CAE to explore the role of allopregnanolone in the eventual resolution of absence seizures, as observed in most cases. Given that our model only considers one sex hormone, which is present in both males and females, and there are other documented sex differences such as network connectivity structure, we do not consider our model as a sex-specific model, but rather a generic exploratory one. Broadly speaking, models can range in complexity and scale, and be categorized as being biophysical or phenomenological. While phenomenological models simply describe an empirical relationship and convey the phenomena, biophysical models also capture the underlying biophysical mechanisms driving the concerned phenomena [86]. Since our study involves exploring mechanisms occurring at the level of ion channels, it was appropriate for us to use a detailed conductance-based model formalism similar to that used in previous studies [49, 46, 194, 106]. In particular, our goal was to gain insight on factors that may predispose some individuals to experience remission or as we have termed it, 'resolving CAE'. This study also explored how the effect of allopregnanolone differs depending on the genetic factors associated with CAE and the consequent ability of the network to transition between a healthy state and diseased state through variation of model parameters.

3.2 Materials and methods

Our thalamocortical model is built upon on the previous work by Knox et al. [106] in which a well-established thalamocortical model by Destexhe [46] was used to study the contribution of the T-type calcium channel in thalamic reticular neurons combined with cortical excitability in the pathogenesis and treatment response in CAE.

The model, a 400-cell thalamocortical network, consists of single-compartment neuron models of four types: cortical pyramidal cells (PY), cortical interneurons (IN), thalamic

reticular cells (RE) and thalamocortical cells (TC). The membrane potential of each cell type is described by the following equations:

$$\begin{aligned} C_m \frac{dV_{PY}}{dt} &= -I_{Leak} - I_{Na} - I_K - I_M \\ &\quad - I_{GABAa_{IN}} - I_{GABAb_{IN}} - I_{AMPA_{PY}} \\ &\quad - I_{AMPA_{TC}} \end{aligned} \tag{3.1}$$

$$\begin{aligned} C_m \frac{dV_{IN}}{dt} &= -I_{Leak} - I_{Na} - I_K - I_{AMPA_{PY}} \\ &\quad - I_{AMPA_{TC}} \end{aligned} \tag{3.2}$$

$$\begin{aligned} C_m \frac{dV_{TC}}{dt} &= -I_{Leak} - I_{Na} - I_K - I_T - I_h \\ &\quad - I_{KLeak} - I_{GABAa_{RE}} - I_{GABAb_{RE}} \\ &\quad - I_{AMPA_{PY}} \end{aligned} \tag{3.3}$$

$$\begin{aligned} C_m \frac{dV_{RE}}{dt} &= -I_{Leak} - I_{Na} - I_K - I_{Ts} \\ &\quad - I_{GABAa_{RE}} - I_{AMPA_{PY}} - I_{AMPA_{TC}} \end{aligned} \tag{3.4}$$

where V_i is the membrane potential for i = PY, IN, TC, RE, $C_m = 1\mu F/cm^2$ is the specific capacity of the membrane. All intrinsic currents follow the same formalism as in Equation (3.5), where $\bar{g}_{ion}$ represents the maximal conductance, and m and h represent the voltage gating of the ion channels. All synaptic currents follow Equation (3.6) with AMPA/GABAa- and GABAb- mediated synapses being described appropriately by the synaptic conductance function, $s(t)$, and $\bar{g}_{syn}$ denotes the maximal conductance. All of the cell types have Na^+ and K^+ currents as described in Traub et al. [194]. The IN cells do not have any additional currents, while the PY cells have one additional slow K^+ current, I_M, which contributes to spike frequency adaptation behaviour. Both the thalamic cells exhibit bursting behaviour due to the presence of a low-threshold Ca^{2+} current, I_T , with slower kinetics in the RE cells. In addition to this, TC cells also have a hyperpolarization-activated current, I_h. The kinetics of all the currents are as described in Destexhe et al. [49], leading to models of the form:

$$I_{ion} = \bar{g}_{ion} \cdot m^N h^M \cdot (V_m - E_{ion}) \tag{3.5}$$

$$I_{syn} = \bar{g}_{syn} \cdot s(t) \cdot (V_m - E_{syn}) \tag{3.6}$$

The details of the individual currents, synaptic dynamics as well as model parameters are described in Section A.1.

Cortical cells represent layer 6 of the cerebral cortex and have excitatory synapses formed with ascending thalamic axons, creating an excitatory feedback loop. The network is made up of 100 cells of each type and each layer of cells is arranged in one dimension as shown in Figure 3.1 with connectivity and synapses varying between cell types as described. All excitatory connections in the network are mediated by AMPA receptors, and inhibitory connections are mediated by either just GABAa or a combination of GABAa and GABAb receptors. Within the thalamus and the cortex, each neuron has connections with 11 postsynaptic neurons, while between the thalamus and cortex, each presynaptic neuron has connections with 21 postsynaptic neurons, as illustrated in Figure 3.1. The synaptic conductance values were chosen to reflect exploration of the parameter space performed in a previous paper by Destexhe [46], and were meant to be interpreted qualitatively. The default mode of the model exhibits spontaneous oscillations due to spontaneous discharges in TC neurons. After allowing the network to reach steady state, a 0.7 nA stimulus was applied for 100 ms to a group of five pyramidal neurons, triggering additional oscillations.

The local field potential (LFP) was calculated using the formalism by Destexhe [46], in which cortical pyramidal neurons are arranged in a single line 20 μm apart. The extracellular site is considered to be 50 μm opposite to the center of the line, and the LFP at this site was calculated from postsynaptic currents of all pyramidal neurons:

$$V_{ext} = \frac{R_e}{4\pi} \sum_i \frac{I_{syn}}{r_i} \tag{3.7}$$

where V_{ext} is the potential at a defined extracellular site, $R_e = 230\Omega cm$ is the extracellular resistivity, I_{syn} is the postsynaptic current, and r_i is the distance between the location of the postsynaptic currents and the extracellular site.

While the original model was implemented in the NEURON simulation environment, we implemented the model in NetPyNE, a Python package developed by Dura-Bernal et al. that allows for high-level specification of network connectivity of biological neuronal networks and simulations using the NEURON simulator [58]. The switch to NetPyNE allows for better and easier control of accessing certain model components, make changes as necessary, and better model reproducibility, keeping in mind future directions. All of the raster plots were created using NetPyNE's *plotRaster* function. All of the spectrograms were created using the *Scipy* Python library. The LFP traces were filtered using a Butterworth filter with a cutoff frequency of 15 Hz, and power spectral density analysis was performed on the filtered LFP traces using Welch's method.

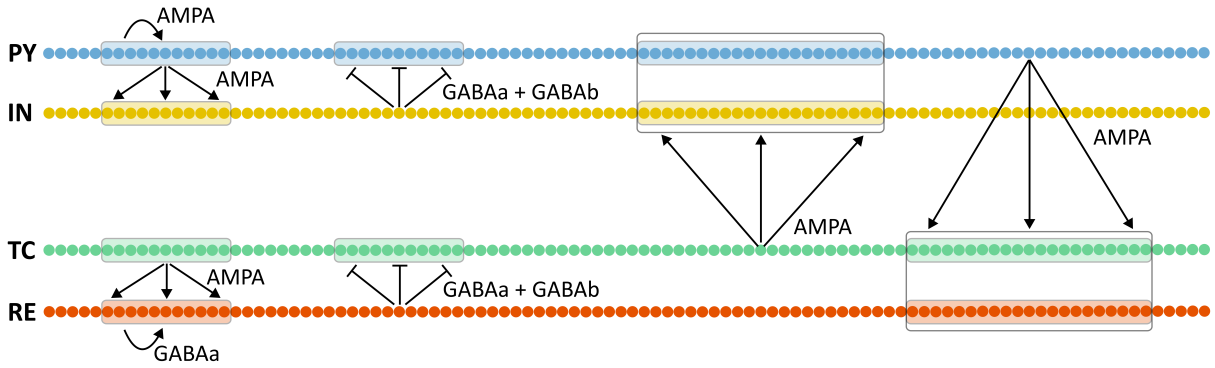

Figure 3.1: Schematic representation of the thalamocortical network. Each neuron is represented by a dot, and each layer consists of 100 cells with synaptic connectivity within and between layers as shown. Within the cortex and thalamus, each neuron connects to 11 postsynaptic neurons while between the cortex and thalamus, each neuron connects to 21 postsynaptic neurons as shown. Adapted from Destexhe et al. [49].

3.2.1 Modelling the effect of genetic mutations on GABAa and T-type Ca^{2+} currents

Several studies have demonstrated the functional consequences of mutations of genes encoding GABAa receptor subunits, particularly $GABRG2$ gene. In the case of mutant receptors containing the γ2(R43Q) subunit, there have been studies using biotinylation of surface receptors and immunoblotting that have demonstrated reduced surface expression [99]. Furthermore, electrophysiological recording studies have shown a reduced amplitude of GABAaR currents in cells containing this particular mutant receptor, consistent with decreased neuronal feedforward inhibition in the cortical circuitry [15, 40]. The effect of the $GABRG2$ mutation was implemented in our model by altering the parameter denoting the maximum conductance of the GABAa current ($\bar{g}_{max}$) in cortical pyramidal neurons, as illustrated below:

$$I_{GABAa} = \boxed{\bar{\boldsymbol{g}}_{\boldsymbol{max}}} \cdot s(t) \cdot (V_m - E_{GABA}) \tag{3.8}$$

The functional consequences of a spectrum of mutations in the $CACNA1H$ gene which encodes the Cav3.2 T-type calcium channel include a significant impact on sustained burst firing in RE neurons and the subsequent propagation of spike wave discharges [28]. In particular, this includes alteration of current peak amplitude as well as activation and

inactivation time [200, 28]. While activation time describes the time it takes for an ion channel to fully open in response to changes in membrane potential, inactivation time describes the time it takes an ion channel to transition from the open state to a closed state. In the model, this is representative of the dynamics implemented through the (in)activation gating variables given by Equations (A.2)-(A.3). A vertical shift in the (in)activation time refers to adding a constant increase to the (in)activation time constant for all values of the voltage. As such, following the formalism by Knox et al. [106], we modelled the effect of $CACNA1H$ mutations by introducing a vertical shift in the inactivation time (τ_0) of the T-type calcium current for RE neurons in our model:

$$\tau_h = \frac{\boxed{\boldsymbol{\tau_0}} + \frac{1}{e^{\frac{V_m+48}{4}} + e^{\frac{-(V_m+407)}{50}}}}{2.5^{1.2}} \tag{3.9}$$

3.2.2 Modelling the effect of allopregnanolone

The effect of allopregnanolone (ALLO) was implemented on the synapse level only, focussing on GABAa-receptor mediated synapses, modelled by Equation (3.8). The conductance function dynamics for these synapses are described by the following equations (details of which can be found in Ermentrout and Terman [61]):

$$s(t) = \begin{cases} s_\infty + (s(t_0) - s_\infty)e^{-\frac{t}{\tau_s}}, & t_0 \leq t < \boxed{\boldsymbol{C_{dur}}} \\ \left[s_\infty + (s(t_0) - s_\infty)e^{-\frac{C_{dur}}{\tau_s}}\right]e^{-\beta(t-C_{dur})}, & t \geq C_{dur} \end{cases} \tag{3.10}$$

where

$$s_\infty = \frac{\boxed{\boldsymbol{\alpha}} C_{max}}{\alpha C_{max} + \boxed{\boldsymbol{\beta}}} \quad \text{and} \quad \tau_s = \frac{1}{\alpha C_{max} + \beta} \tag{3.11}$$

The rise and decay time constants which describe the binding of neurotransmitter are denoted by α and β respectively, the duration of neurotransmitter-mediated pulse is given by C_{dur}, and C_{max} refers to the maximal neurotransmitter concentration value. The effect of ALLO was modelled by making appropriate changes to α and β as well as C_{dur}, as highlighted in Equations (3.10)–(3.11). These changes were informed by fitting our synapse model to available experimental data while relying only on relative changes between control GABAa receptor activity and activity post application of ALLO [127, 162]. In this regard, given that the range of values for these relative changes is based on

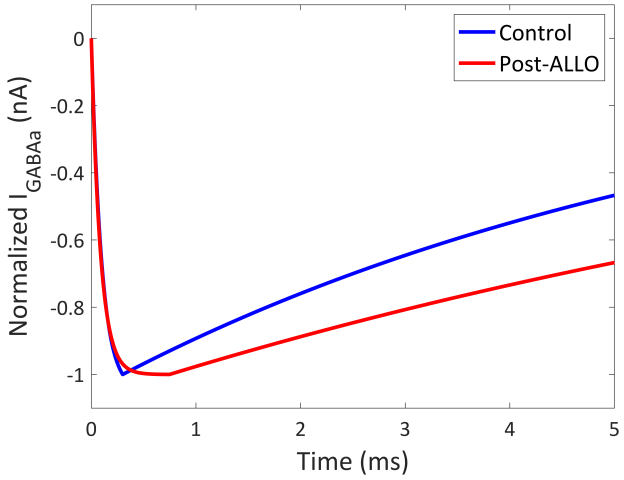

Figure 3.2: A comparison of simulated GABA current for a single spike using parameters corresponding to Control and post-ALLO synapses given by Equations (3.10)–(3.11) and Table 3.1.

experiments conducted under different conditions, the values are meant to be interpreted qualitatively. A comparison of simulated GABAa current using Control synapses and post-ALLO synapses is shown in Figure 3.2 and the parameters of interest for each synapse type is given in Table 3.1.

	α $((\text{ms} \cdot m\text{M})^{-1})$	β (ms^{-1})	C_{dur} (ms)
Control	20	0.162	0.3
post-ALLO	22.87	0.095	0.75

Table 3.1: Rise and decay time constants, and neurotransmitter duration for Control and post-ALLO synapses given by Equations (3.10)–(3.11).

3.3 Results

3.3.1 Baseline healthy and diseased states using control synapses

The first part of this study included modelling and characterizing baseline network behaviour that was either a healthy state exhibiting spindle oscillations (7–10 Hz) or a diseased state exhibiting spike-wave discharges (2.5–5 Hz). For our baseline simulations, all

GABAa synapses were of the Control type, as described in Table 3.1. Network connectivity was initialized to produce a default mode of spindle oscillations with a peak frequency of 8.5 Hz, as shown in Figure 3.3A and 3.3C. In particular, this corresponded to maximal cortical GABAa conductance at 100% baseline and a shift in inactivation time of the T-type calcium current in RE neurons at a baseline value of 28.3 ms. The network could then be transformed to a diseased state using the two mechanisms, namely cortical disinhibition and Ca^{2+} conductance alteration, individually as well as together. Due to a large enough reduction of GABAaR mediated inhibition in the cortex (maximal conductance reduced to 8% of baseline), the network produces a 4.5 Hz SWD pattern as shown in Figure 3.3B and 3.3D. Similarly, an altered inactivation time of the T-type calcium current for RE neurons together with a reduction in cortical GABAa conductance resulted in the network's ability to generate a pattern associated with SWDs, exhibiting a 3.5 Hz peak network frequency as shown in Figure 3.3E. In this mixed-mechanism approach, the shift in inactivation time of the T-type calcium current was increased from 28.3 ms to 60 ms, while the cortical GABAa conductance was reduced to 25% baseline. The individual or combined changes in inactivation time of the T-type calcium current and cortical GABAa conductance were informed by searching this two-parameter space for regions with low and high relative power in frequency range associated with SWDs. Accordingly, there appears to be a distinct region on the heatmap which corresponds to network behaviour that can be classified most strongly as exhibiting spike-wave discharges, as illustrated in Figure 3.4.

3.3.2 Allopregnanolone has an ameliorating effect on SWDs

The second part of this study involved modelling the effect of allopregnanolone by altering parameters associated with the GABAa current as described in the Methods section. The network was initialized to exhibit SWDs using both of the previously described mechanisms. The effect of ALLO was implemented on all GABAa synapses in the model, namely IN-PY, RE-TC, and RE-RE connections. It was observed that allopregnanolone has an ameliorating effect on SWDs such that the spiking frequency of the network increases and transitions from that within the range for SWDs to a range associated with spindle oscillations, as shown in Figure 3.5. The effect of ALLO appeared to cause a more drastic transition in network behaviour from SWDs to spindle oscillations when the underlying pathophysiology was due only to cortical disinhibition (Figure 3.5A and 3.5B). In the case of initializing the network using the altered Ca^{2+} conductance mechanism, the effect of ALLO was not as effective in the resolution of SWDs (Figure 3.5C and 3.5D). While the power in both frequency ranges increased with a greater increase in the range associated with spindle oscillations, the frequency range with maximum power continued to be the

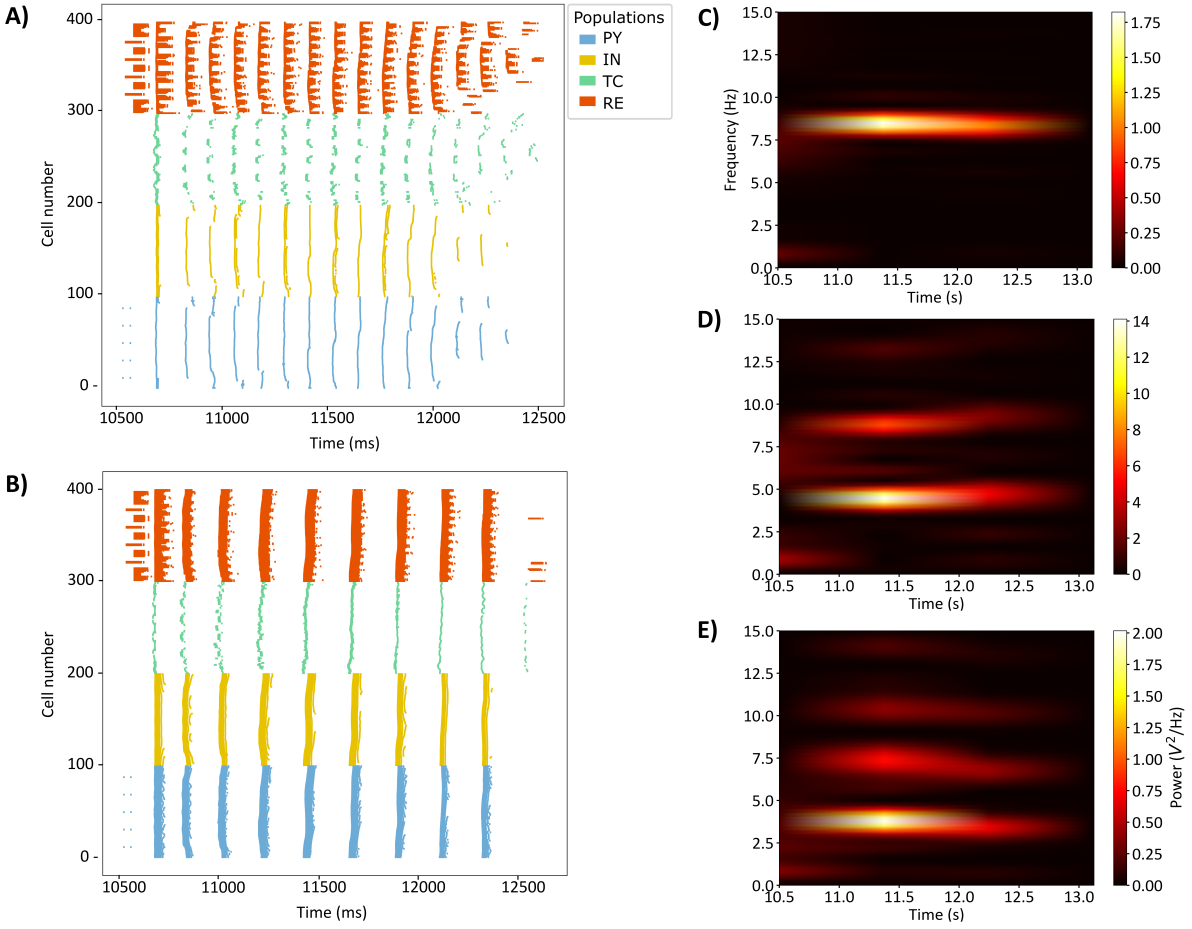

Figure 3.3: A raster plot of the full network exhibiting spindle oscillations (A) and SWD (B) behaviour. The network in (B) was simulated using the cortical disinhibition mechanism only. (C): Network behaviour corresponding to spindle oscillations exhibits maximal power at a frequency of 8.5 Hz. (D): SWD behaviour using the cortical disinhibition mechanism results in maximal power at 4.5 Hz. (E): The network displays SWD behaviour using the altered-Ca^{2+} conductance mechanism with maximal power at approximately 3.5 Hz. All of the simulations were performed using Control GABAa-receptor mediated synapses.

one for SWDs.

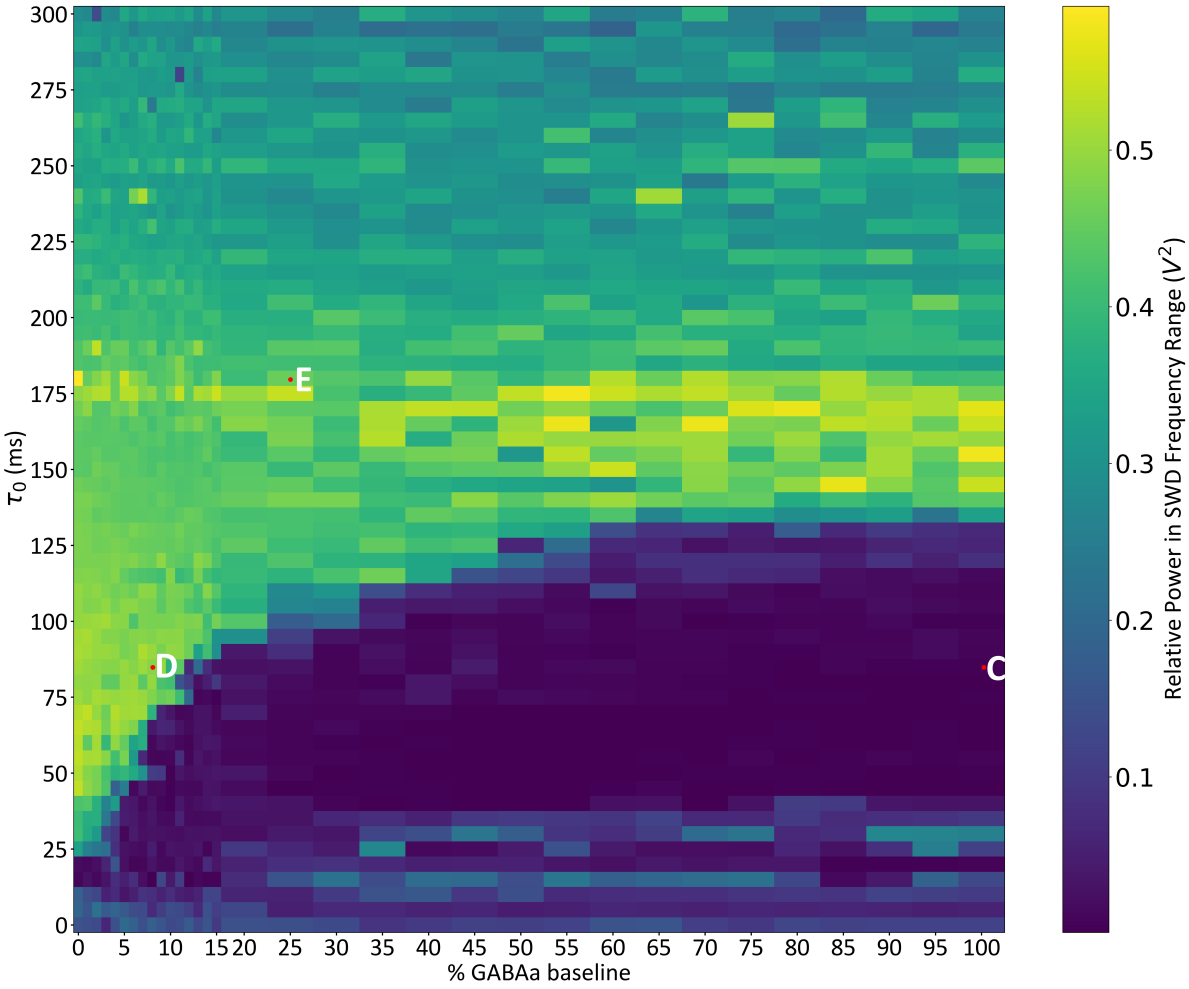

Figure 3.4: Heatmap showing relative power in the frequency range corresponding to SWDs for combinations of cortical GABAa conductance (given as % baseline value) and a vertical shift in the inactivation time of the T-type Ca^{2+} current in RE neurons. Label C corresponds to network behaviour as simulated in Figure 3.3C exhibiting spindle oscillations, Label D corresponds to simulation in Figure 3.3D exhibiting SWDs, and Label E corresponds to simulation in Figure 3.3E exhibiting SWDs using a mixed-mechanism approach as described in Section 3.3.1. Note: there is a change in scale along the horizontal axis at a value of 15% baseline maximal GABAa conductance.

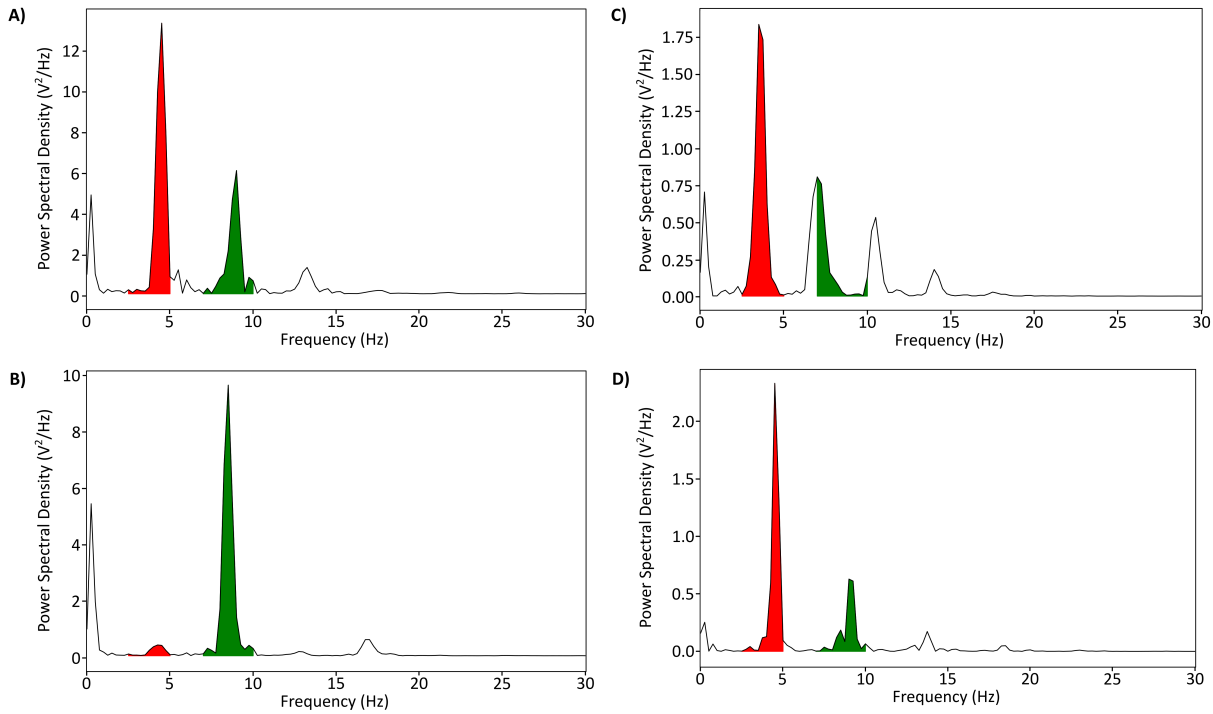

Figure 3.5: Power spectral density for network behaviour simulated using Control synapses (A and C) and post-ALLO synapses (B and D). (A,B): The network was initialized using the cortical disinhibition mechanism only (8% baseline cortical GABAa conductance). (C,D): The network was initialized using the altered Ca^{2+} conductance and GABAa conductance mechanism (τ_0 = 60 ms and cortical GABAa at 25% of baseline). The shaded regions represent relative power in either the SWD (2.5–5 Hz; red) or Spindles (7–10 Hz; green) frequency range. Note that the y-axes differ between panels to reflect differences in maximal power, which result from distinct disease mechanisms.

3.3.3 Exploring the selective action of allopregnanolone

It is known that neurosteroids such as allopregnanolone may be synthesized de novo in the central nervous system, and that endogenous allopregnanolone levels are brain region specific [55, 175]. We modelled these region-specific differences by exploring the selective action of ALLO on synapses between specific neuron types in the cortex and thalamus. In particular, this was implemented by making changes to parameters pertaining to the GABAa current (as described in 3.2.2) for the following synapses: (i) IN-PY (cortex only); (ii) IN-PY and RE-TC; (iii) IN-PY and RE-RE; (iv) RE-TC; (v) RE-RE; (vi) RE-TC and

RE-RE (thalamus only).

The network behaviour in each simulation was characterized using a measure of the relative power within either the frequency range associated with SWDs or that associated with spindle oscillations (Figure 3.6A) as well as the peak frequency of the network (Figure 3.6B). Here we have defined peak network frequency as the frequency with the most power. The initial SWD state in each simulation was generated using the cortical disinhibition mechanism only. When implemented on the cortex alone, the action of ALLO makes little difference to the overall network behaviour in terms of changes in the peak frequency or the relative power in both frequency ranges. On the thalamus alone, there is a clear transition from SWDs to spindle oscillations as demonstrated by a raster plot (not shown) as well as a change in the peak network frequency from 4.5 Hz to 8.0 Hz. Exploring further within the thalamus, the action of ALLO on the RE-TC synapses alone makes little difference but paired with altered synapses in the cortex, there appears to be a very small increase in network frequency. However, the associated pattern of the network is not clearly defined spindle oscillations. Furthermore, alterations in the RE-RE synapses alone resulted in a significant change in network behaviour as demonstrated by alternating bursts in the TC population seen on the raster plot, as well as a change in peak frequency of the network from 4.5 Hz to 8.0 Hz. When paired with alterations in the cortex, this transition in peak frequency was further enhanced to 8.5 Hz.

It is to be noted that except for alterations in the IN-PY and RE-TC synapses together, all of the simulations showed consistency with regards to a relation between the relative power within a given frequency range and the peak frequency of the network. As such, more power within the range corresponding to SWDs was correlated with a peak network frequency within the same range. However, in the case of the effect of ALLO on IN-PY and RE-TC synapses together, the relative power was greater in the 7–10 Hz range corresponding to spindles, even though the peak frequency of the network was 5 Hz, within the range corresponding to SWDs (Figure 3.6C). This was due to a narrower peak around 5 Hz, therefore contributing towards less power as compared to the 7–10 Hz range. Overall, these results suggest that the effect of allopregnanolone is most significant in the thalamus, particularly on the RE-RE synapses which appear to be a critical contributor to the resolution of spike-wave discharges.

3.4 Discussion

In this study, we modelled the effect of allopregnanolone on a thalamocortical circuit associated with childhood absence epilepsy. Our network was initialized to a diseased,

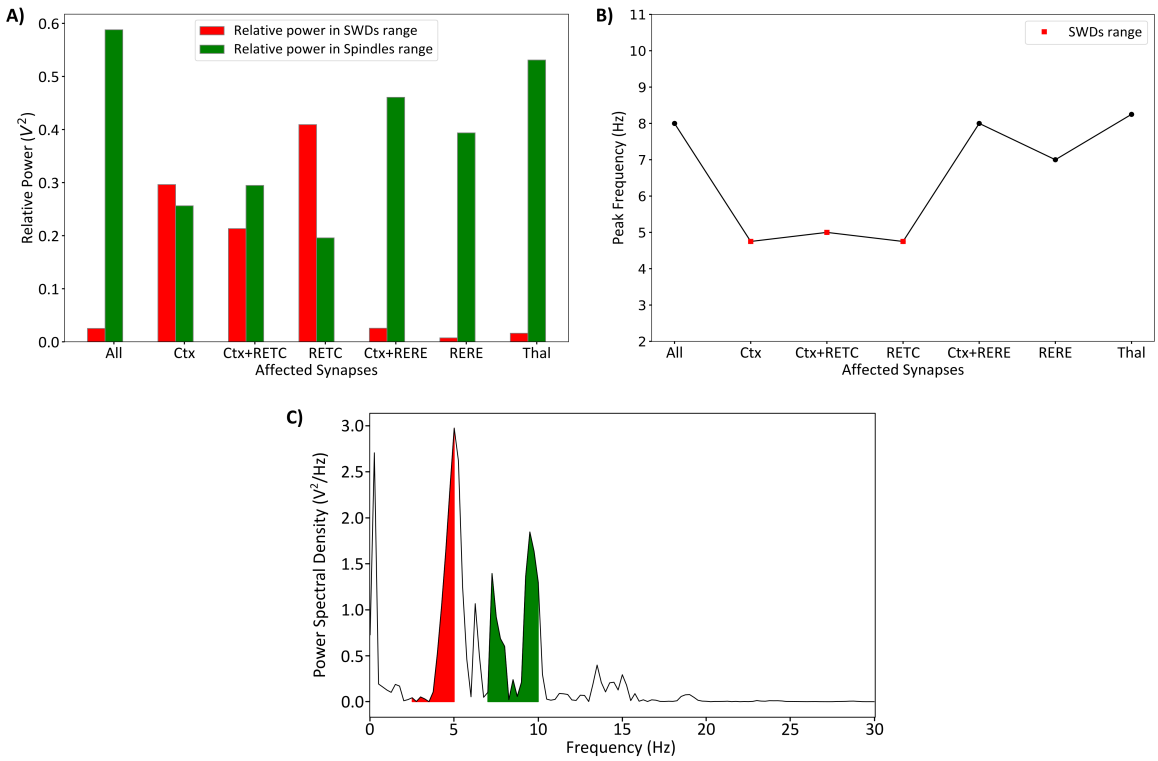

Figure 3.6: Relative power in frequency range corresponding to spindle oscillations and spike-wave discharges (A) and the peak frequency (B) for network simulations with post-ALLO synapses between specific neuron types in the cortex and thalamus. For all the simulations, the diseased state was produced using the cortical disinhibition mechanism only. (C): Power spectral density for network behaviour after implementing the effect of ALLO only on IN-PY and RE-TC synapses together.

spike-wave discharge producing state that was informed by the genetic basis of the disease related particularly to GABAa-mediated inhibition and T-type calcium channel activity. The available data about the effect of hormones and neurosteroids is at two very different scales: the large-scale effect on EEG/seizures, and the small-scale effect on individual neurons/synapses. Our work is intended to fill in the gap as to how or why the in-vitro results lead to the observed EEG or network behaviour. The effect of hormones and neurosteroids on network behaviour has not been modelled previously which makes this study interesting even outside of the context of CAE.

Our results suggest that allopregnanolone has an overall ameliorating effect on absence seizures, pushing a diseased state of the network towards a healthy non-epileptic state when the disease mechanism was due to cortical disinhibition only. On the contrary, the action of ALLO appeared to be insufficient to counteract the aggravating effect of altered T-type Ca^{2+} channel activity contributing to sustained SWDs. As a result, our investigation of ALLO and its interaction within the thalamocortical circuit was limited to the cortical disinhibition mechanism only. Exploring the role of ALLO further on individual synapses comprising the GABAergic system revealed the selective action of this neurosteroid in either sustaining SWDs or resolving them. The importance of the GABAergic system in the pathophysiology of epileptic seizures has existed for a long time and is no different in the case of CAE. Our results are also consistent with the brain region-specific function of GABA across the thalamocortical network in the context of absence seizures. In the cortex, a hypofunction of GABAergic neurons is shown to aggravate SWDs [42, 123]. On the contrary, in the thalamus, a hyperfunction of GABA transmission in the thalamocortical neurons is observed to increase SWD duration while increased GABA in the thalamic reticular neurons suppresses SWDs [164, 119]. The prolonged action of GABA as a consequence of the effect of ALLO in TC neurons resulting in a continued SWD pattern can be correlated with increased SWD duration, or at least as a lack of positive impact on SWD behaviour. Similarly, implementing ALLO-affected synapses in RE neurons very clearly resulted in the suppression of SWD activity in our network. It is interesting to note this consistency in the results considering that the mechanism by which there is increased GABA-mediated activity is different. As such, our approach involves implementing the effect on the intricacies of the binding process of GABAa receptor function via time constants and neurotransmitter duration which is different from the classical approach of a change in channel conductance which is associated with channel blocking or up/down regulation. This provides a new avenue to explore function of GABAa receptors with regards to computational modelling in other contexts.

Our modelling results offer a potential explanation for apparent discrepancies between clinical observations and experimental findings regarding the effects of progesterone and its metabolite allopregnanolone on spike-wave discharges. While clinical and animal studies have suggested that ALLO may exacerbate SWDs, our results indicate an ameliorating effect. We believe this is not contradictory, but rather reflects differences in the types of absence epilepsy models being used. Notably, most existing data are derived from 'non-resolving' absence epilepsy models such as the WAG/Rij or GAERS rodents, which exhibit persistent seizures throughout life. In contrast, our model is designed to represent a 'resolving' CAE network, which captures the characteristic remission of absence seizures during adolescence. This distinction suggests that ALLO's beneficial effect on SWDs may be spe-

cific to resolving CAE networks. Furthermore, given that CAE is a multifactorial disease, assessing relative progesterone levels in patients alone may not be a sufficient predictor of disease progression or remission. It is quite possible that, despite the beneficial effects of ALLO, other mechanisms might compensate for variations in hormone levels and their metabolites, potentially preventing remission from occurring. The discrepancy in networks that exhibit resolution or not prompts us to consider potential underlying sex differences in CAE. Similar to other idiopathic epilepsy types, CAE is more common in girls, accounting for approximately 55-80% of cases [105, 87]. Interestingly, while many studies also report that the majority of individuals who become seizure-free are female, multivariate analyses in most of these studies find this result to be statistically insignificant. The relative rates of remission between sexes often need to be inferred from reported data and vary across studies, ranging from 39-70% in females and 25-47% in males [158, 83, 199]. It is important to note that, given the information incorporated into the model's components, our model is not sex-specific but rather a general, exploratory one. Therefore, since sex hormones are present in both sexes, the effect of allopregnanolone demonstrated in this work is likely to be observed in both sexes, albeit to varying degrees. The aim of this study was to understand this effect in a broad context relative to the disease. However, the predominance of females in both prevalence and disease remission may be attributed to several sex-based differences at various levels. Evidence suggests sexual dimorphism in cerebral connectivity patterns, with females exhibiting increased interhemispheric connectivity and connections within local brain areas, whereas males show increased intrahemispheric connectivity [171]. Additionally, sex-based differences in the endocrine system impact astrocyte organization—such as levels and morphology—as well as the production of neurosteroids, which in turn affect neurotransmitter systems and neuronal communication [115, 111]. In fact, there are studies that have shown there exist pre-treatment intrinsic connectivity differences between patients who ultimately experience remission and those who do not [190]. There is also evidence of enhanced extrasynaptic GABAa-receptor mediated (tonic) inhibition in thalamocortical neurons in the GAERS model [37]. Interestingly, allopregnanolone is one of the most potent extrasynaptic receptor modulators [142]. Both of these differences are not captured in our existing model. This leads us to hypothesize that remission occurring during adolescence in "most cases" could be associated with the action of allopregnanolone bringing a beneficial change only to individuals that are predisposed to remission as a result of intrinsic differences in connectivity or tonic inhibition, which may be further influenced by sexual dimorphism.

Our future directions include exploring some of this very aspect, as it was one of the major limitations of the present work. In particular, this would involve adding greater detail to the cortical component of the model to include different brain regions, especially

the frontal and parietal cortices. By modifying the model components to explore variations in connectivity patterns, we could potentially generate or identify neuronal networks with sexually dimorphic characteristics. Another limitation of our model is the lack of detail in our single-cell models and its potential consequences on network-level behaviour. This can be addressed by using multiple compartments to account for neuron morphology, and incorporating local environmental effects which include intracellular and extracellular dynamics. As is evident in the literature, such detail on the scale of single neurons can also allow for the emergence of pathological activity similar to that observed in network-level models, where individual cells themselves exhibit 'ictogenic' behaviour [203]. Enhanced single-cell modelling can also provide new ways to investigate other mechanisms by which a diseased state can be achieved. This includes investigating mutations in genes encoding other ion channels such as sodium and potassium channels, as well as those encoding specific GABAa receptor subunits, and examining how these mechanisms interact with the effect of ALLO.

3.5 Conclusion

Understanding the role of sex hormones in the resolution of CAE may explain why remission does not occur in nearly a quarter of cases. Results from such research can therefore lead to better informed therapeutic decisions relating to early interventions such as hormonal therapy and/or antiepileptic drug treatment, which can be tailored to intrinsic network connectivity arrangements, perhaps based on functional connectivity analysis of neuroimaging data of patients. In addition, the use of positron emission tomography (PET) combined with magnetic resonance imaging (MRI) and radioligands to study the effects of sex steroids on brain processes may be a powerful approach for tailored interventions. However, this application of PET/MRI is still underdeveloped in the context of brain research [146]. For instance, specific PET tracers could potentially be used to visualize the expression and binding characteristics of different GABA receptor subtypes, enabling the investigation of pre-treatment correlations between sex-specific steroids and the GABA neurotransmitter system [143, 6, 154]. Additionally, chemogenetic and optogenetic approaches may provide powerful tools for modulating neuronal circuits in a cell-type- and region-specific manner [102, 118]. When combined with targeted delivery or modulation of steroid hormones, these techniques could open new avenues for personalized treatment strategies in absence epilepsy.

Chapter 4

A minimal thalamocortical model for investigating regional cortical heterogeneity and frontocortical connectivity in childhood absence epilepsy network dynamics

This chapter is based on the paper: M Ahmed and SA Campbell. 2025. A minimal thalamocortical model for investigating regional cortical heterogeneity and frontocortical connectivity in childhood absence epilepsy network dynamics. In preparation.

4.1 Introduction

Childhood absence epilepsy (CAE) is a common pediatric epilepsy disorder, accounting for approximately 18% of all childhood epilepsies, with onset typically occurring between the ages of 4 and 12 years [84]. Characterized by brief episodes of impaired consciousness, typical absence seizures present with bilateral synchronous 2.5–5 Hz spike-wave discharges (SWDs) on electroencephalography (EEG) [84]. While antiepileptic drugs are effective for most patients, with approximately 70% achieving remission, some cases progress to more severe forms of epilepsy [103]. Interestingly, circumstantial evidence regarding the prognosis of untreated epilepsy suggests spontaneous remission rates between 31–42%, although these figures are not specific to childhood-onset epilepsy syndromes [113, 11]. Several factors, including the use of antiepileptic drugs, genetic predisposition, and intrinsic connectivity differences, are hypothesized to influence remission; however, understanding of these factors remains limited due to their considerable variability among patients.

The thalamocortical circuit—comprising pyramidal neurons in the cortex, thalamic relay neurons, and thalamic reticular neurons—plays a critical role in both normal 7–10 Hz sleep spindle generation and pathological SWD activity, as described in Section 2.6 [180]. Evidence indicates that SWDs may originate from slower oscillations within focal excitable regions, particularly the somatosensory cortex, before being sustained by circuits in the frontal cortex and thalamus [141, 135]. Notably, children with newly diagnosed CAE who do not respond to treatment demonstrate increased frontocortical connectivity prior to treatment initiation, suggesting fundamental differences in network architecture may influence disease trajectory [190].

Neuronal electrophysiology and intrinsic membrane properties vary significantly based on neuron morphology, cortical layer, and cortical region. Pyramidal neurons in the cortex typically exhibit either regular spiking (RS) or intrinsically bursting (IB) behaviour. Intrinsically bursting neurons tend to have thick apical dendrites as compared to those that are regular spiking, as shown in studies of pyramidal neurons in layers 2/3 and 5 of rat visual cortex [134]. In slices of sensorimotor and frontal cortex from guinea pigs, regular spiking pyramidals were found in all layers below layer 1, while bursting cells were located mostly in layers 4/5 and deeper [137]. Additionally, studies in Sprague-Dawley rats indicate a higher percentage (approximately 73%) of layer 5/6 IB neurons in slices of prefrontal cortex, compared to layer 5 cells in slices of somatosensory (parietal) cortex (approximately 50–60%) [32, 210]. These regional differences in neuronal composition may contribute to the pathophysiological variability observed in CAE.

Given that remission in most cases occurs during adolescence, the association of sex steroid hormones with CAE is suspected and further supported by the phenomenon of

catamenial seizure exacerbation [197]. Progesterone and its metabolite allopregnanolone (ALLO) have been implicated in modulating absence seizure activity [80, 204, 26, 197]. In our recent work using a conductance-based thalamocortical model, we found that ALLO's modulation of GABAa-receptor mediated inhibition had an ameliorating effect on spike-wave discharges [3]. This finding appears to contradict established clinical evidence but may reflect limitations in existing experimental models, which do not capture the naturally remitting course typical of most CAE cases.

The thalamocortical model employed in our previous study featured a well-defined thalamic component based on Destexhe's work, but was limited by its lack of a comprehensive cortical representation [49]. The cortical cells in this model incorporated only basic currents (Na^+, K^+, and an additional slow-K^+ current in pyramidal cells) and lacked region-specific or laminar organization.

In this study, we develop an enhanced conductance-based thalamocortical model that retains Destexhe's thalamic circuitry while significantly improving the cortical component. Our revised model incorporates a layered cortical structure with specialized neurons from layers 5 and 6, including region-specific pyramidal cells and deep layer interneurons. These neurons have been characterized morphologically and by their firing patterns [192]. This modification creates a more structured and physiologically diverse thalamocortical network while maintaining computational efficiency. Using this refined model, we systematically investigate the functional consequences of varying neuronal composition across cortical regions on seizure dynamics. Specifically, we examine how different ratios of intrinsically bursting to regular spiking neurons in layer 5 affect the generation, propagation, and maintenance of spike-wave discharges. Furthermore, we explore the impact of enhanced frontocortical connectivity on these different cortical configurations. Through this analysis, we aim to identify distinct network features that might differentiate resolving from non-resolving CAE networks. This computational approach provides a unique opportunity to explore factors that may account for different disease trajectories, addressing a significant gap in our understanding due to the lack of a remitting animal model for CAE.

4.2 Materials and methods

4.2.1 Model description

Our 475-cell thalamocortical network consists of single-compartment neuron models of the following types: layer 5 regular spiking (RS), layer 5 intrinsically bursting (IB), layer

6 non-tufted regular spiking (NRS) pyramidals and a deep low-threshold spiking (LTS) interneuron in the cortex, and thalamic reticular cells (RE) and thalamocortical cells (TC) in the thalamus. The membrane potential of each cell type is described by the following equations:

$$\begin{aligned} C_{m1}\frac{dV_{RS}}{dt} &= I_{hold} - I_{Leak} - I_{Naf} - I_{Nap} - I_{Ka} - I_{K2} - I_{Kdr} - I_{Km} - I_{Kc} - I_{Kahp} \\ &\quad - I_{CaT} - I_{CaL} - I_h - I_{GABAa_{LTS}} - I_{GABAb_{LTS}} - I_{AMPA_{RS}} - I_{AMPA_{IB}} \\ &\quad - I_{AMPA_{NRS}} - I_{AMPA_{TC}} \end{aligned} \tag{4.1}$$

$$\begin{aligned} C_{m1}\frac{dV_{IB}}{dt} &= I_{hold} - I_{Leak} - I_{Naf} - I_{Nap} - I_{Ka} - I_{K2} - I_{Kdr} - I_{Km} - I_{Kc} - I_{Kahp} \\ &\quad - I_{CaT} - I_{CaL} - I_h - I_{GABAa_{LTS}} - I_{GABAb_{LTS}} - I_{AMPA_{RS}} - I_{AMPA_{IB}} \\ &\quad - I_{AMPA_{NRS}} - I_{AMPA_{TC}} \end{aligned} \tag{4.2}$$

$$\begin{aligned} C_{m1}\frac{dV_{NRS}}{dt} &= I_{hold} - I_{Leak} - I_{Naf} - I_{Nap} - I_{Ka} - I_{K2} - I_{Kdr} - I_{Km} - I_{Kc} - I_{Kahp} \\ &\quad - I_{CaT} - I_{CaL} - I_h - I_{GABAa_{LTS}} - I_{GABAb_{LTS}} - I_{AMPA_{RS}} - I_{AMPA_{IB}} \\ &\quad - I_{AMPA_{NRS}} - I_{AMPA_{TC}} \end{aligned} \tag{4.3}$$

$$\begin{aligned} C_{m2}\frac{dV_{LTS}}{dt} &= I_{hold} - I_{Leak} - I_{Naf} - I_{Nap} - I_{Ka} - I_{K2} - I_{Kdr} - I_{Km} - I_{Kc} - I_{Kahp} \\ &\quad - I_{CaT} - I_{CaL} - I_h - I_{AMPA_{RS}} - I_{AMPA_{IB}} - I_{AMPA_{NRS}} - I_{AMPA_{TC}} \end{aligned} \tag{4.4}$$

$$\begin{aligned} C_{m2}\frac{dV_{TC}}{dt} &= -I_{Leak} - I_{KLeak} - I_{Naf} - I_K - I_{CaT} - I_h \\ &\quad - I_{GABAa_{RE}} - I_{GABAb_{RE}} - I_{AMPA_{NRS}} \end{aligned} \tag{4.5}$$

$$C_{m2}\frac{dV_{RE}}{dt} = -I_{Leak} - I_{Naf} - I_K - I_{CaT} - I_{GABAa_{RE}} - I_{AMPA_{NRS}} - I_{AMPA_{TC}} \tag{4.6}$$

where V_i is the membrane potential for i = RS, IB, NRS, LTS, TC, RE, $C_{m1} = 0.9$ and $C_{m2} = 1.0$ is the specific membrane capacitance given in μF/cm^2. I_{hold} is the input current required to hold and maintain the voltage of the neuron (also used in this context for setting the resting membrane potential). A consistent set of units were maintained such that voltage is given in mV, ionic currents in mA/cm^2, membrane conductance densities in S/cm^2, and time in msec. Note that while input currents are given in nA, they are converted to a current density by dividing by the cell compartment's area.

All cortical cells have the same set of ionic currents with different kinetics in some instances. These consist of both transient and persistent sodium currents, potassium currents of the delayed rectifier, transient, slowly inactivating, and Ca^{2+}-dependent types, in

addition to both low- and high-threshold Ca^{2+} currents. The models for these cells were adapted from our previous work [2], which modified single-neuron models from Traub et al. [192]. The original model by Traub et al. featured multi-compartment neurons in a large-scale network, successfully replicating various thalamocortical phenomena. In our work, we simplified these complex neuronal models to single-compartment representations of the soma while preserving essential dynamics. This reduction required careful recalibration of membrane conductance densities to maintain physiologically realistic behaviour. In contrast, the thalamic cells were based on the model by Destexhe et al. [49], which describes thalamic neurons with fewer currents but still exhibits bursting behaviour due to the presence of the low-threshold calcium current, with slower kinetics in the RE cells. All intrinsic currents follow the same formalism, described by the following equation:

$$I_{ion} = \bar{g}_{ion} \cdot m^N h^M \cdot (V_m - E_{ion}) \tag{4.7}$$

where $\bar{g}_{ion}$ represents the maximal conductance, and m and h represent the voltage gating of the ion channels. All synaptic currents are described by the following equation:

$$I_{syn} = \bar{g}_{syn} \cdot s(t) \cdot (V_m - E_{syn}) \tag{4.8}$$

where $\bar{g}_{syn}$ denotes the maximal synaptic conductance, and AMPA/GABAa- and GABAb-mediated synapses are described appropriately by the synaptic conductance function, $s(t)$ which denotes the fraction of open synaptic channels at time t. In the formalism by Destexhe et al. [51, 52], postsynaptic currents mediated by glutamate AMPA and GABAergic GABAa receptors are modelled using the following conductance function:

$$\frac{ds}{dt} = \alpha[T](1 - s) - \beta s \tag{4.9}$$

where $[T]$ represents the neurotransmitter concentration released into the synaptic cleft upon the arrival of a presynaptic spike, and α and β are forward (binding) and backward (unbinding) rate constants describing the binding of neurotransmitter, respectively. The dynamics of GABAb-mediated synapses are described in Section B.1.3.

Upon the arrival of a presynaptic spike at $t = t_0$, $[T]$ jumps to a maximal concentration value C_{max}, and at $t = C_{dur}$ (the duration of neurotransmitter-mediated pulse), $[T]$ falls back to 0. After the neurotransmitter-mediated pulse is gone, $s(t)$ decays exponentially. Thus, solving Equation (4.9), we get:

$$s(t) = \begin{cases} s_\infty + (s(0) - s_\infty)e^{-\frac{t}{\tau_s}}, & 0 \le t < C_{dur} \\ \left[s_\infty + (s(0) - s_\infty)e^{-\frac{C_{dur}}{\tau_s}}\right] e^{-\beta(t - C_{dur})}, & t \ge C_{dur} \end{cases} \tag{4.10}$$

where

$$s_\infty = \frac{\alpha C_{max}}{\alpha C_{max} + \beta} \quad \text{and} \quad \tau_s = \frac{1}{\alpha C_{max} + \beta} \tag{4.11}$$

The details of the individual currents and model parameters are provided in Sections B.1 and B.2, respectively.

The network consists of the following cell populations: 25 layer 5 RS pyramidals, 75 layer 5 IB pyramidals, 75 layer 6 non-tufted RS pyramidals, 100 deep LTS interneurons, 100 thalamocortical cells, and 100 thalamic reticular cells. At baseline, a higher proportion of bursting-type pyramidal cells compared to regular-spiking cells in layer 5 was used to both introduce asymmetry in Layer 5, as well as model the frontal cortex. All cell layers were of equal size, except for layer 6, which had a reduced population size relative to layer 5 to reflect its typically lower density of pyramidal cells [43]. Each layer of cells is arranged in one dimension as shown in Figure 4.1 with synaptic connectivity varying between cell types as described. Cortical input into the thalamus is only from layer 6 of the cortex with excitatory synapses formed with ascending thalamic axons. All excitatory connections in the network are mediated by AMPA receptors, and inhibitory connections are mediated by either GABAa only or a combination of GABAa and GABAb receptors.

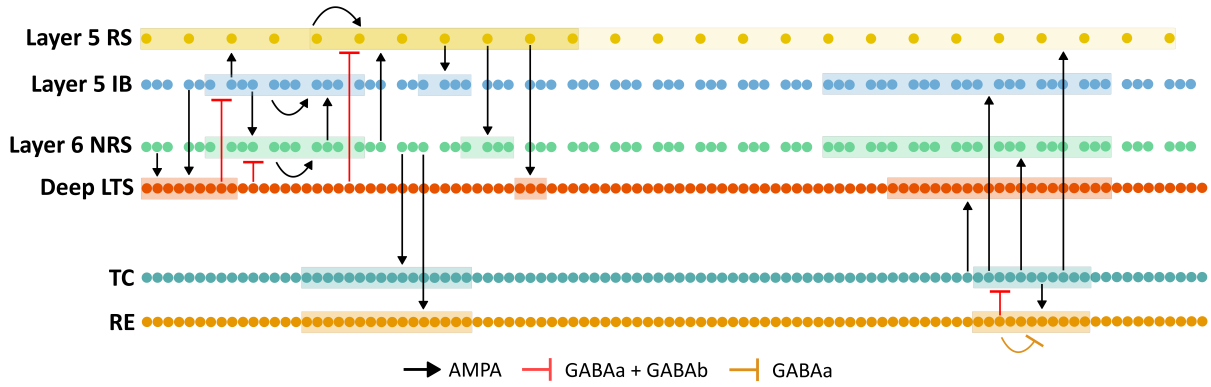

Figure 4.1: Schematic representation of the thalamocortical network. Each neuron is represented by a dot with synaptic connectivity within and between layers as shown. The number of postsynaptic neurons each neuron connects to varies by layer and is represented by the highlighted groups as shown.

Due to the unequal number of cells in some layers, the number of presynaptic neurons each postsynaptic neuron connects to ($nPrePost$) was layer-dependent, as given in Table

4.1. In each network layer, presynaptic cells were indexed relative to the indexing of postsynaptic cells. Within the thalamus and the cortex, each neuron connects to postsynaptic neurons within a radius of 11 indices, while between the thalamus and cortex, each presynaptic neuron connects with neurons within a radius of 21 postsynaptic indices. This cell count affects the weight of individual synapses which is defined by $\bar{g}_{syn}/nPrePost$ where $\bar{g}_{syn}$ is the maximal synaptic conductance for a particular synapse, as given in Table 4.2.

nPrePost	Number of cells	*nPrePost*	Number of cells
nRSRS	11	nLTSRS	11
nRSIB	4	nLTSIB	11
nRSNRS	4	nLTSNRS	11
nRSLTS	3	nTCRE	11
nIBIB	11	nTCNRS	21
nIBRS	11	nTCIB	21
nIBNRS	11	nTCRS	21
nIBLTS	9	nTCLTS	21
nNRSNRS	11	nRERE	11
nNRSRS	11	nRETC	11
nNRSIB	11		
nNRSLTS	9		
nNRSTC	16		
nNRSRE	16		

Table 4.1: The number of presynaptic neurons that each postsynaptic neuron connects to (*nPrePost*) in a network with the following architecture: 25 layer 5 RS cells, 75 layer 5 IB cells, 75 layer 6 NRS cells, 100 deep layer LTS cells, 100 TC cells, and 100 RE cells. For example, nRSIB = 4 means that each IB cell receives input from 4 RS cells.

After allowing the network to reach steady state, a 1 nA stimulus was applied for 100 ms to a group of five layer 6 NRS neurons, inducing additional oscillations. Network behaviour and states were characterized using these triggered oscillations. The model fitting parameters, given in Tables 4.2–4.4 were selected based on the method described in Section 4.2.2, and were intended to be interpreted qualitatively. The same set of fitted parameters was used to model both the default and diseased states. In the default mode, the network exhibits spontaneous oscillations driven by spontaneous discharges in TC neurons, while in the diseased mode, the model exhibits synchronized spike-wave discharges due to alterations in the strength of cortical inhibition.

All models were simulated using NetPyNE and run in parallel on a Dell PowerEdge

R840 with four 20-core Intel processors and 768 GB of RAM. Each simulation ran for 15 seconds of simulation time, with a typical runtime of approximately 12 minutes and memory usage of 13 GB.

	Post-synaptic neuron type					
Pre-synaptic neuron type	RS	IB	NRS	LTS	TC	RE
RS	0.3	0.7	0.3	0.1	-	-
IB	1	0.3	0.05	0.08	-	-
NRS	0.1	0.3	2	0.2	0.02	2.4
LTS	0.09 (GABAa) 0.03 (GABAb)	0.1 (GABAa) 0.03 (GABAb)	0.75 (GABAa) 0.03 (GABAb)	-	-	-
TC	1	0.7	1.2	0.4	-	0.2
RE	-	-	-	-	0.02 (GABAa) 0.04 (GABAb)	0.2

Table 4.2: Maximal synaptic conductance, $\bar{g}_{syn}$ parameters (in μS) for each synapse type, chosen to produce a default network state exhibiting spindle oscillations.

	Post-synaptic neuron type					
Pre-synaptic neuron type	RS	IB	NRS	LTS	TC	RE
RS	0.05	0.05	0.1	0.5	-	-
IB	0.1	0.1	0.1	0.05	-	-
NRS	0.05	0.1	0.05	0.625	0.75	0.8
LTS	0.1	0.05	0.1	-	-	-
TC	1	1	0.07	0.149	-	0.94
RE	-	-	-	-	20	20

Table 4.3: Forward (binding) rate, α parameters (in $(\text{ms} \cdot \text{mM})^{-1}$) for each synapse type, chosen to produce a default network state exhibiting spindle oscillations. Note that α values for inhibitory synapses presented here correspond only to GABAa synapses.

Pre-synaptic neuron type	Post-synaptic neuron type					
	RS	IB	NRS	LTS	TC	RE
RS	0.15	0.05	0.01	0.2	-	-
IB	0.15	0.05	0.01	0.08	-	-
NRS	0.05	0.01	0.03	0.109	0.3	0.09
LTS	0.2	0.7	0.01	-	-	-
TC	0.15	0.15	0.006	0.048	-	0.18
RE	-	-	-	-	0.162	0.162

Table 4.4: Backward (unbinding) rate, β parameters (in ms^{-1}) for each synapse type, chosen to produce a default network state exhibiting spindle oscillations. Note that β values for inhibitory synapses presented here correspond only to GABAa synapses.

4.2.2 Model fitting procedure

Defining model target behaviour

The model fitting procedure aimed to produce target behaviour qualitatively similar to the models upon which we have built this work [46, 192]. To assess model fitness, we defined specific evaluation metrics that characterize network behaviour in two critical states: healthy spindles and pathological spike-wave-discharges (SWDs). Our previous model guided the qualitative and quantitative criteria for both states [3]. For our analysis, we focused on three key populations: layer 5 regular spiking (RS), layer 6 non-tufted regular spiking (NRS) and thalamocortical (TC) neurons. To qualify for classification, each population needed to exhibit persistent spiking within an approximately 2-second post-stimulus window. To achieve a higher temporal resolution, we divided this into two 0.5-second observation windows beginning 1 second after stimulus presentation. Within each window, individual populations were required to exhibit at least as many spikes as their population size.

Spindle oscillations in the cortex were characterized by synchronized spiking with a few doublets in some cells, as illustrated in Figure 4.2. Thalamic activity during spindles showed more prevalent doublet spiking with alternating bursts of synchrony across the population, as shown in Figure 4.3. Quantitatively, spindle oscillations were defined by population synchrony measures greater than or equal to 0.65 for RS and NRS populations and less than or equal to 0.65 for the TC population. In contrast, the spike-wave discharges state was characterized by synchronized bursts in both the cortex and thalamus. The

SWD state was quantitatively defined by synchrony values greater than or equal to 0.65 for RS and NRS populations and greater than or equal to 0.7 for the TC population. We established these classification criteria through extensive trial simulations with our previous model [3]. The synchrony measure used here was adapted from [76, 77, 78], and is explained in greater detail in Section 4.2.3.

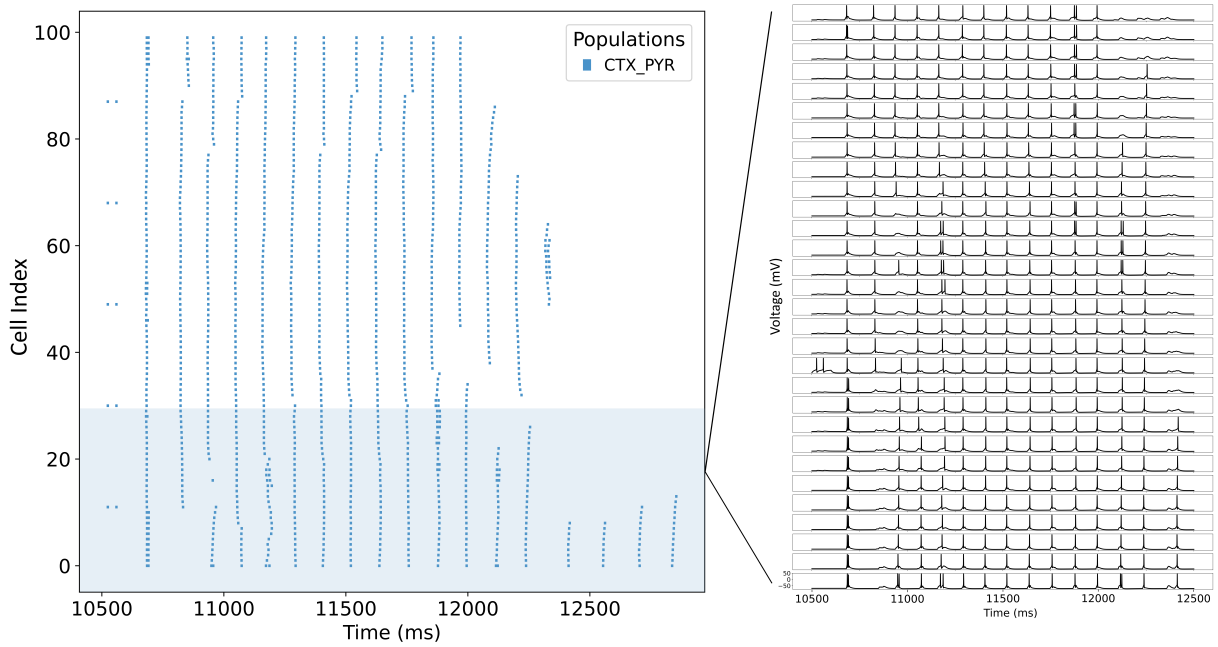

Figure 4.2: Characterizing spindle oscillations in the cortex. (Left): Raster plot of cortical pyramidal (PY) population illustrating across-population synchrony. (Right): Close-up of individual traces of the first 30 PY cells illustrating single spikes with a few doublets. These simulations were obtained using our previous model [3].

Choice of fitting parameters

Since the thalamus component was well-defined in [46], we kept it unchanged, including its synaptic weights and other related parameters. We also kept all parameters corresponding to GABAb synapses unchanged and as defined in [46]. Instead, we focused on fitting parameters corresponding to AMPA and GABAa synapses within the cortex and between the cortex and thalamus. This approach yielded the following 21 synapses each requiring optimization of synaptic parameters: RSRS, RSIB, RSNRS, RSLTS, IBRS, IBIB, IBNRS,

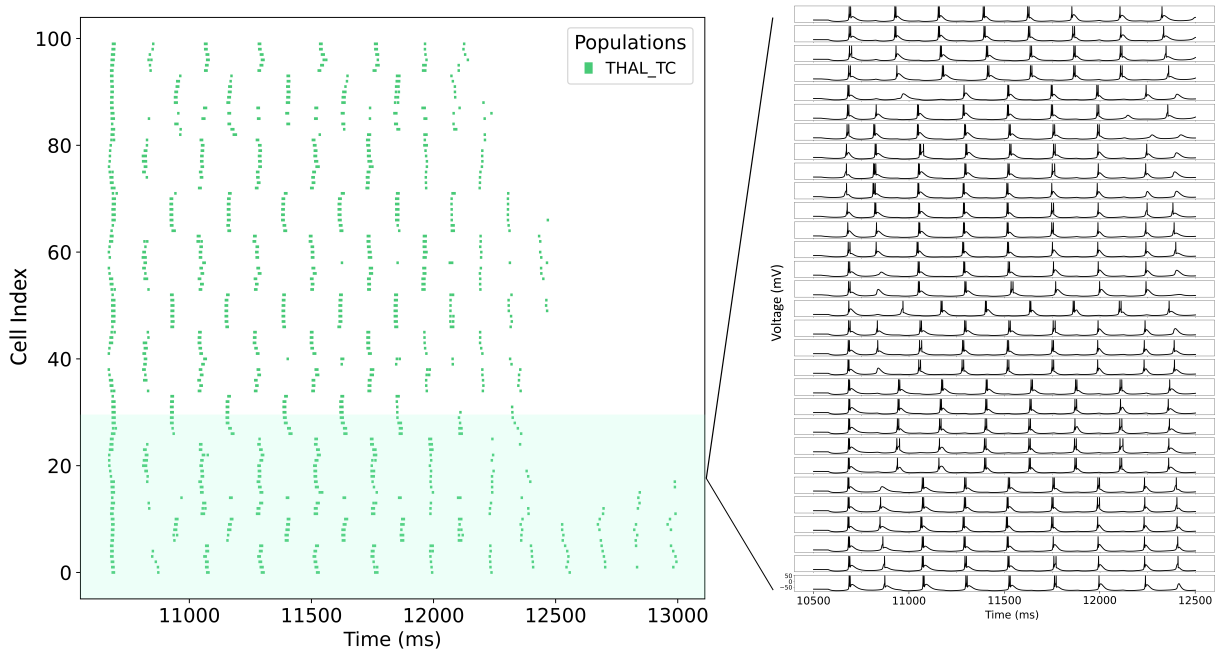

Figure 4.3: Characterizing spindle oscillations in the thalamus. (Left): Raster plot of TC population illustrating alternating bursts of synchrony across population. (Right): Close-up of individual traces of the first 30 TC cells illustrating doublet spiking with some single spikes. These simulations were obtained using our previous model [3].

IBLTS, NRSRS, NRSIB, NRSNRS, NRSLTS, NRSTC, NRSRE, LTSRSa, LTSIBa, LTSNRSa, TCRS, TCIB, TCNRS, and TCLTS. For each synapse, we sought the optimal set of parameters $\bar{g}_{syn}$, α, and β—as defined in Equations (4.8)–(4.9)—that would enable the network to display a default mode of spindle oscillations while maintaining the ability to transition to a spike-wave discharge (SWD) state under cortical disinhibition. This constituted a 63-dimensional parameter search space.

Our selection of $\bar{g}_{syn}$, α, and β as fitting parameters was informed by several earlier optimization approaches. Initial attempts focused on optimizing only the 21 $\bar{g}_{syn}$ values corresponding to each synapse. These efforts employed both single- and multi-objective optimization approaches, including an evolutionary algorithm from *Inspyred*, *Optuna*'s Bayesian optimization, and grid search. The objective and fitness functions were defined using the criteria outlined in Section 4.2.2. When these approaches failed to converge on satisfactory solutions, we attempted parameter range modifications and dimensionality reduction strategies. Parameter bound modifications included: i) using the optimal

synaptic conductance values from [46] and [192] with variations of ±20 to ±60 %, and ii) for each synapse type, constructing minimal one-to-one neuron pairs (single presynaptic to single postsynaptic) to determine the minimum strength required to evoke a postsynaptic spike and the maximum strength for synchronized spiking, then expanding these bounds by orders of magnitude to widen the search space. Dimensionality reduction approaches included: i) grouping synapses by cell type or cortical layer with relative weighting between synapses, and ii) grouping synapses based on presynaptic neuron type.

These approaches achieved the desired population-level spiking patterns in the case of spindle oscillations, as confirmed by raster plot analysis showing appropriate temporal firing patterns. However, a persistent issue emerged when examining individual neuronal behaviour. The action potentials of individual neurons exhibited low-amplitude, distorted spikes. These distortions likely resulted from incomplete repolarization or persistent depolarization, disrupting the normal ionic mechanisms underlying action potential generation. Consequently, while population-level activity appeared to match target spindle patterns, we faced two critical issues, as illustrated in Figure B.2: the irregularities in individual neuron firing suggested a breakdown in normal firing dynamics, undermining the physiological validity of the network activity, and furthermore, none of these solutions demonstrated the required ability to transition to SWD behaviour.

To address the abnormality in individual neuronal firing, we used a simple two-cell network to analyze parameters defining the postsynaptic current and shaping the synaptic strength. Our analysis, included in greater detail in Section B.3, revealed that in addition to the maximal synaptic conductance ($\bar{g}_{syn}$), a careful adjustment of rise (α) and decay (β) time constants is required to achieve physiological postsynaptic firing.

Drawing from previous attempts, we restricted our 63-dimensional parameter space by narrowing $\bar{g}_{syn}$, α and β to select values within particular ranges as illustrated in Figure 4.4. This decision was based on analyses of 2-cell networks, similar to those described earlier. Extensive trial runs helped identify the upper and lower bounds for α and β, ensuring the preservation of intrinsic spiking features and physiological relevance for each cell type. For $\bar{g}_{syn}$, the synaptic conductances were kept within a range consistent with the values observed in the thalamic portion of the model. This targeted approach allowed us to focus on a more constrained region of the parameter space, ensuring key features influencing neuronal firing and subsequent network behaviour were considered. We then ran a grid search using these selected values for all 63 parameters in a sequential fitting approach, as described in detail below.

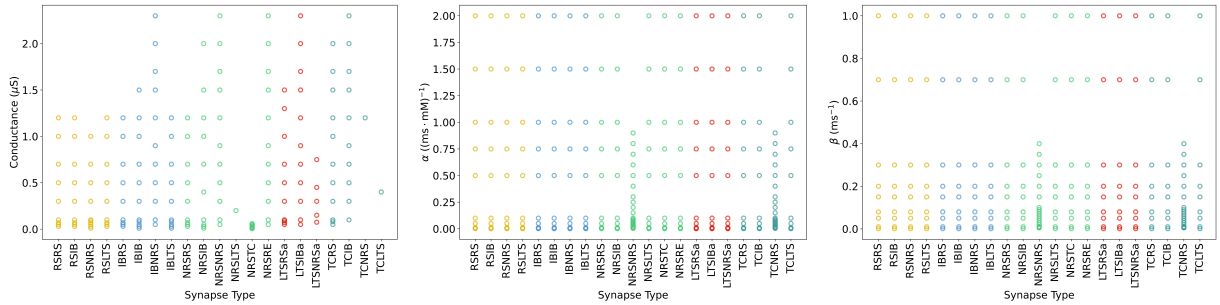

Figure 4.4: For each synapse type, select values of $\bar{g}_{syn}$, α and β used to perform a grid search.

Staged parameter fitting process

We built and fit our model in multiple stages, starting with fitting a cortical layer 6-thalamus circuit first, and then adding cortical layer 5 cells, one population at a time. In each stage, we implemented a sequential parameter fitting strategy where synapses were incrementally added to the network, with the parameter triplet ($\bar{g}_{syn}$, α, β) corresponding specifically to that synapse optimized through a grid search, to maintain target behaviour before introducing the next synaptic connection. In particular, with optimized parameters after each additional synapse, the objective was to see a default mode of spindle oscillations with a transition to spike-wave discharges due to cortical disinhibition.

In the first stage, we adapted the thalamocortical circuit from [46], replacing the cortical components with our layer 6 non-tufted regular spiking (NRS) neurons and deep low-threshold spiking (LTS) interneurons while preserving the original thalamic component. This sequential optimization process involved introducing synaptic connections in the following order: TCNRS, TCLTS, NRSLTS, NRSRE, NRSNRS, LTSNRSa, and NRSTC. For each connection, its corresponding parameter triplet was calibrated, and previously optimized parameters were adjusted as needed to reproduce oscillatory behaviour similar to that observed in the Destexhe model with a comparable architecture. At this stage, the model successfully reproduced the functional characteristics of the Destexhe model, while incorporating our adapted cell types in the cortical component. Next, we added the layer 5 intrinsically bursting cell population, which was chosen arbitrarily between the two types of layer 5 cells. We then repeated the sequential optimization process, adding synaptic connections in the following order: TCIB, IBNRS, LTSIBa, NRSIB, IBLTS, and IBIB. Following this, the layer 5 regular spiking cell population was added, along with the remaining synaptic connections in the following order: TCRS, RSNRS, LTSRSa, NRSRS, RSLTS,

IBRS, RSIB, and RSRS. Throughout the process, we periodically tested the model under two conditions: total cortical inhibition and total disinhibition. This was done to ensure that the optimization was producing the desired target behaviours under both conditions. The validity of the model's output and fit was assessed using an automated procedure that applied predefined network frequency, firing behaviour and synchrony criteria, as described earlier. Additionally, we performed manual checks to examine individual neuronal firing to ensure its physiological relevance.

At each step and for each synapse, multiple parameter triplets (i.e. ($\bar{g}_{syn}$, α, β)) yielded good fits, as shown in Panel A of Figure 4.5 and Figures B.3–B.6 in Section B.4. To test our model's robustness, we explored parameter "clouds" within 30–200% variation around each nominal parameter triplet, shown in Panel B of Figure 4.5 and Figures B.3–B.6. The variation range depended on the synapse type and was informed by qualitative insights from the sequential fitting process. In particular, we tested relatively smaller neighbourhoods around nominal parameter triplets for synapses that strongly influenced network behaviour. During this process, the order in which synapses were perturbed followed the sequence in which they were added to the network. Within these parameter "clouds", multiple triplets produced outputs meeting our filtering criteria, indicating local robustness and parameter degeneracy—where different parameter combinations can yield similar functional outcomes. However, outside of these "clouds" and arbitrary combinations of "good fit triplets" from different synapses, the model failed to maintain target performance. This suggests both bounded robustness as well as global sensitivity and complex parameter interactions within our model. This behaviour likely stems from our sequential fitting approach, which introduces parameter dependencies, since each new parameter triplet is optimized in the context of previously fixed values. Consequently, each parameter triplet may be locally optimal given specific values of previous synapses, but unable to generalize well to arbitrary combinations of triplets. Notably, our model exhibits a common characteristic of neural systems in which relative relationships between parameters across synapses outweigh the importance of individual "good" parameter values.

The sequential parameter fitting approach is a reasonable method for making the process computationally tractable, particularly considering the high dimensionality of our parameter space. By constraining exploration, it provides a structured way to navigate this otherwise overwhelming space. Additionally, this approach improves interpretability, allowing for the analysis of how each synapse contributes to the overall system behaviour and providing more mechanistic insights. It also aligns with biological plausibility, as neural systems often develop sequentially, with new connections forming in the context of existing ones [129, 101]. Despite its advantages, our sequential approach has its limitations. One key challenge is path dependency, where the fitted model depends on the order in which

synapses are added, potentially missing more optimal configurations. This also results in a highly interdependent parameter set, making independent adjustments difficult. While the approach, when combined with a constrained grid search method, does not exhaustively explore all possible parameter combinations, it remains effective in identifying viable parameter regions and providing insights into the underlying structure of the parameter landscape.

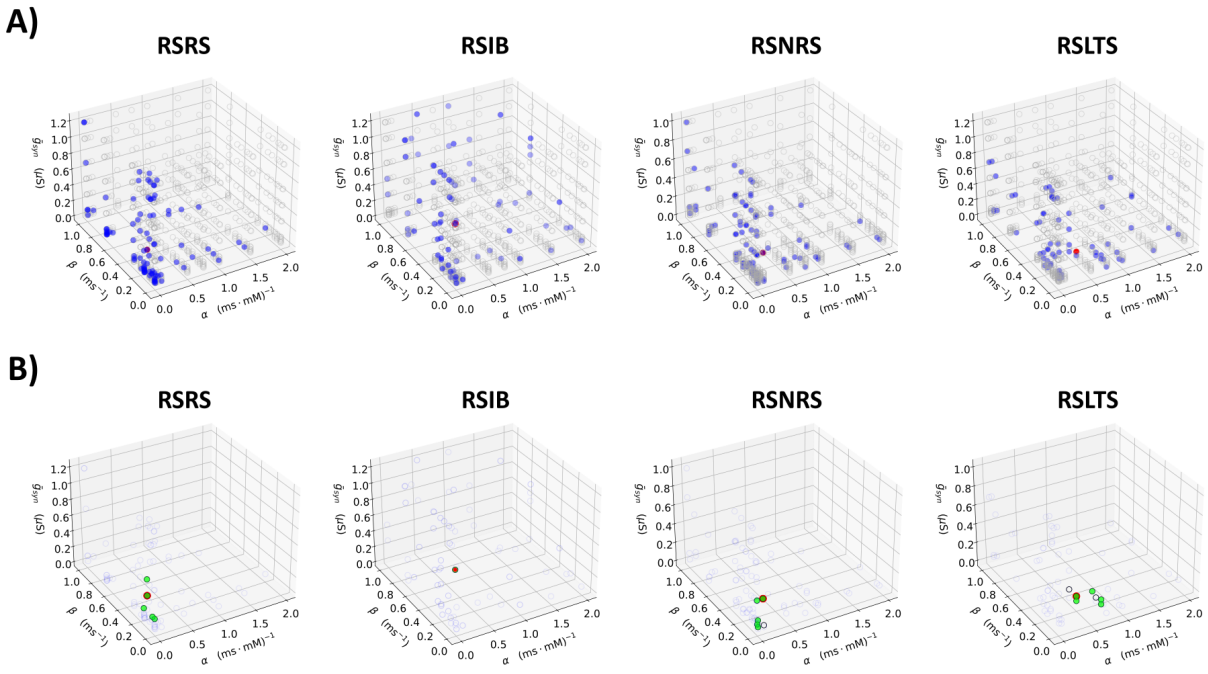

Figure 4.5: (A): For each synapse type, multiple parameter triplets ($\bar{g}_{syn}$, α, β) yielded good fits (solid blue points). Points with gray outlines represent the sampled parameter space, with solid red points indicating our selected parameter triplets. (B): Testing model sensitivity to deviations from the nominal values (solid red points) by up to 75% (RSRS and RSIB), 90% (RSNRS), and 65% (RSLTS) in each parameter dimension. Transparent points with blue outlines represent good fits as in panel A, and in black outlines, the parameter cloud tested for sensitivity. Solid green points indicate parameter sets that maintained good network performance despite these deviations.

4.2.3 Tools for analysis

The model was implemented in NetPyNE, a Python package developed by Dura-Bernal et al. that allows for high-level specification of network connectivity of biological neuronal networks and simulations using the NEURON simulator [58]. Feature extraction from voltage trace data was performed using the *eFEL* Python package. In particular, the *spike_count* function with a default threshold spike detection value of -20 mV was used to calculate the number of spikes across the time interval of interest.

Local field potential and spectral density analysis

The local field potential (LFP) was calculated using a point current source model in which current sources are treated as if they originate from a single point. Due to memory limitations, only a subset of the Layer 5 RS and IB populations was recorded from and used in the LFP calculation. For each population, neurons are arranged in a single line 20 μm apart. The extracellular recording site is considered to be 50 μm opposite to the center of the line, and the LFP at this site was calculated from post-synaptic currents using the following equation:

$$V_{ext} = \frac{R_e}{4\pi} \sum_i \frac{I_{syn}}{r_i} \tag{4.12}$$

where V_{ext} is the potential at a defined extracellular site, $R_e = 230\Omega$cm is the extracellular resistivity, I_{syn} is the post-synaptic current, and r_i is the distance between the location of the postsynaptic currents and the extracellular site. The LFP traces were first detrended using the *Scipy* Python library to eliminate very low-frequency components that could contaminate the power spectrum and cause spectral leakage. The traces were then filtered using a Butterworth bandpass filter, with cutoff frequencies set at 1 Hz and 15 Hz. Power spectral density (PSD) analysis was performed on the filtered LFP traces using Welch's method with a sampling frequency (*fs)* of 10kHz. A Hann window was applied to segments of 20000 samples, with 1000 samples of overlap between consecutive segments.

Synchrony measure

The measure of synchrony used here was based on previous work on synchronization properties of neurons in the reticular thalamic nucleus (RE), which uses a *population*-averaged

voltage as a proxy for the local field potential of many RE neurons [76, 77, 78]. The measure of synchrony defined here uses instead a *pairwise*-averaged voltage $V_{i,j}(t)$ given by the following equation:

$$V_{i,j}(t) = \frac{1}{2}\Big[V_i(t) + V_j(t)\Big] \tag{4.13}$$

where $V_i(t)$ and $V_j(t)$ are the voltages of individual neurons i and j. The reason for this modification is to prevent undesirable averaging effects that are far more sensitive to small differences in synchrony between any two cells, as discussed in greater detail in Section B.5.

The variance of the pairwise-averaged voltage is given by $\sigma_{i,j}$ while the variance of an individual neuron's voltage is given by σ_k, each of which are defined as:

$$\sigma_{i,j} = \langle V_{i,j}(t)^2\rangle - \langle V_{i,j}(t)\rangle^2 \tag{4.14}$$

$$\sigma_k = \langle V_k(t)^2\rangle - \langle V_k(t)\rangle^2 \tag{4.15}$$

where $\langle\cdot\rangle$ indicates a time average over a particular interval of time.

A pairwise measure of synchrony between neuron i and neuron j given by $S_{i,j}$ was defined as the ratio of the pairwise-averaged voltage variance and the variance in the individual neuron's voltage according to

$$S_{i,j} = \frac{\sigma_{i,j}}{\frac{1}{2}\Big(\sigma_i + \sigma_j\Big)} \tag{4.16}$$

Moreover, the average pairwise synchrony measure described as the synchrony measure between neuron i and all other neurons in the population, $\overline{S}_i$ was defined as:

$$\overline{S}_i = \frac{1}{N}\sum_{j=0}^{N-1} S_{i,j} \tag{4.17}$$

where N is the number of neurons in the population.

Altogether, a measure of synchrony for the population, S_{pop} was defined as:

$$S_{pop} = \frac{1}{N}\sum_{i=0}^{N-1} \overline{S}_i \tag{4.18}$$

4.2.4 Modelling the effect of genetic mutations on GABAa current

Consistent with our previous work, the GABRG2 gene mutation (γ2(R43Q)) described in Section 3.2.1, was modelled exclusively in cortical pyramidal neurons in both layers. The mutation effect was implemented by altering the parameter denoting the maximum conductance of the GABAa current ($\bar{g}_{max}$), as illustrated below:

$$I_{GABAa} = \boxed{\bar{\boldsymbol{g}}_{\boldsymbol{max}}} \cdot s(t) \cdot (V_m - E_{GABA}) \tag{4.19}$$

4.2.5 Modelling the effect of allopregnanolone

The effect of allopregnanolone was modelled in a manner similar to that described in Section 3.2.2, by adjusting the $\bar{g}_{max}$, α, β and C_{dur} parameters, as highlighted in Equations (4.19)–(4.21), with the additional consideration of the $\bar{g}_{max}$ parameter, which was not included in our previous work.

$$s(t) = \begin{cases} s_\infty + (s(0) - s_\infty)e^{-\frac{t}{\tau_s}}, & 0 \leq t < \boxed{\boldsymbol{C_{dur}}} \\ \left[s_\infty + (s(0) - s_\infty)e^{-\frac{C_{dur}}{\tau_s}}\right]e^{-\beta(t - C_{dur})}, & t \geq C_{dur} \end{cases} \tag{4.20}$$

where

$$s_\infty = \frac{\boxed{\boldsymbol{\alpha}} C_{max}}{\alpha C_{max} + \boxed{\boldsymbol{\beta}}} \quad \text{and} \quad \tau_s = \frac{1}{\alpha C_{max} + \beta} \tag{4.21}$$

These changes were informed by fitting our synapse model to experimental data, using the relative differences between control GABAa receptor activity and activity after ALLO application. The results of this fitting process are summarized in Figure 4.6, while details of the curve fits can be found in Section B.6. As a modification of our previous work, we incorporate more physiologically relevant data, particularly in comparison to other experiments using central nervous system (CNS) neurons. It is important to note that these experiments vary considerably in their methodologies, including differences in species of CNS neurons and varying concentrations of both GABA (0.005 to 0.1 mM) and allopregnanolone (30 to 1000 nM). While the physiological concentration of GABA released into

the synaptic cleft ranges from 1 to 10 mM, the experimental data used to model the effects of allopregnanolone are based on GABA concentrations that are at least an order of magnitude lower [22, 157, 195, 149]. Similarly, physiological allopregnanolone levels in rat cortex typically range from 1 to 20 nM, yet experimental protocols generally apply concentrations that are one to two orders of magnitude higher [165, 100]. The lack of significant differences in response amplitude (i.e., relative change in $\bar{g}_{max}$) following the application of ALLO in studies using low mM concentrations of GABA could perhaps be explained by these variations. Given these discrepancies, our modelling of these effects should be interpreted qualitatively, with some of our data being more physiologically relevant than others, as illustrated in Figure 4.7.

While the C_{dur} parameter corresponding to Control synapses for each GABAa-receptor mediated synapse was set to 0.3 ms, the values of $\bar{g}_{max}$, α, and β corresponding to Control synapses are presented in Tables 4.2–4.4. For post-ALLO synapses, each parameter was modified based on relative changes between control GABAa receptor activity and activity following the application of ALLO, as follows:

$$\alpha_{post-ALLO} = 1.58 \times \alpha_{Control} \tag{4.22}$$

$$\beta_{post-ALLO} = 0.74 \times \beta_{Control} \tag{4.23}$$

$$\bar{g}_{max_{post-ALLO}} = 1.11 \times \bar{g}_{max_{Control}} \tag{4.24}$$

$$C_{dur_{post-ALLO}} = 1.14 \times C_{dur_{Control}} \tag{4.25}$$

4.2.6 Modelling regional neuronal heterogeneity and enhanced frontocortical connectivity

To model the regional differences in neuronal heterogeneity observed experimentally, as discussed in Section 4.1, we developed two distinct model configurations. Given that layer 5 intrinsically bursting (IB) neurons are more abundant in the frontal cortex and regular spiking (RS) neurons in the parietal cortex [137, 32, 210], we modelled the frontal cortex using IB neurons while the parietal cortex was modelled using RS neurons. Accordingly, we varied their proportions in each model such that the 95-5 (nIB:nRS) configuration is representative of a cortex with a greater frontal cortex contribution, while the 5-95 (nIB:nRS) configuration reflects a cortical component with a greater parietal cortex contribution. Given the differences in model architecture, the number of presynaptic neurons each postsynaptic neuron connects to ($nPrePost$) differs between the two model configurations, as presented in Tables B.3–B.4.

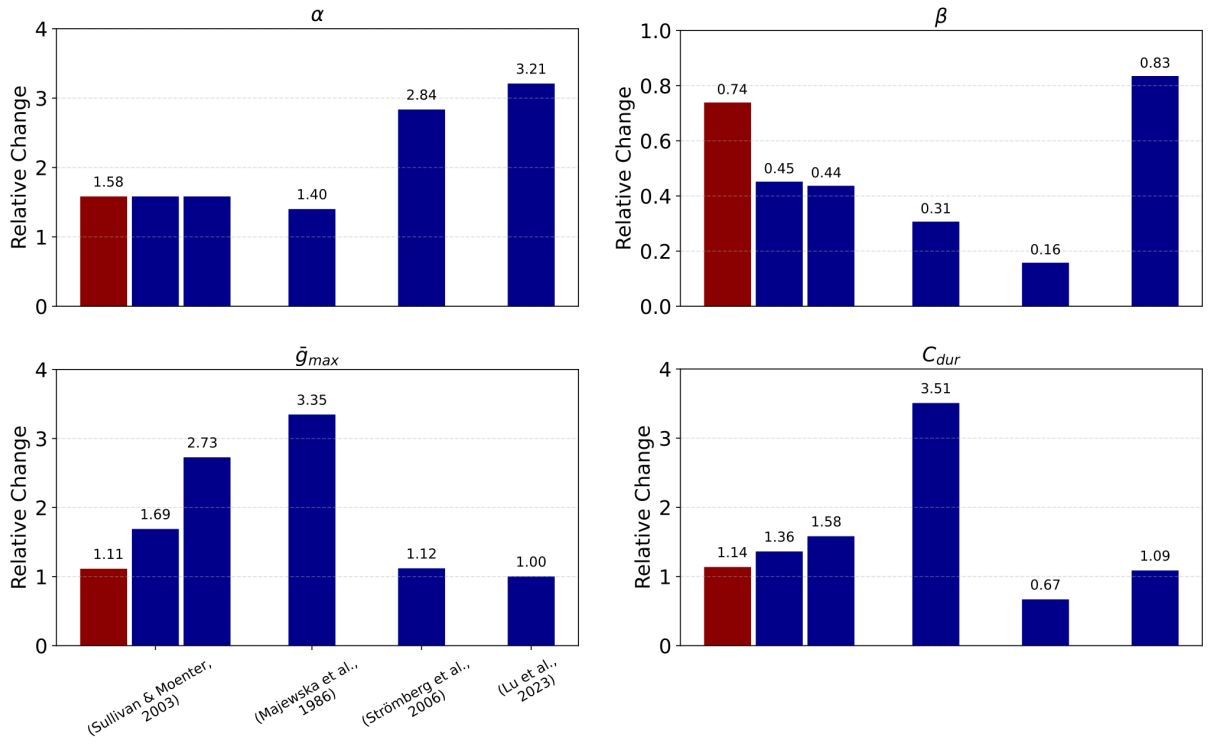

Figure 4.6: A comparison of the relative changes in $\bar{g}_{max}$, α, β and T_{dur} between control GABAa receptor activity and activity post-application of ALLO based on fitting the solution of equation (4.19)–(4.21) to data from different studies. Note that the multiple bars for (Sullivan and Moenter, 2003) represent different amounts of ALLO application used in the same study, in order of increasing concentration. The experimental parameters we used to model the effect of ALLO is highlighted in dark red.

Additionally, for each model configuration, we modelled enhanced connectivity in the frontal cortex by modifying the strength of the following synapses, as illustrated in Figure 4.8: IBIB, IBNRS, and NRSIB. Specifically, we modified the maximal synaptic conductances as follows: $\bar{g}_{IBIB}$ was increased by a factor 7, $\bar{g}_{IBNRS}$ by a factor of 5, and $\bar{g}_{NRSIB}$ by a factor of 3. A detailed description of the method used to determine these parameter adjustments is provided in Section 4.3.3.

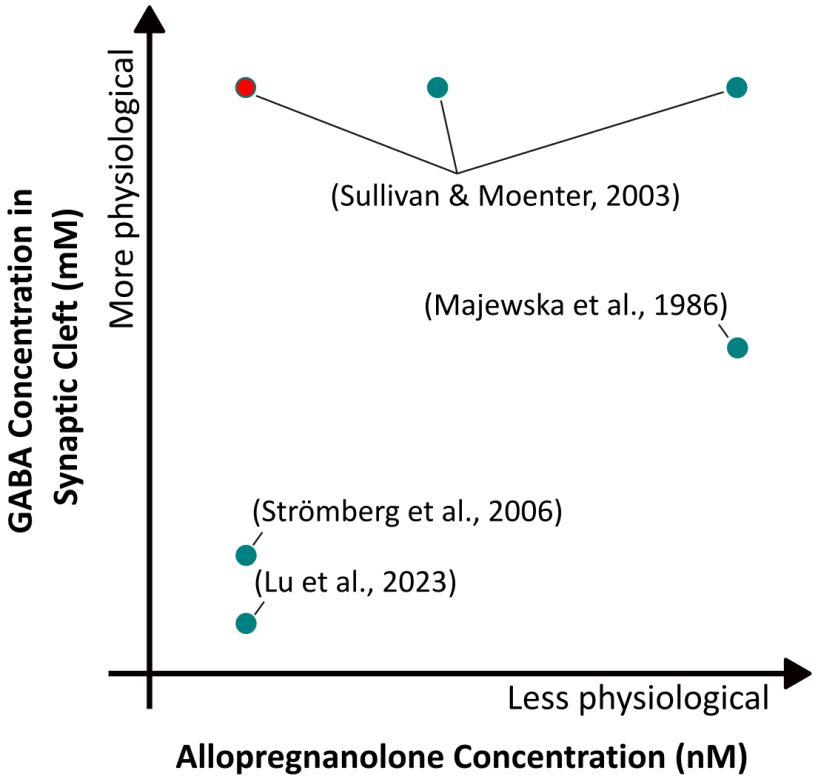

Figure 4.7: A comparison of GABA concentrations versus allopregnanolone concentrations used across different studies, illustrating their physiological relevance. Points in the upper-left corner represent more physiologically relevant conditions (higher GABA, lower allopregnanolone concentrations). The experimental parameters from the study highlighted in red were used as the basis for modelling the effect of ALLO.

4.3 Results

4.3.1 Baseline state characterization and allopregnanolone effects on the fitted model

The goal of our model fitting was to replicate behaviour that is qualitatively consistent with that of prior established models. Specifically, the model needed to exhibit two critical baseline states: a healthy state characterized by spindle oscillations with a network frequency of 7–10 Hz, and a diseased state marked by spike-wave discharges (SWD) with a

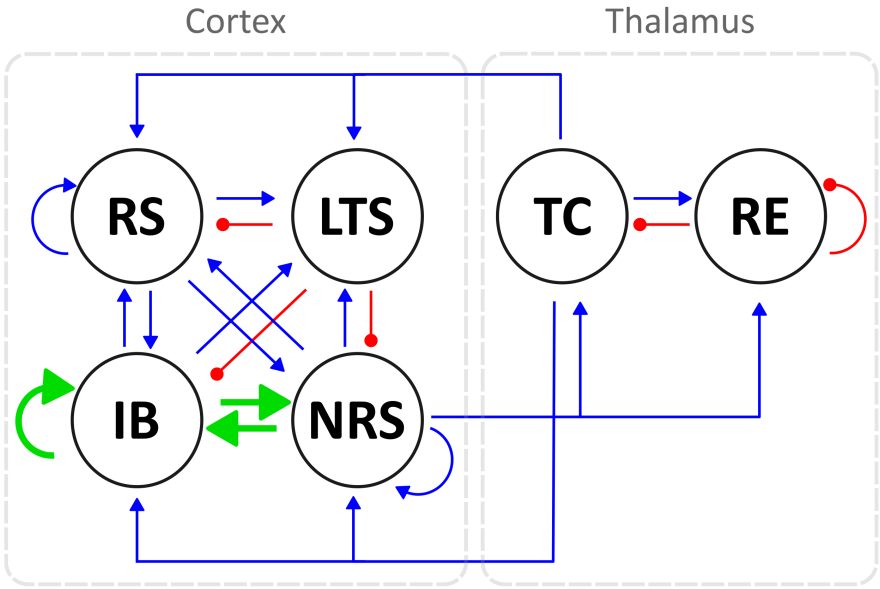

Figure 4.8: A schematic diagram of the thalamocortical circuit shows connections between cortical neurons of the RS, IB, NRS, and LTS type, and thalamic neurons (TC and RE). Blue arrows indicate excitatory synaptic connections, while red arrows represent inhibitory ones. Enhanced frontocortical connectivity is illustrated with thicker green arrows, which also represent excitatory synapses.

network frequency of 2.5–5 Hz. The 75-25 (nIB:nRS) model was simulated using GABAa synapses that were all of the Control type, as described in Table 4.2. At 100% baseline cortical GABAa conductance, the network produces spindle oscillations with a peak network frequency of 7 Hz, as shown in Figures 4.9A and C. In this healthy state, cell populations exhibit organized, alternating bursting patterns—particularly within the TC population—with moderately synchronous activity across other populations, as shown in Figure 4.9B. This activity is reflected in the LFP trace as a low-amplitude rhythmic oscillation. The network could be transformed to a diseased state by means of cortical disinhibition. By reducing GABAa-receptor mediated inhibition in the cortex to 10% baseline conductance, the network produces a dominant 5 Hz SWD pattern as shown in Figures 4.9D and F. In this diseased state, neural firing becomes more synchronous across all populations, with distinctive spike-wave complexes visible in the LFP, as shown in Figure 4.9E. The reduction in cortical GABAa conductance was determined by examining how changes in conductance influence network frequency and the relative power in the SWD frequency range, as shown

in Figure 4.10.

Next, we modelled the effect of allopregnanolone (ALLO) by altering parameters associated with the GABAa current described in Section 4.2.5. The network was initialized to exhibit SWDs, as in Figures 4.9D–F, with cortical GABAa conductance reduced to 10% of baseline. The effect of ALLO was implemented uniformly across all GABAa synapses in the model. Our results show that allopregnanolone effectively suppresses pathological SWDs by altering the temporal firing patterns of neural populations throughout the thalamocortical circuit. As shown in Figure 4.11, there is a shift in the dominant network frequency to 7 Hz, which falls within the frequency band associated with normal spindle oscillations. This transition is also characterized by alternating bursts of synchrony across populations which is reflected in the low-amplitude filtered LFP trace. The shift from pathological to physiological dynamics is consistent with our previous findings and supports the therapeutic potential of positive GABAa modulators in absence epilepsy.

4.3.2 Regional neuronal heterogeneity in the cortex does not alter ALLO-mediated network dynamics

Using the previously described frontal cortex composition (95-5 nIB:nRS) and parietal cortex composition (5-95 nIB:nRS) in Section 4.2.6, we next examined whether regional neuronal heterogeneity affects the network's propensity to generate the two critical network states of interest—healthy spindles and pathological SWDs. Additionally, we investigated whether the effect of ALLO differs across networks with different cortical compositions, and importantly, whether one network composition is more prone to non-resolution than the other.

We first investigated the excitability profiles of both network configurations by examining network frequency responses to varying levels of GABAa-receptor mediated inhibition in the cortex, as shown in Figure 4.12. Both models display a transition from SWD to spindle activity as cortical inhibition increases. However, the thresholds at which this transition occurs differs slightly between the two, with the 95-5 (nIB:nRS) model exhibiting more intermediate oscillatory states compared to the 5-95 (nIB:nRS) model. The latter surprisingly maintains SWD activity across a broader inhibition range and requires stronger inhibition to shift to spindle-generating states. To further explore the influence of cortical composition, we simulated both networks under the same conditions as in Section 4.3.1— 100% and 10% baseline cortical GABAa conductance—to compare their abilities to sustain either physiological spindles or pathological SWDs, and to determine whether baseline dynamics differ across the two models. As shown in Figure 4.13, both network

configurations exhibit qualitatively similar spectral characteristics, across the default mode and under cortical disinhibition. The spectral power distributions show similar frequency bands of activity (both exhibiting peak network frequencies of 7.5 Hz and 5 Hz under each condition), with only subtle differences in power distribution, likely due to variations in oscillatory patterns, as reflected in the LFP traces. This is also characterized by prominent power spectral density peaks within the 7–10 Hz (Figures 4.14A1 and C1) and 2.5–5 Hz ranges (Figures 4.14A2 and C2). At 100% baseline cortical GABAa conductance, both models exhibit 7.5 Hz peak network frequencies with similar relative power in the spindles frequency range (Figure 4.14B1). Similarly, at 10% baseline conductance, both models exhibit network frequencies peaking at 5 Hz with similar relative power in the SWDs frequency range (Figure 4.14B2). These results suggest that despite substantial variation in cortical neuronal composition between models, the fundamental network dynamics remain conserved. This suggests that our fitted model (75-25 nIB:nRS configuration) is robust to changes in network architecture in producing baseline network states.

Following the approach in Section 4.2.5, we modelled the effect of ALLO in all GABAa synapses, in each model configuration by first initializing to the diseased state. After implementing post-ALLO synapses in each compromised network, we observe a restorative effect, with each network transitioning back to spindle oscillations similar to the control state, as shown in Figures 4.14A3 and C3. This transition is characterized by peak network frequencies of 7 Hz and 7.5 Hz for the 5-95 and 95-5 (nIB:nRS) models respectively, with comparable relative power in the spindles frequency range (Figure 4.14B3).

While the differences between the two model configurations is small, there is a more obvious difference between the control network states with cortical GABAa at 100% and network states under the effect of ALLO. Specifically, the relative power in the spindle frequency range is higher in the control condition as compared to the post-ALLO state (Figures 4.14B1 and B3). This is mainly due to the more sharply defined spectral density peak curves in the control condition, resulting in greater area under the curve within the spindle frequency range. In the post-ALLO state, the spectral profiles appear more spread out, resulting in relatively less concentrated power contribution falling within the spindles frequency range, despite restoring the dominant network frequency. Overall, these results suggest that, despite differences in the composition of cortical cell types (with one network having a higher proportion of IB cells), both networks respond similarly to cortical GABAa modulation and the effect of allopregnanolone, with neither showing significantly greater vulnerability to the non-resolution of spike-wave discharges.

4.3.3 Enhanced frontocortical connectivity alters SWD resolution based on network architecture

In this part of the study, we focused on modelling the connectivity differences observed in treatment non-responders prior to treatment in newly diagnosed CAE patients, particularly the increased connectivity in the frontal cortex. By simulating a 50-50 (nIB:nRS) model configuration, we aimed to investigate how, in a network with a balanced composition of cortical cell types in layer 5, increased frontocortical connectivity might influence the modulation of SWDs—particularly in the non-resolution of SWDs (i.e., a lack of effect from ALLO on SWDs). Specifically, we modelled enhanced frontal cortical connectivity by modifying the following synaptic conductance parameters with a multiplicative factor to increase synaptic strength: (i) $\bar{g}_{IBIB} \cdot F_{IBIB}$; (ii) $\bar{g}_{IBNRS} \cdot F_{IBNRS}$; (iii) $\bar{g}_{NRSIB} \cdot F_{NRSIB}$. The factors used and the rationale for their selection are detailed in Figure 4.16. Additionally, we explored how these enhanced synapses affect the other two model configurations (5-95 and 95-5 (nIB:nRS)) to assess whether, in addition to connectivity differences, the composition of cell types within the network influences its responsiveness to the effects of allopregnanolone.

Building on the approach in Section 4.3.1, we simulated the 50-50 (nIB:nRS) model with enhanced synaptic strengths, using $(F_{IBIB}, F_{IBNRS}, F_{NRSIB}) = (7, 5, 3)$. We performed the simulation under the two conditions of cortical inhibition (100% and 10% baseline conductance) to investigate the impact of these changes on network activity. As shown in Figure 4.15, we observed distinct changes in spectral power across different frequencies, depending on the level of cortical inhibition and the presence of allopregnanolone. Specifically, under full cortical inhibition, the network exhibits a maximal power at 5.5 Hz (Figure 4.15A), marking the first instance where the peak network frequency did not coincide with the frequency exhibiting the highest power. However, the relative power within the spindles range (0.282 V^2) was greater than that within the range associated with SWDs (0.195 V^2). When partial disinhibition was applied, the network shifted its maximal power to 4 Hz (Figure 4.15B). After introducing post-ALLO synapses, the network showed a lack of a restorative effect from ALLO, with the maximal frequency dropping to 2.5 Hz (Figure 4.15C). The continued SWD-like behaviour is further reflected in the LFP traces of network activity post-ALLO application, especially when compared to network activity under cortical disinhibition, as shown in Figures 4.15B, C (in blue).

Next, we examined the impact of enhanced synaptic activity, with $(F_{IBIB}, F_{IBNRS}, F_{NRSIB}) = (7, 5, 3)$, on the other two model configurations, 5-95 and 95-5 (nIB:nRS). As illustrated in Figure 4.17A1, B1, C1, both models showed similar network frequencies (6.5 Hz for 5-95 and 7 Hz for 95-5 (nIB:nRS)) and spindle-range relative power (0.339 V^2

and 0.376 V^2, respectively) under the condition of 100% baseline cortical GABAa conductance. Reducing cortical GABAa conductance to 10% resulted in comparable network behaviour across models, with peak power at 4 Hz and 3 Hz, respectively, as shown in Figures 4.17A2, B2, C2. Both of these findings align with results in Section 4.3.2, particularly the shift from spindle oscillations to SWDs under reduced cortical inhibition. Notably, the 95-5 (nIB:nRS) model consistently exhibited higher relative power across both frequency ranges, regardless of frontocortical connectivity alterations, as illustrated in Figures 4.18A, C. Without enhanced synaptic activity, network frequencies were identical between models and changed similarly across levels of cortical inhibition, as shown in Figures 4.18B, D (orange bars). However, when frontocortical connectivity was enhanced, the 95-5 (nIB:nRS) model demonstrated higher frequency under full inhibition and a lower frequency under partial disinhibition, as illustrated in Figures 4.18B, D (purple bars).

Introducing post-ALLO synapses in networks initialized to a pathological state, however, leads to interesting differences between the models. Surprisingly, the effect of ALLO on the 5-95 model mirrors the results from Section 4.3.2, where allopregnanolone exerts a restorative effect, shifting the network's maximal power into the spindles range with a peak network frequency of 7.5 Hz, as shown in Figure 4.17A3. This shift occurs despite there being enhanced frontal cortical connectivity. In contrast, the effect of ALLO on the 95-5 (nIB:nRS) model resembles that seen in the 50-50 (nIB:nRS) model, with maximal power in the SWD-associated frequency range and a peak network frequency of 4.5 Hz.

4.4 Discussion

In this study, we developed a simplified thalamocortical model with layered cortical structure to investigate how differences in frontocortical connectivity might contribute to non-remitting seizures in childhood absence epilepsy (CAE). By modelling cortical region specificity through different neuron firing types in layer 5—specifically intrinsically bursting (IB) neurons representing the frontal cortex and regular spiking (RS) neurons representing the parietal cortex—we examined two different cortical compositions: a 5-95 (nIB:nRS) model and a 95-5 (nIB:nRS) model, reflecting circuits with varying contributions from the parietal and frontal regions, respectively.

Our results demonstrate that both physiological and pathological oscillations are maintained by the thalamocortical circuit regardless of which model configuration is used (5-95 or 95-5 (nIB:nRS) model). Under different conditions of cortical inhibition, both models exhibited similar network behaviour, promoting spindles and spike-wave discharge (SWD) activity. This finding aligns with the classification of absence seizures as a generalized

epilepsy type, where activity that may originate in one region, such as the parietal cortex, can recruit other cortical areas to sustain seizure activity [141, 167]. Similarly, sleep spindles are known to vary in frequency and cortical source across different brain regions [169]. The most striking finding from our study came when we introduced allopregnanolone (ALLO) under conditions of increased frontocortical connectivity. ALLO, a neurosteroid that potentiates GABAa-receptor function, gradually increases during puberty [63], a period that coincides with the remission of CAE in many cases [197]. In our simulations, both models showed a restorative effect of ALLO, helping them recover from the SWD state at baseline connectivity. However, only the 5-95 (nIB:nRS) model was able to recover when frontocortical connectivity was enhanced. This differential response to ALLO is particularly notable, considering that both models initially display similar behaviour under physiological and pathological states. This suggests that individuals with different neuronal composition profiles may follow distinct clinical trajectories despite similar initial presentations. Specifically, our results suggest that patients with connectivity profiles resembling the 5-95 network (i.e., parietal-dominant configuration) may experience remission following hormonal changes involving allopregnanolone, whereas those with profiles resembling the 95-5 network (i.e., frontal-dominant configuration) may be predisposed to non-remission. While direct identification of neuronal composition profiles in patients is currently not feasible, these findings raise the possibility that clinically accessible markers—such as dominant seizure onset regions from EEG or specific patterns of functional connectivity from neuroimaging—could serve as proxies. Furthermore, future identification of region-specific biomarkers or hormonal sensitivity patterns may help guide personalized therapeutic strategies based on likely clinical trajectory.

Our results suggest that non-resolving CAE may result not only from increased strength of connections in the frontal cortex but also from the composition of cell types within the network, with a higher proportion of bursting-type cells preventing the therapeutic effects of allopregnanolone. This highlights the significance of individual neuronal components in network dynamics—much like the concept of ictogenic neurons, where even in a network with largely non-pathological connectivity, specific neuronal populations can contribute to pathological activity patterns [45, 167]. Our findings are consistent with clinical studies using functional connectivity analysis that have identified pre-treatment ictal connectivity differences between patients who ultimately experience remission and those who do not. In particular, increased frontal cortical connectivity has been observed in patients with non-remitting seizures, and treatment non-responders [190]. It is important to note that these clinical studies employ functional connectivity analyses, whereas our modelling involves structural connectivity alterations. Functional connectivity measures the relationship between neural activity in different brain regions, without directly reflecting physical

connections [184]. On the contrary, structural connectivity in our model refers to the actual synaptic connections between neurons. Despite this difference in approach, our ability to reproduce similar results by modifying synaptic strengths suggests that structural alterations may underlie the functional connectivity patterns observed clinically. This provides a potential mechanistic explanation for the clinical heterogeneity observed in CAE outcomes.

Some of the limitations of this work include our simplified representation of frontal and parietal cortices, with neuronal firing types (bursting versus regular spiking) serving as the primary distinguishing feature between cortical regions. In reality, both firing types exist across cortical regions, albeit in different proportions [32, 210]. Future models could be improved by incorporating additional distinguishing features of these regions, such as region-specific distributions of receptors mediating excitation or inhibition. To address the multifactorial nature of this disease, our future directions include exploring whether connectivity differences that prevent SWD resolution hold for other genetic mechanisms contributing to the initial diseased state, beyond the reduced cortical inhibition caused by GABRG2 mutations. It would be valuable to explore whether certain genetic mechanisms might better compensate for increased frontocortical connectivity to promote the resolution of SWD activity. Our model is particularly well-suited for investigating differential drug responses based on connectivity profiles. Future studies could test whether specific pharmacological interventions are better suited for particular connectivity patterns. This approach would be similar to existing computational studies that evaluate treatment responses in models with specific genetic mechanisms underlying the disease state, providing insights into potential treatment response trajectories and personalized therapeutic strategies [106].

4.5 Conclusion

In conclusion, our findings suggest that both the composition of neuronal cell types and the intrinsic connectivity patterns in the thalamocortical circuit may influence remission in childhood absence epilepsy. Specifically, our model demonstrates that increased frontocortical connectivity may prevent allopregnanolone-mediated recovery from spike-wave discharge states in networks with higher proportions of intrinsically bursting neurons in deep cortical layers. This may help explain why some patients experience non-remitting seizures despite the hormonal changes associated with puberty. One of our main contributions is that our model provides a computational framework for developing more targeted therapeutic approaches, particularly for patients with distinct excitability and connectivity

profiles that may predict a predisposition to poor treatment response or a disease course leading to non-resolution.

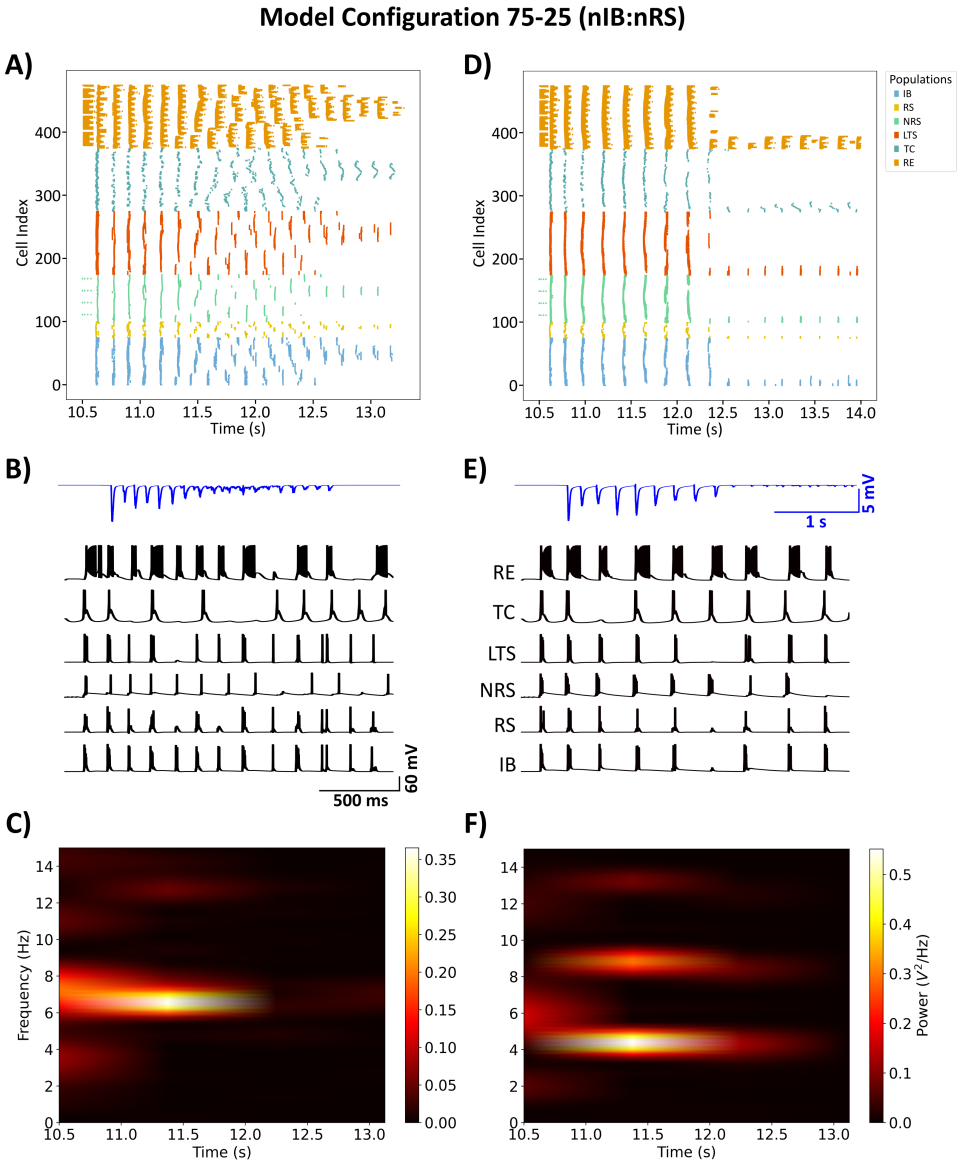

Figure 4.9: Raster plot of the 72-25 (nIB:nRS) fitted model demonstrates spindle oscillations (A), transitioning to spike-wave discharges (D) through cortical disinhibition, modelled as a reduction in baseline GABAa conductance from 100% to 10%. (B) and (E): Sample voltage traces from cell index 0 in each population, with LFP traces (in blue) computed using the method outlined in Section 4.2.3. The network activity during spindle oscillations exhibits a peak power at 7 Hz (C), whereas the SWD state shows peak power at 5 Hz (F). All simulations were conducted using Control GABAa-receptor mediated synapses.

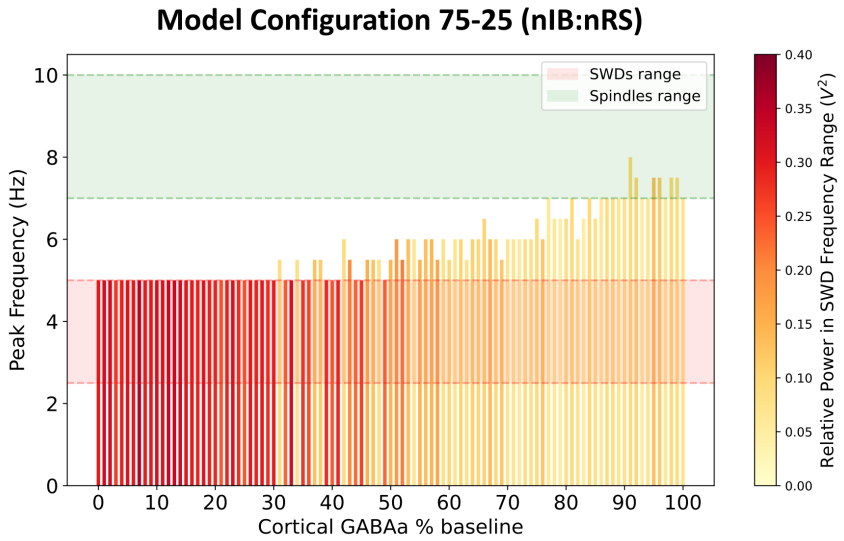

Figure 4.10: Network frequency response to varying levels of cortical GABAa-receptor mediated inhibition. The colour of each bar represents the relative power within the frequency range associated with SWDs.

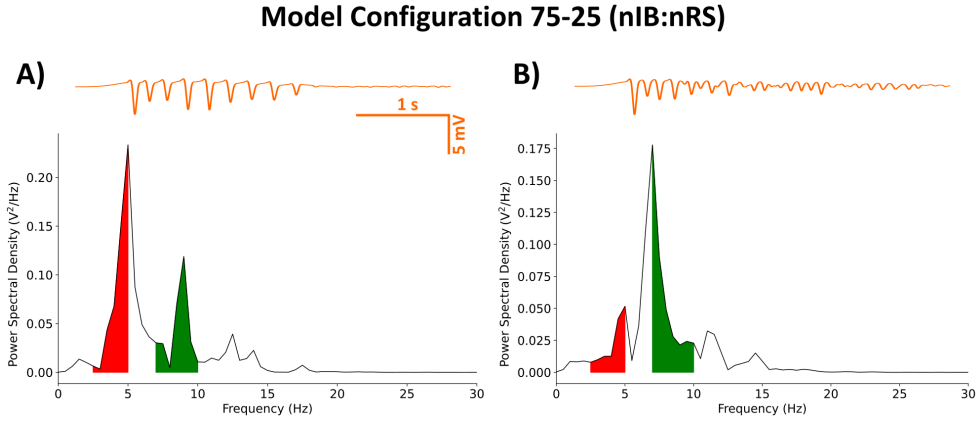

Figure 4.11: Power spectral density of the 75-25 (nIB:nRS) fitted model using Control synapses (A) and post-ALLO synapses (B), calculated from filtered LFP traces (in orange), as described in Section 4.2.3. The network was initialized with cortical disinhibition (10% baseline cortical GABAa conductance). Shaded regions indicate relative power within the frequency ranges associated with SWDs (2.5–5 Hz; red) or Spindle oscillations (7–10 Hz; green).

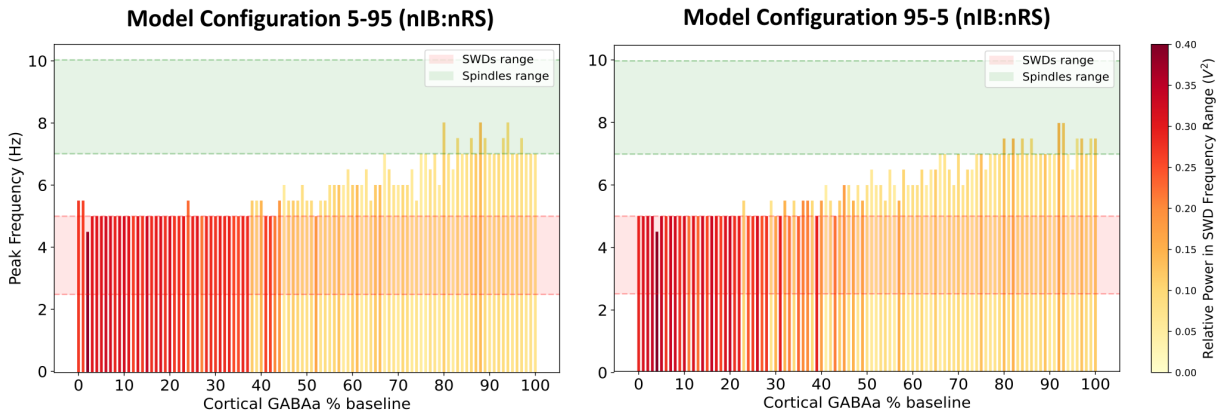

Figure 4.12: Network frequency response to varying levels of cortical GABAa-receptor mediated inhibition, using the 5-95 (left) and 95-5 (right) (nIB:nRS) model configurations. The colour of each bar represents the relative power within the frequency range associated with SWDs.

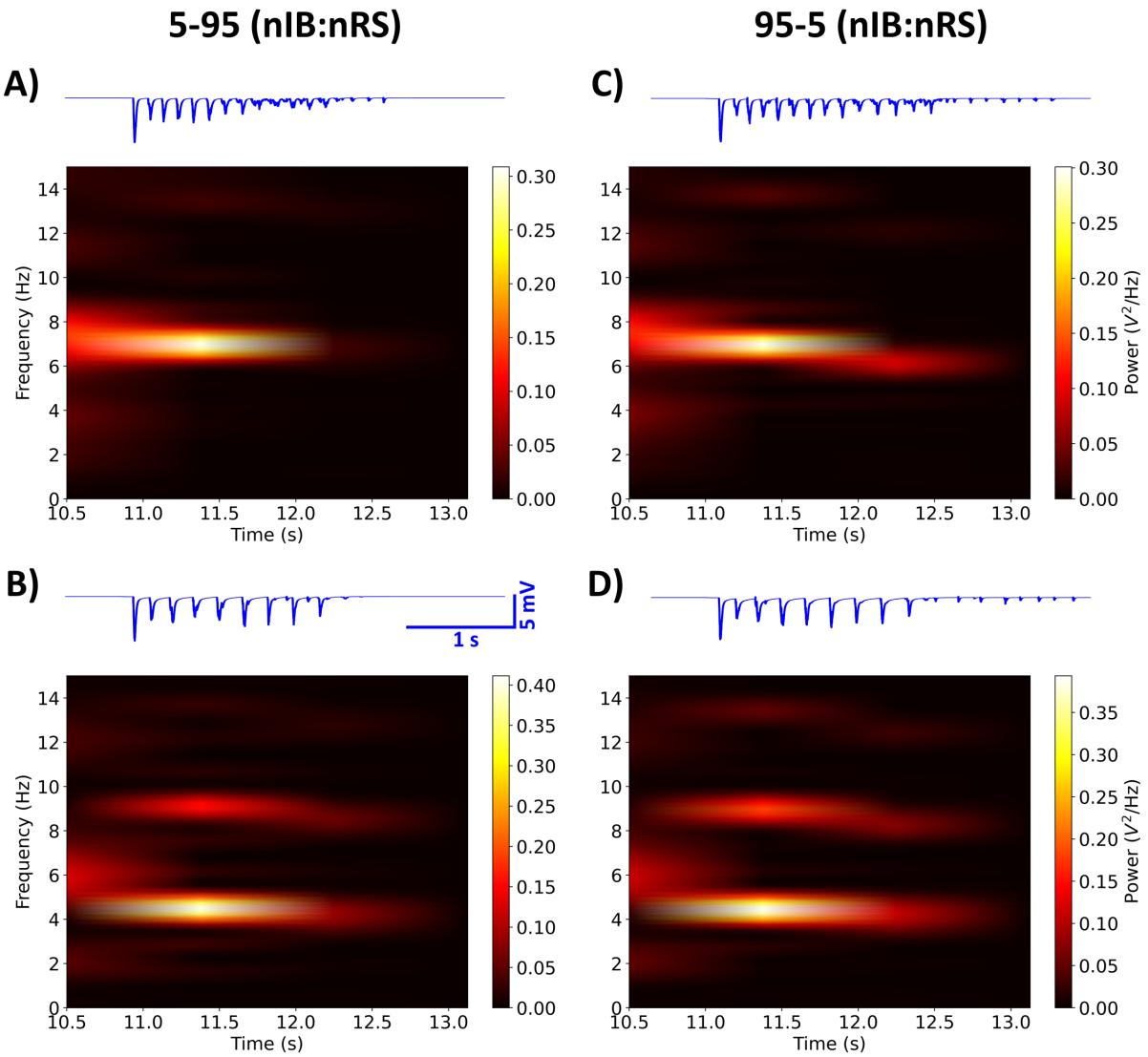

Figure 4.13: Spectral power analysis showing time-frequency representations of network activity for the 5-95 and 95-5 (nIB:nRS) model configurations, using 100% (A, C) and 10% (B, D) baseline cortical GABAa conductance. For both models, fully inhibited networks exhibit maximal power at 7.5 Hz, while partially disinhibited networks show maximal power at 5 Hz. LFP traces (in blue) were calculated using the population-based method described in Section 4.2.3.

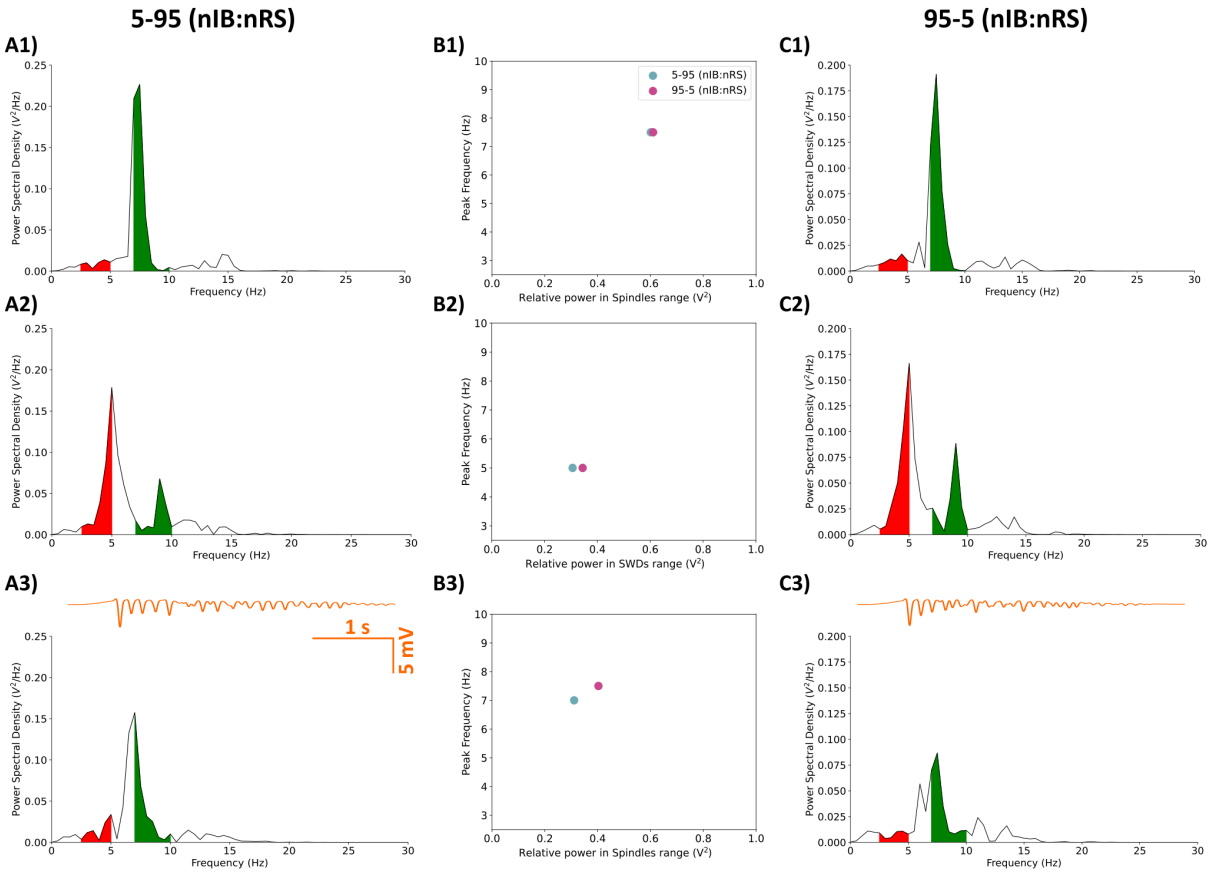

Figure 4.14: Power spectral density of the 5-95 (A1–A3) and 95-5 (C1–C3) (nIB:nRS) model configurations, calculated from filtered LFP traces (in orange). Shaded regions indicate relative power within the frequency ranges associated with SWDs (2.5–5 Hz; red) or Spindle oscillations (7–10 Hz; green). (A1, C1): Networks with Control synapses and full cortical inhibition, exhibiting spindle oscillations at 7.5 Hz. (A2, C2): Networks with Control synapses and reduced cortical GABAa conductance (10% baseline), exhibiting SWDs at 5 Hz. (A3, C3): Networks initialized with cortical disinhibition as in (A2, C2) but using post-ALLO synapses, showing transition to a physiological state under the effect of allopregnanolone. (B1): Relationship between relative power in spindles range and peak network frequency for fully inhibited networks. (B2): Relationship between relative power in SWDs range and peak network frequency for partially disinhibited networks. (B3): Relationship between relative power in spindles range and peak network frequency for networks under the effect of ALLO.

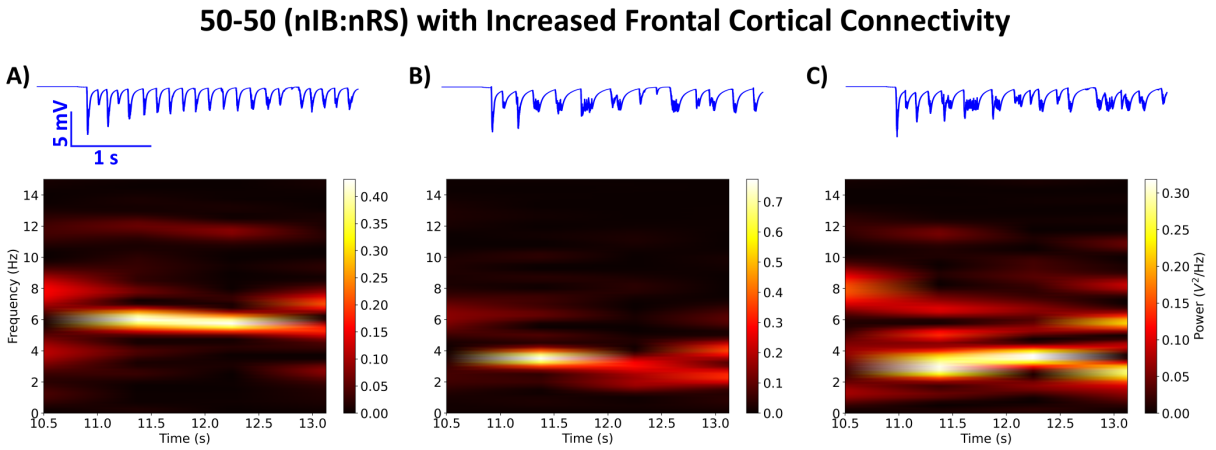

Figure 4.15: Spectral power analysis showing time-frequency representations of network activity for the 50-50 (nIB:nRS) model configuration with enhanced frontal cortical connectivity, using $(F_{IBIB}, F_{IBNRS}, F_{NRSIB}) = (7, 5, 3)$. (A): Network behaviour using Control synapses and full cortical inhibition exhibits maximal power at 5.5 Hz. (B): Network behaviour using Control synapses under partial disinhibition (10% baseline cortical GABAa conductance) shows maximal power at 4 Hz. (C) Network initialized with cortical disinhibition as in (B) but using post-ALLO synapses shows a lack of restorative effect from ALLO, with a maximal frequency of 2.5 Hz. LFP traces (in blue) were calculated using the method described in Section 4.2.3.

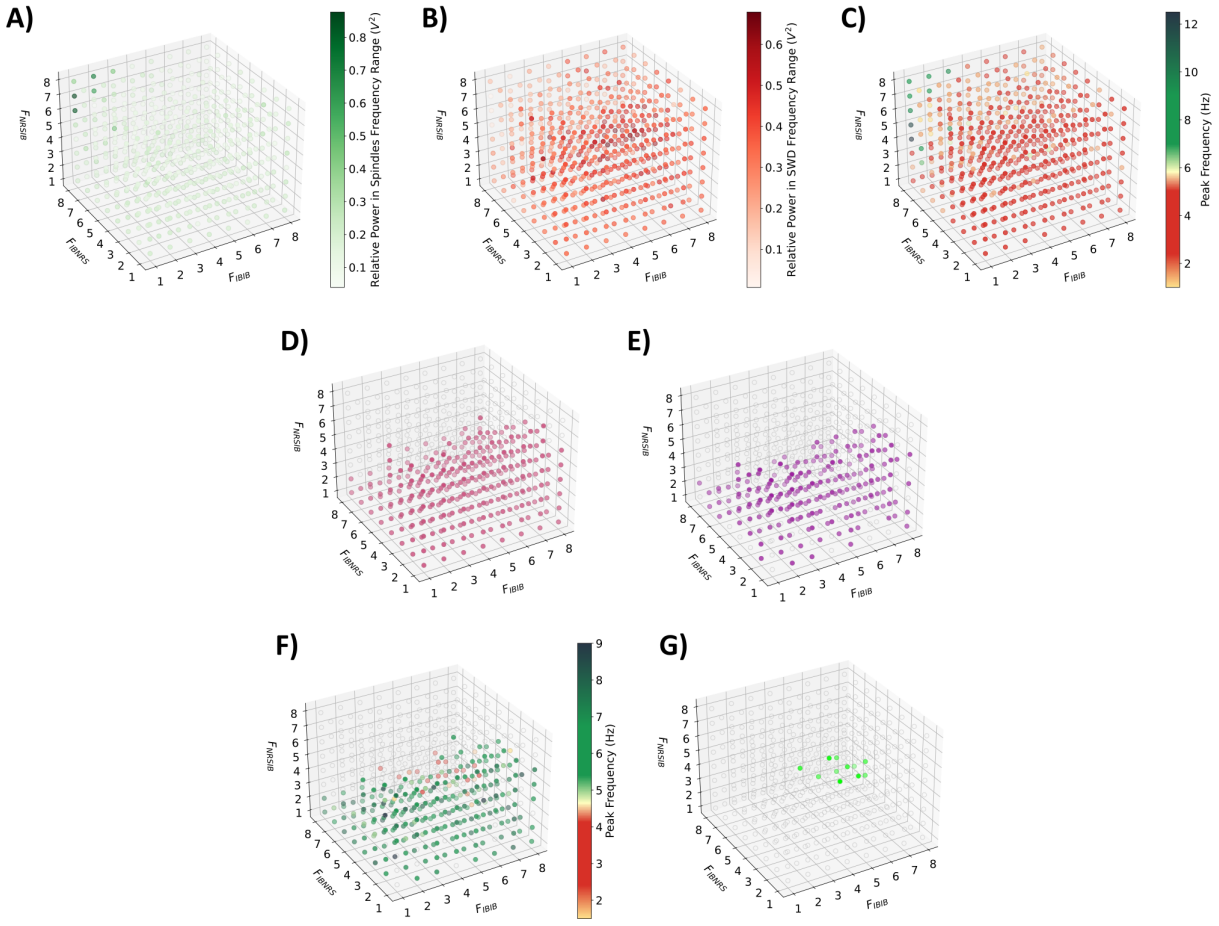

Figure 4.16: 3D visualization of the grid search results across $8^3 = 512$ parameter combinations within the $(F_{IBIB}, F_{IBNRS}, F_{NRSIB})$ parameter space using the 50-50 (nIB:nRS) model configuration. (A–C): Initial search using Control synapses with cortical GABAa conductance at 10% baseline, were filtered by examining the magnitude of: (A): relative power within spindles range, (B) relative power within SWDs range, and (C): peak frequency from power spectral density analysis. (D): Filtered parameter combinations from the initial search. (E): Parameter combinations that produce spindle-like oscillations when simulated with cortical GABAa conductance restored to normal (100% baseline) levels. (F): Parameter combinations that produce continued SWDs (in red) when the network is simulated using 10% baseline cortical GABAa conductance and post-ALLO synapses. (G): Final parameter set of $(F_{IBIB}, F_{IBNRS}, F_{NRSIB})$ for which the 50-50 (nIB:nRS) model exhibits continued SWDs post application of ALLO.

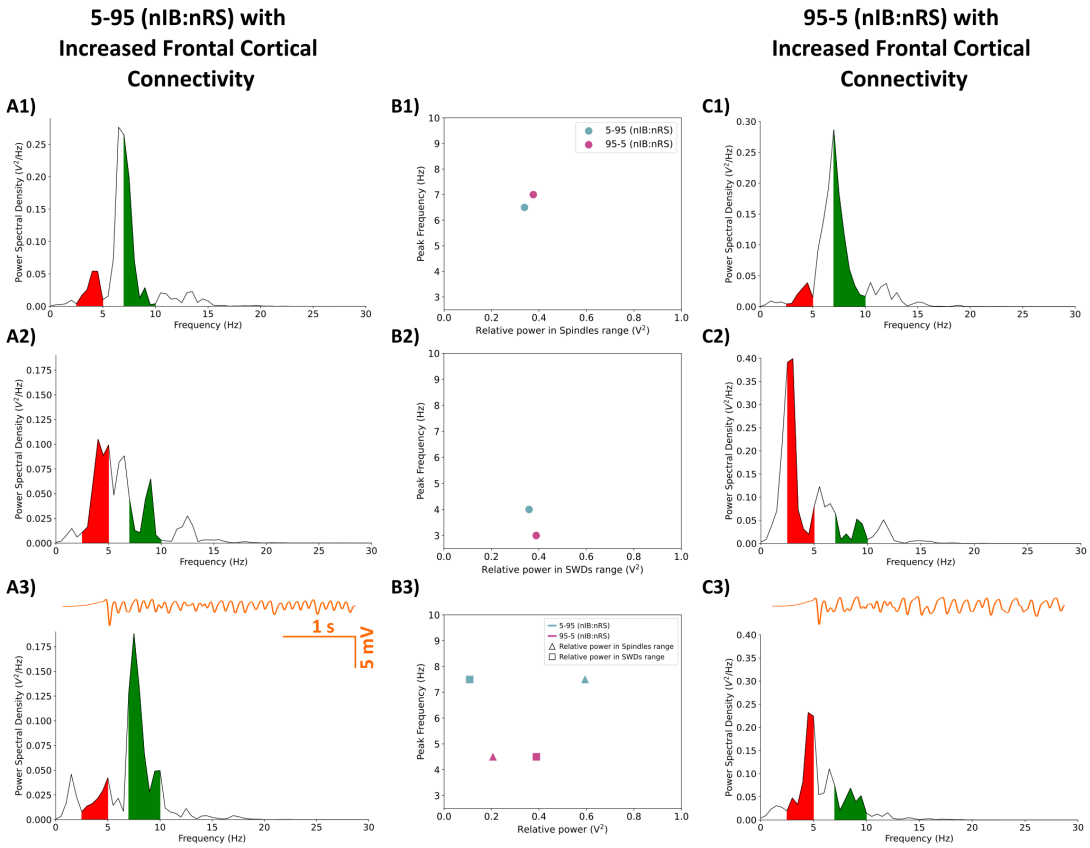

Figure 4.17: Power spectral density of the 5-95 (A1–A3) and 95-5 (C1–C3) (nIB:nRS) model configurations with enhanced frontal cortical connectivity, calculated from filtered LFP traces (in orange). Shaded regions represent relative power within frequency ranges associated with SWDs (2.5–5 Hz; red) or Spindle oscillations (7–10 Hz; green). (A1, C1): Networks with Control synapses and full cortical inhibition, exhibiting spindle oscillations at 6.5 Hz and 7 Hz for the 5-95 and 95-5 models, respectively. (A2, C2): Networks with Control synapses and reduced cortical GABAa conductance (10% baseline), exhibiting SWDs at 4 Hz and 3 Hz for the 5-95 and 95-5 model, respectively. (A3, C3): Networks initialized with cortical disinhibition as in (A2, C2) but using post-ALLO synapses. The transition to a physiological state under the effect of allopregnanolone occurs for the 5-95 model configuration, but not the 95-5 model. (B1): Relationship between relative power in spindles range and peak network frequency for fully inhibited networks (B1) and networks under the effect of ALLO (B3). (B2): Relationship between relative power in SWDs range and peak network frequency for partially disinhibited networks.

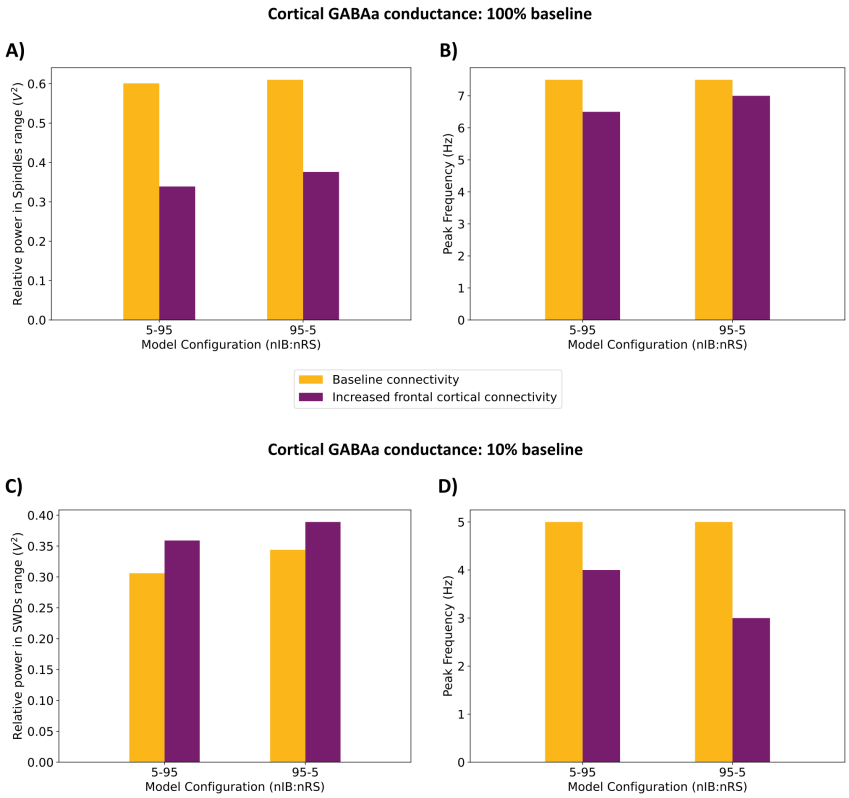

Figure 4.18: Comparison of network responses between the 5-95 and 95-5 (nIB:nRS) model configurations under two cortical GABAa conductance conditions (100% and 10% baseline). (A, C): Relative power in the spindle/SWDs frequency range. (B, D): Corresponding peak frequencies of network activity. Each condition is shown under baseline (orange) and increased frontocortical connectivity (purple).

Chapter 5

Modelling the impact of sodium channel mutations on remission and non-remission in childhood absence epilepsy

This chapter is based on the paper: M Ahmed and SA Campbell. 2025. Modelling genetic mutations in resolving and non-resolving childhood absence epilepsy. In preparation.

5.1 Introduction

Childhood absence epilepsy is a genetically complex disorder with many different genetic mutations implicated. It typically affects children between the ages of 4 and 12 years and has a fascinating tendency to resolve during adolescence in most cases, as discussed in Section 1. CAE is characterized by pathological 2.5–5 Hz spike-wave discharge (SWD) activity, which often arises from the transformation of physiological 7–10 Hz spindle oscillations generated by the thalamocortical circuit, as described in Section 2.6. Genetic studies in patients with CAE have identified mutations in genes encoding ion channels and neurotransmitter receptors. These include genes encoding sodium channels, calcium channels, chloride channels, h-channels, and GABA receptors [35, 208, 156, 209, 109]. Among these, several specific variants have been particularly implicated in CAE pathophysiology. Different types of mutations are possible such as missense, and null. A missense mutation refers to the substitution of one amino acid for another in the protein, thereby affecting the protein's function, while a null mutation refers to the loss of channel expression [151]. Genetic variants of these channels can manifest as gain- or loss-of-function mutations, resulting in either neuronal hyperexcitability or hypoexcitability. When combined with cell-type-specific gene expression patterns, these variants can significantly alter the excitatory/inhibitory balance within neuronal networks, thereby modifying the underlying mechanisms of seizure generation.

Voltage-gated sodium channels (VGSCs) are crucial for neuronal excitability, generating depolarizing sodium currents that initiate and propagate action potentials. In mammals, the Nav1.1, Nav1.2, Nav1.3 and Nav1.6 channels encoded by $SCN1A$, $SCN2A$, $SCN3A$ and $SCN8A$ respectively, are expressed primarily in the central nervous system, and usually concentrated on the axon initial segments (AIS) of neurons [173]. Each of these genes is characterized by distinct patterns of spatial and temporal expression [132]. In the context of absence epilepsy, mutations in the genes encoding Nav1.2 and Nav1.6 are primarily responsible for the disease pathology, with $SCN2A$ and $SCN8A$ consistently expressed in both humans and rodents across different brain regions, including the cortex and thalamus [208, 57, 71].

Several studies have investigated $SCN8A$ mutations in rodent models, revealing strain-specific effects on absence seizures. Papale et al. specifically identified three $SCN8A$ alleles ($Scn8a^{V929F}$, $Scn8a^{med}$, and $Scn8a^{med-jo}$) that demonstrated significant variations in spike-wave discharge (SWD) patterns, with higher average seizure frequency and SWD amplitude in any of the $SCN8A$ mutants as compared to the wild-type [160]. The functional impact of each of these alleles was investigated in other studies. $Scn8a^{med}$ is a spontaneous mutation, causing the production of a disrupted protein that is unlikely to retain channel

function. This mutations leads to the loss of expression of the $SCN8A$ sodium channel, and as a result, $Scn8a^{med}$ is classified as a null allele [107]. $Scn8a^{med-jo}$ and $Scn8a^{V929F}$ are both missense mutations that alter the voltage dependence of channel gating [108, 156]. All three of these variants result in decreased function of the Nav1.6 sodium channel, suggesting overall neuronal hypoexcitability. In a study by Ogiwara et al., $SCN2A$-knockout ($Scn2a^{+/-}$) mice were found to exhibit ethosuximide-sensitive absence-like seizures accompanied by spike-wave discharges in adulthood [155]. Interestingly, selective deletion of $SCN2A$ in excitatory neurons, but not in inhibitory neurons, led to increased occurrence of SWDs, and seizures were effectively suppressed by ethosuximide administration.

Several animal models of absence epilepsy have been developed, resulting from spontaneous mutations in mice (e.g., *tottering*, *lethargic*, and *stargazer* models) and in rats (e.g., GAERS and WAG/Rij) [38, 95]. These models provide a valuable and accessible platform for further exploration of the genetic basis of CAE, particularly with regard to the functional consequences of specific mutations, which would be challenging to study directly in human patients. However, animal models present significant limitations when it comes to studying the phenomenon of remission in CAE. A major limitation is the inability of these animals to exhibit remitting seizures, a critical feature of CAE in most human cases [202].

This gap between animal models and human disease progression significantly impacts our understanding of prognosis factors. While research has identified various mutations implicated in CAE, as discussed earlier, there is currently limited understanding of how specific genetic variants correlate with improved treatment response and prognosis. Given the multifactorial nature of the disease, we still lack genetic markers that can predict disease outcome. Moreover, it remains unclear whether specific genetic mechanisms underlying the manifestation of CAE inherently contribute to a higher likelihood of disease remission, or whether other factors could modulate the impact of these mechanisms on disease progression and eventual outcome. In this study, we utilize a previously developed conductance-based model of the thalamocortical circuit, described in Section 4.2.1, to investigate whether specific genetic mutations implicated in CAE predispose individuals to non-remission. Additionally, we examine whether factors such as increased frontocortical connectivity contribute to non-remission, even in individuals with genetic mutations found to be associated with remission.

5.2 Materials and methods

We utilized a 475-cell thalamocortical network defined exactly as in Section 4.2.1. The model consists of the following populations: 25 layer 5 RS pyramidals, 75 layer 5 IB

pyramidals, 75 layer 6 non-tufted RS pyramidals, 100 deep LTS interneurons, 100 thalamocortical cells, and 100 thalamic reticular cells. Each neuron is modelled using a single compartment, and its own set of ionic currents ranging from transient and persistent sodium currents, potassium currents of the delayed rectifier, transient, slowly inactivating, and Ca^{2+}-dependent types, in addition to both low- and high-threshold Ca^{2+} currents, described by Equations (3.1)–(3.6). As illustrated in the network schematic in Figure 4.1, all excitatory connections in the network are mediated by AMPA receptors, and inhibitory connections are mediated by either GABAa only or a combination of GABAa and GABAb receptors, defined appropriately using equations (4.7)–(4.11). The model parameters are given in Tables 4.1–4.4, while details of the individual currents, and synaptic dynamics are provided in Appendix B.

All models were simulated using NetPyNE and run in parallel on a Dell PowerEdge R840 with four 20-core Intel processors and 768 GB of RAM. Each simulation ran for 15 seconds of simulation time, with a typical runtime of approximately 12 minutes and memory usage of 13 GB.

5.2.1 Modelling voltage-gated sodium channel mutations

We modelled the effects of various $SCN2A$ and $SCN8A$ mutations in single neurons in a mutation-dependent manner by modifying parameters related to the fast sodium current (I_{Naf}) and the slowly activating and inactivating potassium current (I_{K2}). The selection of I_{Naf} was driven by the critical roles of both Nav1.2 and Nav1.6 in action potential generation as well as their involvement in the fast sodium current. In contrast, I_{K2} was chosen due to its analogy to the delayed rectifier, with Kv1.1 being a voltage-gated delayed rectifier channel [89, 59]. The alterations to channel kinetics were based on relative changes in channel activity between wild-type and mutant forms, as reported in the literature and outlined below.

The functional impact of the $Scn8a^{med}$ mutation is reported to be a loss of Nav1.6 channel expression [107]. We modelled this effect by modifying the parameter denoting the maximum conductance of the fast sodium current (g_{Naf}), as illustrated below:

$$I_{Naf} = \boxed{\boldsymbol{g_{Naf}}} \cdot m_{Naf}^3 \cdot h_{Naf} \cdot (V - V_{Na}) \tag{5.1}$$

The $Scn8a^{med-jo}$ mutation is reported to alter the voltage dependence of channel gating [108]. In a study by Kohrman et al, electrophysiological analysis using voltage clamp techniques in Xenopus oocytes expressing a mutant sodium channel showed the voltage

dependence of both activation and inactivation to be shifted in the depolarizing direction. This shift means that, for a given depolarization, the mutant channels open less readily than the wild-type, resulting in a reduced percentage of open channels at the same membrane potential. The experimental results were presented using standard Boltzmann functions representing steady state activation and inactivation, as described in Section 2.3.1. The resulting parameters for both wild-type and mutant channel activity are given in Table 5.1.

Similarly, the $Scn8a^{V929F}$ mutation is also reported to affect the voltage-dependent channel gating properties in a manner that suggests a general reduction in channel activity [156]. In particular, there is a depolarizing shift in the activation curve compared to the wild-type, suggesting that the mutant has a decreased number of open channels at a given voltage. There is also a large hyperpolarizing shift in the inactivation curve compared to the Nav1.6 wild-type, consistent with a further decrease in channel activity. These changes, as reported experimentally, are presented in Table 5.1.

	Activation (m_∞)			
	Wild-type		Mutant	
Mutation Type	$V_{1/2}$ (mV)	k	$V_{1/2}$ (mV)	k
$Scn8a^{med-jo}$	-23.9 ± 1.9	4.4 ± 0.8	-9.8 ± 1.5	4.1 ± 0.6
$Scn8a^{V929F}$	-15.2 ± 1.7	9.37 ± 1.4	-9.33 ± 1.6	7.53 ± 0.6
	Inactivation (h_∞)			
	Wild-type		Mutant	
Mutation Type	$V_{1/2}$ (mV)	k	$V_{1/2}$ (mV)	k
$Scn8a^{med-jo}$	-51.1 ± 0.6	5.7 ± 0.3	-44.3 ± 0.9	5.0 ± 0.3
$Scn8a^{V929F}$	-36.58 ± 2.2	7.32 ± 0.2	-48.37 ± 1.9	6.11±0.2

Table 5.1: Comparison of parameters of the steady-state activation and inactivation properties of wild-type and $SCN8A$ variants as reported by Kohrman et al. [108] ($Scn8a^{med-jo}$) and Oliva et al. [156] ($Scn8a^{V929F}$).

In our model, the steady-state activation and inactivation properties of the fast sodium channel in all the cortical cells were represented by Boltzmann-like sigmoid functions, as in Equations (2.12)–(2.13), which describe the voltage-dependent probability of channel opening or closing. However, in both the thalamic cells, the dynamics of the fast sodium channel were described using forward (α) and backward (β) rate constants that control the transitions between channel states, as described in Equation (2.9). The steady-state

activation and inactivation variables were defined as the equilibrium solutions of these state transitions, as given in Equation (2.10). Since alterations in channel activity due to $SCN8A$ mutations were specific to half-activation voltage and the slope factor in the Boltzmann functional form, we needed to redefine the existing $m_{Na\infty}$ and $h_{Na\infty}$ expressions for both thalamic cell types in terms of a Boltzmann-like function. The details of this redefinition are provided in Appendix C.1.

The effects of both $Scn8a^{med-jo}$ and $Scn8a^{V929F}$ mutations were modelled by introducing a shift in the half-activation voltage ($V_{shift,i}$) as well as a shift in the slope factor ($k_{shift,i}$) parameters in the steady-state activation/inactivation functions for the fast sodium current, as highlighted in the following equations:

$$m_{Naf\infty} = \frac{1}{1 + \exp\left(\frac{-V + \left(V_{1/2,m} + \boxed{\boldsymbol{V_{shift,m}}}\right)}{k_m + \boxed{\boldsymbol{k_{shift,m}}}}\right)} \tag{5.2}$$

$$h_{Naf\infty} = \frac{1}{1 + \exp\left(\frac{V - \left(V_{1/2,h} + \boxed{\boldsymbol{V_{shift,h}}}\right)}{k_h + \boxed{\boldsymbol{k_{shift,h}}}}\right)} \tag{5.3}$$

where $m_{Naf\infty}$ and $h_{Naf\infty}$ denote steady state activation and inactivation, respectively, $V_{1/2}$ denotes the half-activation voltage, and k denotes the slope factor. Each shift factor was defined by the following equations:

$$V_{shift,i} = \frac{\Delta V_{1/2,i} \cdot |V_{1/2,i}|}{100} \qquad \text{for } i = m, h \tag{5.4}$$

$$k_{shift,i} = \frac{\Delta k_i \cdot |k_i|}{100} \qquad \text{for } i = m, h \tag{5.5}$$

where the $\Delta V_{1/2,i}$ and Δk_i values correspond to the relative changes between wild-type and mutant channel properties. The relative change was calculated using the following equation:

$$\Delta X_i = \left[\frac{X_{Mut} - X_{WT}}{X_{WT}}\right] \times 100\% \quad \text{for } X = V_{1/2}, k \tag{5.6}$$

where X_{Mut} and X_{WT} denote values corresponding to the mutant and wild-type channel, respectively. The parameters used to model the $SCN8A$ mutations are given in Table 5.2.

At a cellular level, voltage-clamp analysis of cultured $Scn2a^{+/-}$ hippocampal pyramidal neurons showed an approximate 45% reduction in maximum sodium conductance density

[155]. As per the findings of Zhang et al., severe Nav1.2 deficiency significantly downregulates the expression of multiple potassium channels, particularly Kv1.1, altogether leading to neuronal hyperexcitability [212, 181]. Accordingly, we modelled the $Scn2a^{+/-}$ mutation by modifying the parameter corresponding to the maximal conductance of the I_{Naf} current as in Equation 5.1 as well as adjusting the maximal I_{K2} conductance parameter (g_{K2}) to account for increased neuronal firing observed experimentally, as highlighted below:

$$I_{K2} = \boxed{\boldsymbol{g_{K2}}} \cdot m_{K2} \cdot h_{K2} \cdot (V - V_K) \tag{5.7}$$

Specifically, this involved reducing the maximal I_{K2} conductance by approximately two-fold relative to the reported value, changing it from roughly 33% to 75% [212]. The analysis underlying this modification is discussed in Figure C.2 of Appendix C. The parameters used to model the $SCN2A$ mutation are given in Table 5.3.

	Activation ($m_{Naf\infty}$)		Inactivation ($h_{Naf\infty}$)		
Mutation Type	$\Delta V_{1/2,m}$	Δk_m	$\Delta V_{1/2,h}$	Δk_h	g_{Naf}
$Scn2a^{+/-}$	-	-	-	-	0.55× baseline value
$Scn8a^{med}$	-	-	-	-	0× baseline value
$Scn8a^{med-jo}$	59	-6.8	13.3	-12.3	-
$Scn8a^{V929F}$	38.6	-19.6	-32.2	-16.5	-

Table 5.2: Modifications to the fast sodium current (I_{Naf}) parameters as a result of mutations of $SCN2A$ or $SCN8A$. Note that alterations to the activation and inactivation curve parameters were implemented as a relative change (given in %) between the wild-type and mutant channel activity.

Mutation Type	g_{K2}
$Scn2a^{+/-}$	0.25 × baseline value

Table 5.3: Modification to the slowly activating and inactivating potassium current (I_{K2}) maximal conductance as a result of $SCN2A$ mutation.

5.2.2 Modelling and evaluating the effect of mutations on network activity

To implement the effect of a particular mutation on channel activity, we consider relative changes between the wild-type and mutant channels, as described in Section 5.2.1, and

introduce a *mutation strength* parameter that controls the intensity of the mutation's effect, M_{effect}, defined by the following equation:

$$M_{effect} = M_{max} \times \frac{\text{mutation strength}}{100} \tag{5.8}$$

where M_{max} is the maximum possible effect of the mutation (i.e., the relative magnitude of the change). When the mutation strength is set to 100%, the mutation causes the full intended effect. As the mutation strength changes, the magnitude of its impact is scaled proportionally.

Recall that the peak network frequency and relative power in spindles/SWD frequency range are calculated from the power spectral density (PSD) curve, the computation of which is described in detail in Section 4.2.3. We use these to define a metric, *mutation score*, for evaluating and characterizing the effectiveness of a given mutation in inducing network activity that exhibits pathological spike-wave discharges (SWDs), given by the following equation:

$$M_{score} = \delta_{\text{SWD range}} + R_{\text{spindles}} \tag{5.9}$$

where $\delta_{\text{SWD range}}$ denotes the distance of the peak network frequency from the frequency range associated with SWDs, and R_{spindles} represents the relative power in the spindles range, normalized by the total relative power in both the spindles and SWD frequency ranges. Each term is defined using the following equations:

$$\delta_{\text{SWD range}} = \begin{cases} 0.5 \cdot |f_{peak} - 2.5|, & \text{if } \ f_{peak} < 2.5 \\ 0, & \text{if } 2.5 \leq f_{peak} \leq 5 \\ 2 \cdot |f_{peak} - 5|, & \text{if } f_{peak} > 5 \\ 10, & \text{if no triggered oscillations} \end{cases} \tag{5.10}$$

where f_{peak} denotes the peak frequency in the PSD curve, and,

$$R_{\text{spindles}} = \begin{cases} \frac{P_{spindles}}{P_{spindles}+P_{SWDs}} & \\ 10, & \text{if no triggered oscillations} \end{cases} \tag{5.11}$$

where $P_{spindles}$ and P_{SWDs} denote the relative power in spindles and SWD frequency range, respectively. The mutation score is defined such that low scores correspond to network behaviour characteristic of SWD activity, while high scores indicate deviations from this pattern.

5.3 Results

5.3.1 Effects of $SCN2A$ and $SCN8A$ mutations on single neuron activity in the cortex and thalamus

The varying impacts of $SCN2A$ and $SCN8A$ mutations on single neuron activity across different cell types are shown in Figures 5.1-5.10. We modelled $Scn2a^{+/-}$ only in cortical cells due to a lack of evidence on the effects of this mutation type on thalamic cells. Across all excitatory cells in the cortex, for a fixed mutation strength, the $Scn2a^{+/-}$ mutation increases neuronal firing, as illustrated by the spike-count response curves in Figures 5.1-5.3 (panel C, green curves). In the case of the IB cell, notches are observed in the spike-count response curve. These notches can be explained by the emergence of transitory firing patterns, particularly sub-threshold doublet spikes, which eventually develop into full action potentials, resulting in a subsequent increase in the spike count. Interestingly, neuronal hyperexcitability was not observed in the cortical inhibitory cell, as shown in Figure 5.4C (green curve). However, this is likely due to its low baseline conductance of the $K2$ current, as compared to the excitatory cells, since the observed increase in spike count is largely dependent on the reduction in $K2$ conductance caused by $SCN2A$ haplodeficiency. A consistent feature across all cortical cells was depolarization block, which occurred as a result of excessive input current and ultimately reduced the number of actions potentials to zero. Consistent with findings in the literature, the $Scn2a^{+/-}$ mutation led to a reduced mean action potential amplitude and a broader action potential half-width in excitatory cortical neurons [181, 212]. As shown in Table 5.4 and Figure 5.5 (top row), this effect was consistent across cell types and became more pronounced with increased mutation strength. The spike-count response to varying mutation strength (Figure 5.5, bottom row) was similar to the response to increasing input current: in excitatory cortical cells, neuronal firing increased with mutation strength, while the inhibitory LTS cell exhibited a decrease in firing, until all neurons eventually entered depolarization block and ceased firing. In addition to changes in firing frequency, the mean action potential amplitude decreased with increasing mutation strength, as shown in Figures 5.1–5.3 (panel B) and Figure 5.5 (top row). This effect was consistent across all cell types and suggests that the loss of firing observed with the $Scn2a^{+/-}$ mutation may be attributed to a reduction in action potential amplitude.

The different $SCN8A$ mutations exhibited region-specific differences between the cortex and thalamus, along with cell-specific effects in the thalamus. Across cortical cells, all mutations were loss-of-function types, as shown in Figures 5.1-5.4 (panels B and C). For a fixed mutation strength, each mutation type decreases the firing frequency as well as

		Mean AP Amplitude (mV)				Mean AP Half-width (ms)			
Cell Type	I_{app} (nA)	0%	50%	75%	100%	0%	50%	75%	100%
Layer 5 RS	1.7	93.66	84.74	77.65	65.60	0.44	0.51	0.58	0.84
Layer 5 IB*	1.2	98.84	90.61	85.87	77.12	0.36	0.41	0.43	1.07
Layer 6 NRS	1.4	96.09	86.66	78.63	66.09	0.43	0.49	0.57	0.73

* The second spike in a doublet burst was removed from all calculations as these were small-amplitude oscillations that emerged due to hyperexcitability and consequently biased the measurements.

Table 5.4: Average action potential amplitude and half-width as a result of $Scn2a^{+/-}$ with varying mutation strengths (given as percentages) on different cortical cells. Both spike features were measured using the *eFEL* Python package's *AP_amplitude_from_voltagebase* and *spike_half_width* functions. Both features were averaged across all spikes.

the maximal input current before depolarization block, as shown in Figures 5.1-5.4 (panel C). Notably, $Scn8a^{V929F}$ had the most debilitating effect on neuronal firing, followed by $Scn8a^{med-jo}$ and $Scn8a^{med}$ in that order. Generally speaking, the notches observed in the spike-count response curves are a consequence of the emergence of subthreshold doublets or triplet bursts, which momentarily reduces the spike count. These local minima occur at specific current intensities where the neuron transitions between different firing patterns. As input current continues to increase, the subthreshold oscillations develop into full action potentials, causing the spike count to rise. This creates the characteristic non-monotonic regions in the response curves. Eventually, when there is excessive input current, the cell reaches a sustained depolarized state, leading to depolarization block, and the number of action potentials reduces to zero. The loss of firing particularly occurs through decreased action potential amplitude, resulting from reduced fast sodium current, as illustrated in Figures 5.1-5.4 (panel B). This behaviour is consistent across all three mutation types and cortical cells. As shown in Figure 5.6, increasing mutation strength leads to decreased mean action potential amplitude (top row) and reduced firing frequency (bottom row), eventually causing the neuron to cease firing. The spike-count response to mutation strength is similar to that seen with varying input current in that occasional peaks due to transitions in firing patterns are present. These transitions manifest as high-frequency sub-threshold oscillations that progressively decrease in amplitude.

The effect of $SCN8A$ mutations on the thalamocortical (TC) cell is type-dependent. As shown in Figure 5.7B, for a fixed mutation strength, generally all three mutations do

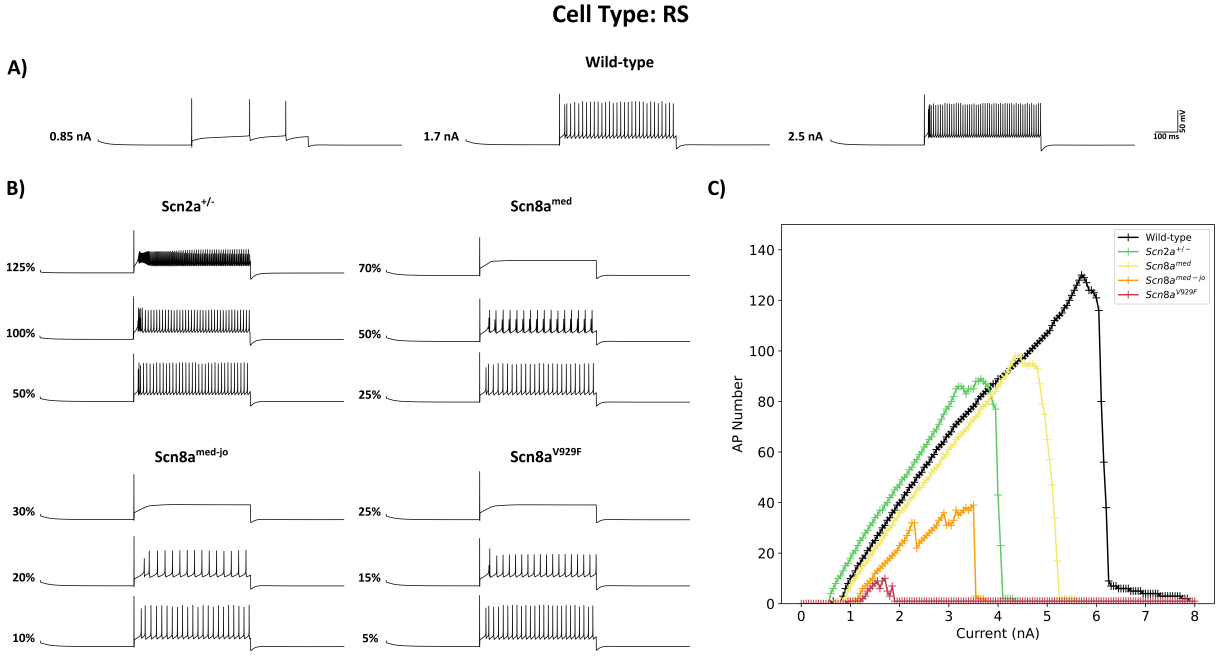

Figure 5.1: (A) and (B): Voltage traces of Layer 5 Regular Spiking (RS) cortical neuron for varying input currents and mutation strengths (with input current held at 1.7 nA for 500 ms) for each $SCN2A$ and $SCN8A$ mutation type. (C): Spike-count response curve with each $SCN2A$ and $SCN8A$ mutation strength fixed at 75% and 20% respectively.

not cause significant deviations of the spike-count response curves from the wild-type. This is consistent with the effect of $SCN8A$ haplodeficiency in TC cells as reported in [128] (see Figure 4D1). While $Scn8a^{V929F}$ lowers the curve more than $Scn8a^{med-jo}$, the $Scn8a^{med}$ mutation moves the curve in the opposite direction. As illustrated in Figure 5.8, for a fixed input current, increasing $Scn8a^{med}$ mutation strength decreases both mean action potential amplitude (panel A) and reduces firing frequency (panel B) by 100%, eventually. On the contrary, increases in mutation strength of both $Scn8a^{med-jo}$ and $Scn8a^{V929F}$ results in a 0.21% and 0.34% decrease in mean amplitude, and 12.5% and 25% decrease in spike count, respectively. Thus, only the null mutation results in a total loss-of-function of the TC cell at maximal mutation strength.

The effect of $SCN8A$ mutations on thalamic reticular (RE) neurons is also type-dependent. As shown in Figure 5.9B, for a fixed mutation strength, $Scn8a^{med-jo}$ and $Scn8a^{V929F}$ result in reduced neuronal firing with varying input current, thus shifting the spike-count response curves down relative to the wild-type. The $Scn8a^{med}$ mutation main-

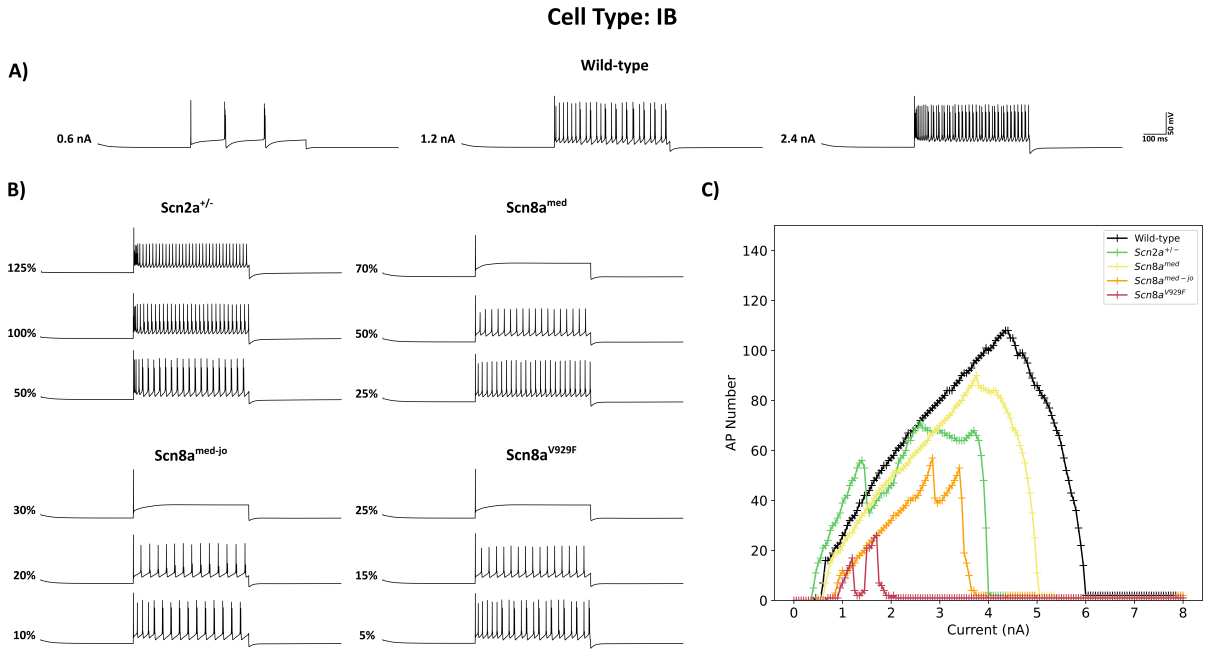

Figure 5.2: (A) and (B): Voltage traces of Layer 5 Intrinsically Bursting (IB) cortical neuron for varying input currents and mutation strengths (with input current held at 1.2 nA for 500 ms) for each $SCN2A$ and $SCN8A$ mutation type. (C): Spike-count response curve with each $SCN2A$ and $SCN8A$ mutation strength fixed at 75% and 20% respectively.

tains more robust firing across mutation strengths, showing greater resilience to changes in maximal conductance. In contrast with the excitatory thalamic cell, the $Scn8a^{med-jo}$ mutation has a more debilitating effect on neuronal response than $Scn8a^{V929F}$. Exploring variation in mutation strength for a fixed input current illustrates the different mutation-dependent mechanisms by which RE firing is affected, as shown in Figure 5.10. With increases in $Scn8a^{med}$ strength, the main effect is a gradual reduction in spike amplitude of the initial burst of spikes during the first 100ms post-stimulus (Figure 5.10B). The total spike count (Figure 5.10A) appears to remain relatively stable until high mutation strengths, and firing appears more regular across moderate mutation strengths. In contrast, spike amplitude reduction of the initial burst is not observed to the same level with increases in $Scn8a^{V929F}$ strength. Instead, there is a gradual decrease in firing frequency until there is insufficient activation of sodium channels to allow sustained steady-state firing. The main effect of $Scn8a^{med-jo}$ is distinctly different, primarily affecting the cell's ability to sustain firing as indicated by the duration until last spike illustrated in Figure

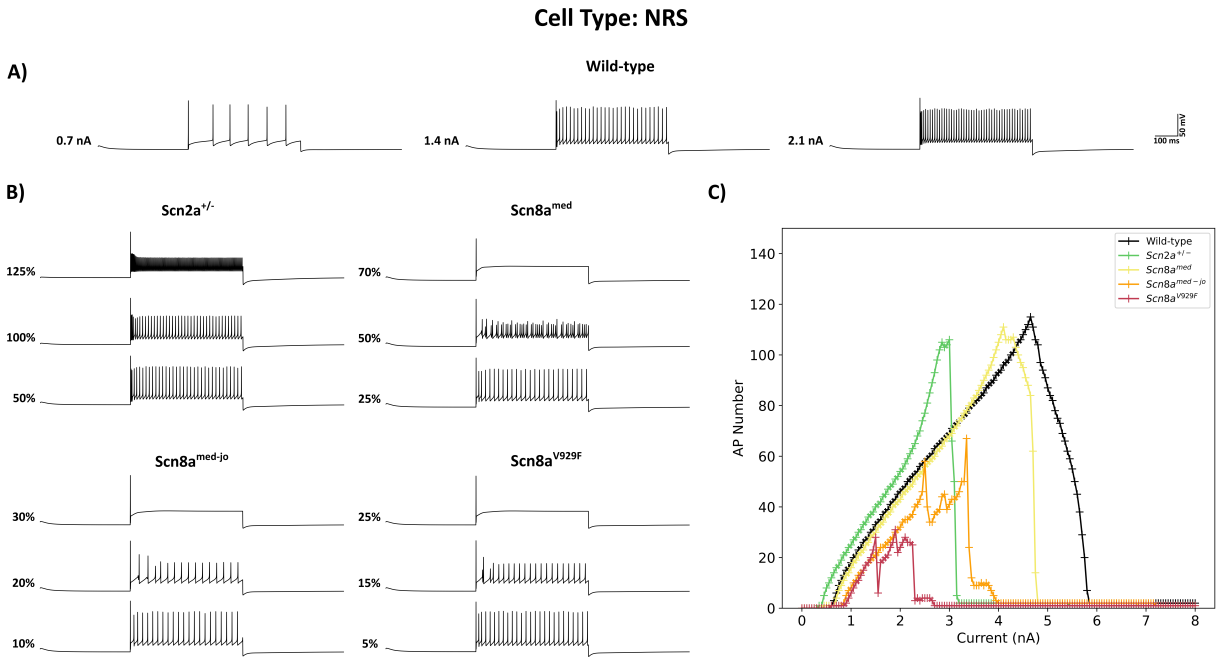

Figure 5.3: (A) and (B): Voltage traces of Layer 6 Non-tufted Regular Spiking (NRS) cortical neuron for varying input currents and mutation strengths (with input current held at 1.4 nA for 500 ms) for each $SCN2A$ and $SCN8A$ mutation type. (C): Spike-count response curve with each $SCN2A$ and $SCN8A$ mutation strength fixed at 75% and 15% respectively.

5.10C as well as mutation strength-dependent voltage traces in Figure 5.9A . This "burst-then-cease" transition in firing behaviour suggests a qualitatively different mechanism of firing reduction compared to the other mutations.

With increases in mutation strength, all three mutation types eventually lead to complete loss of firing at 100% strength, though through different trajectories. As illustrated in Figures 5.9A and 5.10A,B, at moderate strengths, $Scn8a^{med}$ shows a gradual reduction in initial burst amplitude while maintaining firing patterns. $Scn8a^{V929F}$ exhibits a progressive decrease in firing frequency. $Scn8a^{med-jo}$ displays a distinctive "burst-then-cease" pattern. This suggests that while the final outcome is similar, the path to firing loss differs between mutations affecting channel conductance versus voltage-dependent properties. In particular, alterations in voltage dependence of activation and inactivation ($Scn8a^{med-jo}$ and $Scn8a^{V929F}$) affect the channel's ability to properly transition between states, leading

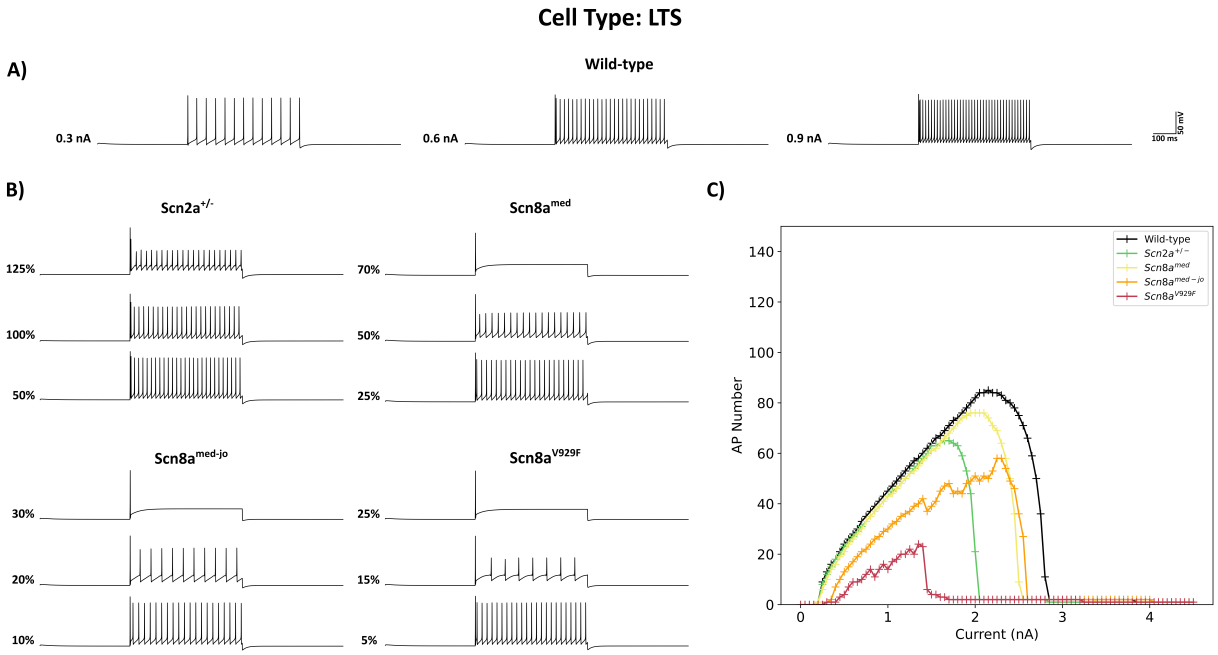

Figure 5.4: (A) and (B): Voltage traces of Low-threshold Spiking (LTS) Interneuron in the cortex for varying input currents and mutation strengths (with input current held at 0.6 nA for 500 ms) for each $SCN2A$ and $SCN8A$ mutation type. (C): Spike-count response curve with each $SCN2A$ and $SCN8A$ mutation strength fixed at 75% and 15% respectively.

to premature inactivation or impaired activation that compromises sustained firing. In contrast, reduced maximal conductance ($Scn8a^{med}$) simply decreases the number of available functional channels, resulting in smaller amplitude spikes during the initial burst, while maintaining normal voltage-dependent properties that enable sustained firing patterns. Our modelling provides strong evidence that reduced $SCN8A$ expression in RE cells likely affects channel kinetics rather than just conductance. The fact that reduced conductance alone cannot reproduce the firing patterns observed in $SCN8A$-deficient RE neurons (see Figure 4C1 of [128]), while altered voltage dependence can, suggests kinetic changes play an important role. However, experimental validation through voltage clamp recordings would still be needed to confirm this hypothesis.

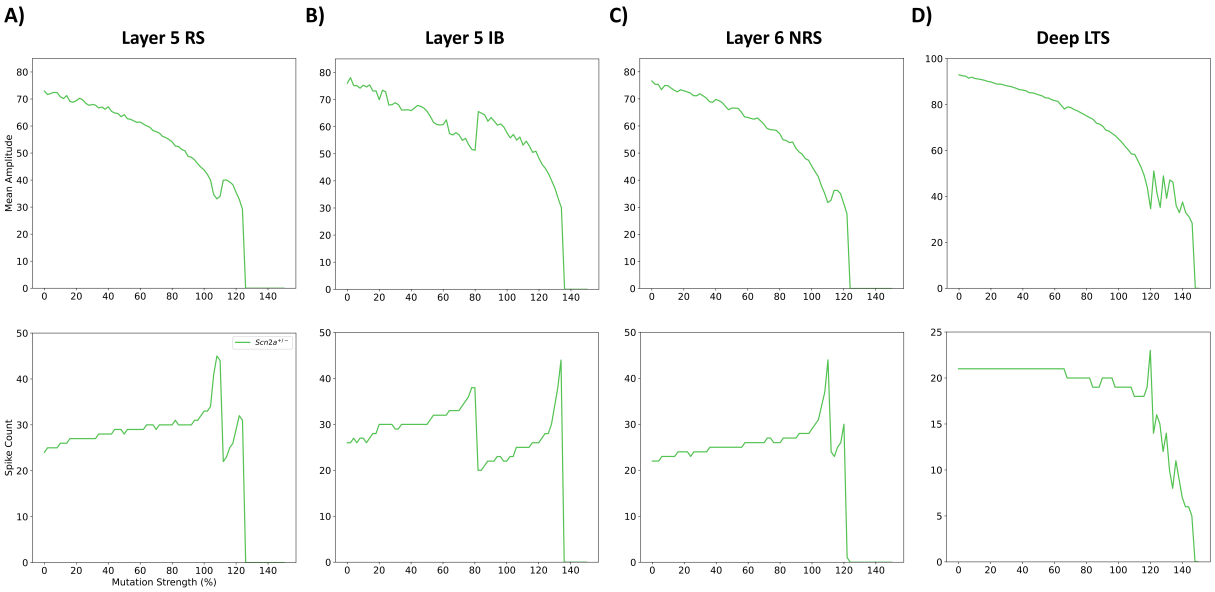

Figure 5.5: Exploring the effect of the strength of $SCN2A$ mutation on the mean amplitude of action potentials and spike count in Layer 5 RS (A), Layer 5 IB (B), Layer 6 NRS (C), and Deep LTS (D) cortical cells. The applied input current was held at 1.7, 1.2, 1.4, and 0.6 nA respectively.

5.3.2 $SCN2A$ and $SCN8A$ mutations associated with remission are modulated by frontocortical connectivity and variant-specific factors

Building on our previous analysis, where we explored the effects of SCN mutations in single cells, we extended our investigation to examine how these mutations influence network-level dynamics. Specifically, we targeted certain cell populations or combinations of populations within the thalamocortical circuit, focusing on how these mutations contribute to pathological network behaviour. Next, following the approach in Section 4.2.5, we investigated the effect of allopregnanolone (ALLO) on the disease states caused by these genetic mutations to determine whether ALLO could modify the mutation's effects, particularly in its ability to promote the resolution of SWDs. Additionally, we explored the role of ALLO under the condition of increased frontocortical connectivity, a factor previously shown to contribute to non-resolving SWDs (see Section 4.3.3).

For the $Scn2a^{+/-}$ mutation, we investigated its effect on network behaviour by targeting

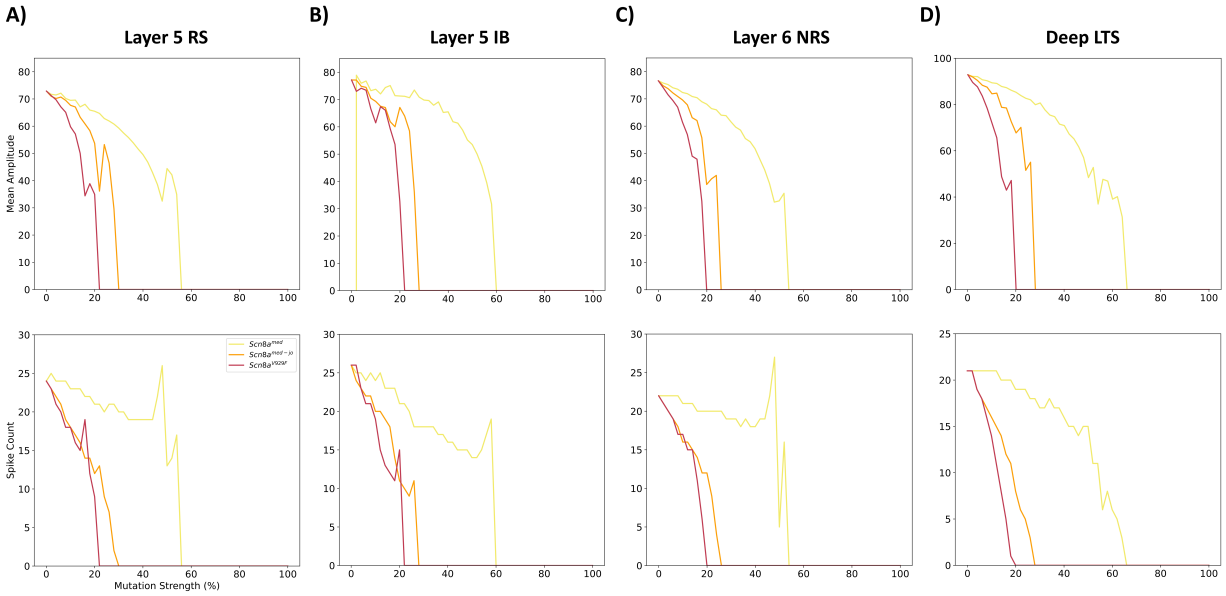

Figure 5.6: Exploring the effect of the strength of each $SCN8A$ mutation type on the mean amplitude of action potentials and spike count in Layer 5 RS (A), Layer 5 IB (B), Layer 6 NRS (C), and Deep LTS (D) cortical cells. The applied input current was held at 1.7, 1.2, 1.4, and 0.6 nA respectively.

individual cortical cell populations, as well as specific cortical layers (layer 5, and layers 5 and 6 combined), with mutation strengths ranging up to 150%, as shown in Figure 5.11A. Using the mutation score metric as defined in Section 5.2.2, we identified specific populations and mutation strengths that increased the network's propensity to enter a pathological state of spike-wave discharges (SWDs). A network was classified as being in a SWDs state if its frequency ranged between 2.5–5 Hz and if it exhibited maximal power in the frequency range associated with SWDs. Accordingly, the network entered a SWDs state only when the target population was LTS cells and the mutation strength was greater than or equal to 125%, as illustrated in Figure 5.11B. Then, we initialized the network to each identified diseased state and implemented the effect of allopregnanolone (ALLO) on all GABAa-receptor mediated synapses. The effect of ALLO was found to be ameliorating in causing a transition in network activity from SWDs to spindle oscillations, as indicated by both an increase in mutation score as well as the peak frequency of the network, as shown in Figures 5.11C1, C2. The seemingly absent measurement of peak frequency at mutation strengths of 130% and 140% was due to the network activity not persisting long enough to be considered for evaluation, based on our criteria outlined in Section 4.2.2. Next, we

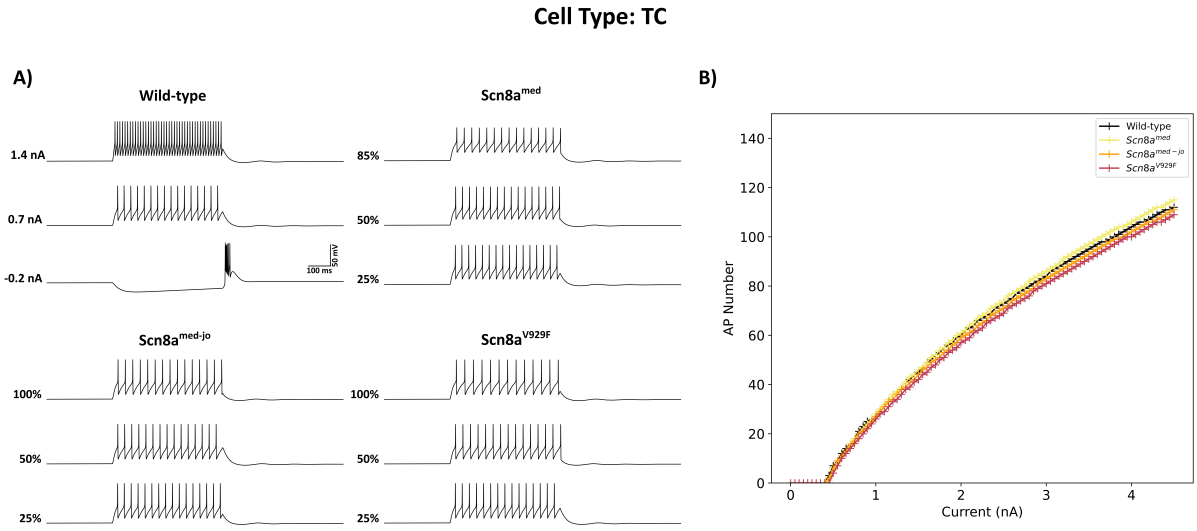

Figure 5.7: (A): Voltage traces of thalamacortical (TC) neuron for varying input currents and mutation strengths (with input current held at 0.7 nA for 500 ms) for each $SCN8A$ mutation type. (B): Spike-count response curve with each mutation strength fixed at 60%.

examined this ameliorating effect with increased frontocortical connectivity and found it to push the network further away from a pathological state, as indicated by a further increase in both the mutation score and peak network frequency compared to when frontocortical connectivity was at baseline levels, as shown in Figures 5.11D1,D2. Overall, while the effect of $Scn2a^{+/-}$ in causing a SWD state remains consistent across mutation strengths equal to or greater than 125%, the effect of ALLO, either alone or in combination with increased frontocortical connectivity, peaks at 140% mutation strength. This highlights the variability in the effects of the $Scn2a^{+/-}$ mutation, even within the same mutation type.

The target populations for all the $SCN8A$ mutations included individual cortical and thalamic populations, as well as whole cortex or thalamus, excitatory or inhibitory cells, and combinations of both excitatory and inhibitory cells from cortex and thalamus, with mutation strengths ranging up to 100%, as illustrated in Figures 5.12–5.14 (panel A). Under the effect of the $Scn8a^{V929F}$ mutation, the network exhibited an SWD state either when the target population was LTS cells and the mutation strength was greater than or equal to 25%, or when the mutation affected all inhibitory cells in the network (i.e., both LTS and RE cells) at a mutation strength of 25%, as illustrated in Figure 5.12B. The effect of ALLO on networks initialized to each of these diseased states was consistent across

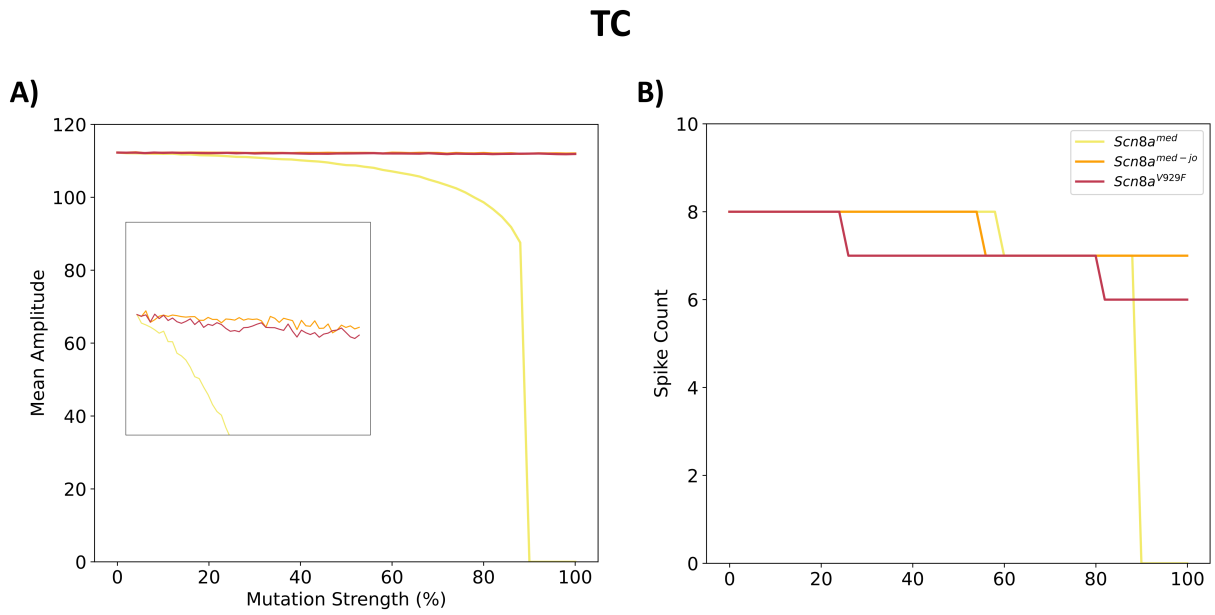

Figure 5.8: Exploring the effect of the strength of each $SCN8A$ mutation type on the mean amplitude of action potentials (A) and spike count (B) in the TC cell. The applied input current was held at 0.7 nA. The inset in the left panel is a close-up of the curves corresponding to $Scn8a^{med-jo}$ and $Scn8a^{V929F}$.

target population groups. In particular, ALLO facilitated the network's recovery from the SWD state, as indicated by increases in both mutation score and peak network frequency (Figures 5.12C1, C2, D1, D2). However, ALLO's effect differed when combined with increased frontocortical connectivity. When the target population consisted of both LTS and RE cells, along with increased frontocortical connectivity, ALLO caused the network to enter a more pronounced physiological spindles state, as shown by an increase in both mutation score and network frequency (Figures 5.12D3, D4). This effect was also observed in the case where the target population was only LTS cells, although it was mutation strength-dependent and occurred only for strengths between 25–35%, as shown in Figures 5.12C3, C4. When the mutation strength exceeded 35%, ALLO was no longer effective in mitigating the effects of increased frontocortical connectivity. In this case, the network activity shifted to a state of unresolved SWDs, with a network frequency even lower than the baseline SWD states shown in Figure 5.12C2.

When simulated under the effect of the $Scn8a^{med-jo}$ mutation, the network exhibited a pathological SWD state when the target population consisted only of LTS cells and

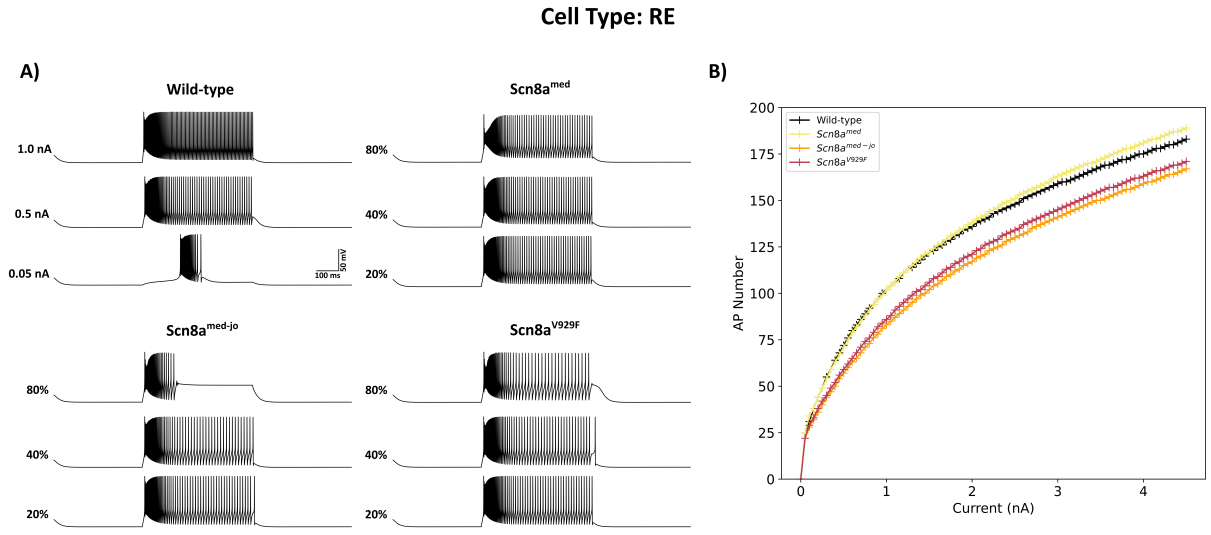

Figure 5.9: (A): Voltage traces of thalamic reticular (RE) neuron for varying input currents and mutation strengths (with input current held at 0.5 nA for 500 ms) for each $SCN8A$ mutation type. (B): Spike-count response curve with each mutation strength fixed at 60%.

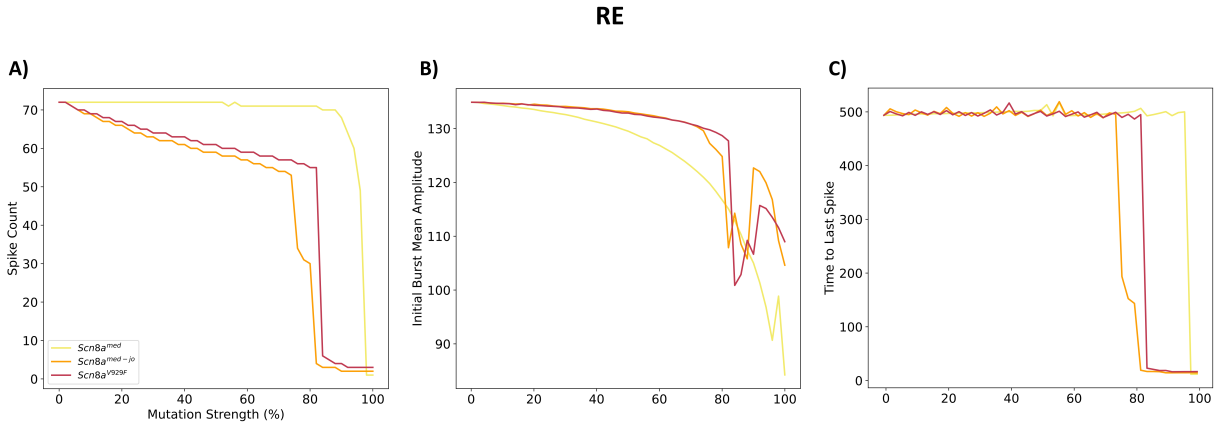

Figure 5.10: Exploring the effect of the strength of each $SCN8A$ mutation type on the spike count (A), mean spike amplitude of the initial burst (B) and the time to last spike (C) in the RE cell. The applied input current was held at 0.5 nA.

the mutation strength was greater than or equal to 40%, as illustrated in Figure 5.13B. Across mutation strengths, introducing the effect of ALLO on all GABAa-receptor me-

diated synapses facilitated the network's recovery from an SWD state, as indicated by increases in both mutation scores and peak network frequency, shown in Figures 5.13C1, C2. However, with increased frontocortical connectivity, ALLO's effect was no longer ameliorative, and the network displayed a more prominent pathological SWD state, as illustrated in Figures 5.13C3, C4. This effect was consistent across mutation strengths, with network frequency lower than the baseline SWD states shown in Figure 5.13C2.

In the case of the $Scn8a^{med}$ mutation, similar to all other SCN mutations considered in this study, diseased SWD states were observed when the target population consisted only of LTS cells. Specifically, this was seen for mutation strengths greater than or equal to 60%, as illustrated in Figure 5.14B. Consistent with the role of ALLO in promoting recovery from network states exhibiting SWDs, its application led to increases in both mutation scores and peak network frequency (Figures 5.14 C1, C2). When combined with increased frontal cortical connectivity, ALLO's effect was mutation strength-dependent, similar to what was observed for networks under the influence of the $Scn8a^{V929F}$ mutation (Figures 5.12C3, C4). In particular, ALLO was effective in resolving SWDs at mutation strengths between 60–70%, whereas mutation strengths exceeding 70% resulted in a state of non-remission, as shown in Figure 5.14C3, C4.

5.4 Discussion

In this study, we used a conductance-based model of the thalamocortical circuit to investigate how mutations in $SCN2A$ and $SCN8A$, genes encoding voltage-gated sodium channels and implicated in childhood absence epilepsy, influence the likelihood of remission in the absence of anti-epileptic drug treatment. First, we identified which cell types, when carrying these mutations, give rise to a pathological spike-wave discharge (SWD) state. Next, we investigated which genetic variants are associated with remission. Additionally, we examined the role of increased frontocortical connectivity in influencing non-resolution of spike-wave discharges, particularly in the context of genetic variants associated with favourable disease outcomes.

Our results demonstrate that, across all mutation types, mutations in the cortical deep low-threshold spiking (LTS) interneuron population contribute to an SWD state. This is consistent with our model, where both $SCN2A$ and $SCN8A$ mutations in the LTS population result in loss-of-function mutations, leading to reduced neuronal excitability. The resulting decrease in excitability within inhibitory cells suggests a reduction in network-level inhibition, which makes it reasonable that these mutations contribute to the SWD state. This finding aligns with the net effects observed in the comparison between $SCN2A$

and $SCN8A$ alterations in cortical inhibitory cells and the $GABRG2$ mutation, which reduces GABAa-receptor mediated inhibition in the cortex, giving rise to spike-wave discharge behaviour, as discussed in Section 3.2.1. However, the mechanisms underlying these effects differ. In the case of $SCN2A$ and $SCN8A$ mutations, the primary effect is on the intrinsic properties of the interneurons, whereas the $GABRG2$ mutation impairs synapse-mediated firing in postsynaptic cells. Despite these mechanistic differences, both mutations result in a decrease in inhibitory signalling at the network level, potentially leading to distinct temporal or spatial effects on neuronal firing patterns, which influence SWD dynamics in subtle ways. Additionally, $Scn8a^{V929F}$ mutations affecting thalamic reticular (RE) neurons, along with LTS neurons, gave rise to pathological SWDs in our model. This finding aligns with the results from Makinson et al., who reported spontaneous absence seizures in mice with broad inhibitory cell deletion of $SCN8A$ [128]. Their findings on the effects of of $SCN8A$ deficiency in individual RE neurons were also similar to our modelling results, which demonstrated neuronal hypoexcitability. In our model, the network's ability to exhibit a pathological SWD state was only possible when the intensity of the mutation's effect was sufficiently high, as measured by our *mutation strength* parameter discussed in Section 5.2.2. This held true for all mutation types and both target cell populations (i.e., inhibitory cells in the cortex alone, and inhibitory cells in both the cortex and thalamus), suggesting that the effects of the mutation may vary in degree, even within the same mutation type.

Interestingly, we found that, irrespective of the underlying disease mechanism (alterations in $SCN2A$ or $SCN8A$), at baseline levels of frontocortical connectivity, all $SCN2A$ and $SCN8A$ variants were associated with remission. Specifically, the impact of allopregnanolone (ALLO) on GABAa-receptor mediated inhibition facilitates recovery of the network from an SWD state. This suggests that ALLO's action on the thalamocortical network is robust across varying degrees of mutation effects and disease mechanisms, including alterations in both synapse-mediated inhibition and the intrinsic properties of inhibitory network components.

The role of ALLO in contributing to remission was influenced by increased frontocortical connectivity within the network, with this influence depending on the gene, target cell population, variant type, and the intensity of mutation effects within a given variant. Specifically, for $SCN2A$ mutations, the effect of ALLO on the network was consistent with the resolution of SWDs, with or without increased frontocortical connectivity. For $SCN8A$ mutations, when the target population consisted of inhibitory cells in both the cortex and thalamus, alterations in frontocortical connectivity had no debilitating impact, and the network was able to exhibit resolution from a pathological state. However, when the target population was restricted to LTS cells, the outcome diverged in a variant- and mutation

intensity-dependent manner. Specifically, $Scn8a^{med-jo}$ mutations, under the condition of increased frontocortical connectivity, were associated with non-remission, regardless of mutation intensity. In contrast, $Scn8a^{med}$ and $Scn8a^{V929F}$ mutations were associated with remission at lower mutation strengths, but with non-remission at higher mutation strengths. This behaviour was consistent with how increased frontocortical connectivity influenced network configurations, as discussed in Section 4.3.3.

These observations further reflect the variability seen in patients, even when their initial presentations appear similar. The genetic landscape is complex, making it difficult to determine which cells potentially carry specific mutations, without invasive procedures. However, advances in non-invasive techniques like magnetic resonance spectroscopy (MRS) could help infer the effects of mutations based on brain activity patterns [170]. MRS measures metabolites like glutamate and GABA, which are involved in excitatory and inhibitory signaling. Imbalances in these neurotransmitters—such as increased glutamate and decreased GABA—could indicate hyperexcitability, suggesting dysfunction in excitatory cells or inhibition failure. While MRS cannot pinpoint the exact cellular origin, it could provide valuable indirect evidence of excitatory or inhibitory disruptions. When combined with initial genetic sequencing, this approach may offer insights into whether mutations primarily affect inhibitory or excitatory cells, or the extent of disruption in each cell type. Building on such data, computational simulations and digital twin models can further enhance personalized medicine by integrating genetic, neuroimaging, and metabolic information to simulate individual brain network behaviour. These models can help predict how specific patients may respond to treatments and provide forecasts for the likelihood of symptom worsening or remission during puberty, enabling more informed and individualized clinical decisions.

One limitation of this study is that we focused on the effects of individual mutations, rather than considering how co-occurring mutations might interact. As with other idiopathic epilepsies, childhood absence epilepsy is a polygenic disorder characterized by complex interactions among multiple genes that shape the CAE phenotype [130, 14]. Moreover, mutations in one gene may not only contribute directly to the syndrome, but also modify the effects of mutations in other genes [153]. By examining the combined influence of $SCN2A$ and $SCN8A$ mutations, we could gain deeper insights into this complex genetic landscape. Another major limitation of this study is that we focused solely on genetic predispositions in the absence of antiepileptic drug (AED) treatment, a scenario that does not reflect typical clinical practice, where patients are routinely treated with AEDs [148]. Furthermore, AEDs may have disease-modifying effects, potentially altering the course of the disease in various ways, including changes in ion channel expression and activity-dependent reorganization of neural circuits [54, 18, 166]. In particular, the mechanisms involved in

seizure control may, with frequent use, compensate for mutations that, in a drug-naive context, are predicted in our model to result in non-remission. A key strength of this study, however, is that it provides a foundation for future computational modelling of these drug-treatment effects. By simulating how AEDs interact with genetic factors, these models can identify effective therapeutic strategies that may modify disease progression, even in cases where mutations are predicted to limit recovery. Moreover, such simulations can be further refined to identify optimal interventions for individual patients. For example, in silico comparisons of conventional AEDs versus neurosteroid-based treatments may reveal approaches that are most effective for specific genetic profiles. This predictive capacity would be particularly valuable for guiding personalized treatment plans in clinical settings.

5.5 Conclusion

In conclusion, our findings suggest that in a drug-naive context, where the underlying disease mechanism in childhood absence epilepsy involves $SCN2A$ or $SCN8A$ mutations, disease outcomes may be influenced by allopregnanolone-mediated recovery from spike-wave discharge (SWD) states, contributing to eventual remission. Our model demonstrates that this effect can be modulated by increased frontocortical connectivity, which may prevent the resolution of SWDs in certain $SCN8A$ variants. This is particularly evident in our model simulations when the mutation affects inhibitory neurons in the cortex alone and when the intensity of mutation effects is sufficiently high. These results underscore the complexity of the genetic landscape in CAE and highlight the challenge of translating such findings into reliable predictive markers for remission. Our contribution—through the development of a computational framework to model the effects of mutations implicated in CAE—represents a key step toward personalized therapeutic strategies, particularly if such a framework can simulate disease trajectories based on patient-specific factors, including underlying mutations. This could help predict outcomes like remission and guide treatment decisions, leading to more personalized interventions.

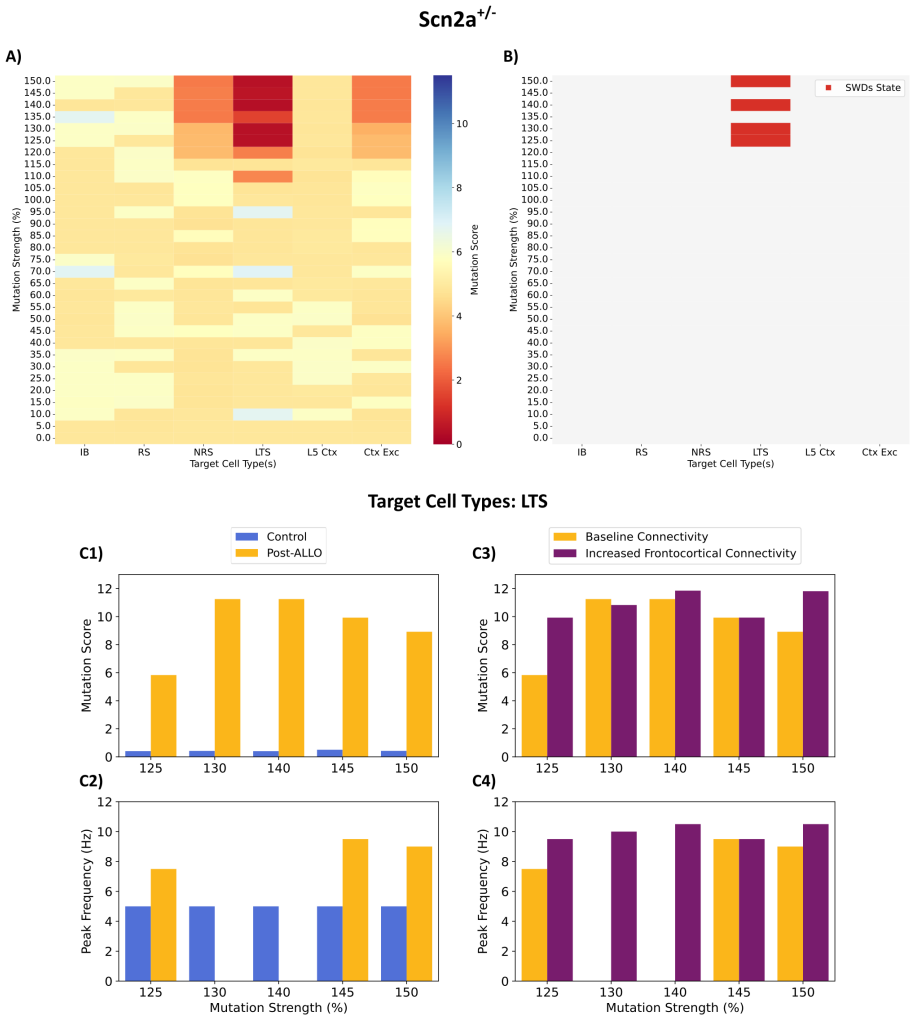

Figure 5.11: Effects of the $Scn2a^{+/-}$ mutation on network behaviour and response to allopregnanolone. (A): Mutation scores across different target cell types and mutation strengths up to 150%. Lower scores (red) indicate pathological activity, while higher scores (blue) indicate deviations away from this pattern. (B): Occurrence of spike-wave discharge (SWD) states, defined as network frequency between 2.5–5 Hz and maximal power within the SWD-associated frequency range. (C1–C2): Comparison of mutation scores (C1) and peak network frequency (C2) between Control (blue) and post-ALLO (orange) conditions at varying mutation strengths during which the network exhibited a SWD state. (C3–C4): Comparison of mutation scores (C3) and peak network frequency (C4) between networks with frontocortical connectivity at baseline levels (orange) and increased levels (purple). The orange bars are identical to those shown in (C1–C2) for comparison.

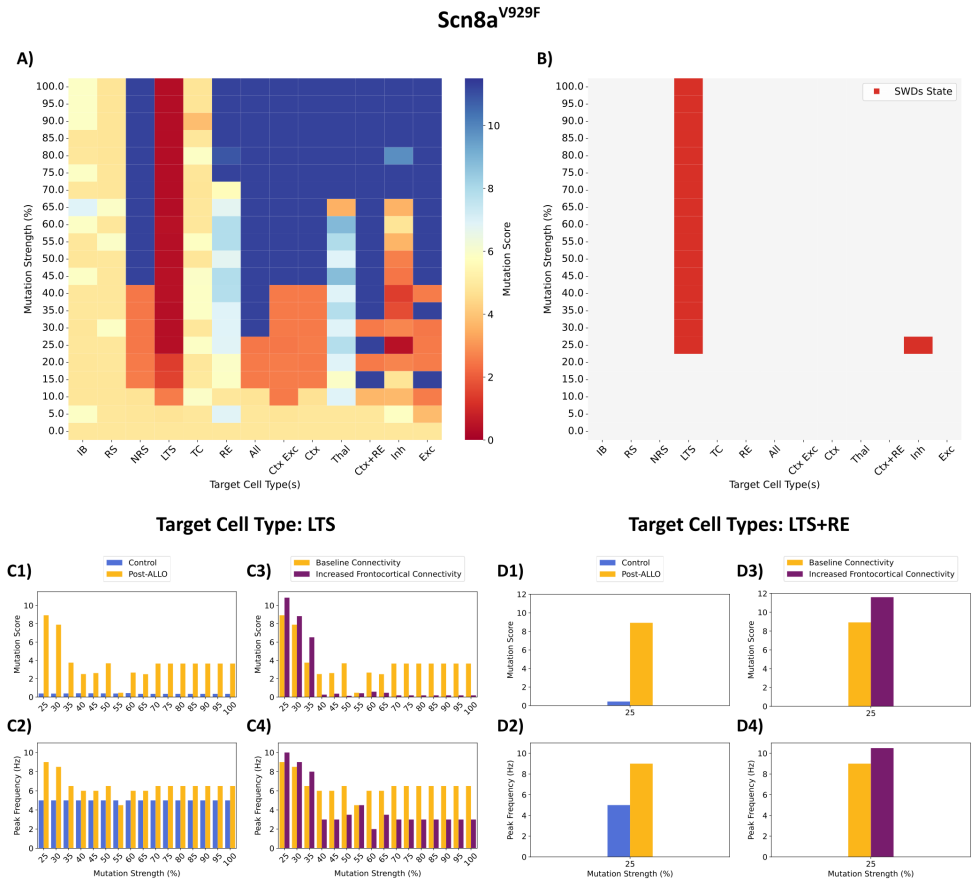

Figure 5.12: Effects of the $Scn8a^{V929F}$ mutation on network behaviour and response to allopregnanolone. (A): Mutation scores across different target cell types and mutation strengths up to 100%. Lower scores (red) indicate pathological activity, while higher scores (blue) indicate deviations away from this pattern. (B): Occurrence of spike-wave discharge (SWD) states, defined as network frequency between 2.5–5 Hz and maximal power within the SWD-associated frequency range. SWD states were observed when the target population included only LTS cells or both LTS and RE cells, at specific mutation strengths. (C1–C2, D1–D2): Comparison of mutation scores (C1, D1) and peak network frequency (C2, D2) between Control (blue) and post-ALLO (orange) conditions at varying mutation strengths during which the network exhibited an SWD state—when the target population consisted only of LTS cells (C1–C2) or both LTS and RE cells (D1–D2). (C3–C4, D3–D4): Comparison of mutation scores (C3, D3) and peak network frequency (C4, D4) between networks with frontocortical connectivity at baseline levels (orange) and increased levels (purple) for each corresponding target population group. The orange bars are identical to those shown in (C1–C2, D1–D2) for comparison.

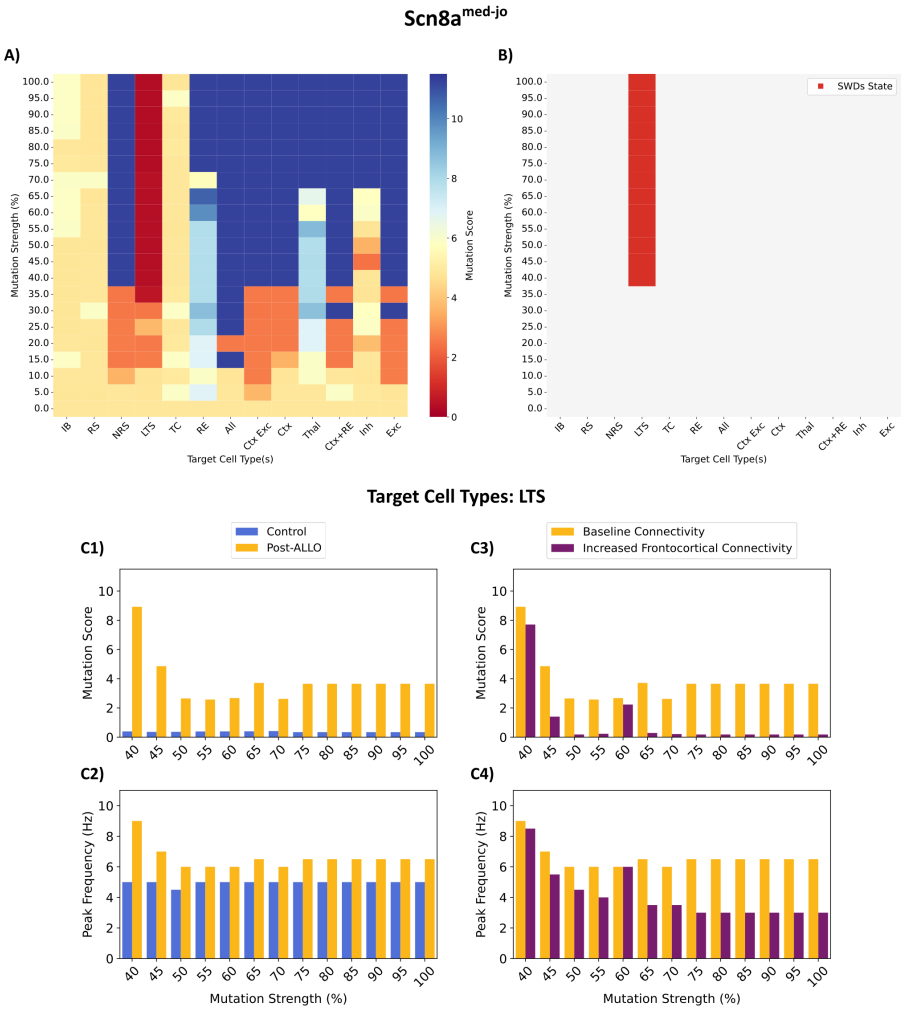

Figure 5.13: Effects of the $Scn8a^{med-jo}$ mutation on network behaviour and response to allopregnanolone. (A): Mutation scores across different target cell types and mutation strengths up to 100%. Lower scores (red) indicate pathological activity, while higher scores (blue) indicate deviations away from this pattern. (B): Occurrence of spike-wave discharge (SWD) states, defined as network frequency between 2.5–5 Hz and maximal power within the SWD-associated frequency range. (C1–C2): Comparison of mutation scores (C1) and peak network frequency (C2) between Control (blue) and post-ALLO (orange) conditions at varying mutation strengths during which the network exhibited a SWD state. (C3–C4): Comparison of mutation scores (C3) and peak network frequency (C4) between networks with frontocortical connectivity at baseline levels (orange) and increased levels (purple). The orange bars are identical to those shown in (C1–C2) for comparison.

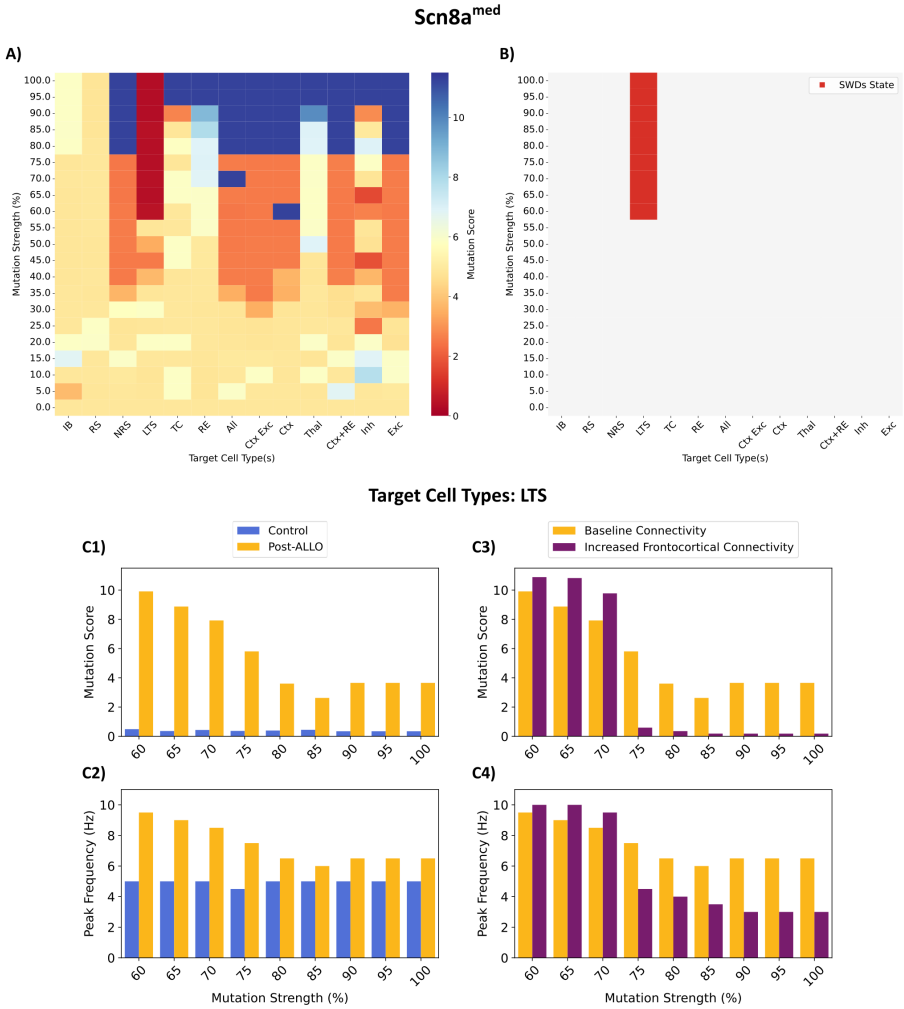

Figure 5.14: Effects of the $Scn8a^{med}$ mutation on network behaviour and response to allopregnanolone. (A): Mutation scores across different target cell types and mutation strengths up to 100%. Lower scores (red) indicate pathological activity, while higher scores (blue) indicate deviations away from this pattern. (B): Occurrence of spike-wave discharge (SWD) states, defined as network frequency between 2.5–5 Hz and maximal power within the SWD-associated frequency range. (C1–C2): Comparison of mutation scores (C1) and peak network frequency (C2) between Control (blue) and post-ALLO (orange) conditions at varying mutation strengths during which the network exhibited a SWD state. (C3–C4): Comparison of mutation scores (C3) and peak network frequency (C4) between networks with frontocortical connectivity at baseline levels (orange) and increased levels (purple). The orange bars are identical to those shown in (C1–C2) for comparison.

Chapter 6

Conclusions

Childhood absence epilepsy (CAE) represents a complex, multifactorial disorder characterized by brief episodes of loss of consciousness and distinctive 2.5–5 Hz spike-wave discharges (SWDs) on electroencephalography. One of the most intriguing aspects of CAE is its tendency toward disease remission during adolescence, a phenomenon that coincides with the onset of puberty. This temporal association suggests a potential role for sex hormones in the disease trajectory—a hypothesis that formed the foundation of this thesis. This thesis investigated the complex interplay between hormonal influences, genetic factors, and network connectivity in CAE, with particular emphasis on the mechanisms underlying disease remission. Our computational modelling approach bridged multiple scales—from molecular-level hormone effects to network-level pathological activity associated with absence seizures—to provide insights into this poorly understood phenomenon.

To begin our investigation into remission mechanisms, we first utilized a well-established computational model of the thalamocortical network exhibiting SWDs characteristic of CAE. By incorporating mutations in genes encoding GABAa receptors (causing cortical disinhibition) and low-threshold calcium channels, we successfully reproduced the pathological network activity associated with absence seizures. Given the known effects of allopregnanolone (ALLO), a neurosteroid metabolite of progesterone, in enhancing GABAa receptor-mediated inhibition, we modelled its impact on the network. Our results demonstrated that ALLO has an ameliorating effect on SWDs. Moreover, we observed that region-specific ALLO effects are consistent with the differential role of GABA across the thalamocortical network. These findings support the hypothesis that hormonal changes during puberty may contribute to disease remission in CAE patients.

Despite this promising mechanism for remission, the clinical reality shows that not

all patients experience remission despite undergoing pubertal hormonal changes, albeit to different degrees. This observation led us to investigate potential resistance factors to ALLO-mediated recovery. Drawing from literature suggesting pre-treatment connectivity differences between treatment responders and non-responders, we developed an enhanced thalamocortical model to distinguish between frontal and parietal cortical contributions. The development of this model presented significant challenges, including identifying appropriate model fitting parameters to ensure a valid model fit was possible. Even when network-level patterns appeared correct, abnormalities frequently emerged in individual neuronal firing patterns. Thus, our model fitting process required a principled approach with careful consideration of both the emergent network dynamics and the underlying neuronal behaviours. Our enhanced thalamocortical network incorporated layer 5 cortical neurons of the intrinsically bursting (IB) type to represent frontal cortical influence and regular spiking (RS) type to represent parietal cortical influence. We found no significant difference in the ability to generate and maintain SWDs between networks dominated by either IB or RS neurons, consistent with the concept of a cortical initiation network with different possible initiation sites. ALLO-mediated recovery occurred in both network configurations under baseline conditions. However, enhanced frontocortical connectivity—modelled by strengthening reciprocal synapses from IB neurons to cortical layer 6 and within the IB population—prevented ALLO-mediated recovery in networks with equal numbers of IB and RS neurons. Interestingly, networks with greater parietal influence (i.e., more RS neurons) maintained ALLO-mediated recovery even with enhanced frontocortical connectivity.

We extended our investigation to examine whether our findings applied to CAE caused by different genetic mechanisms, particularly mutations in sodium channel genes (i.e., $SCN2A$ and $SCN8A$). We modelled the effects of these mutations at the individual neuron level and examined the degree to which these alterations lead to network-level pathological activity, as well as the influence of ALLO on these genetically distinct networks. Our results demonstrated that ALLO facilitates recovery from SWDs regardless of the underlying mutation type. However, enhanced frontocortical connectivity prevents ALLO-mediated recovery in some mutation types, particularly when mutation effects are severe.

The computational framework developed in this thesis provides several important insights into CAE pathophysiology and remission. Our findings reinforce the complex, multifactorial nature of CAE remission, involving interactions between hormonal influences, genetic mutations, and synaptic connectivity patterns. The results suggest that certain genetic mutations may predispose individuals toward either remission or non-remission, with this predisposition further modulated by individual connectivity profiles. In particular, enhanced frontocortical connectivity appears to be a significant factor in resistance to hormone-mediated remission, which aligns with clinical observations of treatment non-

responders. From a therapeutic perspective, our findings highlight the potential value of considering both genetic profiles and connectivity patterns when formulating treatment strategies for CAE patients. The differential responses to ALLO based on network architecture suggest that personalized approaches may be necessary to optimize outcomes.

A notable limitation of our current work is the absence of antiepileptic drug effects in our models. Future research using this framework should incorporate pharmacological interventions to evaluate their impact on the mechanistic pathways we have identified. Additionally, this framework provides opportunities to investigate sex differences in CAE, particularly given the sexual dimorphism observed in generalized epilepsy disorders and the known sex-related variation in GABA receptor subunit composition across brain regions [105, 87, 62]. Beyond childhood absence epilepsy, our modelling approach has broader applicability to neurological conditions characterized by spontaneous shifts in brain dynamics. The framework can be adapted to leverage patient electrophysiology data across diverse neurological conditions, potentially incorporating patient-derived neuronal data to enable the emergence of pathological activity where individual neurons exhibit "diseased" behaviour [183, 152]. Ultimately, using such frameworks can be helpful in gaining insight on new therapeutic targets for specific neuronal dysfunctions, advancing personalized treatment approaches for epilepsy and related disorders.

In conclusion, this thesis presents a computational framework that bridges molecular, cellular, and network scales to investigate the mechanisms of remission in childhood absence epilepsy. Our findings highlight the multifactorial nature of CAE and provide insights into why some patients experience remission while others do not. By exploring the relationship between hormonal influences, genetic factors, and network connectivity, this work contributes to our understanding of disease remission in CAE, an aspect that has previously been underexplored. Additionally, our computational approaches not only advance our understanding of CAE specifically, but offer generalizable insights into the mathematical modelling of neurological conditions characterized by spontaneous shifts in brain dynamics.

References

[1] L. F. Abbott and P. Dayan. *Theoretical Neuroscience: Computational and Mathematical Modeling of Neural Systems*. MIT Press, Cambridge, Massachusetts, 2001.

[2] M. Ahmed. Model for a cortical circuit associated with childhood absence epilepsy. Master's thesis, University of Waterloo, 2019.

[3] M. Ahmed and S. A. Campbell. Modelling the effect of allopregnanolone on the resolution of spike-wave discharges. *Journal of Computational Neuroscience*, 53:115–130, 2024.

[4] D. J. Aidley. *The Physiology of Excitable Cells*. Cambridge University Press, 1998.

[5] M. J. Aminoff. Electroencephalography: general principles and clinical applications. In *Aminoff's Electrodiagnosis in Clinical Neurology*, pages 37–84. WB Saunders, 2012.

[6] J. D. Andersson, D. Matuskey, and S. J. Finnema. Positron emission tomography imaging of the γ-aminobutyric acid system. *Neuroscience Letters*, 691:35–43, 2019.

[7] S. Andjelic, T. Gallopin, B. Cauli, E. L. Hill, L. Roux, S. Badr, E. Hu, G. Tamás, and B. Lambolez. Glutamatergic nonpyramidal neurons from neocortical layer VI and their comparison with pyramidal and spiny stellate neurons. *Journal of Neurophysiology*, 101(2):641–654, 2009.

[8] T. Bal, D. Debay, and A. Destexhe. Cortical feedback controls the frequency and synchrony of oscillations in the visual thalamus. *Journal of Neuroscience*, 20(19):7478–7488, 2000.

[9] M. P. Beenhakker and J. R. Huguenard. Neurons that fire together also conspire together: is normal sleep circuitry hijacked to generate epilepsy? *Neuron*, 62(5):612–632, 2009.

[10] E. Beghi. The epidemiology of epilepsy. *Neuroepidemiology*, 54(2):185–191, 2020.

[11] E. Beghi, G. Giussani, and J. W. Sander. The natural history and prognosis of epilepsy. *Epileptic Disorders*, 17(3):243–253, 2015.

[12] D. Belelli and J. J. Lambert. Neurosteroids: endogenous regulators of the GABAA receptor. *Nature Reviews Neuroscience*, 6(7):565–575, 2005.

[13] A. T. Berg, S. R. Levy, F. M. Testa, and H. Blumenfeld. Long-term seizure remission in childhood absence epilepsy: might initial treatment matter? *Epilepsia*, 55(4):551–557, 2014.

[14] S. F. Berkovic, J. C. Mulley, I. E. Scheffer, and S. Petrou. Human epilepsies: interaction of genetic and acquired factors. *Trends in Neurosciences*, 29(7):391–397, 2006.

[15] M. T. Bianchi, L. Song, H. Zhang, and R. L. Macdonald. Two different mechanisms of disinhibition produced by GABAa receptor mutations linked to epilepsy in humans. *Journal of Neuroscience*, 22(13):5321–5327, 2002.

[16] H. Blumenfeld. The thalamus and seizures. *Archives of Neurology*, 59(1):135–137, 2002.

[17] H. Blumenfeld. Cellular and network mechanisms of spike-wave seizures. *Epilepsia*, 46:21–33, 2005.

[18] H. Blumenfeld, J. P. Klein, U. Schridde, M. Vestal, T. Rice, D. S. Khera, C. Bashyal, K. Giblin, C. Paul-Laughinghouse, F. Wang, et al. Early treatment suppresses the development of spike-wave epilepsy in a rat model. *Epilepsia*, 49(3):400–409, 2008.

[19] H. Blumenfeld and D. A. McCormick. Corticothalamic inputs control the pattern of activity generated in thalamocortical networks. *Journal of Neuroscience*, 20(13):5153–5162, 2000.

[20] F. S. Borges, J. V. S. Moreira, L. M. Takarabe, W. W. Lytton, and S. Dura-Bernal. Large-scale biophysically detailed model of somatosensory thalamocortical circuits in NetPyNE. *Frontiers in Neuroinformatics*, 16:884245, 2022.

[21] B. M. Bouwman, P. Suffczynski, I. S. Midzyanovskaya, E. Maris, P. L. C. van den Broek, and C. M. van Rijn. The effects of vigabatrin on spike and wave discharges in WAG/Rij rats. *Epilepsy Research*, 76(1):34–40, 2007.

[22] S. G. Brickley and I. Mody. Extrasynaptic GABAA receptors: their function in the CNS and implications for disease. *Neuron*, 73(1):23–34, 2012.

[23] R. D. Brinton, R. F. Thompson, M. R. Foy, M. Baudry, J. Wang, C. E. Finch, T. E. Morgan, C. J. Pike, W. J. Mack, F. Z. Stanczyk, et al. Progesterone receptors: form and function in brain. *Frontiers in Neuroendocrinology*, 29(2):313–339, 2008.

[24] E. B. Bromfield, J. E. Cavazos, and J. I. Sirven. Basic mechanisms underlying seizures and epilepsy. In *An Introduction to Epilepsy [Internet]*. American Epilepsy Society, 2006.

[25] A. G. Brown. *Nerve Cells and Nervous Systems: An Introduction to Neuroscience.* Springer, London, 2001.

[26] B. Budziszewska, G. van Luijtelaar, A. M. L. Coenen, M. Leśkiewicz, and W. Lasoń. Effects of neurosteroids on spike-wave discharges in the genetic epileptic WAG/Rij rat. *Epilepsy Research*, 33(1):23–29, 1999.

[27] J. H. Byrne, R. Heidelberger, and M. N. Waxham. *From Molecules to Networks: An Introduction to Cellular and Molecular Neuroscience*. Academic Press, 2014.

[28] S. M. Cain, J. R. Tyson, H. B. Choi, R. Ko, P. J. C. Lin, J. M. LeDue, K. L. Powell, L. P. Bernier, R. L. Rungta, Y. Yang, et al. Cav3.2 drives sustained burst-firing, which is critical for absence seizure propagation in reticular thalamic neurons. *Epilepsia*, 59(4):778–791, 2018.

[29] L. Canafoglia, M. S. Dettori, D. Duran, F. Ragona, E. Freri, S. Casellato, T. Granata, S. Franceschetti, and F. Panzica. Early clinical and EEG findings associated with the outcome in childhood absence epilepsy. *Epilepsy & Behavior*, 98:273–278, 2019.

[30] N. T. Carnevale and M. L. Hines. *The NEURON Book*. Cambridge University Press, 2006.

[31] M. A. Castro-Alamancos. Neocortical synchronized oscillations induced by thalamic disinhibition in vivo. *The Journal of Neuroscience*, 19(18):RC27, 1999.

[32] Y. Chagnac-Amitai, H. J. Luhmann, and D. A. Prince. Burst generating and regular spiking layer 5 pyramidal neurons of rat neocortex have different morphological features. *Journal of Comparative Neurology*, 296(4):598–613, 1990.

[33] L. Chen and S. A. Campbell. Population dynamics in networks of izhikevich neurons with global delayed coupling. *SIAM Journal on Applied Dynamical Systems*, 23(3):2293–2322, 2024.

[34] Y. Chen, W. D. Parker, and K. Wang. The role of T-type calcium channel genes in absence seizures. *Frontiers in Neurology*, 5:45, 2014.

[35] N. Chourasia, H. Ossó-Rivera, A. Ghosh, G. Von Allmen, and M. K. Koenig. Expanding the phenotypic spectrum of CACNA1H mutations. *Pediatric Neurology*, 93:50–55, 2019.

[36] A. M. L. Coenen and E. L. J. M. van Luijtelaar. Genetic animal models for absence epilepsy: a review of the WAG/Rij strain of rats. *Behavior Genetics*, 33(6):635–655, 2003.

[37] D. W. Cope, G. Di Giovanni, S. J. Fyson, G. Orbán, A. C. Errington, M. L. Lőrincz, T. M. Gould, D. A. Carter, and V. Crunelli. Enhanced tonic GABAa inhibition in typical absence epilepsy. *Nature Medicine*, 15(12):1392–1398, 2009.

[38] V. Crunelli and N. Leresche. Childhood absence epilepsy: genes, channels, neurons and networks. *Nature Reviews Neuroscience*, 3(5):371–382, 2002.

[39] V. Crunelli, M. L. Lőrincz, C. McCafferty, R. C. Lambert, N. Leresche, G. Di Giovanni, and F. David. Clinical and experimental insight into pathophysiology, comorbidity and therapy of absence seizures. *Brain*, 143(8):2341–2368, 2020.

[40] S. P. Currie, L. L. Luz, S. A. Booker, D. J. A. Wyllie, P. C. Kind, and M. I. Daw. Reduced local input to fast-spiking interneurons in the somatosensory cortex in the GABAa γ2 R43Q mouse model of absence epilepsy. *Epilepsia*, 58(4):597–607, 2017.

[41] L. Danober, C. Deransart, A. Depaulis, M. Vergnes, and C. Marescaux. Pathophysiological mechanisms of genetic absence epilepsy in the rat. *Progress in Neurobiology*, 55(1):27–57, 1998.

[42] M. D'antuono, Y. Inaba, G. Biagini, G. D'arcangelo, V. Tancredi, and M. Avoli. Synaptic hyperexcitability of deep layer neocortical cells in a genetic model of absence seizures. *Genes, Brain and Behavior*, 5(1):73–84, 2006.

[43] J. DeFelipe, L. Alonso-Nanclares, and J. I. Arellano. Microstructure of the neocortex: comparative aspects. *Journal of Neurocytology*, 31:299–316, 2002.

[44] B. J. Delgado and W. Lopez-Ojeda. Estrogen. In *StatPearls [Internet]*. StatPearls Publishing, 2021.

[45] A. Depaulis and S. Charpier. Pathophysiology of absence epilepsy: insights from genetic models. *Neuroscience Letters*, 667:53–65, 2018.

[46] A. Destexhe. Spike-and-wave oscillations based on the properties of GABAB receptors. *Journal of Neuroscience*, 18(21):9099–9111, 1998.

[47] A. Destexhe, A. Babloyantz, and T. J. Sejnowski. Ionic mechanisms for intrinsic slow oscillations in thalamic relay neurons. *Biophysical Journal*, 65(4):1538–1552, 1993.

[48] A. Destexhe, T. Bal, D. A. McCormick, and T. J. Sejnowski. Ionic mechanisms underlying synchronized oscillations and propagating waves in a model of ferret thalamic slices. *Journal of Neurophysiology*, 76(3):2049–2070, 1996.

[49] A. Destexhe, D. Contreras, and M. Steriade. Mechanisms underlying the synchronizing action of corticothalamic feedback through inhibition of thalamic relay cells. *Journal of Neurophysiology*, 79(2):999–1016, 1998.

[50] A. Destexhe, D. Contreras, M. Steriade, T. J. Sejnowski, and J. R. Huguenard. In vivo, in vitro, and computational analysis of dendritic calcium currents in thalamic reticular neurons. *Journal of Neuroscience*, 16(1):169–185, 1996.

[51] A. Destexhe, Z. F. Mainen, and T. J. Sejnowski. Synthesis of models for excitable membranes, synaptic transmission and neuromodulation using a common kinetic formalism. *Journal of Computational Neuroscience*, 1(3):195–230, 1994.

[52] A. Destexhe, Z. F Mainen, T. J. Sejnowski, et al. Kinetic models of synaptic transmission. *Methods in Neuronal Modeling*, 2:1–25, 1998.

[53] A. Destexhe, D. A. McCormick, and T. J. Sejnowski. Thalamic and thalamocortical mechanisms underlying 3 Hz spike-and-wave discharges. *Progress in Brain Research*, 121:289–307, 1999.

[54] G. Dezsi, E. Ozturk, D. Stanic, K. L. Powell, H. Blumenfeld, T. J. O'Brien, and N. C. Jones. Ethosuximide reduces epileptogenesis and behavioral comorbidity in the GAERS model of genetic generalized epilepsy. *Epilepsia*, 54(4):635–643, 2013.

[55] S. Diviccaro, L. Cioffi, E. Falvo, S. Giatti, and R. C. Melcangi. Allopregnanolone: An overview on its synthesis and effects. *Journal of Neuroendocrinology*, 34(2):e12996, 2022.

[56] J. E. Dowling. *Neurons and Networks: An Introduction to Behavioral Neuroscience*. Harvard University Press, 2001.

[57] J. Du, S. Simmons, A. Brunklaus, X. Adiconis, C. C. Hession, Z. Fu, Y. Li, R. Shema, R. S. Møller, B. Barak, et al. Differential excitatory vs inhibitory SCN expression at single cell level regulates brain sodium channel function in neurodevelopmental disorders. *European Journal of Paediatric Neurology*, 24:129–133, 2020.

[58] S. Dura-Bernal, B. A. Suter, P. Gleeson, M. Cantarelli, A. Quintana, F. Rodriguez, D. J. Kedziora, G. L. Chadderdon, C. C. Kerr, S. A. Neymotin, et al. NetPyNE, a tool for data-driven multiscale modeling of brain circuits. *Elife*, 8:e44494, 2019.

[59] M. C. D'adamo, A. Liantonio, J. F. Rolland, M. Pessia, and P. Imbrici. Kv1.1 channelopathies: pathophysiological mechanisms and therapeutic approaches. *International Journal of Molecular Sciences*, 21(8):2935, 2020.

[60] International League Against Epilepsy. Seizure classification. https://www.epilepsydiagnosis.org/seizure/seizure-classification-groupoverview.html, n.d.

[61] G. B. Ermentrout and D. H. Terman. *Mathematical Foundations of Neuroscience*, chapter Synaptic Channels, pages 157–170. Springer New York, 2010.

[62] J. Ethiraj, T. H. Palpagama, C. Turner, B. van der Werf, H. J. Waldvogel, R. L. M. Faull, and A. Kwakowsky. The effect of age and sex on the expression of GABA signaling components in the human hippocampus and entorhinal cortex. *Scientific Reports*, 11(1):21470, 2021.

[63] M. Fadalti, F. Petraglia, S. Luisi, F. Bernardi, E. Casarosa, E. Ferrari, M. Luisi, G. Saggese, A. R. Genazzani, and S. Bernasconi. Changes of serum allopregnanolone levels in the first 2 years of life and during pubertal development. *Pediatric Research*, 46(3):323–327, 1999.

[64] B. Fischl and A. M. Dale. Measuring the thickness of the human cerebral cortex from magnetic resonance images. *Proceedings of the National Academy of Sciences*, 97(20):11050–11055, 2000.

[65] R. FitzHugh. Impulses and physiological states in theoretical models of nerve membrane. *Biophysical Journal*, 1(6):445–466, 1961.

[66] N. Foldvary-Schaefer and T. Falcone. Catamenial epilepsy: pathophysiology, diagnosis, and management. *Neurology*, 61(6 suppl 2):S2–S15, 2003.

[67] G. C. Y. Fong, P. U. Shah, M. N. Gee, J. M. Serratosa, I. P. Castroviejo, S. Khan, S. H. Ravat, J. Mani, Y. Huang, H. Z. Zhao, et al. Childhood absence epilepsy with tonic-clonic seizures and electroencephalogram 3–4-Hz spike and multispike–slow wave complexes: Linkage to chromosome 8q24. *The American Journal of Human Genetics*, 63(4):1117–1129, 1998.

[68] T. Freund and S. Kali. Interneurons. *Scholarpedia*, 3(9):4720, 2008.

[69] C. A. Frye, C. J. Koonce, and A. A. Walf. Novel receptor targets for production and action of allopregnanolone in the central nervous system: a focus on pregnane xenobiotic receptor. *Frontiers in Cellular Neuroscience*, 8:106, 2014.

[70] X. Fu, Y. J. Wang, J. Q. Kang, and T. W. Mu. GABAa receptor variants in epilepsy. *Epilepsy [Internet]*, 2022.

[71] E. V. Gazina, K. L. Richards, M. B. C. Mokhtar, E. A. Thomas, C. A. Reid, and S. Petrou. Differential expression of exon 5 splice variants of sodium channel α subunit mRNAs in the developing mouse brain. *Neuroscience*, 166(1):195–200, 2010.

[72] Y. Ge, Y. Cao, G. Yi, C. Han, Y. Qin, J. Wang, and Y. Che. Robust closed-loop control of spike-and-wave discharges in a thalamocortical computational model of absence epilepsy. *Scientific Reports*, 9(1):9093, 2019.

[73] A. Ghoumari, J. P. Oudinet, P. Liere, and R. Guennoun. Revisiting the roles of progesterone and allopregnanolone in the nervous system: resurgence of the progesterone receptors. *Progress in Neurobiology*, 113:6–39, 2014.

[74] T. A. Glauser, K. Holland, V. P. O'Brien, M. Keddache, L. J. Martin, P. O. Clark, A. Cnaan, D. Dlugos, D. G. Hirtz, S. Shinnar, et al. Pharmacogenetics of antiepileptic drug efficacy in childhood absence epilepsy. *Annals of Neurology*, 81(3):444–453, 2017.

[75] P. Gloor. Generalized epilepsy with bilateral synchronous spike and wave discharge. New findings concerning its physiological mechanisms. *Electroencephalography and Clinical neurophysiology. Supplement*, (34):245–249, 1978.

[76] D. Golomb and J. Rinzel. Dynamics of globally coupled inhibitory neurons with heterogeneity. *Physical Review E*, 48(6):4810, 1993.

[77] D. Golomb and J. Rinzel. Clustering in globally coupled inhibitory neurons. *Physica D: Nonlinear Phenomena*, 72(3):259–282, 1994.

[78] D. Golomb, X. J. Wang, and J. Rinzel. Synchronization properties of spindle oscillations in a thalamic reticular nucleus model. *Journal of Neurophysiology*, 72(3):1109–1126, 1994.

[79] R. A. Grünewald, V. Aliberti, and C. P. Panayiotopoulos. Exacerbation of typical absence seizures by progesterone. *Seizure*, 1(2):137–138, 1992.

[80] R. Guennoun. Progesterone in the brain: hormone, neurosteroid and neuroprotectant. *International Journal of Molecular Sciences*, 21(15):5271, 2020.

[81] J. A. Harris, S. Mihalas, K. E. Hirokawa, J. D. Whitesell, H. Choi, A. Bernard, P. Bohn, S. Caldejon, L. Casal, A. Cho, et al. Hierarchical organization of cortical and thalamic connectivity. *Nature*, 575(7781):195–202, 2019.

[82] M. Häusser. The Hodgkin-Huxley theory of the action potential. *Nature Neuroscience*, 3(11):1165–1165, 2000.

[83] P. Hertoft. The clinical, electroencephalographic and social prognosis in petit mai epilepsy. *Epilepsia*, 4(1-4):298–314, 1963.

[84] E. Hirsch, J. French, I. E. Scheffer, A. Bogacz, T. Alsaadi, M. R. Sperling, F. Abdulla, S. M. Zuberi, E. Trinka, Nicola Specchio, et al. ILAE definition of the idiopathic generalized epilepsy syndromes: position statement by the ILAE task force on nosology and definitions. *Epilepsia*, 63(6):1475–1499, 2022.

[85] A. L. Hodgkin and A. F. Huxley. A quantitative description of membrane current and its application to conduction and excitation in nerve. *The Journal of Physiology*, 117(4):500, 1952.

[86] A. B. Holt and T. I. Netoff. Computational modeling of epilepsy for an experimental neurologist. *Experimental Neurology*, 244:75–86, 2013.

[87] J. R. Hughes. Absence seizures: a review of recent reports with new concepts. *Epilepsy & Behavior*, 15(4):404–412, 2009.

[88] J. R. Huguenard and D. A. McCormick. Simulation of the currents involved in rhythmic oscillations in thalamic relay neurons. *Journal of Neurophysiology*, 68(4):1373–1383, 1992.

[89] J. R. Huguenard and D. A. Prince. Slow inactivation of a TEA-sensitive K current in acutely isolated rat thalamic relay neurons. *Journal of Neurophysiology*, 66(4):1316–1328, 1991.

[90] I. B. Iotchev and E. Kubinyi. Shared and unique features of mammalian sleep spindles–insights from new and old animal models. *Biological Reviews*, 96(3):1021–1034, 2021.

[91] E. M. Izhikevich. Simple model of spiking neurons. *IEEE Transactions on Neural Networks*, 14(6):1569–1572, 2003.

[92] E. M. Izhikevich. *Dynamical Systems in Neuroscience: The Geometry of Excitability and Bursting*. MIT Press, Cambridge, Massachusetts, 2007.

[93] E. M. Izhikevich and G. M. Edelman. Large-scale model of mammalian thalamocortical systems. *Proceedings of the National Academy of Sciences*, 105(9):3593–3598, 2008.

[94] R. B. Jacobsen, D. Ulrich, and H. R. Huguenard. GABAB and NMDA receptors contribute to spindle-like oscillations in rat thalamus in vitro. *Journal of Neurophysiology*, 86(3):1365–1375, 2001.

[95] M. Jafarian, M. E. Alipour, and F. Karimzadeh. Experimental models of absence epilepsy. *Basic and Clinical Neuroscience*, 11(6):715, 2020.

[96] K. Javed, V. Reddy, and F. Lui. Neuroanatomy, cerebral cortex. In *StatPearls [Internet]*. StatPearls Publishing, 2023.

[97] D. Johnston and S. M. Wu. *Foundations of Cellular Neurophysiology*. MIT Press, 1994.

[98] E. R. Kandel, J. H. Schwartz, T. M. Jessell, S. Siegelbaum, A. J. Hudspeth, S. Mack, et al. *Principles of Neural Science*, volume 4. McGraw-Hill New York, 2000.

[99] J. Kang and R. L. Macdonald. The GABAa receptor $\gamma 2$ subunit R43Q mutation linked to childhood absence epilepsy and febrile seizures causes retention of $\alpha 1\beta 2\gamma 2$s receptors in the endoplasmic reticulum. *Journal of Neuroscience*, 24(40):8672–8677, 2004.

[100] M. H. Kelley, M. Kuroiwa, N. Taguchi, and P. S. Herson. Sex difference in sensitivity to allopregnanolone neuroprotection in mice correlates with effect on spontaneous inhibitory post synaptic currents. *Neuropharmacology*, 61(4):724–729, 2011.

[101] W. Kelsch, C. W. Lin, and C. Lois. Sequential development of synapses in dendritic domains during adult neurogenesis. *Proceedings of the National Academy of Sciences*, 105(43):16803–16808, 2008.

[102] C. C. Kerr, D. J. O'Shea, W. Goo, S. Dura-Bernal, J. T. Francis, I. Diester, P. Kalanithi, K. Deisseroth, K. V. Shenoy, and W. W. Lytton. Network-level effects of optogenetic stimulation in a computer model of macaque primary motor cortex. *BMC Neuroscience*, 15:1–2, 2014.

[103] S. K. Kessler and E. McGinnis. A practical guide to treatment of childhood absence epilepsy. *Pediatric Drugs*, 21:15–24, 2019.

[104] E. H. Kim, W. H. Shim, J. S. Lee, H. M. Yoon, T. S. Ko, and M. S. Yum. Altered structural network in newly onset childhood absence epilepsy. *Journal of Clinical Neurology*, 16(4):573, 2020.

[105] H. R. Kim, G. H. Kim, S. H. Eun, B. L. Eun, and J. H. Byeon. Therapeutic outcomes and prognostic factors in childhood absence epilepsy. *Journal of Clinical Neurology*, 12(2):160–165, 2016.

[106] A. T. Knox, T. Glauser, J. Tenney, W. W. Lytton, and K. Holland. Modeling pathogenesis and treatment response in childhood absence epilepsy. *Epilepsia*, 59(1):135–145, 2018.

[107] D. C. Kohrman, J. B. Harris, and M. H. Meisler. Mutation detection in the med and medj alleles of the sodium channel SCN8A. unusual splicing due to a minor class AT-AC intron. *Journal of Biological Chemistry*, 271(29):17576–17581, 1996.

[108] D. C. Kohrman, M. R. Smith, A. L. Goldin, J. Harris, and M. H. Meisler. A missense mutation in the sodium channel SCN8A is responsible for cerebellar ataxia in the mouse mutant jolting. *Journal of Neuroscience*, 16(19):5993–5999, 1996.

[109] M. H. P. Kole, A. U. Bräuer, and G. J. Stuart. Inherited cortical HCN1 channel loss amplifies dendritic calcium electrogenesis and burst firing in a rat absence epilepsy model. *The Journal of Physiology*, 578(2):507–525, 2007.

[110] G. K. Kostopoulos. Spike-and-wave discharges of absence seizures as a transformation of sleep spindles: the continuing development of a hypothesis. *Clinical Neurophysiology*, 111:S27–S38, 2000.

[111] E. Kudova. Rapid effects of neurosteroids on neuronal plasticity and their physiological and pathological implications. *Neuroscience Letters*, 750:135771, 2021.

[112] J. S. Kumar and P. Bhuvaneswari. Analysis of electroencephalography (EEG) signals and its categorization–a study. *Procedia Engineering*, 38:2525–2536, 2012.

[113] P. Kwan and J. W. Sander. The natural history of epilepsy: an epidemiological view. *Journal of Neurology, Neurosurgery & Psychiatry*, 75(10):1376–1381, 2004.

[114] J. J. Lambert, M. A. Cooper, R. D. J. Simmons, C. J. Weir, and D. Belelli. Neurosteroids: endogenous allosteric modulators of GABAA receptors. *Psychoneuroendocrinology*, 34:S48–S58, 2009.

[115] K. M. Lenz and M. M. McCarthy. A starring role for microglia in brain sex differences. *The Neuroscientist*, 21(3):306–321, 2015.

[116] A. Leo, C. De Caro, V. Nesci, E. Palma, M. Tallarico, M. Iannone, A. Constanti, G. De Sarro, E. Russo, and R. Citraro. Antiepileptogenic effects of ethosuximide and levetiracetam in WAG/Rij rats are only temporary. *Pharmacological Reports*, 71:833–838, 2019.

[117] I. B. Levitan and L. K. Kaczmarek. *The Neuron: Cell and Molecular Biology*. Oxford University Press, USA, 2002.

[118] S. Li, J. Zhang, J. Li, Y. Hu, M. Zhang, and H. Wang. Optogenetics and chemogenetics: key tools for modulating neural circuits in rodent models of depression. *Frontiers in Neural Circuits*, 19:1516839, 2025.

[119] Z. Liu, M. Vergnes, A. Depaulis, and C. Marescaux. Evidence for a critical role of GABAergic transmission within the thalamus in the genesis and control of absence seizures in the rat. *Brain Research*, 545(1-2):1–7, 1991.

[120] R. Llinás, F. J. Urbano, E. Leznik, R. R. Ramírez, and H. J. F. Van Marle. Rhythmic and dysrhythmic thalamocortical dynamics: GABA systems and the edge effect. *Trends in Neurosciences*, 28(6):325–333, 2005.

[121] X. Lu, P. Lambert, A. Benz, C. F. Zorumski, and S. J. Mennerick. Allopregnanolone effects on inhibition in hippocampal parvalbumin interneurons. *eNeuro*, 10(3), 2023.

[122] A. Ludwig, T. Budde, J. Stieber, S. Moosmang, C. Wahl, K. Holthoff, A. Langebartels, C. Wotjak, T. Munsch, X. Zong, et al. Absence epilepsy and sinus dysrhythmia

in mice lacking the pacemaker channel HCN2. *The EMBO Journal*, 22(2):216–224, 2003.

[123] H. J. Luhmann, T. Mittmann, G. van Luijtelaar, and U. Heinemann. Impairment of intracortical GABAergic inhibition in a rat model of absence epilepsy. *Epilepsy Research*, 22(1):43–51, 1995.

[124] W. W. Lytton, A. Destexhe, and T. J. Sejnowski. Control of slow oscillations in the thalamocortical neuron: a computer model. *Neuroscience*, 70(3):673–684, 1996.

[125] R. L. Macdonald, J. Q. Kang, and M. J. Gallagher. Mutations in GABAa receptor subunits associated with genetic epilepsies. *The Journal of Physiology*, 588(11):1861–1869, 2010.

[126] R. K. Maganti and P. Rutecki. EEG and epilepsy monitoring. *CONTINUUM: Lifelong Learning in Neurology*, 19(3):598–622, 2013.

[127] M. D. Majewska, N. L. Harrison, R. D. Schwartz, J. L. Barker, and S. M. Paul. Steroid hormone metabolites are barbiturate-like modulators of the GABA receptor. *Science*, 232(4753):1004–1007, 1986.

[128] C. D. Makinson, B. S. Tanaka, J. M. Sorokin, J. C. Wong, C. A. Christian, A. L. Goldin, A. Escayg, and J. R. Huguenard. Regulation of thalamic and cortical network synchrony by SCN8A. *Neuron*, 93(5):1165–1179, 2017.

[129] A. Marin-Burgin, F. J. Eisenhart, S. M. Baca, W. B. Kristan, and K. A. French. Sequential development of electrical and chemical synaptic connections generates a specific behavioral circuit in the leech. *Journal of Neuroscience*, 25(10):2478–2489, 2005.

[130] C. Marini, L. A. Harkin, R. H. Wallace, J. C. Mulley, I. E. Scheffer, and S. F. Berkovic. Childhood absence epilepsy and febrile seizures: a family with a GABAa receptor mutation. *Brain*, 126(1):230–240, 2003.

[131] H. Markram, M. Toledo-Rodriguez, Y. Wang, A. Gupta, G. Silberberg, and C. Wu. Interneurons of the neocortical inhibitory system. *Nature Reviews Neuroscience*, 5(10):793–807, 2004.

[132] M. S. Martin, B. Tang, L. A. Papale, F. H. Yu, W. A. Catterall, and A. Escayg. The voltage-gated sodium channel SCN8A is a genetic modifier of severe myoclonic epilepsy of infancy. *Human Molecular Genetics*, 16(23):2892–2899, 2007.

[133] M. Martina and P. Jonas. Functional differences in Na^+ channel gating between fast-spiking interneurones and principal neurones of rat hippocampus. *The Journal of Physiology*, 505(Pt 3):593, 1997.

[134] A. Mason and A. Larkman. Correlations between morphology and electrophysiology of pyramidal neurons in slices of rat visual cortex. II. Electrophysiology. *Journal of Neuroscience*, 10(5):1415–1428, 1990.

[135] R. A. J. Masterton, P. W. Carney, D. F. Abbott, and G. D. Jackson. Absence epilepsy subnetworks revealed by event-related independent components analysis of functional magnetic resonance imaging. *Epilepsia*, 54(5):801–808, 2013.

[136] S. Matricardi, A. Verrotti, F. Chiarelli, C. Cerminara, and P. Curatolo. Current advances in childhood absence epilepsy. *Pediatric Neurology*, 50(3):205–212, 2014.

[137] D. A. McCormick, B. W. Connors, J. W. Lighthall, and D. A. Prince. Comparative electrophysiology of pyramidal and sparsely spiny stellate neurons of the neocortex. *Journal of Neurophysiology*, 54(4):782–806, 1985.

[138] D. A. McCormick and J. R. Huguenard. A model of the electrophysiological properties of thalamocortical relay neurons. *Journal of Neurophysiology*, 68(4):1384–1400, 1992.

[139] D. A. McCormick, Z. Wang, and J. Huguenard. Neurotransmitter control of neocortical neuronal activity and excitability. *Cerebral Cortex*, 3(5):387–398, 1993.

[140] H. Meeren, G. van Luijtelaar, F. L. da Silva, and A. Coenen. Evolving concepts on the pathophysiology of absence seizures: the cortical focus theory. *Archives of Neurology*, 62(3):371–376, 2005.

[141] H. K. M. Meeren, J. P. M. Pijn, E. L. J. M. van Luijtelaar, A. M. L. Coenen, and F. H. L. da Silva. Cortical focus drives widespread corticothalamic networks during spontaneous absence seizures in rats. *Journal of Neuroscience*, 22(4):1480–1495, 2002.

[142] S. Meltzer-Brody and S. J. Kanes. Allopregnanolone in postpartum depression: Role in pathophysiology and treatment. *Neurobiology of Stress*, 12:100212, 2020.

[143] V. Michopoulos, M. Embree, K. Reding, M. M. Sanchez, D. Toufexis, J. R. Votaw, R. J. Voll, M. M. Goodman, J. Rivier, M. E. Wilson, et al. CRH receptor antagonism reverses the effect of social subordination upon central GABAA receptor binding in

estradiol-treated ovariectomized female rhesus monkeys. *Neuroscience*, 250:300–308, 2013.

[144] T. A. Milligan. Epilepsy: a clinical overview. *The American Journal of Medicine*, 134(7):840–847, 2021.

[145] A. S. Mitchell, N. Leresche, and V. Crunelli. Corticothalamic network abnormalities underlying absence seizures. In *The Cerebral Cortex and Thalamus*. Oxford University Press, 12 2023.

[146] R. Moraga-Amaro, A. Van Waarde, J. Doorduin, and E. F. J. De Vries. Sex steroid hormones and brain function: PET imaging as a tool for research. *Journal of Neuroendocrinology*, 30(2):e12565, 2018.

[147] C. Morris and H. Lecar. Voltage oscillations in the barnacle giant muscle fiber. *Biophysical Journal*, 35(1):193–213, 1981.

[148] E. Morse, K. Giblin, M. H. Chung, C. Dohle, A. T. Berg, and H. Blumenfeld. Historical trend toward improved long-term outcome in childhood absence epilepsy. *Epilepsy Research*, 152:7–10, 2019.

[149] J. W. Mozrzymas, E. D. Żarmowska, M. Pytel, and K. Mercik. Modulation of GABAA receptors by hydrogen ions reveals synaptic GABA transient and a crucial role of the desensitization process. *Journal of Neuroscience*, 23(22):7981–7992, 2003.

[150] J. Nagumo, S. Arimoto, and S. Yoshizawa. An active pulse transmission line simulating nerve axon. *Proceedings of the IRE*, 50(10):2061–2070, 1962.

[151] National Human Genome Research Institute. Genetics glossary. National Institutes of Health, U.S. Department of Health and Human Services, n.d.

[152] B. Ng, H. A. Rowland, T. Wei, K. Arunasalam, E. M. Hayes, I. Koychev, A. Hedegaard, E. M. Ribe, D. Chan, T. Chessell, et al. Neurons derived from individual early alzheimer's disease patients reflect their clinical vulnerability. *Brain Communications*, 4(6):fcac267, 2022.

[153] J. J. Nieto-Barcelo, N. G. Montes, I. G. Alonso, F. Martinez, M. J. Aparisi, M. Martinez-Matilla, A. V. M. Hernandez, and M. T. Vila. Variant in CACNA1G as a possible genetic modifier of neonatal epilepsy in an infant with a de novo SCN2A mutation. *Journal of Pediatric Genetics*, 12(02):159–162, 2023.

[154] M. Nørgaard, V. Beliveau, M. Ganz, C. Svarer, L. H. Pinborg, S. H. Keller, P. S. Jensen, D. N. Greve, and G. M. Knudsen. A high-resolution in vivo atlas of the human brain's benzodiazepine binding site of GABAA receptors. *NeuroImage*, 232:117878, 2021.

[155] I. Ogiwara, H. Miyamoto, T. Tatsukawa, T. Yamagata, T. Nakayama, N. Atapour, E. Miura, E. Mazaki, S. J. Ernst, D. Cao, et al. Nav1.2 haplodeficiency in excitatory neurons causes absence-like seizures in mice. *Communications Biology*, 1(1):96, 2018.

[156] M. K. Oliva, T. C. McGarr, B. J. Beyer, E. Gazina, D. I. Kaplan, L. Cordeiro, E. Thomas, S. D. Dib-Hajj, S. G. Waxman, W. N. Frankel, et al. Physiological and genetic analysis of multiple sodium channel variants in a model of genetic absence epilepsy. *Neurobiology of Disease*, 67:180–190, 2014.

[157] L. S. Overstreet, G. L. Westbrook, and M. V. Jones. Measuring and modeling the spatiotemporal profile of GABA at the synapse. *Transmembrane Transporters*, pages 259–275, 2002.

[158] G. Paal. Catamnestic studies & EEG in pyknolepsy. *Archiv fur Psychiatrie und Nervenkrankheiten, Vereinigt mit Zeitschrift fur die Gesamte Neurologie und Psychiatrie*, 196(1):48–62, 1957.

[159] M. Papadopoulou, M. Leite, P. van Mierlo, K. Vonck, L. Lemieux, K. Friston, and D. Marinazzo. Tracking slow modulations in synaptic gain using dynamic causal modelling: validation in epilepsy. *NeuroImage*, 107:117–126, 2015.

[160] L. A. Papale, B. Beyer, J. M. Jones, L. M. Sharkey, S. Tufik, M. Epstein, V. A. Letts, M. H. Meisler, W. N. Frankel, and A. Escayg. Heterozygous mutations of the voltage-gated sodium channel SCN8A are associated with spike-wave discharges and absence epilepsy in mice. *Human Molecular Genetics*, 18(9):1633–1641, 2009.

[161] M. A. Patestas and L. P. Gartner. *A Textbook of Neuroanatomy*. John Wiley & Sons, 2016.

[162] S. M. Paul and R. H. Purdy. Neuroactive steroids. *The FASEB Journal*, 6(6):2311–2322, 1992.

[163] B. W. M. M. Peeters, C. M. Van Rijn, J. M. H. Vossen, and A. M. L. Coenen. Effects of GABA-ergic agents on spontaneous non-convulsive epilepsy, EEG and behaviour, in the WAG/Rij inbred strain of rats. *Life Sciences*, 45(13):1171–1176, 1989.

[164] D. Pinault, N. Leresche, S. Charpier, J. M. Deniau, C. Marescaux, M. Vergnes, and V. Crunelli. Intracellular recordings in thalamic neurones during spontaneous spike and wave discharges in rats with absence epilepsy. *The Journal of Physiology*, 509(2):449–456, 1998.

[165] G. Pinna, V. Uzunova, K. Matsumoto, G. Puia, J. M. Mienville, E. Costa, and A. Guidotti. Brain allopregnanolone regulates the potency of the GABAA receptor agonist muscimol. *Neuropharmacology*, 39(3):440–448, 2000.

[166] A. Pitkänen and T. P. Sutula. Is epilepsy a progressive disorder? Prospects for new therapeutic approaches in temporal-lobe epilepsy. *The Lancet Neurology*, 1(3):173–181, 2002.

[167] P. Polack, I. Guillemain, E. Hu, C. Deransart, A. Depaulis, and S. Charpier. Deep layer somatosensory cortical neurons initiate spike-and-wave discharges in a genetic model of absence seizures. *Journal of Neuroscience*, 27(24):6590–6599, 2007.

[168] G. Puia, J. M. Mienville, K. Matsumoto, H. Takahata, H. Watanabe, E. Costa, and A. Guidotti. On the putative physiological role of allopregnanolone on GABAA receptor function. *Neuropharmacology*, 44(1):49–55, 2003.

[169] S. M. Purcell, D. S. Manoach, C. Demanuele, B. E. Cade, S. Mariani, R. Cox, G. Panagiotaropoulou, R. Saxena, J. Q. Pan, J. W. Smoller, et al. Characterizing sleep spindles in 11,630 individuals from the national sleep research resource. *Nature Communications*, 8(1):1–16, 2017.

[170] N. A. J. Puts and R. A. E. Edden. In vivo magnetic resonance spectroscopy of GABA: a methodological review. *Progress in Nuclear Magnetic Resonance Spectroscopy*, 60:29–41, 2012.

[171] D. S. Reddy, W. Thompson, and G. Calderara. Molecular mechanisms of sex differences in epilepsy and seizure susceptibility in chemical, genetic and acquired epileptogenesis. *Neuroscience Letters*, 750:135753, 2021.

[172] V. E. Rinaldi, G. Di Cara, E. Mencaroni, and A. Verrotti. Therapeutic options for childhood absence epilepsy. *Pediatric Reports*, 13(4):658–667, 2021.

[173] E. Rusina, M. Simonti, F. Duprat, S. Cestèle, and M. Mantegazza. Voltage-gated sodium channels in genetic epilepsy: up and down of excitability. *Journal of Neurochemistry*, 168(12):3872–3890, 2024.

[174] M. Schumacher, R. Hussain, N. Gago, J. P. Oudinet, C. Mattern, and A. M. Ghoumari. Progesterone synthesis in the nervous system: implications for myelination and myelin repair. *Frontiers in Neuroscience*, 6:10, 2012.

[175] M. Schumacher, C. Mattern, A. Ghoumari, J. P. Oudinet, P. Liere, F. Labombarda, R. Sitruk-Ware, A. F. De Nicola, and R. Guennoun. Revisiting the roles of progesterone and allopregnanolone in the nervous system: resurgence of the progesterone receptors. *Progress in Neurobiology*, 113:6–39, 2014.

[176] C. J. Schwiening. A brief historical perspective: Hodgkin and Huxley. *The Journal of Physiology*, 590(Pt 11):2571, 2012.

[177] H. S. Seung and U. Sümbül. Neuronal cell types and connectivity: lessons from the retina. *Neuron*, 83(6):1262–1272, 2014.

[178] V. A. Shaposhnik. Walter Nernst and analytical chemistry. *Journal of Analytical Chemistry*, 63:199–201, 2008.

[179] G. M. G. Shepherd and N. Yamawaki. Untangling the cortico-thalamo-cortical loop: cellular pieces of a knotty circuit puzzle. *Nature Reviews Neuroscience*, 22(7):389–406, 2021.

[180] E. Sitnikova, A. E. Hramov, V. Grubov, and A. A. Koronovsky. Time-frequency characteristics and dynamics of sleep spindles in WAG/Rij rats with absence epilepsy. *Brain Research*, 1543:290–299, 2014.

[181] P. W. E. Spratt, R. P. D. Alexander, R. Ben-Shalom, A. Sahagun, H. Kyoung, C. M. Keeshen, S. J. Sanders, and K. J. Bender. Paradoxical hyperexcitability from Nav1.2 sodium channel loss in neocortical pyramidal cells. *Cell Reports*, 36(5), 2021.

[182] M. Steriade and D. Contreras. Relations between cortical and thalamic cellular events during transition from sleep patterns to paroxysmal activity. *Journal of Neuroscience*, 15(1):623–642, 1995.

[183] S. Stern, A. Sarkar, D. Galor, T. Stern, A. Mei, Y. Stern, A. P. D. Mendes, L. Randolph-Moore, G. Rouleau, A. G. Bang, et al. A physiological instability displayed in hippocampal neurons derived from lithium-nonresponsive bipolar disorder patients. *Biological Psychiatry*, 88(2):150–158, 2020.

[184] M. Straathof, M. R. T. Sinke, R. M. Dijkhuizen, and W. M. Otte. A systematic review on the quantitative relationship between structural and functional network connectivity strength in mammalian brains. *Journal of Cerebral Blood Flow & Metabolism*, 39(2):189–209, 2019.

[185] J. Strömberg, D. Haage, M. Taube, T. Bäckström, and P. Lundgren. Neurosteroid modulation of allopregnanolone and GABA effect on the GABA-A receptor. *Neuroscience*, 143(1):73–81, 2006.

[186] F. Studer, E. Laghouati, G. Jarre, O. David, B. Pouyatos, and A. Depaulis. Sensory coding is impaired in rat absence epilepsy. *The Journal of Physiology*, 597(3):951–966, 2019.

[187] S. D. Sullivan and S. M. Moenter. Neurosteroids alter GABAergic postsynaptic currents in GnRH neurons: a possible mechanism for direct steroidal control. *Endocrinology*, 144:4366–4375, 2003.

[188] D. J. Surmeier, C. J. Wilson, and J. Eberwine. Patch-clamp techniques for studying potassium currents in mammalian brain neurons. In *Methods in Neurosciences*, volume 19, pages 39–67. Elsevier, 1994.

[189] H. O. Tan, C. A. Reid, F. N. Single, P. J. Davies, C. Chiu, S. Murphy, A. L. Clarke, L. Dibbens, H. Krestel, J. C. Mulley, et al. Reduced cortical inhibition in a mouse model of familial childhood absence epilepsy. *Proceedings of the National Academy of Sciences*, 104(44):17536–17541, 2007.

[190] J. R. Tenney, D. S. Kadis, W. Agler, L. Rozhkov, M. Altaye, J. Xiang, J. Vannest, and T. A. Glauser. Ictal connectivity in childhood absence epilepsy: associations with outcome. *Epilepsia*, 59(5):971–981, 2018.

[191] R. D. Traub, E. H. Buhl, T. Gloveli, and M. A. Whittington. Fast rhythmic bursting can be induced in layer 2/3 cortical neurons by enhancing persistent Na^+ conductance or by blocking BK channels. *Journal of Neurophysiology*, 89(2):909–921, 2003.

[192] R. D. Traub, D. Contreras, M. O. Cunningham, H. Murray, F. E. N. LeBeau, A. Roopun, A. Bibbig, W. B. Wilent, M. J. Higley, and M. A. Whittington. Single-column thalamocortical network model exhibiting gamma oscillations, sleep spindles, and epileptogenic bursts. *Journal of Neurophysiology*, 93(4):2194–2232, 2005.

[193] R. D. Traub, J. G. Jefferys, R. Miles, M. A. Whittington, and K. Tóth. A branching dendritic model of a rodent CA3 pyramidal neurone. *The Journal of Physiology*, 481(1):79–95, 1994.

[194] R. D. Traub, R. K. Wong, R. Miles, and H. Michelson. A model of a CA3 hippocampal pyramidal neuron incorporating voltage-clamp data on intrinsic conductances. *Journal of Neurophysiology*, 66(2):635–650, 1991.

[195] V. Tretter and S. J. Moss. GABAAreceptor dynamics and constructing GABAergic synapses. *Frontiers in Molecular Neuroscience*, 1:244, 2008.

[196] S. Turkmen, T. Backstrom, G. Wahlstrom, L. Andreen, and I. M. Johansson. Tolerance to allopregnanolone with focus on the GABA-a receptor. *British Journal of Pharmacology*, 162(2):311–327, 2011.

[197] G. van Luijtelaar, B. Budziszewska, L. Jaworska-Feil, J. Ellis, A. Coenen, and W. Lasoń. The ovarian hormones and absence epilepsy: a long-term EEG study and pharmacological effects in a genetic absence epilepsy model. *Epilepsy Research*, 46(3):225–239, 2001.

[198] G. van Luijtelaar and G. Van Oijen. Establishing drug effects on electrocorticographic activity in a genetic absence epilepsy model: advances and pitfalls. *Frontiers in Pharmacology*, 11:395, 2020.

[199] A. Verrotti, C. Cerminara, S. Domizio, A. Mohn, E. Franzoni, G. Coppola, N. Zamponi, P. Parisi, P. Iannetti, and P. Curatolo. Levetiracetam in absence epilepsy. *Developmental Medicine & Child Neurology*, 50(11):850–853, 2008.

[200] I. Vitko, Y. Chen, J. M. Arias, Y. Shen, X. R. Wu, and E. Perez-Reyes. Functional characterization and neuronal modeling of the effects of childhood absence epilepsy variants of CACNA1H, a T-type calcium channel. *Journal of Neuroscience*, 25(19):4844–4855, 2005.

[201] R. H. Wallace, C. Marini, S. Petrou, L. A. Harkin, D. N. Bowser, R. G. Panchal, D. A. Williams, G. R. Sutherland, J. C. Mulley, I. E. Scheffer, et al. Mutant GABAa receptor γ2-subunit in childhood absence epilepsy and febrile seizures. *Nature Genetics*, 28(1):49–52, 2001.

[202] Y. Wang, P. Wei, F. Yan, Y. Luo, and G. Zhao. Animal models of epilepsy: a phenotype-oriented review. *Aging and Disease*, 13(1):215, 2022.

[203] Y. Wei, G. Ullah, and S. J. Schiff. Unification of neuronal spikes, seizures, and spreading depression. *Journal of Neuroscience*, 34(35):11733–11743, 2014.

[204] J. W. Wheless and H. L. Kim. Adolescent seizures and epilepsy syndromes. *Epilepsia*, 43:33–52, 2002.

[205] H. R. Wilson and J. D. Cowan. Excitatory and inhibitory interactions in localized populations of model neurons. *Biophysical Journal*, 12(1):1–24, 1972.

[206] E. C. Wirrell, C. S. Camfield, P. R. Camfield, K. E. Gordon, and J. M. Dooley. Long-term prognosis of typical childhood absence epilepsy: remission or progression to juvenile myoclonic epilepsy. *Neurology*, 47(4):912–918, 1996.

[207] C. S. Woolley and P. A. Schwartzkroin. Hormonal effects on the brain. *Epilepsia*, 39:S2–S8, 1998.

[208] H. Xie, W. Su, J. Pei, Y. Zhang, K. Gao, J. Li, X. Ma, Y. Zhang, X. Wu, and Y. Jiang. De novo SCN1A, SCN8A, and CLCN2 mutations in childhood absence epilepsy. *Epilepsy Research*, 154:55–61, 2019.

[209] O. Yalçın. Genes and molecular mechanisms involved in the epileptogenesis of idiopathic absence epilepsies. *Seizure*, 21(2):79–86, 2012.

[210] C. R. Yang, J. K. Seamans, and N. Gorelova. Electrophysiological and morphological properties of layers V-VI principal pyramidal cells in rat prefrontal cortex in vitro. *Journal of Neuroscience*, 16(5):1904–1921, 1996.

[211] C. J. Zamora-Sánchez and I. Camacho-Arroyo. Allopregnanolone: metabolism, mechanisms of action, and its role in cancer. *International Journal of Molecular Sciences*, 24(1):560, 2022.

[212] J. Zhang, X. Chen, M. Eaton, J. Wu, Z. Ma, S. Lai, A. Park, T. S. Ahmad, Z. Que, J. H. Lee, et al. Severe deficiency of the voltage-gated sodium channel Nav1.2 elevates neuronal excitability in adult mice. *Cell Reports*, 36(5), 2021.

APPENDICES

Appendix A

Appendix for Chapter 3

A.1 Model components

All of the neurons were described using a single compartment representing the soma. The soma was modelled as a cylinder with a surface area of πdl, where d is the diameter and l is the length. The diameter was 96 μm for all PY and TC neurons, 67 μm for all IN neurons, and 70 μm for all RE neurons. The length was 96 μm for all PY and TC neurons, 67 μm for all IN neurons, and 64.86 μm for all RE neurons. The axial resistance, Ra was equal to 100 Ωcm for all neurons. The membrane conductance density distributions as well as the type of current differed between neuron type. Ionic currents were described with the general form given by the following equation:

$$I_{ion} = \bar{g}_{ion} \cdot m^N \cdot h^M \cdot (V - V_{eq}) \tag{A.1}$$

where $\bar{g}_{ion}$ represents the maximal conductance for a particular ion channel, m and h are gating variables, N and M are integer powers, and V_{eq} represents the equilbirium potential. The dynamics of the gating variables were described by the following general form:

$$\frac{dx}{dt} = \frac{x_\infty - x}{\tau_x} \tag{A.2}$$

$$x_\infty = \frac{\alpha_x}{\alpha_x + \beta_x} \quad \text{and} \quad \tau_x = \frac{1}{\alpha_x + \beta_x} \tag{A.3}$$

where x_∞ is the steady-state gating variable function, τ_x represents the time course for approaching the steady state, α_x and β_x represent the forward and backward rate functions.

The incorporated Na^+, K^+, and Ca^{2+} currents included in the model are summarized in Table A.1.

Current	Current Description
I_{Leak}	leak current
I_{Na}	fast Na^+ current
I_K	fast K^+ current
I_M	slow voltage-dependent K^+ current
I_T	low-threshold Ca^{2+} current
I_{KLeak}	leak K^+ current
I_h	slowly non-inactivating mixed Na^+/K^+ current

Table A.1: Description of the currents used for all neuron types.

A.1.1 Summary of currents

I_{Leak}

The leak current for all neuron types was described as a simple ohmic current:

$$I_{Leak} = g_{Leak} \cdot (V - V_{Leak}) \tag{A.4}$$

where g_{Leak} is the constant conductance and V_{Leak}, the equilibrium potential, was assumed to be -70 mV for neurons of the PY, IN, and TC type, and -90 mV for neurons of the RE type.

I_{Na}

The fast Na^+ current was described using a Hodgkin-Huxley style equation

$$I_{Na} = g_{Na} \cdot m_{Na}^3 \cdot h_{Na} \cdot (V - V_{Na}) \tag{A.5}$$

where V_{Na} is the equilibrium potential for sodium equal to 50 mV for all neurons, g_{Na} is the maximal conductance, m_{Na} is the activation variable, and h_{Na} is the inactivation variable.

The kinetics for this current were based on dynamics described in Traub and Miles [194]:

$$\alpha_{m_{Na}} = \frac{0.32 \cdot (-V - 50)}{\exp(\frac{-V-50}{4}) - 1} \tag{A.6}$$

$$\beta_{m_{Na}} = \frac{0.28 \cdot (V + 23)}{\exp(\frac{V+23}{5}) - 1} \tag{A.7}$$

$$\alpha_{h_{Na}} = 0.128 \cdot \exp\left(\frac{-V - 46}{18}\right) \tag{A.8}$$

$$\beta_{h_{Na}} = \frac{4}{1 + \exp\left(\frac{-V-23}{5}\right)} \tag{A.9}$$

I_K

The fast K^+ current was described using the following equation:

$$I_K = g_K \cdot n_K^4 \cdot (V - V_K) \tag{A.10}$$

where V_K is the equilibrium potential for potassium equal to -100 mV for all neurons, g_K is the maximal conductance, and n_K is the inactivation variable. All functions corresponding to the gating variable was based on dynamics described in Traub and Miles [194]:

$$\alpha_{n_K} = \frac{0.032 \cdot (-V - 48)}{\exp(\frac{-V-48}{5}) - 1} \tag{A.11}$$

$$\beta_{n_K} = 0.5 \cdot \exp\left(\frac{-V - 53}{40}\right) \tag{A.12}$$

I_M

The non-inactivating, slow voltage-dependent K^+ current was described using kinetics presented by McCormick et al. [139]:

$$I_M = g_M \cdot m_M \cdot (V - V_K) \tag{A.13}$$

where g_M is the maximal conductance, and m_M is the activation variable. The steady state activation function and decay time constant were described by the following:

$$m_{M_\infty} = \frac{1}{1 + \exp\left(\frac{-V-35}{10}\right)} \tag{A.14}$$

$$\tau_{m_M} = \frac{1000}{3.3 \cdot (\exp\left(\frac{V+35}{20}\right) + \exp\left(\frac{-V-35}{20}\right))} \tag{A.15}$$

I_T

The low-threshold Ca^{2+} current was modelled using the following equation:

$$I_{IT} = g_{IT} \cdot m_{IT}^2 \cdot h_{IT} \cdot (V - V_{Ca}) \tag{A.16}$$

where V_{Ca} is the equilibrium potential for calcium given by the intracellular calcium dynamics described in Section A.1.2, g_{IT} is the maximal conductance, m_{IT} and h_{IT} are the activation and inactivation gating variables, respectively. The dynamics were described differently for each thalamic neuron. The subscript IT corresponds to dynamics for TC neurons while the subscript ITs corresponds to dynamics for RE neurons.

All functions corresponding to the gating variables for RE neurons were as described by Destexhe et al. [50]. The gating variable dynamics given here correspond to network behaviour exhibiting spindle oscillations:

$$m_{ITs\infty} = \frac{1}{1 + \exp\left(\frac{-V-50}{7.4}\right)} \tag{A.17}$$

$$\tau_{m_{ITs}} = \frac{3 + \frac{1}{\exp\left(\frac{V+25}{10}\right) + \exp\left(\frac{-V-100}{15}\right)}}{2.5^{1.2}} \tag{A.18}$$

$$h_{ITs\infty} = \frac{1}{1 + \exp\left(\frac{V+78}{5}\right)} \tag{A.19}$$

$$\tau_{h_{ITs}} = \frac{85 + \frac{1}{\exp\left(\frac{V+48}{4}\right) + \exp\left(\frac{-V-407}{50}\right)}}{2.5^{1.2}} \tag{A.20}$$

For TC neurons, activation m_{IT} was taken to be at steady-state equal to $m_{IT\infty}$. The steady-state activation and inactivation functions were based on the description by Huguenard and McCormick [88], and the inactivation time constant was as described by Destexhe et al. [48]:

$$m_{IT\infty} = \frac{1}{1 + \exp\left(\frac{-V-57}{6.2}\right)} \tag{A.21}$$

$$h_{IT\infty} = \frac{1}{1 + \exp\left(\frac{V+81}{4}\right)} \tag{A.22}$$

$$\tau_{h_{IT}} = \frac{30.8 + \frac{211.4 + \exp\left(\frac{V+113.2}{5}\right)}{1 + \exp\left(\frac{V+84}{3.2}\right)}}{3^{1.2}} \tag{A.23}$$

I_{KLeak}

The leak K^+ current was described by the following Ohmic equation:

$$I_{KLeak} = g_{KLeak} \cdot (V - V_K) \tag{A.24}$$

where g_{KLeak} is the maximal conductance.

I_h

The mixed Na^+/K^+ cation current was modelled by the following equation:

$$I_h = g_h \cdot m_h \cdot (V - V_h) \tag{A.25}$$

where V_h is the equilibrium potential for this mixed cation current equal to -40 mV, g_h is the maximal conductance, and m_h is the activation variable dependent on both voltage and intracellular Ca^{2+} concentration.

The dependence of activation on voltage was based on the description by Huguenard and McCormick [88]:

$$m_{h\infty} = \frac{1}{1 + \exp\left(\frac{V+75}{5.5}\right)} \tag{A.26}$$

$$\tau_{m_h} = 20 + \frac{1000}{\exp\left(\frac{V+71.5}{14.2}\right) + \exp\left(\frac{-V-89}{11.6}\right)} \tag{A.27}$$

The dependence of activation on intracellular Ca^{2+} was based on the kinetic scheme described by Destexhe et al. [48]:

$$C \underset{\beta(V)}{\overset{\alpha(V)}{\rightleftharpoons}} O \tag{A.28}$$

$$P_0 + 2Ca_i^{2+} \underset{k_2}{\overset{k_1}{\rightleftharpoons}} P_1 \tag{A.29}$$

$$O + P_1 \underset{k_4}{\overset{k_3}{\rightleftharpoons}} O_L \tag{A.30}$$

where voltage-dependent transitions between closed (C) and open (O) forms occur with rates described by $\alpha(V)$ and $\beta(V)$, and intracellular Ca^{2+} ions bind to a regulating factor given by P_0 (unbound) and P_1 (bound) with rates of $k_1 = 2.5 \times 10^7$ $\mathrm{mM}^{-4}\mathrm{ms}^{-1}$ and

$k_2 = 4 \times 10^{-4}$ ms^{-1}. The dynamics of Ca^{2+} ions is described in Section A.1.2. Furthermore, the open form of the channel binds with the calcium-bound regulator P_1 to form O_L with rates $k_3 = 0.1$ ms^{-1} and $k_4 = 0.001$ ms^{-1}.

In particular, the activation is dependent on the relative concentration of open channels given by the following equation:

$$m_h = [O] + 2 \cdot [O_L] \tag{A.31}$$

The voltage-dependent transition rates between closed and open forms are described by:

$$\alpha(V) = \frac{m_{h\infty}}{\tau_{m_h}} \tag{A.32}$$

$$\beta(V) = \frac{1 - m_{h\infty}}{\tau_{m_h}} \tag{A.33}$$

A.1.2 Calcium dynamics

Intracellular calcium dynamics were based on the model described by Destexhe et al. [47]. A simple proportional model of Ca^{2+} diffusion was used with the change in calcium concentration described by:

$$\frac{d[Ca^{2+}]_{\mathrm{i}}}{dt} = -\frac{k}{2Fd} \cdot I_T + \frac{[Ca^{2+}]_{\mathrm{i}\infty} - [Ca^{2+}]_{\mathrm{i}}}{\tau_r} \tag{A.34}$$

where $[Ca^{2+}]_{\mathrm{i}}$ is measured in mM, $F = 96489$ Cmol^{-1} is Faraday's constant, $d = 1\mu$m denotes the depth at which calcium concentration was calculated beneath the membrane, $k = 10^{-4}$ is a dimensionless unit conversion factor, I_T is the calcium current measured in mAcm^2, $[Ca^{2+}]_{\mathrm{i}\infty} = 2.4 \times 10^{-4}$ mM is the steady state calcium concentration, and $\tau_r = 5$ ms is the decay time constant.

Equilibrium Potential for Ca^{2+}

The equilibrium potential for calcium, V_{Ca} was calculated according to the Nernst relation:

$$V_{Ca} = k' \frac{RT}{2F} \log \frac{[Ca^{2+}]_{\mathrm{o}}}{[Ca^{2+}]_{\mathrm{i}}} \tag{A.35}$$

where $R = 8.31$ J mol^{-1}K^{-1}, $T = 309.15$°K, $F = 96489$ Cmol^{-1} is Faraday's constant, $[Ca^{2+}]_{\mathrm{o}}$ and $[Ca^{2+}]_{\mathrm{i}}$ denote extracellular and intracellular calcium concentrations respectively, and $k' = 1000$ is a unit conversation factor for V_{Ca} in mV.

A.1.3 Synaptic dynamics

Synaptic currents were modelled in a manner similar to ionic currents as given by the following equation:

$$I_{syn} = \bar{g}_{syn} \cdot s(t) \cdot (V_m - E_{syn}) \tag{A.36}$$

where $\bar{g}_{syn}$ is the maximal synaptic conductance, $s(t)$ is the synaptic conductance function and E_{syn} is the reversal potential of the synapse. The time-dependent conductance $s(t)$ can be modelled in several ways depending on the type of neurotransmitter-mediated synapse, as described below [52].

AMPA/GABAa-mediated synapse modelling

In the formalism by Destexhe et al. [51][52], postsynaptic currents mediated by glutamate AMPA and GABAergic GABAa receptors are modelled using a gating variable $s(t)$ which denotes the fraction of open synaptic channels at time t. Open synaptic channels refer to postsynaptic receptors that neurotransmitter molecules bind to, followed by the opening of ion channels. In this way, the synaptic conductance function is described by:

$$\frac{ds}{dt} = \alpha[T](1 - s) - \beta s \tag{A.37}$$

where $[T]$ represents the neurotransmitter concentration released into the synaptic cleft upon the arrival of a presynaptic spike, and α and β are rate constants describing the binding of neurotransmitter.

Upon the arrival of a presynaptic spike at $t = t_0$, $[T]$ jumps to a maximal concentration value C_{max}, and at $t = T_{dur}$ (the duration of neurotransmitter-mediated pulse), $[T]$ falls back to 0. After the neurotransmitter-mediated pulse is gone, $s(t)$ decays exponentially. Thus, solving Equation (A.37), we get:

$$s(t) = \begin{cases} s_\infty + (s(0) - s_\infty)e^{-\frac{t}{\tau_s}}, & 0 \leq t < T_{dur} \\ \left[s_\infty + (s(0) - s_\infty)e^{-\frac{T_{dur}}{\tau_s}}\right]e^{-\beta(t - T_{dur})}, & t \geq T_{dur} \end{cases} \tag{A.38}$$

where

$$s_\infty = \frac{\alpha C_{max}}{\alpha C_{max} + \beta} \quad \text{and} \quad \tau_s = \frac{1}{\alpha C_{max} + \beta} \tag{A.39}$$

For AMPA-mediated synapses, $E_{syn} = 0$ mV, $C_{max} = 0.5$ mM, $T_{dur} = 0.3$ ms, $\alpha = 0.94$ (ms mM)$^{-1}$, $\beta = 0.18$ ms^{-1}. For GABAa-mediated synapses, $E_{syn} = -85$ mV, $C_{max} = 0.5$ mM, $T_{dur_{Control}} = 0.3$ ms, $T_{dur_{Post-ALLO}} = 0.75$ ms, $\alpha_{Control} = 20$ (ms mM)$^{-1}$, $\alpha_{Post-ALLO} = 22.87$ (ms mM)$^{-1}$, $\beta_{Control} = 0.162$ ms^{-1} and $\beta_{Post-ALLO} = 0.095$ ms^{-1}.

GABAb-mediated synapse modelling

The dynamics of GABAb-mediated synapses followed the formalism by Destexhe et al. [**?**]. GABAb-mediated synapses active *indirectly*, following a series of intracellular events. In particular, the neurotransmitter binding event activates an intracellular complex called a G-protein which activates potassium channels ultimately hyperpolarizing and causing inhibition of the postsynaptic neuron. In this way, the synaptic conductance function is described by:

$$s(t) = \frac{g^4}{g^4 + K_d} \tag{A.40}$$

$$\frac{dr}{dt} = K_1[T](1 - r) - K_2 r \tag{A.41}$$

$$\frac{dg}{dt} = K_3 r - K_4 g \tag{A.42}$$

where r is the fraction of GABAb receptors in the activated form, g is the normalized G-protein concentration in activated form given in μM, $K_d = 100$ μM^4 is the dissociation constant of G-protein binding on potassium channels, $K_1 = 0.09$ (ms mM)$^{-1}$ is the forward binding rate to the receptor, $K_2 = 0.0012$ ms^{-1} is the unbinding rate, $K_3 = 0.18$ ms^{-1} is the rate of G-protein production, $K_4 = 0.034$ ms^{-1} is the rate of G-protein decay, and $E_{syn} = -95$ mV.

A.2 Model parameters

The maximal conductance parameters for each ionic current is given in Table A.2.

All excitatory synapses were mediated by AMPA receptors, while inhibitory synapses were mediated by either GABAa alone, or a mixture of GABAa and GABAb receptors. The conductance parameters used to produce a default network state exhibiting spindle oscillations is given in Table A.3.

g_{ion}	PY	IN	TC	RE
g_{Leak}	0.1	0.15	0.01	0.05
g_{Na}	50	50	90	200
g_K	5	10	10	20
g_M	0.07	-	-	-
g_{IT}	-	-	2	-
g_{ITs}	-	-	-	3
g_{KLeak}	-	-	4	-
g_h	-	-	0.02	-

Table A.2: Maximal conductance parameters (in mS/cm^2) for each neuron type.

	Post-synaptic neuron type			
Pre-synaptic neuron type	PY	IN	TC	RE
PY	0.6	0.2	0.01	1.2
IN	0.15 (GABAa) 0.03 (GABAb)	-	-	-
TC	1.2	0.4	-	0.2
RE	-	-	0.02 (GABAa) 0.04 (GABAb)	0.2 (GABAa)

Table A.3: Maximal synaptic conductance parameters (in μS) for each synapse type to produce a default network state exhibiting spindle oscillations.

Appendix B

Appendix for Chapter 4

B.1 Model components

All of the neurons were described using a single compartment representing the soma. The soma was modelled as a cylinder with a surface area of πdl, where d is the diameter and l is the length. The diameter was 18 μm for both IB and RS neurons, 16 μm for NRS and LTS neurons, 96 μm for TC neurons, and 70 μm for all RE neurons. The length was 25 μm for both IB and RS cells, 20 μm for NRS and LTS cells, 96 μm for TC cells, and 64.86 μm for RE neurons. The axial resistance, Ra was equal to 250 Ωcm for all cortical cells and 100 Ωcm for both thalamic neurons. The membrane conductance density distributions as well as the type of current differed between neuron type. Ionic currents were described with the general form given by the following equation:

$$I_{ion} = \bar{g}_{ion} \cdot m^N \cdot h^M \cdot (V - V_{eq}) \tag{B.1}$$

where $\bar{g}_{ion}$ represents the maximal conductance for a particular ion channel, m and h are gating variables, N and M are integer powers, and V_{eq} represents the equilibrium potential. The dynamics of the gating variables were described by one of two general forms: rise and decay rate functions, or a Boltzmann function combined with a voltage-dependent time constant function.

Using rise and decay rate functions, the dynamics were described by the following form:

$$\frac{dx}{dt} = \frac{x_\infty - x}{\tau_x} \tag{B.2}$$

$$x_\infty = \frac{\alpha_x}{\alpha_x + \beta_x} \quad \text{and} \quad \tau_x = \frac{1}{\alpha_x + \beta_x} \tag{B.3}$$

where x_∞ is the steady-state gating variable function, τ_x represents the time course for approaching the steady state, α_x and β_x represent the forward and backward rate functions.

Alternatively, the gating variable dynamics were described by the following Boltzmann function:

$$x_\infty = \frac{1}{1 + \exp(\frac{V_{1/2} - V}{k})} \tag{B.4}$$

where x_∞ is the steady-state gating variable function, V is the membrane potential, $V_{1/2}$ is the voltage at half-activation, and k is the slope factor representing the steepness of the voltage-dependent transition between closed and open states of the channel. The voltage-dependent time constant function (τ_x) describes how quickly the gating variable approaches steady state and its form varies according to the channel type.

The incorporated Na^+, K^+, and Ca^{2+} currents included in the model are summarized in Table B.1.

Current	Current Description
I_{Naf}	fast and transient inactivating Na^+ current
I_{Nap}	persistent Na^+ current
I_K	fast K^+ current
I_{Kdr}	delayed rectifier K^+ current
I_{Ka}	transient inactivating K^+ current
I_{K2}	slowly activating and inactivating K^+ current
I_{Km}	muscarinic receptor-suppressed K^+ current
I_{Kc}	fast voltage and Ca^{2+}-dependent K^+ current
I_{Kahp}	slow Ca^{2+}-dependent K^+ current
I_{CaT}	low-threshold Ca^{2+} current
I_{CaL}	high-threshold Ca^{2+} current
I_h	slowly non-inactivated mixed Na^+/K^+ current
I_{Leak}	leak current
I_{KLeak}	leak K^+ current

Table B.1: Description of the currents used for all neuron types.

The equilibrium potentials were defined as follows: $V_{Na} = 50$ mV (all cells), $V_K = -100$ mV (for LTS, TC, RE) and -95 mV (for RS, IB, NRS), $V_h = -40$ mV (for LTS, TC, RE) and -43 mV (for RS, IB, NRS), $V_{Leak} = -70$ mV (for RS, IB, NRS, TC), -65 mV for LTS and -90 mV for RE neurons, V_{Ca} was given by intracellular calcium dynamics described in Section B.1.2.

B.1.1 Summary of currents

I_{Leak}

The leak current for all neuron types was described as a simple ohmic current:

$$I_{Leak} = g_{Leak} \cdot (V - V_{Leak}) \tag{B.5}$$

where g_{Leak} is the constant conductance.

I_{KLeak}

The leak K^+ current in TC neurons was described by the following Ohmic equation:

$$I_{KLeak} = g_{KLeak} \cdot (V - V_K) \tag{B.6}$$

where g_{KLeak} is the maximal conductance.

I_{Naf}

The fast Na^+ current was described using a Hodgkin-Huxley style equation:

$$I_{Naf} = g_{Naf} \cdot m_{Naf}^3 \cdot h_{Naf} \cdot (V - V_{Na}) \tag{B.7}$$

where g_{Naf} is the maximal conductance, m_{Naf} is the activation variable, and h_{Naf} is the inactivation variable.

In neurons of the RS, IB and NRS type, kinetics were based on dynamics described in Traub et al. [192]:

$$m_{Naf\infty} = \frac{1}{1 + \exp\left(\frac{-V-38}{10}\right)} \tag{B.8}$$

$$\tau_{m_{Naf}} = \begin{cases} 0.025 + 0.14 \cdot \exp\left(\frac{V+30}{10}\right), & V \leq -30\text{mV} \\ 0.02 + 0.145 \cdot \exp\left(\frac{-V-30}{10}\right), & V > -30\text{mV} \end{cases} \tag{B.9}$$

$$h_{Naf\infty} = \frac{1}{1 + \exp\left(\frac{V+62.9}{10.7}\right)} \tag{B.10}$$

$$\tau_{h_{Naf}} = 0.15 + \frac{1.15}{1 + \exp\left(\frac{V+37}{15}\right)} \tag{B.11}$$

In LTS neurons, the steady state activation function, $m_{Naf\infty}$, was the same as described above for other cortical neurons, while the remaining kinetics were based on dynamics described in Martina and Jonas [133]:

$$\tau_{m_{Naf}} = \begin{cases} 0.0125 + 0.1525 \cdot \exp\left(\frac{V+30}{10}\right), & V \leq -30\text{mV} \\ 0.02 + 0.145 \cdot \exp\left(\frac{-V-30}{10}\right), & V > -30\text{mV} \end{cases} \tag{B.12}$$

$$h_{Naf\infty} = \frac{1}{1 + \exp\left(\frac{V+58.3}{6.7}\right)} \tag{B.13}$$

$$\tau_{h_{Naf}} = 0.225 + \frac{1.125}{1 + \exp\left(\frac{V+37}{15}\right)} \tag{B.14}$$

In TC and RE neurons, the kinetics for this current were based on dynamics described in Traub and Miles [194]:

$$\alpha_{m_{Naf}} = \frac{0.32 \cdot (-V - 50)}{\exp(\frac{-V-50}{4}) - 1} \tag{B.15}$$

$$\beta_{m_{Naf}} = \frac{0.28 \cdot (V + 23)}{\exp(\frac{V+23}{5}) - 1} \tag{B.16}$$

$$\alpha_{h_{Naf}} = 0.128 \cdot \exp\left(\frac{-V - 46}{18}\right) \tag{B.17}$$

$$\beta_{h_{Naf}} = \frac{4}{1 + \exp\left(\frac{-V-23}{5}\right)} \tag{B.18}$$

I_{Nap}

The persistent, depolarization-activated Na^+ current was described using kinetics presented by Traub et al. [191]:

$$I_{Nap} = g_{Nap} \cdot m_{Nap} \cdot (V - V_{Na}) \tag{B.19}$$

where g_{Nap} is the maximal conductance, and m_{Nap} is the activation variable. For all cortical neurons, the steady state activation function and decay time constant were described by the following:

$$m_{Nap\infty} = \frac{1}{1 + \exp\left(\frac{-V-48}{10}\right)} \tag{B.20}$$

$$\tau_{m_{Nap}} = \begin{cases} 0.025 + 0.14 \cdot \exp\left(\frac{V+40}{10}\right), & V \leq -40\text{mV} \\ 0.02 + 0.145 \cdot \exp\left(\frac{-V-40}{10}\right), & V > -40\text{mV} \end{cases} \tag{B.21}$$

I_K

The fast K^+ current in both thalamic cells was described using the following equation:

$$I_K = g_K \cdot n_K^4 \cdot (V - V_K) \tag{B.22}$$

where g_K is the maximal conductance, n_K is the inactivation variable. All functions were based on dynamics described in Traub et al. [194]:

$$\alpha_{n_K} = \frac{0.032 \cdot (-V - 48)}{\exp(\frac{-V-48}{5}) - 1} \tag{B.23}$$

$$\beta_{n_K} = 0.5 \cdot \exp\left(\frac{-V - 53}{40}\right) \tag{B.24}$$

I_{Kdr}

The delayed rectifier K^+ current was described using kinetics presented by Traub et al. [191]:

$$I_{Kdr} = g_{Kdr} \cdot m_{Kdr}^4 \cdot (V - V_K) \tag{B.25}$$

where g_{Kdr} is the maximal conductance and m_{Kdr} is the activation variable.

In neurons of the RS, IB and NRS type, the steady state activation function was described by the following:

$$m_{Kdr\infty} = \frac{1}{1 + \exp\left(\frac{-V-29.5}{10}\right)} \tag{B.26}$$

In LTS neurons, the steady activation function was defined as:

$$m_{Kdr\infty} = \frac{1}{1 + \exp\left(\frac{-V-27}{11.5}\right)} \tag{B.27}$$

The time constant for all cortical neurons was described by the following:

$$\tau_{m_{Kdr}} = \begin{cases} 0.25 + 4.35 \cdot \exp\left(\frac{V+10}{10}\right), & V \leq -10\text{mV} \\ 0.25 + 4.35 \cdot \exp\left(\frac{-V-10}{10}\right), & V > -10\text{mV} \end{cases} \tag{B.28}$$

I_{Ka}

The transient inactivating K^+ current was modelled in all cortical cells using the following equation:

$$I_{Ka} = g_{Ka} \cdot m_{Ka}^4 \cdot h_{Ka} \cdot (V - V_K) \tag{B.29}$$

where g_{Ka} is the maximal conductance, and m_{Ka} and h_{Ka} are the activation and inactivation variables, respectively. The kinetics were based on dynamics described by Huguenard and McCormick [88]:

$$m_{Ka\infty} = \frac{1}{1 + \exp\left(\frac{-V-60}{8.5}\right)} \tag{B.30}$$

$$\tau_{m_{Ka}} = 0.185 + \frac{0.5}{\exp\left(\frac{V+35.8}{19.7}\right) + \exp\left(\frac{-V-79.7}{12.7}\right)} \tag{B.31}$$

$$h_{Ka\infty} = \frac{1}{1 + \exp\left(\frac{V+78}{6}\right)} \tag{B.32}$$

$$\tau_{m_{Naf}} = \begin{cases} \frac{0.5}{\exp\left(\frac{V+46}{5}\right)+\exp\left(\frac{-V-238}{37.5}\right)}, & V \leq -63\text{mV} \\ 9.5, & V > -63\text{mV} \end{cases} \tag{B.33}$$

I_{K2}

The slowly activating and inactivating K^+ current equations followed Huguenard and McCormick [88] and McCormick and Huguenard [138]:

$$I_{K2} = g_{K2} \cdot m_{K2} \cdot h_{K2} \cdot (V - V_K) \tag{B.34}$$

where g_{K2} is the maximal conductance, and m_{K2} and h_{K2} are the activation and inactivation variables, respectively. The kinetics for all cortical neurons were described by the

following equations:

$$m_{K2\infty} = \frac{1}{1 + \exp\left(\frac{-V-10}{17}\right)} \tag{B.35}$$

$$\tau_{m_{K2}} = 4.95 + \frac{0.5}{\exp\left(\frac{V-81}{25.6}\right) + \exp\left(\frac{-V-132}{18}\right)} \tag{B.36}$$

$$h_{K2\infty} = \frac{1}{1 + \exp\left(\frac{V+58}{10.6}\right)} \tag{B.37}$$

$$\tau_{h_{K2}} = 60 + \frac{0.5}{\exp\left(\frac{V-1.33}{200}\right) + \exp\left(\frac{-V-130}{7.1}\right)} \tag{B.38}$$

$$\tag{B.39}$$

I_{Km}

The non-inactivating, slow voltage-dependent K^+ current was modelled using the following equation:

$$I_{Km} = g_{Km} \cdot m_{Km} \cdot (V - V_K) \tag{B.40}$$

where g_{Km} is the maximal conductance, and m_{Km} is the activation variable.

In all cortical neurons, kinetics were based on dynamics presented by Traub et al. [191]:

$$\alpha_{m_{Km}} = \frac{0.02}{1 + \exp\left(\frac{-V-20}{5}\right)} \tag{B.41}$$

$$\beta_{m_{Km}} = 0.5 \cdot \exp\left(\frac{-V-43}{18}\right) \tag{B.42}$$

In TC and RE neurons, the kinetics were based on dynamics described in McCormick et al. [139]:

$$m_{Km_\infty} = \frac{1}{1 + \exp\left(\frac{-V-35}{10}\right)} \tag{B.43}$$

$$\tau_{m_{Km}} = \frac{1000}{3.3 \cdot \left(\exp\left(\frac{V+35}{20}\right) + \exp\left(\frac{-V-35}{20}\right)\right)} \tag{B.44}$$

I_{Kc}

The fast voltage and Ca^{2+}-dependent K^+ current was modelled using the equation presented by Traub et al. [193]:

$$I_{Kc} = g_{Kc} \cdot m_{Kc} \cdot \min(0.004[Ca^{2+}]_{\mathrm{i}}, 1) \cdot (V - V_K) \tag{B.45}$$

where g_{Kc} is the maximal conductance, m_{Kc} is the activation variable, and $[Ca^{2+}]_{\mathrm{i}}$ dynamics are governed by dynamics described in B.1.2.

The forward and backward rate functions for all neurons of the RS, IB, and NRS type were based on kinetics described in Traub et al. [191]:

$$\alpha_{m_{Kc}} = \begin{cases} 0.053 \cdot \exp\left(\frac{V+50}{11} - \frac{V+53.5}{27}\right), & V \leq -10\mathrm{mV} \\ 2 \cdot \exp\left(\frac{-V-53.5}{27}\right), & V > -10\mathrm{mV} \end{cases} \tag{B.46}$$

$$\beta_{m_{Kc}} = \begin{cases} 2 \cdot \exp\left(\frac{-V-53.5}{27}\right) - \alpha_{m_{Kc}}, & V \leq -10\mathrm{mV} \\ 0, & V > -10\mathrm{mV} \end{cases} \tag{B.47}$$

For LTS neurons, the forward and backward rate functions as described above were multiplied by a factor of 2.

I_{Kahp}

The slow Ca^{2+}-dependent K^+ current responsible for afterhypolarization, was described using kinetics presented by Traub et al. [193]:

$$I_{Kahp} = g_{Kahp} \cdot m_{Kahp} \cdot (V - V_K) \tag{B.48}$$

where g_{Kahp} is the maximal conductance, and m_{Kahp} is the activation variable. The forward rate function for all cortical neurons was dependent on the intracellular calcium dynamics described in Section B.1.2:

$$\alpha_{m_{Kahp}} = \min(0.0001[Ca^{2+}]_{\mathrm{i}}, 0.01) \tag{B.49}$$

$$\beta_{m_{Kahp}} = 0.01 \tag{B.50}$$

I_{CaT}

The low-threshold Ca^{2+} current was modelled using the following equation:

$$I_{CaT} = g_{CaT} \cdot m_{CaT}^2 \cdot h_{CaT} \cdot (V - V_{Ca}) \tag{B.51}$$

where g_{CaT} is the maximal conductance, m_{CaT} and h_{CaT} are the activation and inactivation gating variables, respectively. The dynamics were described differently for each thalamic neuron, as well as within the cortical cells.

For cortical neurons of the RS, IB, and NRS type, the kinetics were based on descriptions by Traub et al. [191]:

$$m_{CaT\infty} = \frac{1}{1 + \exp\left(\frac{-V-56}{6.2}\right)} \tag{B.52}$$

$$\tau_{m_{CaT}} = 0.204 + \frac{0.333}{\exp\left(\frac{-V-131}{16.7}\right) + \exp\left(\frac{V+15.8}{18.2}\right)} \tag{B.53}$$

$$h_{CaT\infty} = \frac{1}{1 + \exp\left(\frac{80}{4}\right)} \tag{B.54}$$

$$\tau_{h_{CaT}} = \begin{cases} 0.333 \cdot \exp\left(\frac{V+466}{66.6}\right), & V \leq -81\text{mV} \\ 9.32 + 0.333 \cdot \exp\left(\frac{-V-21}{10.5}\right), & V > -81\text{mV} \end{cases} \tag{B.55}$$

For the LTS interneuron, kinetics were based on descriptions by Destexhe et al. [50]:

$$m_{CaT\infty} = \frac{1}{1 + \exp\left(\frac{-V-52}{7.4}\right)} \tag{B.56}$$

$$\tau_{m_{CaT}} = 1 + \frac{0.333}{\exp\left(\frac{V+27}{10}\right) + \exp\left(\frac{-V-102}{15}\right)} \tag{B.57}$$

$$h_{CaT\infty} = \frac{1}{1 + \exp\left(\frac{V+80}{5}\right)} \tag{B.58}$$

$$\tau_{h_{CaT}} = 28.3 + \frac{0.33}{\exp\left(\frac{V+48}{4}\right) + \exp\left(\frac{-V-407}{50}\right)} \tag{B.59}$$

For RE neurons, kinetics were slightly modified from the description for LTS cells, as

given by Traub et al. [192]:

$$m_{CaT\infty} = \frac{1}{1 + \exp\left(\frac{-V-50}{7.4}\right)} \tag{B.60}$$

$$\tau_{m_{CaT}} = \frac{3 + \frac{1}{\exp\left(\frac{V+25}{10}\right)+\exp\left(\frac{-V-100}{15}\right)}}{2.5^{1.2}} \tag{B.61}$$

$$h_{CaT\infty} = \frac{1}{1 + \exp\left(\frac{V+78}{5}\right)} \tag{B.62}$$

$$\tau_{h_{CaT}} = \frac{85 + \frac{1}{\exp\left(\frac{V+48}{4}\right)+\exp\left(\frac{-V-407}{50}\right)}}{2.5^{1.2}} \tag{B.63}$$

For TC neurons, activation m_{CaT} was taken to be at steady-state equal to $m_{CaT\infty}$, and all steady-state activation and inactivation functions were based on the description by Huguenard and McCormick [88], and the inactivation time constant was as described by Destexhe et al. [48]:

$$m_{CaT\infty} = \frac{1}{1 + \exp\left(\frac{-V-57}{6.2}\right)} \tag{B.64}$$

$$h_{CaT\infty} = \frac{1}{1 + \exp\left(\frac{V+81}{4}\right)} \tag{B.65}$$

$$\tau_{h_{CaT}} = \frac{30.8 + \frac{211.4+\exp\left(\frac{V+113.2}{5}\right)}{1+\exp\left(\frac{V+84}{3.2}\right)}}{3^{1.2}} \tag{B.66}$$

I_{CaL}

The high-threshold Ca^{2+} current was modelled using the following equation:

$$I_{CaL} = g_{CaL} \cdot m_{CaL}^2 \cdot (V - V_{Ca}) \tag{B.67}$$

where g_{CaL} is the maximal conductance, and m_{CaL} is the activation variable. The forward and backward rate function for all cortical neurons were as described by Traub et al. [191]:

$$\alpha_{m_{CaL}} = \frac{1.6}{1 + \exp\left(-0.072 \cdot (V - 5)\right)} \tag{B.68}$$

$$\beta_{m_{CaL}} = 0.1 \cdot \frac{\frac{V+8.9}{5}}{\exp\left(\frac{V+8.9}{5}\right) - 1} \tag{B.69}$$

I_h

The mixed Na^+/K^+ cation current was modelled differently for cortical cells and the TC cell. For all cortical cells, this was modelled using the following equation:

$$I_h = g_h \cdot m_h \cdot (V - V_h) \tag{B.70}$$

where g_h is the maximal conductance, and m_h is the voltage-dependent activation variable, based on the description by Huguenard and McCormick [88]:

$$m_{h\infty} = \frac{1}{1 + \exp\left(\frac{V+75}{5.5}\right)} \tag{B.71}$$

$$\tau_{m_h} = \frac{1}{\exp\left(-14.59 - 0.086 \cdot V\right) + \exp\left(-1.87 + 0.0701 \cdot V\right)} \tag{B.72}$$

For TC cells, in addition to being voltage-dependent, the current dynamics were also dependent on intracellular Ca^{2+} concentration:

$$I_h = g_h \cdot ([O] + 2 \cdot [O_L]) \cdot (V - V_h) \tag{B.73}$$

where g_h is the maximal conductance, and the activation variable, m_h, is replaced by a weighted sum of channels in the open form and calcium-bound open form, based on the kinetic scheme described by Destexhe et al. [48]:

$$C \underset{\beta(V)}{\overset{\alpha(V)}{\rightleftharpoons}} O \tag{B.74}$$

$$P_0 + 2Ca_i^{2+} \underset{k_2}{\overset{k_1}{\rightleftharpoons}} P_1 \tag{B.75}$$

$$O + P_1 \underset{k_4}{\overset{k_3}{\rightleftharpoons}} O_L \tag{B.76}$$

where voltage-dependent transitions between closed (C) and open (O) forms occur with rates described by $\alpha(V)$ and $\beta(V)$, and intracellular Ca^{2+} ions bind to a regulating factor given by P_0 (unbound) and P_1 (bound) with rates of $k_1 = 2.5 \times 10^7$ $\text{mM}^{-4}\text{ms}^{-1}$ and $k_2 = 4 \times 10^{-4}$ ms^{-1}. The dynamics of Ca^{2+} ions is described in Section B.1.2. Furthermore, the open form of the channel binds with the calcium-bound regulator P_1 to form O_L with rates $k_3 = 0.1$ ms^{-1} and $k_4 = 0.001$ ms^{-1}.

The voltage-dependent transition rates between closed and open forms are described by:

$$\alpha(V) = \frac{m_{h\infty}}{\tau_{m_h}} \tag{B.77}$$

$$\beta(V) = \frac{1 - m_{h\infty}}{\tau_{m_h}} \tag{B.78}$$

where

$$m_{h\infty} = \frac{1}{1 + \exp\left(\frac{V+75}{5.5}\right)} \tag{B.79}$$

$$\tau_{m_h} = 20 + \frac{1000}{\exp\left(\frac{-V-89}{11.6}\right) + \exp\left(\frac{V+71.5}{14.2}\right)} \tag{B.80}$$

B.1.2 Calcium dynamics

Intracellular calcium dynamics were based on the model described by Destexhe et al. [47]. A simple proportional model of Ca^{2+} diffusion was used with the change in calcium concentration described by:

$$\frac{d[Ca^{2+}]_{\mathrm{i}}}{dt} = -\frac{k}{2Fd} \cdot I_T + \frac{[Ca^{2+}]_{\mathrm{i}\infty} - [Ca^{2+}]_{\mathrm{i}}}{\tau_r} \tag{B.81}$$

where $[Ca^{2+}]_{\mathrm{i}}$ is measured in mM, $F = 96489$ Cmol^{-1} is Faraday's constant, d denotes the depth at which calcium concentration was calculated beneath the membrane, $k = 10^{-4}$ is a dimensionless unit conversion factor, I_T is the calcium current measured in mA/cm^2, $[Ca^{2+}]_{\mathrm{i}\infty} = 2.4 \times 10^{-4}$ mM is the steady state calcium concentration, and τ_r is the decay time constant. The depth at which the calcium concentration was calculated was $12 \times 10^{-3}\mu$m for the IB and RS neuron, $4 \times 10^{-3}\mu$m for the NRS neuron, $2 \times 10^{-4}\mu$m for the LTS neuron, and 1μm for both the TC and RE neurons. The decay time constants were 100ms for cortical cells of the IB, RS, and NRS type, 50 ms for the LTS type, and 5 ms for both TC and RE cells.

Equilibrium potential for Ca^{2+}

The equilibrium potential for calcium, V_{Ca} was calculated according to the Nernst relation described in [47]:

$$V_{Ca} = k' \frac{RT}{2F} \log \frac{[Ca^{2+}]_{\mathrm{o}}}{[Ca^{2+}]_{\mathrm{i}}} \tag{B.82}$$

where $R = 8.31$ J mol^{-1}K^{-1}, $T = 309.15$°K, $F = 96489$ Cmol^{-1} is Faraday's constant, $[Ca^{2+}]_o$ and $[Ca^{2+}]_i$ denote extracellular and intracellular calcium concentrations respectively, and $k' = 1000$ is a unit conversation factor for V_{Ca} in mV.

B.1.3 Synaptic dynamics

Synaptic currents were modelled in a manner similar to ionic currents as given by the following equation:

$$I_{syn} = \bar{g}_{syn} \cdot s(t) \cdot (V_m - E_{syn}) \tag{B.83}$$

where $\bar{g}_{syn}$ is the maximal synaptic conductance, $s(t)$ is the synaptic conductance function and E_{syn} is the reversal potential of the synapse. The time-dependent conductance $s(t)$ can be modelled in several ways depending on the type of neurotransmitter-mediated synapse, as described below [52].

AMPA/GABAa-mediated synapse modelling

In the formalism by Destexhe et al. [51, 52], postsynaptic currents mediated by glutamate AMPA and GABAergic GABAa receptors are modelled using a gating variable $s(t)$ which denotes the fraction of open synaptic channels at time t. Open synaptic channels refer to postsynaptic receptors that neurotransmitter molecules bind to, followed by the opening of ion channels. In this way, the synaptic conductance function is described by:

$$\frac{ds}{dt} = \alpha[T](1 - s) - \beta s \tag{B.84}$$

where $[T]$ represents the neurotransmitter concentration released into the synaptic cleft upon the arrival of a presynaptic spike, and α and β are rate constants describing the binding of neurotransmitter.

Upon the arrival of a presynaptic spike at $t = t_0$, $[T]$ jumps to a maximal concentration value C_{max}, and at $t = C_{dur}$ (the duration of neurotransmitter-mediated pulse), $[T]$ falls back to 0. After the neurotransmitter-mediated pulse is gone, $s(t)$ decays exponentially. Thus, solving Equation (B.84), we get:

$$s(t) = \begin{cases} s_\infty + (s(t_0) - s_\infty)e^{-\frac{t}{\tau_s}}, & t_0 \leq t < C_{dur} \\ \left[s_\infty + (s(t_0) - s_\infty)e^{-\frac{C_{dur}}{\tau_s}}\right]e^{-\beta(t - C_{dur})}, & t \geq C_{dur} \end{cases} \tag{B.85}$$

where

$$s_\infty = \frac{\alpha C_{max}}{\alpha C_{max} + \beta} \quad \text{and} \quad \tau_s = \frac{1}{\alpha C_{max} + \beta} \tag{B.86}$$

For AMPA-mediated synapses, $E_{syn} = 0$ mV, $C_{max} = 0.5$ mM and $C_{dur} = 0.3$ ms, while α and β parameters vary according to the synapse type, as presented in Tables 4.3–4.4. For GABAa-mediated synapses, $E_{syn} = -85$ mV, $C_{max} = 0.5$ mM, and $C_{dur_{Control}} = 0.3$ ms, while values of $\alpha_{Control}$ and $\beta_{Control}$ vary according to the synapse type, as presented in Tables 4.3–4.4. To model post-ALLO GABAa-mediated synapses, $\alpha_{post-ALLO} = \alpha_{Control} \times 1.58$, $\beta_{post-ALLO} = \beta_{Control} \times 0.74$, and $C_{dur_{post-ALLO}} = C_{dur_{Control}} \times 1.14$.

GABAb-mediated synapse modelling

The dynamics of GABAb-mediated synapses followed the formalism by Destexhe et al. [52]. GABAb-mediated synapses active *indirectly*, following a series of intracellular events. In particular, the neurotransmitter binding event activates an intracellular complex called a G-protein which activates potassium channels ultimately hyperpolarizing and causing inhibition of the postsynaptic neuron. In this way, the synaptic conductance function is described by:

$$s(t) = \frac{g^4}{g^4 + K_d} \tag{B.87}$$

$$\frac{dr}{dt} = K_1[T](1 - r) - K_2 r \tag{B.88}$$

$$\frac{dg}{dt} = K_3 r - K_4 g \tag{B.89}$$

where r is the fraction of GABAb receptors in the activated form, g is the normalized G-protein concentration in activated form given in μM, $K_d = 100$ μM^4 is the dissociation constant of G-protein binding on potassium channels, $K_1 = 0.09$ (ms mM)$^{-1}$ is the forward binding rate to the receptor, $K_2 = 0.0012$ ms^{-1} is the unbinding rate, $K_3 = 0.18$ ms^{-1} is the rate of G-protein production, $K_4 = 0.034$ ms^{-1} is the rate of G-protein decay, and $E_{syn} = -95$ mV.

B.2 Model parameters

g_{ion}	RS	IB	NRS	LTS	TC	RE
g_{Naf}	200	200	200	170	90	200
g_{Nap}	0.16	0.16	0.1	0.16	-	-
g_{K}	-	-	-	-	10	20
g_{Kdr}	170	170	170	100	-	-
g_{Ka}	75	17	20	1	-	-
g_{K2}	35	27	40	9	-	-
g_{Km}	43	40	55	35	-	-
g_{Kc}	20	20	15	15	-	-
g_{Kahp}	0.5	3.5	35	0.1	-	-
g_{CaT}	0.1	0.1	0.1	0.05	2	3
g_{CaL}	10	11	2	0.1	-	-
g_{h}	0.1	0.1	0.1	0.1	$\mathcal{N}(0.0175, (8 \times 10^{-7})^2)$	-
g_{Leak}	2	2	2	2.4	0.01	0.05
g_{KLeak}	-	-	-	-	$\mathcal{N}(4, (3 \times 10^{-4})^2)$	-

Table B.2: Maximal conductance parameters (in mS/cm^2) for each neuron type.

B.3 Model fitting: choice of fitting parameters

To address the abnormality in individual neuronal firing, we analyzed the dynamics between two layer 6 non-tufted regular-spiking (NRS) neurons as an example, illustrated in Figure B.1: *Cell 0*, receiving a constant input current, and *Cell 1*, receiving input from *Cell 0* through an AMPA synapse. The key difference between spiking behaviours of *Cell 0* and *Cell 1* lies in the applied current (I_{app}) versus synaptic current (I_{syn}), with parameters g_{max}, α, and β shaping the synaptic strength. Modifying other synaptic parameters such as C_{max} and C_{dur} had effects similar to adjusting g_{max} or α, as shown in Figure B.1C. Notably, increasing α led to excessive depolarization, resembling a depolarization block, while decreasing β suppressed firing due to synaptic inputs decaying too rapidly. As shown in Figure B.1A-B, we found that by using default α and β parameters defined in previous work, the magnitude of I_{syn} was too high, similar to having an overly strong constant I_{app}, leading to distorted spikes in the postsynaptic cell that did not resemble its typical firing characteristics. Additionally, factors like presynaptic spike width and neurotransmitter dynamics further influenced I_{syn}, reinforcing the need for careful adjustment of rise (α)

nPrePost	Number of cells	*nPrePost*	Number of cells
nRSRS	11	nLTSRS	11
nRSIB	11	nLTSIB	11
nRSNRS	11	nLTSNRS	11
nRSLTS	10	nTCRE	11
nIBIB	11	nTCNRS	21
nIBRS	1	nTCIB	21
nIBNRS	1	nTCRS	21
nIBLTS	1	nTCLTS	21
nNRSNRS	11	nRERE	11
nNRSRS	9	nRETC	11
nNRSIB	11		
nNRSLTS	8		
nNRSTC	16		
nNRSRE	16		

Table B.3: The number of presynaptic neurons that each postsynaptic neuron connects to ($nPrePost$) in the 5-95 (nIB:nRS) model configuration.

nPrePost	Number of cells	*nPrePost*	Number of cells
nRSRS	11	nLTSRS	11
nRSIB	1	nLTSIB	11
nRSNRS	1	nLTSNRS	11
nRSLTS	1	nTCRE	11
nIBIB	11	nTCNRS	21
nIBRS	11	nTCIB	21
nIBNRS	11	nTCRS	21
nIBLTS	10	nTCLTS	21
nNRSNRS	11	nRERE	11
nNRSRS	11	nRETC	11
nNRSIB	9		
nNRSLTS	8		
nNRSTC	16		
nNRSRE	16		

Table B.4: The number of presynaptic neurons that each postsynaptic neuron connects to ($nPrePost$) in the 95-5 (nIB:nRS) model configuration.

and decay (β) time constants in addition to the maximal synaptic conductance (g_{max}) to achieve physiological neuronal firing.

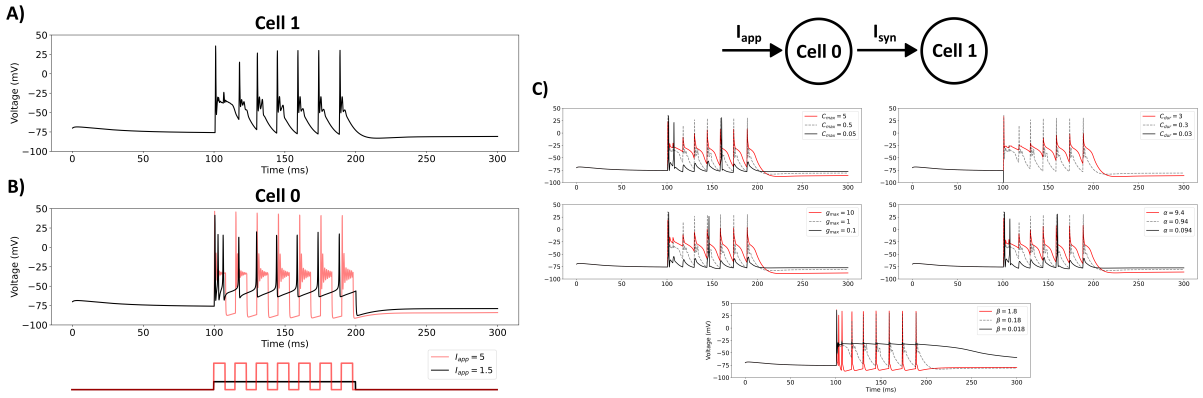

Figure B.1: Exploring how variations in synaptic parameters affect postsynaptic firing in a 2-cell network of layer 6 non-tufted regular spiking (NRS) neurons. Using default parameters ($g_{max} = 1\mu$S, $\alpha = 0.94(\text{ms}\cdot\text{mM})^{-1}$, $\beta = 0.18\text{ms}^{-1}$, $C_{max} = 0.5$ and $C_{dur} = 0.3$), distorted firing is observed in *Cell 1* (A), which is similar in effect to a strong applied current in *Cell 0* (B). (C): Firing behaviour of *Cell 1* under one-at-a-time variation of each synaptic parameter. The units of applied current are in nA.

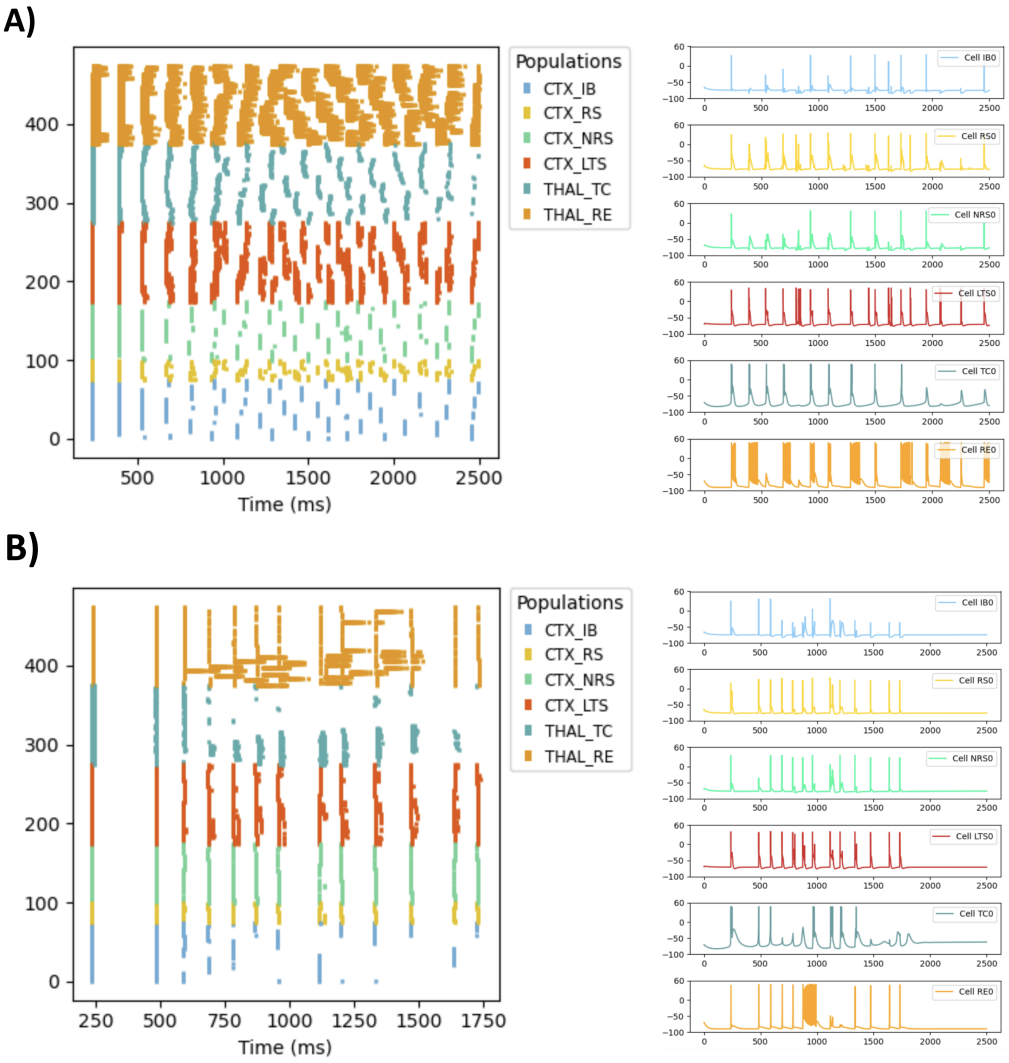

Figure B.2: Poor model fitting results for (A) spindle oscillations and (B) spike-wave discharges using only maximal synaptic conductances as fitting parameters. Population-level activity matches target metrics while individual neuron voltage traces show distorted action potentials.

B.4 Model fitting: staged parameter fitting process

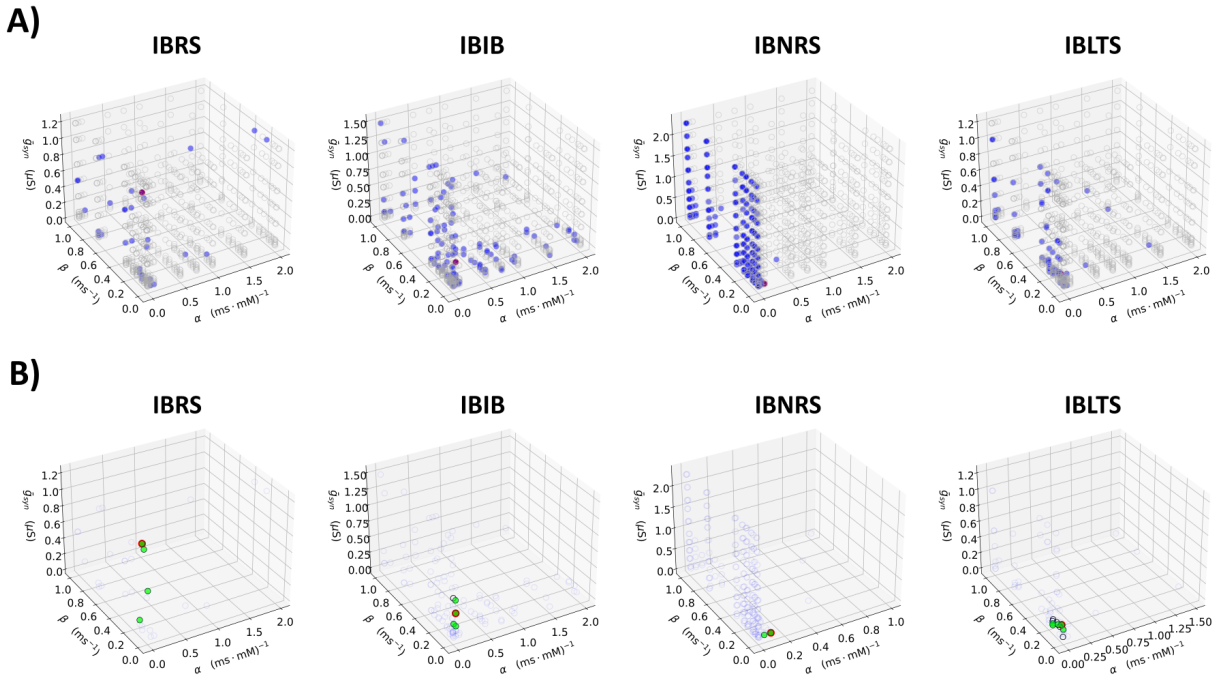

Figure B.3: (A): For each synapse type, multiple parameter triplets ($\bar{g}_{syn}$, α, β) yielded good fits (solid blue points). Points with gray outlines represent the sampled parameter space, with solid red points indicating our selected parameter triplets. (B): Testing model sensitivity to deviations from the nominal values (solid red points) by up to 90% (IBRS and IBLTS), 70% (IBIB), and 75% (IBNRS) in each parameter dimension. Transparent points with blue outlines represent good fits as in panel A, and in black outlines, the parameter cloud tested for sensitivity. Solid green points indicate parameter sets that maintained good network performance despite these deviations.

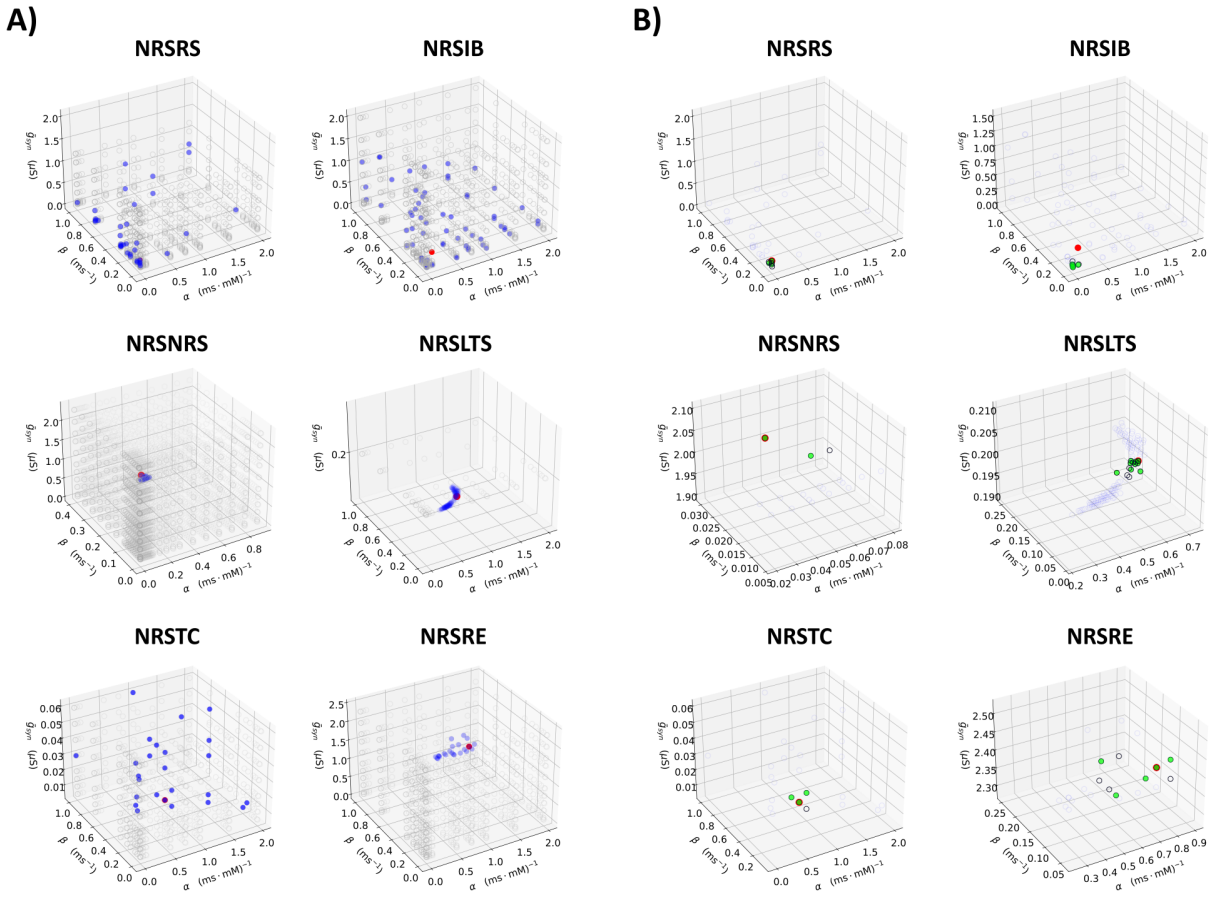

Figure B.4: (A): For each synapse type, multiple parameter triplets ($\bar{g}_{syn}$, α, β) yielded good fits (solid blue points). Points with gray outlines represent the sampled parameter space, with solid red points indicating our selected parameter triplets. (B): Testing model sensitivity to deviations from the nominal values (solid red points) by up to 100% (NRSRS and NRSIB), 30% (NRSLTS), and 50% (NRSNRS, NRSTC and NRSRE) in each parameter dimension. Transparent points with blue outlines represent good fits as in panel A, and in black outlines, the parameter cloud tested for sensitivity. Solid green points indicate parameter sets that maintained good network performance despite these deviations.

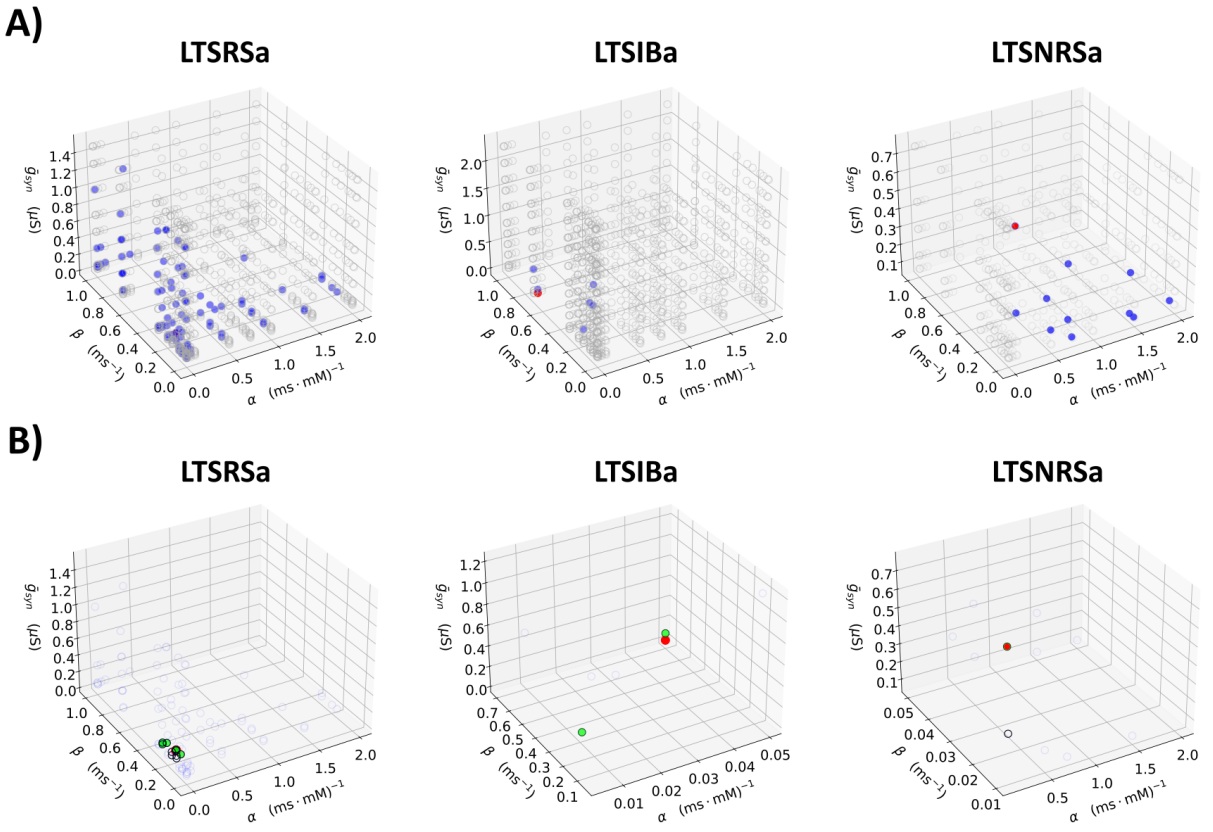

Figure B.5: (A): For each synapse type, multiple parameter triplets ($\bar{g}_{syn}$, α, β) yielded good fits (solid blue points). Points with gray outlines represent the sampled parameter space, with solid red points indicating our selected parameter triplets. (B): Testing model sensitivity to deviations from the nominal values (solid red points) by up to 50% (LTSRSa), 200% (LTSIBa), and 75% (LTSNRSa) in each parameter dimension. Transparent points with blue outlines represent good fits as in panel A, and in black outlines, the parameter cloud tested for sensitivity. Solid green points indicate parameter sets that maintained good network performance despite these deviations.

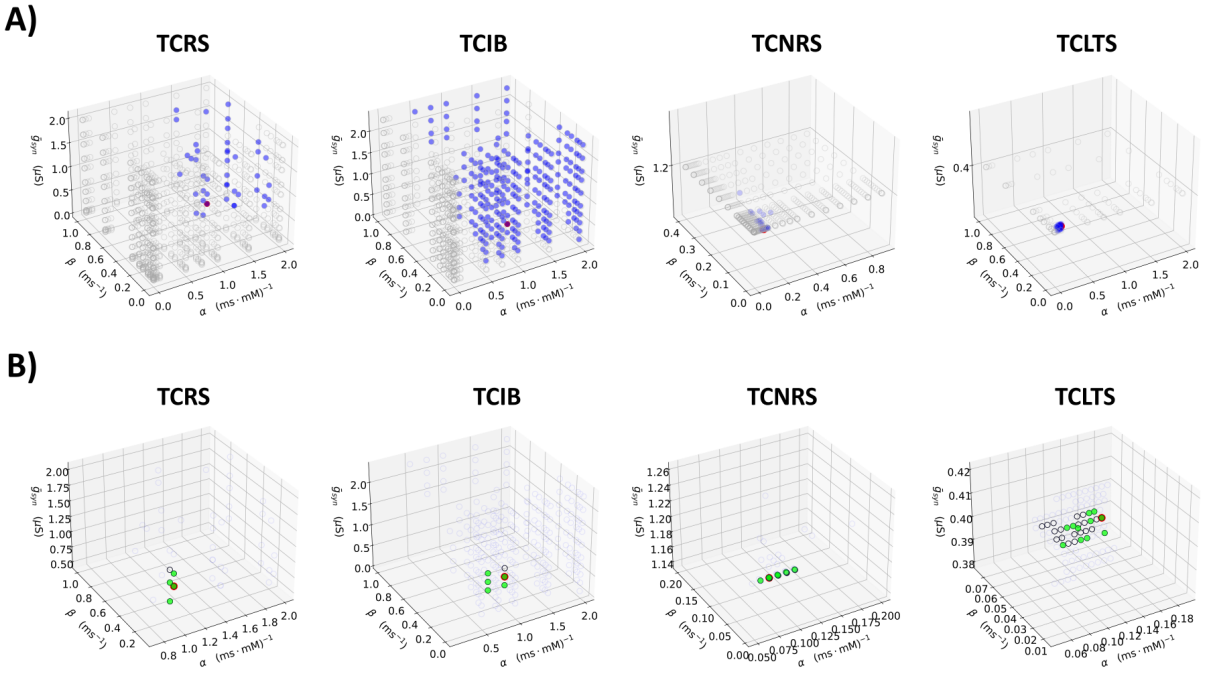

Figure B.6: (A): For each synapse type, multiple parameter triplets ($\bar{g}_{syn}$, α, β) yielded good fits (solid blue points). Points with gray outlines represent the sampled parameter space, with solid red points indicating our selected parameter triplets. (B): Testing model sensitivity to deviations from the nominal values (solid red points) by up to 35% (TCRS), and 30% (TCIB, TCNRS and TCLTS) in each parameter dimension. Transparent points with blue outlines represent good fits as in panel A, and in black outlines, the parameter cloud tested for sensitivity. Solid green points indicate parameter sets that maintained good network performance despite these deviations.

B.5 Synchrony measure

The model fitting process required using a measure of synchrony to characterize the two network states of interest: spindle oscillations and spike-wave discharges. We used our previous model, specifically the behaviour of the cortical pyramidal (PY) and thalamocortical (TC) populations to obtain target metrics. The pattern of synchronization was significantly different between the PY and TC populations. Namely, for the PY population it is observed that synchronization mostly occurs between all cells. It would seem reasonable to calculate the measure of synchrony S using a population averaged $V(t)$, as defined in [76, 77, 78]. However, it is observed that using such a quantity results in undesirable averaging effects that are far more sensitive to small differences in synchrony between any two cells, as illustrated in Figure B.7. Given that the synchrony measure is dependent on the variance of the voltage, using an average voltage of the full population results in a lower variance of such a population average as compared to the variance of a pairwise-average. Moreover, if the population is as synchronized as suggested by a raster plot, it is expected that the synchrony measure between any two cells should be similar. This is illustrated in Figure B.8 by considering the pairwise synchrony for all cells in the PY population.

In the case of the TC population, the spindles state consists of alternate bursts of synchrony generated by two distinct clusters. Due to the connectivity structure within the population, it is observed that neurons organize themselves to belong to either one of the clusters. In particular, neurons that belong to the same cluster exhibit a higher degree of synchrony (measured by $S_{i,j}$) between each other, while exhibiting a relatively lower degree of synchrony with neurons in the other cluster, as illustrated in Figure B.9.

Given these differences in synchronization patterns both within and across populations, as well as our observations of potential issues arising from the use of a population-averaged voltage, it was essential to modify the synchrony measure defined in [76, 77, 78] to more accurately characterize the synchrony of our neural populations of interest.

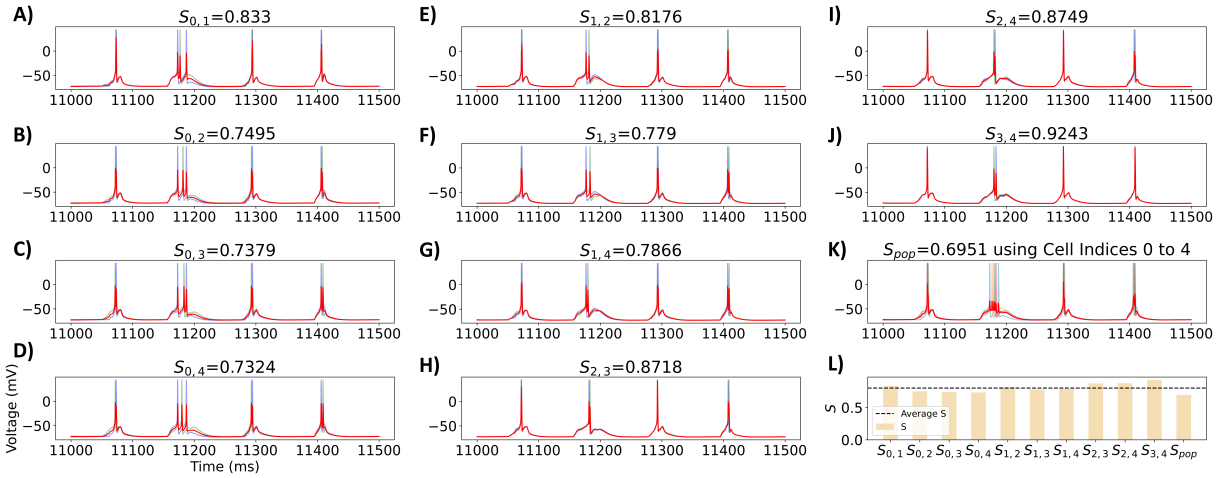

Figure B.7: An illustration of undesirable averaging effects of using a population average $V(t)$ to calculate synchrony measure for a small subset of the PY population (cell indices 0 to 4). Voltage traces of pairs of cells from the subset are given in (A)-(J) while voltage traces of the full subset are given in (K). In each case, the average voltage is plotted in red, and the synchrony measure is given in the heading. (L): A comparison of the synchrony measure between individual pairs ($S_{i,j}$) and a measure using the full subset (S_{pop}). The synchrony measure using the full subset is significantly lower than the measure between any pairs of cells in the subset.

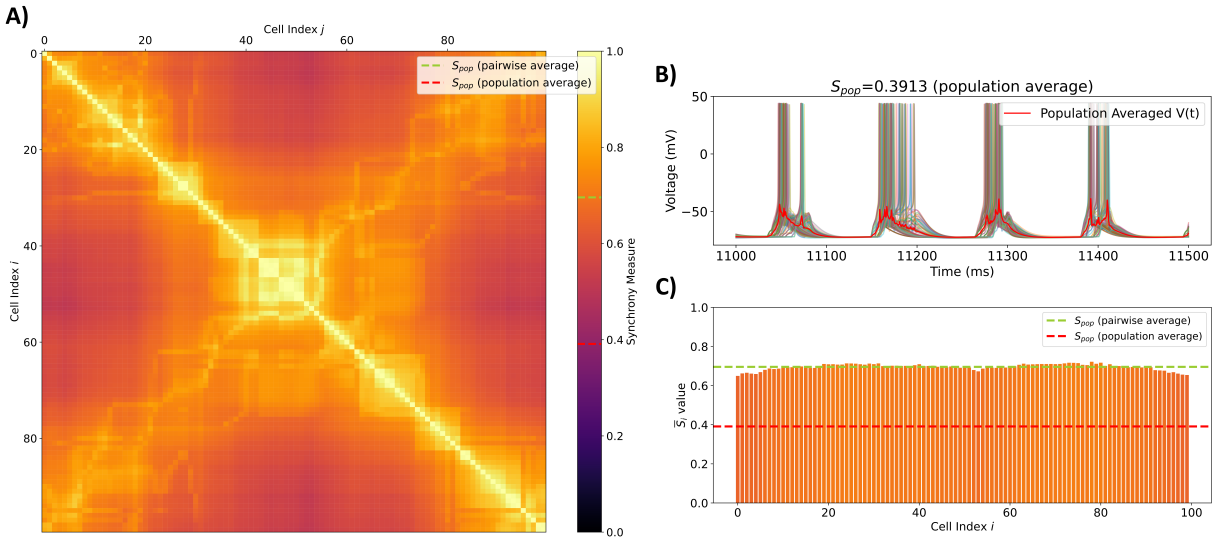

Figure B.8: (A): Synchrony matrix with a measure $S_{i,j}$ for every pair of cells in the PY population from 11 to 11.5s for the simulated experiment using GABAa conductance at 100% baseline value. S_{pop} (pairwise average) equal to 0.6959 refers to our modified population synchrony, whereas S_{pop} (population average) equal to 0.3913 refers to a population synchrony using a population-averaged voltage as described in [76, 77, 78]. (B): Voltage traces of the PY population with the population average voltage given in red. (C) Average pairwise synchrony measure $\overline{S}_i$ for PY cells.

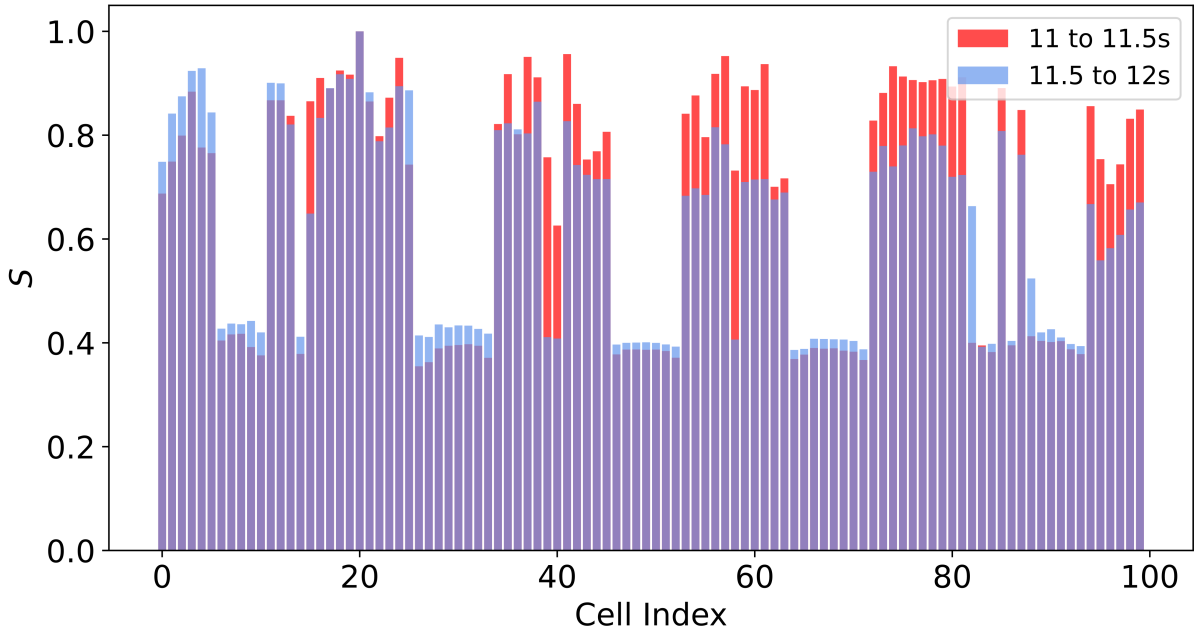

Figure B.9: Distribution of synchrony measure $S_{20,j}$ (between neuron of index 20 and all other neurons in the TC population) over two different time intervals.

B.6 Allopregnanolone application experiment curve fitting

Inhibitory postsynaptic currents mediated by GABAa receptors post application of allopregnanolone, obtained from experimental works (thereby referred to as I_{data}), were fit using the following equation:

$$I_{GABAa} = -\min(\tilde{I}_{data}) \cdot \frac{1}{s(T_{dur})} \cdot s(t) \tag{B.90}$$

where

$$\tilde{I}_{data} = \frac{I_{data}}{(V_{hold} + 85)} \quad \text{and} \quad s(t) = \begin{cases} \frac{\alpha C_{max}}{\alpha C_{max}+\beta}\left(1 - e^{-t(\alpha C_{max}+\beta)}\right), & 0 \leq t < T_{dur} \\ \left[\frac{\alpha C_{max}}{\alpha C_{max}+\beta}\left(1 - e^{-T_{dur}(\alpha C_{max}+\beta)}\right)\right] e^{-\beta(t-T_{dur})}, & t \geq T_{dur} \end{cases} \tag{B.91}$$

All experimental data were scaled by factoring out the voltage dependent term for curve fitting purposes. This allowed for the isolation of the synaptic gating variable $s(t)$ dynamics, making the analysis of the synaptic gating more direct and interpretable. We interpret the scaling factor $\min(\tilde{I}_{data}) \cdot \frac{1}{s(T_{dur})}$ as the channel's maximal intrinsic conductance where $s(T_{dur})$ is equal to the maximum of the gating variable and $\min(\tilde{I}_{data})$ represents the maximal conductance.

We used MATLAB's *lsqcurvefit* function to find the best-fitting α, β and T_{dur} parameters in Equation (B.90), for the given data. By pre-scaling the data, these parameters could be estimated to directly fit $s(t)$. As illustrated in Figure B.10, without pre-scaling, the relative importance of fitting different parts of the curve changes. This results in the optimization converging to different (non-ideal) local minima in the parameter space.

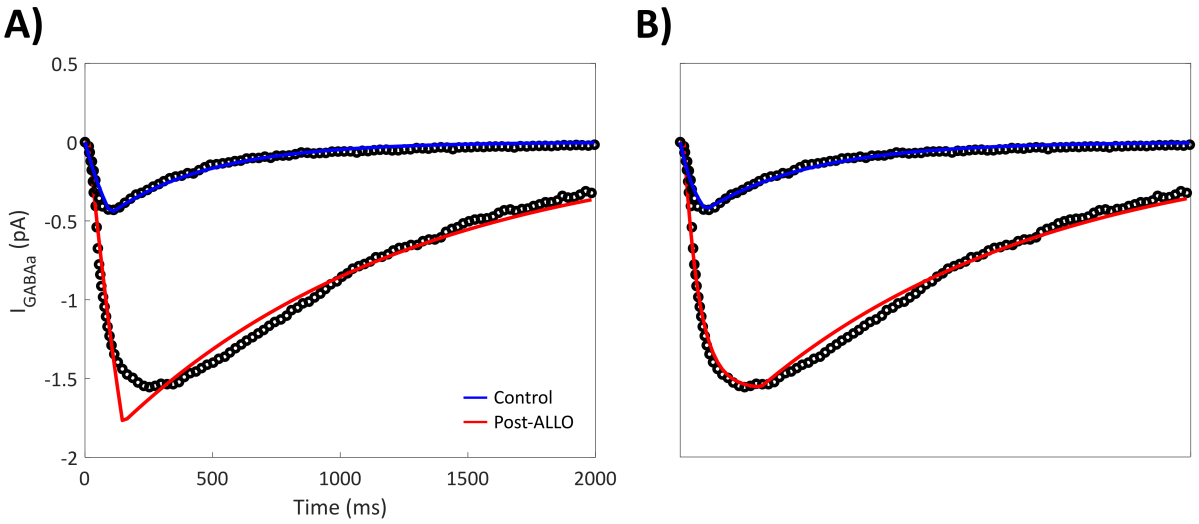

Figure B.10: Sample curve fits of inhibitory postsynaptic currents post application of allopregnanolone, without (A) and with (B) pre-scaling data by factoring out the voltage dependent term.

Appendix C

Appendix for Chapter 5

C.1 Redefining steady-state activation/inactivation of I_{Naf} in TC and RE cells

In both the thalamic cells, the dynamics of the fast sodium channel were described using voltage-dependent forward (α) and backward (β) rate constants that control the transitions between channel states. The steady-state activation and inactivation variables were defined as the equilibrium solutions of these state transitions, given by the following equations:

$$m_{Naf\infty} = \frac{\alpha_m}{\alpha_m + \beta_m} \tag{C.1}$$

$$h_{Naf\infty} = \frac{\alpha_h}{\alpha_h + \beta_h} \tag{C.2}$$

where $m_{Naf\infty}$ and $h_{Naf\infty}$ denote steady-state activation and inactivation, respectively.

For TC cells, rate constants were given by:

$$\alpha_{m_{Naf}} = \frac{0.32 \cdot (-V - 12)}{\exp(\frac{-V-12}{4}) - 1} \quad \text{and} \quad \beta_{m_{Naf}} = \frac{0.28 \cdot (V - 15)}{\exp(\frac{V-15}{5}) - 1} \tag{C.3}$$

$$\alpha_{h_{Naf}} = 0.128 \cdot \exp\left(\frac{-V - 8}{18}\right) \quad \text{and} \quad \beta_{h_{Naf}} = \frac{4}{1 + \exp(\frac{-V+15}{5})} \tag{C.4}$$

While for RE cells, rate constants were given by:

$$\alpha_{m_{Naf}} = \frac{0.32 \cdot (-V - 42)}{\exp(\frac{-V-42}{4}) - 1} \quad \text{and} \quad \beta_{m_{Naf}} = \frac{0.28 \cdot (V + 15)}{\exp(\frac{V+15}{5}) - 1} \tag{C.5}$$

$$\alpha_{h_{Naf}} = 0.128 \cdot \exp\left(\frac{-V-38}{18}\right) \qquad \text{and} \qquad \beta_{h_{Naf}} = \frac{4}{1+\exp(\frac{-V-15}{5})} \tag{C.6}$$

Since alterations in channel activity due to $SCN8A$ mutations were specific to half-activation voltage and the slope factor in the Boltzmann functional form, we needed to redefine the existing $m_{Na\infty}$ and $h_{Na\infty}$ expressions for both thalamic cell types in terms of a Boltzmann-like function. By employing MATLAB's $lsqcurvefit$ function, we found the best-fitting $V_{1/2}$ and k parameters that fit the steady-state activation/inactivation curves given in Equations (C.3)- (C.6).

For TC cells, the redefined steady-state functions were given by:

$$m_{Naf\infty} = \frac{1}{1+\exp(\frac{-V+0.978}{7.434})} \qquad \text{and} \qquad h_{Naf\infty} = \frac{1}{1+\exp(\frac{V+3.317}{4.036})}$$

While, for RE cells, the redefined steady-state variables were defined by the following equations:

$$m_{Naf\infty} = \frac{1}{1+\exp(\frac{-V-29.017}{7.415})} \qquad \text{and} \qquad h_{Naf\infty} = \frac{1}{1+\exp(\frac{V+33.333}{4.055})}$$

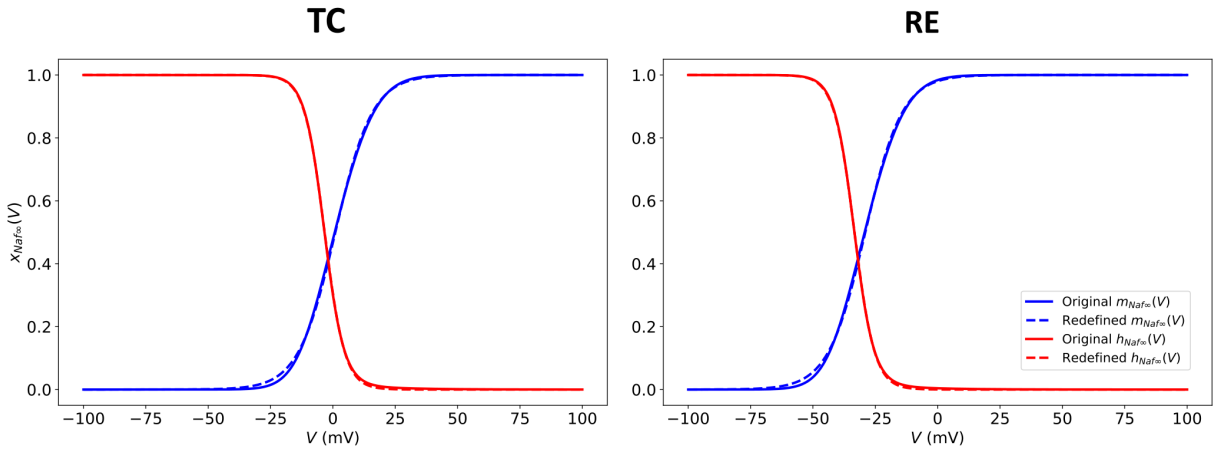

Figure C.1: Comparison of the original and redefined steady-state activation and inactivation functions for the fast sodium channel in TC and RE cells.

C.2 Effect of modifying the maximal I_{K2} conductance in modelling the $SCN2A$ mutation

The effect of the $Scn2a^{+/-}$ mutation has been reported to involve a reduction in maximal sodium conductance density, along with down-regulation of multiple potassium channels. To model this, we modified the parameter corresponding to the maximal conductance of the fast sodium current, I_{Naf}, as described in Equation (5.1). Additionally, we adjusted the maximal conductance parameter for I_{K2} (g_{K2}). However, using the g_{K2} value reported in the literature did not reproduce the increased neuronal firing observed experimentally, as shown in the top row of Figure C.2. To investigate this further, we analyzed spike-count response curves of excitatory cortical cells across varying levels of g_{K2} reduction (Figure C.2, bottom row). Based on this analysis, and in order to qualitatively match the experimentally observed firing patterns, we adjusted g_{K2} to approximately twice the reported reduction—changing it from about 33% to 75%.

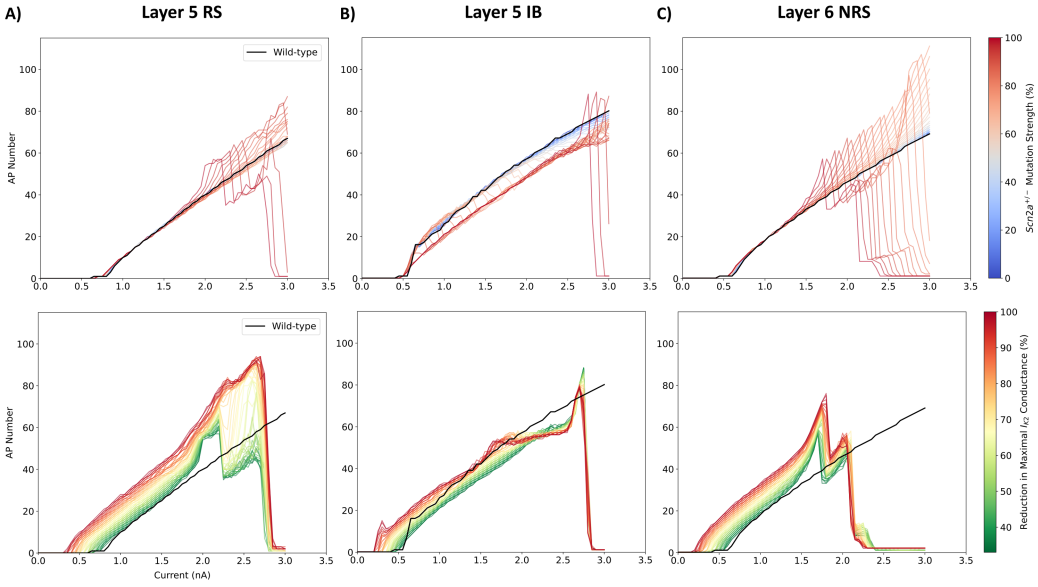

Figure C.2: Spike-count responses of excitatory cortical cells under the $Scn2a^{+/-}$ mutation. (Top row): Responses with a fixed 33% reduction in I_{K2} conductance, across varying mutation strengths. (Bottom row): Responses at 100% mutation strength, with varying levels of I_{K2} conductance reduction (33-100%). Based on this analysis, we set the I_{K2} conductance reduction to 75% (adjusted from 33% reported in [212]) to qualitatively match experimentally observed neuronal firing patterns.